Development of Metabolite- and ROS-Responsive Lipid Switches for Controlled Liposomal Drug Release

A Dissertation Presented for the

Doctor of Philosophy

Degree

The University of Tennessee, Knoxville

Brooke E. Smith

May 2026

Copyright © 2026 by Brooke Smith.

All rights reserved.

ACKNOWLEDGEMENTS

The growth through my time in graduate school has been immense and would not be possible without the many individuals who have supported me in both my personal and academic life. I am so very grateful for each of you.

The foundation of my success I credit first to my parents, who have pushed and supported me throughout my life. From a young age, I remember that whenever I tried hard things, you both were there to encourage, guide, comfort, correct, and push me. I deeply value your guidance and appreciate the sacrifices you both have made. Thank you for your continued encouragement and confidence in me, and for instilling core values that have shaped me into who I am. To my siblings, I thank you each for the happiness and joy you have each brought into my life. To Blake and Addie, I am so thankful for you both as role models in your pursuit of the things you love. To Brenna and Bryce, thank you for supporting me with the many visits which have been such a light these past years and for motivating me to be a better role model for each of you. And to my friends Ashlynn and Colson, thank you for your constant encouragement and lasting friendship that has been such a source of happiness for many years.

I am also incredibly grateful for the many teachers, advisors, and mentors that have impacted me over the many years. Thank you to Krista Mauldin for first sparking my interest in chemistry, your knowledge and passion for science are what first motivated me to pursue chemistry. To Dr. Royce Dansby-Sparks, thank you first introducing me to chemistry research and encouraging me to pursue graduate school. Your guidance and support shaped my future in research and helped push me through doors I did not know

existed, and your mentorship was the driving force behind my aspirations. Dr. Thompson, thank you for your mentorship in both faith and science. Your teaching made organic chemistry incredibly memorable and fun and ultimately laid the groundwork for the research I've pursued. And to Dr. Herbert, thank you for your confidence in me, it has encouraged me in a multitude of ways. I remember fondly the fun of flannel Fridays and the laughs you brought to each of us in Rogers.

I am also thankful to my committee members, Dr. Joshua Baccile, Dr. Fred Heberle, and Dr. Todd Reynolds. Your intellectual guidance and valuable discussions at my defenses have improved me as a researcher and have deepened my understanding. I would also like to acknowledge the support of my collaborators, Dr. Joshua Baccile, Dr. Dillon McBee, Robert Turner, and Miranda Phillips, for their extensive help and expertise. Finally, I am profoundly grateful to Dr. Michael Best. Thank you for welcoming me into your lab and for your constant guidance and mentorship. The research environment you foster has been pivotal in my growth as an independent researcher, and your dedication, patience, and guidance are qualities I hope to emulate as a researcher and mentor.

A sincere appreciation also belongs to my Best lab coworkers, who I've had the privilege of working with. I am especially grateful for Mayesha, Annaleena, and Caitlyn, who are each incredible scientists, but also great friends. Thank you for the many laughs, your encouragement, and for making the lab struggles more bearable. I am also thankful for the past and present members of the Best lab, Megan, Ruhani, Jinchao, Christelle, Justin, Kazi, Michael, Mahbub, Rob, and Ellen. Thank you for the camaraderie within the lab, for the outings and celebrations we've shared, and for fostering a collaborative lab

environment that has been a pleasure to work in. I also am deeply honored and thankful to have mentored Caleb Russell as an undergraduate student. Your growth in lab has been a joy to watch, and I am thankful to you for growing with me as a mentor and mentee. Graduate school is difficult, and those with the best understanding and support are those also going through it with you. My dear friends Christy, Susan, and Abby, I am so very thankful for your friendship and that graduate school brought us together. Each of you is an incredible scientist and friend, and I will always treasure our weekly get togethers and friendships.

The most important thanks belong to my husband Austin Smith. Without his support over the last five years, this journey would have been exponentially more difficult. I am so blessed with your love and support. Thank you for taking this journey with me, through the long hours, late nights, and tears, but also through the milestones, celebrations, and the many happy memories we've made during this period in our lives. Thank you for your constant belief in me, and for your never-ending love and patience. I am excited as we continue to explore our future together, I love you so very much.

ABSTRACT

Liposomes are lipid-based nanoscale vesicles widely used in therapeutic delivery and biological membrane modeling. Their bilayer structure enables encapsulation of both hydrophobic and hydrophilic cargo, making them valuable drug delivery platforms. Although liposomes improve therapeutic pharmacokinetics, only a fraction of encapsulated cargo is typically released before liposomal clearance. This dissertation investigates stimuli-responsive lipid architectures that convert endogenous biochemical signals into controlled cargo release. Rather than relying solely on passive delivery, these systems incorporate responsive motifs directly within the membrane to induce localized perturbation and therapeutic activation, enhancing cargo release specifically at disease sites.

Chapter 2 details the development of a bis-triphenylphosphonium lipid switch responsive to nucleotide-derived and phosphate-containing metabolites when incorporated within liposomes. Systematic variation of liposomal membrane composition revealed that cargo release depends not only on headgroup recognition, but also on bilayer packing stress and lipid organization. Both hydrophobic and hydrophilic release were tuned through compositional adjustment. Selectivity between guanosine triphosphate and sodium triphosphate was achieved by modifying liposomal membrane composition, highlighting the central role of membrane dynamics in switch behavior.

Chapter 3 examines a reactive oxygen species-responsive doxorubicin lipid prodrug incorporated directly into liposomal membranes, combining liposomal delivery with prodrug-based masking. An arylboronate self-immolative linker between doxorubicin and

the lipid scaffold enabled hydrogen peroxide-triggered release under oxidative conditions associated with diseased cells. Electrospray ionization mass spectrometry confirmed prodrug cleavage, and cellular studies demonstrated concentration-dependent cytotoxicity in A375 melanoma cells. This hybrid lipid–prodrug strategy combines the pharmacokinetic advantages of liposomes with redox-triggered therapeutic activation, establishing a modular platform for disease-selective delivery.

Chapter 4 explores expansion of the lipid switch framework toward succinate recognition using nitrogen-based anion-binding headgroups, including cyclic guanidinium derivatives. Although mechanistic reassessment introduced structural uncertainty, these studies provided insight into dicarboxylate binding, headgroup-mediated membrane perturbation, and the challenges of translating small-molecule recognition motifs into bilayer systems.

Overall, this dissertation demonstrates that membrane-integrated chemical responsiveness is a versatile strategy for stimulus-selective drug delivery by linking molecular recognition to membrane reorganization. These systems provide a foundation for future liposomal platforms designed to respond to metabolic and redox imbalance in disease.

TABLE OF CONTENTS

Chapter 1. Introduction to Lipids, Liposomes, and Stimuli-Responsive Drug Delivery.... 1

1.1 Lipids in Biological Systems 1

1.2 Lipid Structure and Physicochemical Properties 2

1.3 Lipid Self-Assembly and Liposomal Membranes 6

1.3.1 Lipid Packing Parameters and Self-Assembly 6

1.3.2 Liposomal Structure, Classification, and Properties 8

1.3.3 Liposomal Membrane Phase Behavior and Stability 10

1.3.4 Liposome Preparation and Characterization 12

1.4 Liposomes in Drug Delivery 14

1.4.1 Nanoscale Drug Delivery Vehicles 14

1.4.2 Liposomes as Drug Delivery Platforms 15

1.4.3 Surface-Based Liposome Modifications 17

1.5 Stimuli-Responsive and Triggered Liposomal Release 20

1.5.1 Passive and Active Triggered Release Strategies 20

1.5.2 Lipid Switches and Membrane Perturbation Mechanisms 22

1.6 Scope and Organization 24

Chapter 2. Engineering Tunable GTP/TPi-Responsive Liposomes 26

2.1 Project Overview 26

2.2 Introduction and Motivation 27

2.2.1 Biological Relevance of GTP 29

2.2.2 Nucleotide-Responsive Liposomal Systems 30

2.3 Design of Bis-Triphenylphosphonium Lipid Switch 33
2.4 Hydrophobic Dye Release Experiments 35
2.4.1 Initial Metabolite Selectivity Screening 35
2.4.2 Formulation Development and Identification of Tunable Metabolite Responses 36
2.4.3 Time-Dependent Fluorescence Release Assays for GTP/TPi 38
2.4.4 Fluorescence Release Assays in Competing Environments 46
2.5 Size and Morphology Change Studies 54
2.5.1 GTP/TPi-Lipid Binding Studies 54
2.5.2 Dynamic Light Scattering Studies 54
2.5.3 Zeta Potential Studies 57
2.5.4 Transmission Electron Microscopy Imaging 60
2.6 Hydrophilic Cargo Release Experiments 61
2.6.1 Formulation Development for GTP/TPi Release 61
2.6.2 Time-Dependent Fluorescence Release Assays for GTP/TPi 64
2.6.3 Therapeutic Release Assays for GTP/TPi 65
2.7 Miscellaneous Experiments 69
2.7.1 Cargo Encapsulation Efficiency Studies and Calculations 69
2.7.2 Alternate Synthetic Routes for Triphenylphosphonium Addition 71
2.8 Conclusions 72
2.9 Synthesis and Experimental Procedures 74

Chapter 3. Reactive Oxygen Species-Responsive Lipid-Prodrug Liposomes for Doxorubicin Delivery 92
3.1 Project Overview 93
3.2 Introduction and Motivation 94
3.2.1 Biological Relevance of ROS 94
3.2.2 ROS-Responsive Prodrug Strategies 96
3.2.3 ROS-Responsive Lipids and Liposomal Delivery Systems 98
3.3 Design of ROS-Responsive Dox Lipid Prodrug and Control 100
3.4 Electrospray Ionization Mass Spectrometry Experiments 104
3.5 Size and Morphology Change Studies 105
3.5.1 Dynamic Light Scattering Studies 105
3.5.2 Zeta Potential Studies 107
3.6 Cell Viability Experiments 108
3.6.1 Initial Testing of Free Lipid-Prodrug 110
3.6.2 Concentration-Dependent Cell Viability Assays with A375 Cells 108
3.6.3 ROS Quantification Among Cancerous Cell Lines 112
3.7 Conclusions 114
3.8 Synthesis and Experimental Procedures 116
Chapter 4. Development and Mechanistic Evaluation of Additional Succinate-Responsive Lipid Switches 121
4.1 Project Overview 121
4.2 Introduction and Motivation 122

4.3 Design and Development of a Cyclic Guanidinium Lipid Switch 125
4.3.1 Synthetic Design of a Cyclic Guanidinium Lipid Switch..... 125
4.3.2 Hydrophobic Dye Release and Kinetic Evaluation 128
4.3.3 Structural Characterization Studies..... 133
4.3.4 Metabolite Selectivity Screening 135
4.3.5 Fluorescence Microscopy Studies..... 138
4.3.6 Mechanistic Reassessment and Structural Considerations 139
4.4 Alternate Nitrogen-Based Lipid Switches 141
4.5 Design of Thiourea Lipid Switch..... 144
4.6 Conclusions..... 146
4.7 Synthesis and Experimental Procedures 147
Chapter 5. Conclusions 160
List of References 163
Appendix..... 197
Vita..... 230

LIST OF TABLES

Table 1.1. Example T_m values for common liposomal lipids. 11

Table 2.1. Summary of formulations explored for hydrophobic NR release..... 39

LIST OF FIGURES

Figure 1.1. Representative structures of the three lipid classes. 3

Figure 1.2. Structure breakdown of phospholipids showing the headgroups of some important lipids. 4

Figure 1.3. Lipid assemblies from the associated packing parameter and lipid shape. 7

Figure 1.4. Classification of liposomes based on lamellarity and size. 9

Figure 1.5. Polymeric, inorganic, and lipid-based nanoparticles for drug delivery applications. 15

Figure 1.6. Representation of the different categories of liposomes for therapeutic delivery. 19

Figure 2.1. Overall system design graphic for BPLS 2.6 with tunable release. 27

Figure 2.2. Previous ATP- and GTP-responsive lipid switches. 32

Figure 2.3. Metabolite selectivity screening for 2.6. 37

Figure 2.4. NR dye release highlighting tunable metabolite-triggered response through variation of membrane composition. 40

Figure 2.5. NR endpoint release assays comparing both formulation types with either TPi or GTP treatment. 41

Figure 2.6. Kinetic NR release studies over 15 hours with TPi or GTP treatment. 43

Figure 2.7. Curve fittings of kinetic NR release curves for k_2 and $t_{1/2}$ calculations. 44

Figure 2.8. Long-term stability and leakage of liposomes over 7 days. 46

Figure 2.9. Additional metabolite selectivity screen with optimized 2.6 formulations. ... 48

Figure 2.10. Passive leakage of PBS-hydrated liposomes in phosphate rich and altered osmolarity environments. 50
Figure 2.11. NR release from liposomes in complex metabolite environments. 51
Figure 2.12. NR release from liposomes in DMEM + 10% FBS. 53
Figure 2.13. Binding isotherms for 2.6-TPi and 2.6-GTP. 2.6-TPi solution binding study was completed through fluorescence titration. 55
Figure 2.14. DLS comparisons of both 2.6 liposome formulations treated with TPi and GTP. 56
Figure 2.15. Raw DLS curves of 2.6 liposomes from both formulations. 58
Figure 2.16. ZP of both liposome formulations with buffer, TPi or GTP treatment. 60
Figure 2.17. TEM images of 35/35/30 2.6/DOPE/PC liposomes before and after GTP and TPi treatment. 62
Figure 2.18. Kinetic SRB studies investigating both formulations over 16 hours with either TPi or GTP treatment. 66
Figure 2.19. Curve fittings of kinetic SRB release curves for k2 and t1/2 calculations. .. 67
Figure 2.20. Release of Dox from 2.6 liposomes treated with TPi or GTP. 68
Figure 2.21. Fluorescence calibration curves of NR, SRB, and Dox for encapsulation efficiency calculations. 70
Figure 2.22. NMR comparison of Staudinger reduction products for experimental reactions. 73
Figure 3.1. Drug release mechanism for arylboronate containing ROS-responsive prodrugs. 98

Figure 3.2. ESI-MS study highlighting Dox release from 3.5 while 3.9 remains uncleaved. 105
Figure 3.3. DLS of untreated and ROS-treated ROSDoxL 3.5 and DoxL 3.9 liposomes. 106
Figure 3.4. PDI of untreated and treated ROSDoxL 3.5 and DoxL 3.9 liposomes. 107
Figure 3.5. ZP of untreated and treated ROSDoxL 3.5 and DoxL 3.9 liposomes. 108
Figure 3.6. MTS cell viability studies with free and liposomal ROSDoxL 3.5 and DoxL 3.9, free Dox, and control PC liposomes over a range of concentrations. 109
Figure 3.7. MTS cell viability studies with free 3.5 with and without H_2O_2. 111
Figure 3.8. MTS cell viability controls with ROS, buffer, and DMSO treatments. 112
Figure 3.9. Relative ROS production comparison of A375, HeLa, and Hep-G2. 113
Figure 4.1. Previously developed carboxylate sensors and their potential interactions. 124
Figure 4.2. NR release from liposomes with varying CG 4.3%. 129
Figure 4.3. NR release from liposomes with varying DOPE%. 131
Figure 4.4. NR release from liposomes with varying destabilizing lipids. 132
Figure 4.5. DLS studies with varying concentrations of CG 4.3. 134
Figure 4.6. TEM images of 35 4.3/40 DOPE/25 PC liposomes before and after treatment with succinate. 135
Figure 4.7. Metabolite selectivity screening through NR release for 4.3 liposomes. 136
Figure 4.8. Confocal microscopy aggregation study of 4.3 liposomes treated with succinate and imaged over 60 minutes. 139
Figure 4.9. Metabolite selectivity screening through NR release for QA 4.4. 143

LIST OF SCHEMES

Scheme 2.1. Synthesis of bis-phosphonium lipid switch 2.6. 34

Scheme 3.1. ROS-triggered cleavage of ROSDoxL 3.5 for release of Dox. 101

Scheme 3.2. Synthetic route for ROSDoxL 3.5. 102

Scheme 3.3. Synthetic route for DoxL 3.9. 103

Scheme 4.1. Synthetic reaction scheme for CG 4.3. 127

Scheme 4.2. CG 4.3 proposed binding to succinate with potential conformational change. 128

Scheme 4.3. Synthesis of QA 4.4 and guanidinium 4.5. 142

Scheme 4.4. Synthetic reaction scheme for TUL 4.10. 145

LIST OF ABBREVIATIONS

ADP: Adenosine 5’-diphosphate

AMP: Adenosine 5’-monophosphate

ANTS: 8-aminonaphthalene-1,3,6-trisulfonic acid

ATP: Adenosine triphosphate

BPLS: Bis-phosphonium lipid switch

CG: Cyclic guanidinium

CTP: Cytidine 5’-triphosphate

CuAAC: Copper azide alkyne cycloaddition

DCF-DA: 2′,7′-dichlorodihydrofluorescein diacetate

DLS: Dynamic light scattering

DOPE: 1,2-Dioleoyl-*sn*-glycero-3-phosphoethanolamine

Dox: Doxorubicin

DoxL: Non-responsive control Dox lipid

DPX: 1,1'-(1,4-phenylenebis(methylene))bis(pyridin-1-ium) bromide

EGFR: Epidermal growth factor receptor

EM: Electron microscopy

EPR: Enhanced permeation and retention

ER: Endoplasmic reticulum

ESI-MS: Electrospray ionization mass spectrometry

ETC: Electron transport chain

FBP: D-fructose-1,6-bisphosphate

FBS: Fetal bovine serum

FP: D-fructose-6-phosphate

Fum: Fumaric acid

GTP: Guanosine triphosphate

GUV: Giant unilamellar vesicle

HEPES: 4-(2-hydroxyethyl)piperazine-1-ethane-sulfonic acid

HIF-1α: Hypoxia-inducible factor

LNP: Lipid nanoparticle

LPC: Lysophosphatidylcholine

LUV: Large unilamellar vesicle

Mal: Malic acid

MLV: Multilamellar vesicle

MTS: 3-(4,5-dimethylthiazol-2-yl)-5-(3-carboxymethoxyphenyl)-2-(4-sulfophenyl)-2H-tetrazolium

NR: Nile red

Oxa: Oxaloacetic acid

PC: Phosphatidylcholine

PE: Phosphatidylethanolamine

PEG: Polyethylene glycol

Pen/strep: Penicillin-streptomycin

PG: Phosphatidylglycerol

PI: Phosphatidylinositol

Pi: Inorganic phosphate

PLA_2: Phospholipase A2

PPi: Sodium pyrophosphate

PS: Phosphatidylserine

Rd-PE: Rhodamine-PE

RES: Reticuloendothelial system

ROS: Reactive oxygen species

ROSDoxL: Reactive oxygen species-responsive doxorubicin lipid prodrug conjugate

SAXS: Small-angle X-ray scattering

SDH: Succinate dehydrogenase

SEC: Size exclusion chromatography

SIL: Self-immolating linker

SRB: Sulforhodamine B

Suc: Succinic acid

SUV: Small unilamellar vesicle

TBS: Tris-buffered saline

TCA: Tricarboxylic acid

TEM: Transmission electron microscopy

TPi: Tripolyphosphate

TPP: Triphenylphosphonium

TUL: Thiourea lipid

UTP: Uridine triphosphate

ZP: Zeta potential

CHAPTER 1.

INTRODUCTION TO LIPIDS, LIPOSOMES, AND STIMULI-RESPONSIVE DRUG DELIVERY

1.1 Lipids in Biological Systems

Lipids are a chemically diverse class of biomolecules that support the structure and function of biological membranes while regulating interactions at cellular surfaces. Central to these roles is their amphipathic nature, in which hydrophobic and hydrophilic regions within these molecules promote spontaneous membrane formation through the hydrophobic effect.[1] Within aqueous biological systems, water exposure entropically drives lipid self-assembly into ordered membrane structures. Polar headgroups and aliphatic lipid chains provide the necessary components for stable bilayer membranes that define cellular and organelle boundaries. While their structural role within membranes is significant, lipids additionally serve as signaling mediators for cellular communication and regulation as well as long-term energy storage molecules. Rapid enzymatic remodeling enables conversion of membrane lipids into intra- and extracellular signaling species in response to cellular stimuli.[2] As energy storage molecules, triacylglycerols are sequestered within lipid droplets for later energy metabolism and membrane biogenesis.[3,4] These lipid droplets additionally serve roles in hydrophobic storage for vitamins and signaling molecules, endoplasmic reticulum management, oxidative stress relief, and protein handling.[5–7] The capacity for rapid compositional remodeling and multifunctional behavior highlights the inherently dynamic nature of lipids as biomolecules. Their dynamic combination of mechanical stability and chemical adaptability in biological systems

motivates their use as design elements in synthetic membrane systems capable of responding to defined chemical and environmental cues.

1.2 Lipid Structure and Physicochemical Properties

The physicochemical properties of lipids, which arise from their molecular structure, play a central role in determining membrane behavior and responsiveness. When compared to genes and proteins, which consist of linear combinations of four nucleic acids or twenty amino acids respectively, lipid biosynthesis is much more complex. The diversity of potential biochemical transformations for lipids gives rise to a much larger, more varied collection of possible lipids, each with their own associated classifications and properties.[8] Lipids are generally defined as hydrophobic molecules soluble in organic solvents, encompassing a large range of molecules including terpenes, sphingolipids, phospholipids, and fatty acids.[9] However, a more appropriate definition of lipids arises from both a structural and biosynthetic consideration, in which lipids can first be divided into simple and complex groups based on the number of products produced after their hydrolysis.[9] Focusing on lipids specifically within biological membranes, the three main classes include sterols, glycolipids, and phospholipids, depicted in Figure 1.1.

As simple lipids, sterols play a crucial role in dictating membrane fluidity and integrity.[10] Within mammalian cellular membranes, cholesterol is the major sterol responsible for these dynamic membrane changes. As complex lipids, glycolipids and phospholipids make up the majority of membrane lipids.[11] They possess an amphipathic structure with a polar “head” and non-polar “tails”, the key features for membrane formation and organization.[12] While glycolipids serve important roles in transmembrane

signaling through carbohydrate binding, the bulk of the lipid matrix is composed of phospholipids.[13]

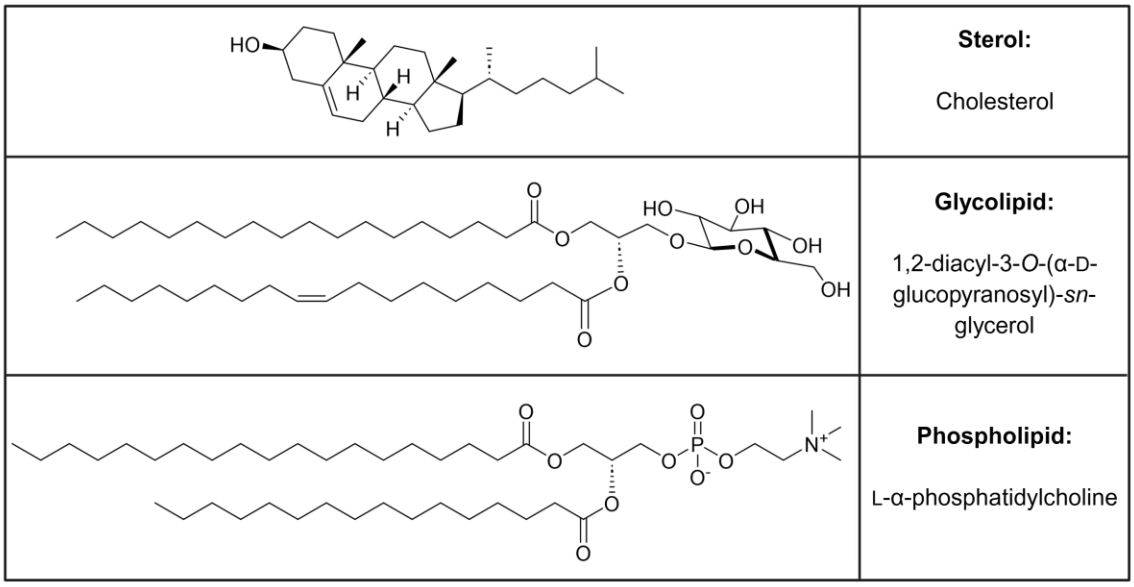

Figure 1.1. Representative structures of the three lipid classes. Sterols, glycolipids, and phospholipids compose the major lipid classes found in biological membranes, with one representative molecule shown for each.

The majority of phospholipids are derived from an esterified glycerol backbone bearing two hydrophobic acyl chains in positions *sn*-1 and *sn*-2, and a phosphate-linked polar headgroup in position *sn*-3, establishing the amphipathic character necessary for bilayer formation (Figure 1.2). Within membrane phospholipids, an additional alcohol group is attached to the esterified phosphate.[14] Phospholipids constitute a major fraction of mammalian membrane lipid mass, with phosphatidylcholine (PC) representing the most abundant species. Due to its abundance, PC is an appealing bulk lipid to include within therapeutic applications for increased stability and compatibility, which are demonstrated in this work.[15,16] Given the central role of phospholipids in membrane architecture, their

headgroup chemistry, hydrophobic domain composition, and molecular geometry represent key parameters that can be modified to alter membrane behavior and responsiveness.

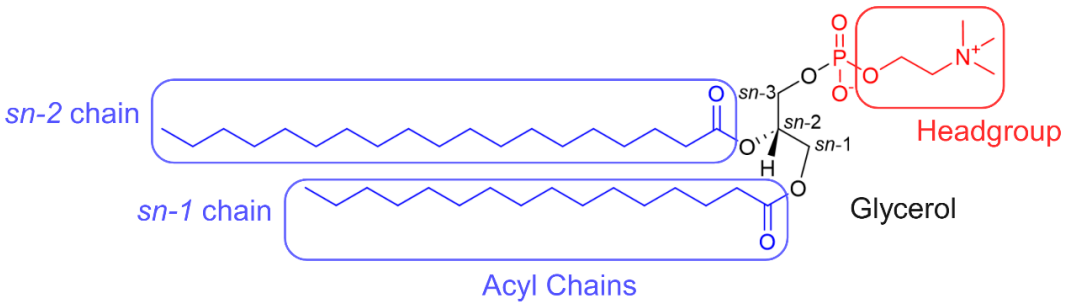

Common Phospholipids	Headgroup	Headgroup Structure
Phosphatidic acid (PA)	None	—OH
Phosphatidylcholine (PC)	Choline	
Phosphatidylethanolamine (PE)	Ethanolamine	
Phosphatidylserine (PS)	Serine	
Phosphatidylinositol (PI)	Inositol	R = H or PO_3^{2-}

Figure 1.2. Structure breakdown of phospholipids showing the headgroups of some important lipids.

Acyl chains, a glycerol backbone, and a phosphodiester headgroup are all components of phospholipids, but classification of a phospholipid relies on the headgroup. The polar headgroup constitutes the primary chemically active region of a phospholipid and plays a dominant role in governing intermolecular interactions at the membrane interface. Variations in headgroup size, charge, and functional groups give rise to distinct classes, including zwitterionic (PC, phosphatidylethanolamine [PE]), anionic (phosphatidylserine [PS], phosphatidylinositol [PI]), and synthetic cationic lipids. These features control membrane surface charge, hydration, and hydrogen-bonding interactions, influencing lipid-lipid association and membrane interactions with ions, metabolites, and proteins.[14,17] As a result, subtle modifications to headgroup structure can lead to pronounced changes in membrane behavior. In the systems described in this dissertation, this structural sensitivity is leveraged to amplify small chemical interactions into functional membrane disruption.

Complementing headgroup effects, the structure of the hydrophobic acyl chains plays a central role in regulating membrane packing, fluidity, and permeability. Membrane packing, or lipid order, directly dictates membrane fluidity and long-range diffusion of lipids. Fluidity and diffusion are integral indicators of membrane integrity, facilitating processes in cell signaling and enzyme binding.[18,19] As saturated lipid tail length increases, stronger van der Waals interactions result in tighter lipid packing, increased membrane order, and less fluidity.[20] In contrast, cis-unsaturated chains disrupt membrane packing through tail kinks, reducing membrane organization and increasing fluidity.[13] In turn, bilayer thickness and lateral compressibility are then altered, where thicker hydrophobic bilayer portions are observed with saturated lipids and unsaturated chain introduction

reduces the hydrophobic bilayer thickness.[21] As membranes become more disordered through packing defects, chain mismatch can increase transient pores within the bilayer, allowing molecule passage that is normally blocked.[22] These variations in lipid headgroup chemistry and hydrophobic domain structure define the physicochemical properties of membranes and provide the foundation for understanding lipid self-assembly and bilayer formation.

1.3 Lipid Self-Assembly and Liposomal Membranes

1.3.1 Lipid Packing Parameters and Self-Assembly

The self-assembly of lipids into higher-order structures is governed by several factors, including thermodynamics, entropy, and the balance between headgroup size and hydrophobic volume, which can be quantitatively described by the lipid packing parameter or P-value.[1] This is an important consideration for the work described in this dissertation, in which we leverage changes in lipid self-assembly to trigger the release of encapsulated contents. Packing parameter provides the framework for relating lipid molecular structure to predictions of preferred self-assembled morphology.[23] Calculated packing parameter values determine the promoted membrane curvature and can be assigned to three main lipid shapes: inverted cone, cylindrical, and conical (Figure 1.3). Lipids with larger headgroups and smaller hydrophobic regions resemble inverted cones and possess a calculated P-value below 1/3. These lipids favor micellar assemblies with positive curvature, such as *lyso*-phosphatidylcholine (LPC), with one acyl chain at the *sn*-1 position.[23,24] Lipids with comparable cross-sectional areas and a P-value near 1 adopt a cylindrical geometry and preferentially form planar bilayers, observed with biological membranes where PC lipids

are the most abundant with a packing parameter around 1.[25] Lastly, conical lipids with a P-value greater than 1 exhibit negative spontaneous curvatures and form inverted micellar (hexagonal phase) structures. These lipids typically possess two acyl chains but small headgroup areas, such as with PE, with unsaturated acyl chains exaggerating the conical effect observed with dioleoylphosphatidylethanolamine (DOPE).[26]

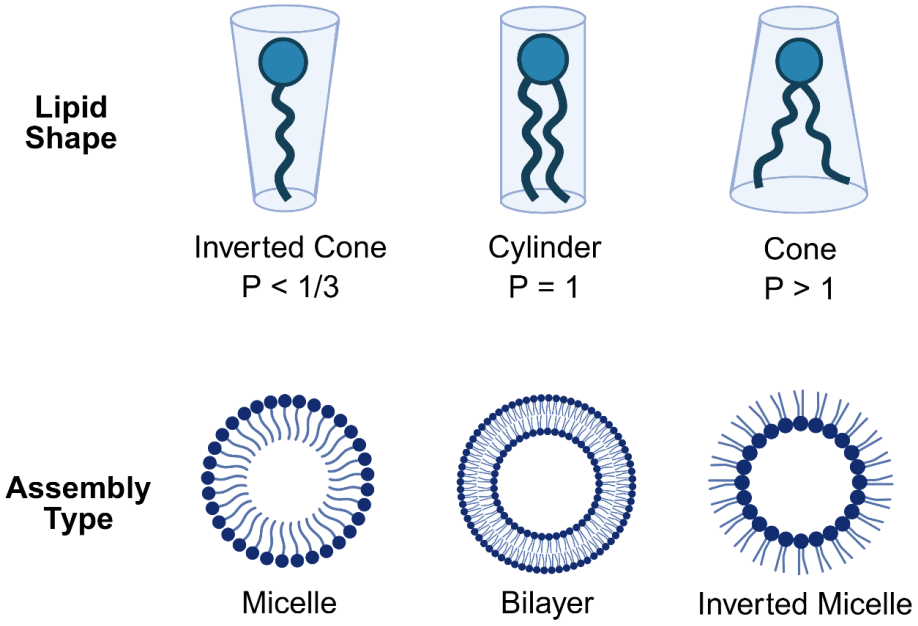

Figure 1.3. Lipid assemblies from the associated packing parameter and lipid shape. Three main types of lipid assemblies are determined by packing parameter value, linked to the shape of the lipid. The packing parameter value, or critical packing parameter, can be calculated by the equation: $P = \frac{V}{a_0 l}$ where V is tail volume, a_0 is the cross-sectional area of the headgroup, and l is tail length. A P-value < 1/3 indicates an inverted cone lipid with micellar assemblies, P-value = 1 indicates a cylindrical lipid shape with bilayer assemblies, and a P-value > 1 indicates conical lipids with an inverted micellar assembly and negative membrane curvature.

While individual lipids will have favored assemblies based on P-value, biological systems are seldom composed of homogeneous lipid assemblies. In mixed lipid systems, the effective packing parameter is determined by the collective composition of the membrane rather than by any single lipid species.[27,28] Small changes in lipid ratios can therefore shift the preferred membrane curvature and self-assembled structures.[29] The ability to control this shift through formulation design forms the basis of the tunable lipid systems developed in later chapters. Additionally, when lipids are constrained to adopt assemblies that differ from their preferred geometry, elastic stress is stored within the membrane. This packing frustration can promote local defects, phase transitions, and membrane destabilization, leading to fusion, pore formation, and permeability changes.[30] This sensitivity to composition provides a powerful means to tune membrane behavior and responsiveness. Understanding how self-assembly principles govern membrane curvature and stability is essential for rational vesicle design and controlled membrane dynamics.

1.3.2 Liposomal Structure, Classification, and Properties

The self-assembly of near-cylindrical lipids in aqueous media produces vesicles known as liposomes. Liposomes are spherical, bilayer-enclosed lipid assemblies formed based on the packing principles where P-value is close to 1. As a result, liposomes closely mimic features of biological membranes. Structurally, liposomes consist of one or more concentric lipid bilayers surrounding an aqueous interior. The hydrophobic acyl chains form the membrane core, while polar headgroups interface with the surrounding aqueous environment.[31] This architecture enables liposomes to encapsulate hydrophilic cargo within the aqueous core and hydrophobic cargo within the acyl chain portion of the bilayer,

providing a versatile platform for delivery and modeling purposes.[32]

Liposomes can be commonly classified according to both lamellarity and size (Figure 1.4). Multilamellar vesicles (MLVs) contain multiple concentric bilayers and are typically several hundred nanometers to micrometers in diameter. Unilamellar vesicles contain a single bilayer and can be further categorized according to their diameter, with small unilamellar vesicles (SUVs) below 100 nm, large unilamellar vesicles (LUVs) ranging between 100 to 1000 nm, and giant unilamellar vesicles (GUVs) above 1 µm. Unilamellar vesicles are more structurally similar to biological membranes and have been used as model-membrane systems.[33] These structural distinctions not only define basic architecture, but also influence encapsulation efficiency and cargo release through size-dependent membrane curvature stress.[34]

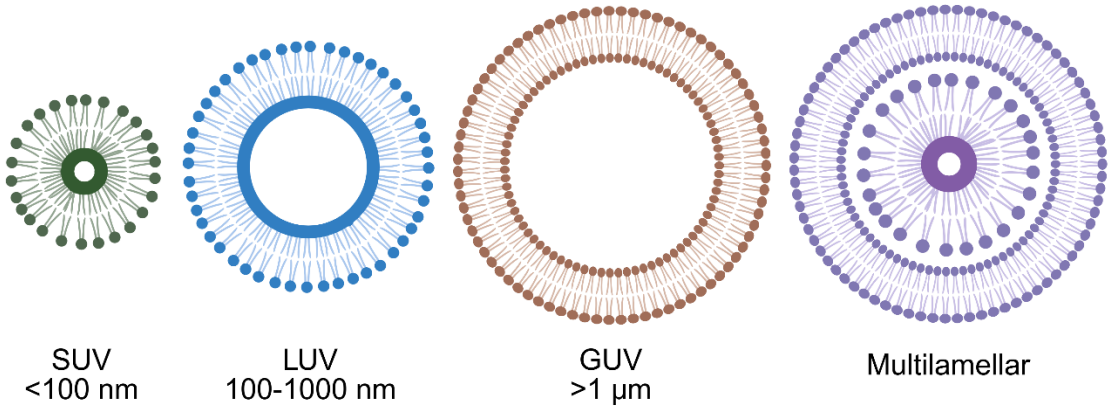

Figure 1.4. Classification of liposomes based on lamellarity and size. Small unilamellar vesicles are classified under 100 nm, large unilamellar vesicles range from 100 to 1000 nm, and giant unilamellar vesicles include sizes above 1 µm. Multilamellar vesicles can have a range of sizes, usually larger, but are classified by multiple, concentric lipid bilayers. LUVs are used in this work near the 200 nm size range.

1.3.3 Liposomal Membrane Phase Behavior and Stability

The stability and dynamic behavior of liposomal membranes are governed by lipid phase behavior and the molecular interactions that regulate bilayer organization. Bilayer behavior is not static, but instead dynamically fluctuates between gel, liquid-crystalline, and ripple phases based on external temperature inputs.[35] This allows membranes to reorganize in the presence of environmental changes without breakage. Transition from the ordered gel phase to the liquid-crystalline phase occurs at specific temperatures for each lipid and is defined as the phase transition temperature or melting temperature (T_m). T_m values give insight into membrane fluidity by quantifying the strength of intermolecular forces between lipids in a membrane.[36] Higher T_m values indicate stronger intermolecular forces, and therefore closer packing and less fluidity, whereas lower T_m values denote weaker forces, looser packing, and more fluidity, which can lead to higher permeability.[37] When a membrane is exposed to temperatures above its T_m, it exists in the liquid-crystalline phase with random tail orientation and increased permeability. At temperatures lower than the T_m, the tails are fully extended and tightly packed to form the gel phase. The most ordered low temperature phase is the sub-gel L_c where tails are tightly packed and tilted. This tilt may also exist in the gel phase $L_{\beta'}$, where tilting occurs due to hexagonal or pseudo-hexagonal packing, whereas the gel phase L_β does not exhibit tilt with its high ordered packing. Between the gel phase and liquid crystalline phase L_α, the ripple phase $P_{\beta'}$ exists as a transition characterized by continued hydration of the membrane, rippling with ordered chains and maintaining a tilt.[38] This transition phase does not exist for all lipids, as chains above 20 carbon atoms and PE lipids with the L_β do not exhibit it. Smaller hydrocarbon

chains exhibiting the $L_{\beta'}$ phase, like PCs, do exhibit this transition, with the temperature range for the transition phase increasing as chain length decreases.

As these phases are directly correlated to intermolecular forces, lipid structure directly influences T_m through headgroup species and hydrocarbon tail length, saturation, and charge (Table 1.1).[38] As tail length increases, van der Waals interactions between packed lipids significantly increase, raising the required energy input to disrupt packing into a more disordered phase. An additional packing disruptor is tail saturation, where points of unsaturation introduce tail kinks that disrupt packing and lower the necessary energy for a phase transition.

Table 1.1. Example T_m values for common liposomal lipids. Examples of common liposomal lipids highlighting the changes in T_m as chain length increases, when unsaturation is introduced, or when a headgroup is changed.

Lipid	**Acyl Chain**	**T_m (°C)**
Dimyristoyl phosphatidylcholine (DMPC)	14:0	23
Distearoyl phosphatidylcholine (DSPC)	18:0	55
Dioleoyl phosphatidylcholine (DOPC)	18:1	-20
Dioleoyl phosphatidylethanolamine (DOPE)	18:1	-16
1,2-Dioleoyl-3-trimethylammonium propane (DOTAP)	18:1	0

In the same way that membrane composition affects assembly morphology, membrane composition also determines overall T_m and in turn, permeability. Thus, heterogeneous systems can be manipulated for desirable T_m values and associated permeability changes between their fluid and gel states. Understanding these phase-dependent behaviors is

essential for the rational design, preparation, and characterization of stable and responsive liposomal systems.

1.3.4 Liposome Preparation and Characterization

The preparation, loading, and characterization of liposomes are critical for ensuring stable and controlled membrane behavior. Liposome preparation involves both vesicle formation and cargo loading, which together dictate encapsulation efficiency, membrane organization, and release properties. One of the most widely used approaches for liposome preparation is thin-film hydration. In this method, the desired lipids in appropriate composition ratios are first dissolved in an organic solvent and dried to form a uniform thin film, which is subsequently hydrated with an aqueous buffer. Gentle hydration usually results in GUV formation, whereas agitation during hydration produces MLVs. During hydration, hydrophilic molecules present in the aqueous phase are passively encapsulated within the liposomal interior, while hydrophobic compounds partition into the lipid bilayer.[39] Passive loading is simple and broadly applicable, though encapsulation efficiency can be low.[40] To increase encapsulation efficiency, active loading strategies have been developed that exploit transmembrane gradients to drive cargo accumulation into preformed liposomes.[41] Common approaches utilize pH gradients or ion gradients to create a chemical driving force for weakly basic drugs to cross the membrane and become trapped within the vesicle interior.[42] These methods enable substantially higher loading efficiencies and improved cargo retention compared to passive techniques, and are commonly employed for clinically relevant liposomal formulations.[43] Both passive and active loading methods are utilized in the systems described in this dissertation, where the differences in

cargo encapsulation efficiency are highlighted.

Following vesicle formation and loading, mechanical processing is applied to control liposome size and lamellarity. Freeze-thaw cycling is often performed to improve encapsulation homogeneity and promote equilibration of internal contents.[44] Size reduction and lamellarity can be achieved through sonication or extrusion through a polycarbonate membrane. SUVs can be prepared via sonication, however this method can further lower encapsulation efficiency and possibly degrade lipids.[45] Extrusion through polycarbonate membranes of defined pore size generates uniform unilamellar vesicles with lower risks of cargo leakage, and homogeneity correlates to the number of extrusion cycles. Alternative liposome preparation methods include ethanol injection,[46] reverse phase evaporation,[47] microfluidic channel methods,[48] and freeze-drying methods[49] that are more involved but offer advantages of their own. Liposomes presented in this dissertation were prepared utilizing thin film hydration and extrusion with a combination of both active and passive loading.

Characterization of liposomes is essential to determine their size and polydispersity, and to correlate liposomal structure with functional performance. Dynamic light scattering (DLS) is routinely used to determine vesicle size and polydispersity, while zeta potential (ZP) provides insight into surface charge and colloidal stability. Electron microscopy (EM) techniques, including transmission electron microscopy (TEM) and cryo-EM, are employed to visualize vesicle morphology and lamellarity. Lamellarity can be further determined through small-angle X-ray scattering (SAXS)[50] or ^{31}P NMR.[51] Encapsulation efficiency and release kinetics are typically determined through spectroscopic methods,

such as UV-Vis or fluorescence, as later discussed within this dissertation.[52] Understanding how preparation, loading, and characterization strategies influence membrane behavior enables the strategic design of liposomal systems with functional and tunable properties.

1.4 Liposomes in Drug Delivery

1.4.1 Nanoscale Drug Delivery Vehicles

Nanoscale drug delivery vehicles, or nanocarriers, have been developed to improve the pharmacokinetics, biodistribution, and therapeutic index of free therapeutics. Certain therapeutics alone face drawbacks such as limited solubility, rapid system clearance, and nonspecific biodistribution, which in turn limit their clinical efficacy and increase off-target toxicity.[53] To combat these drawbacks, the use of nanocarriers for therapeutic delivery is becoming more prevalent with their abilities to protect cargo, improve solubility, and extend circulation time.

There are a large variety of nanocarrier types, but these can be broadly categorized as polymeric, inorganic, and lipid-based (Figure 1.5).[54] While polymeric nanoparticles possess a large range of diverse structures that improve solubility and maintain stability, they face additional challenges with particle aggregation and toxicity, making them riskier choices in clinical applications.[55] Inorganic nanocarriers have unique applications in imaging and diagnostics due to the radioactive, plasmonic, or magnetic properties these materials possess. However, due to the inclusion of heavy metals, they face their own set of challenges with low solubility and toxicity.[56] Among clinically successful nanomedicines, lipid-based nanoparticle systems are the most promising of these three nanocarrier types and are currently the largest type of FDA-approved nanomedicines, the

two most prevalent subsets being lipid nanoparticles (LNPs) and liposomes. With excellent biocompatibility, tunability, and low-cost, liposomes remain one of the most extensively studied and clinically successful systems.[55,57]

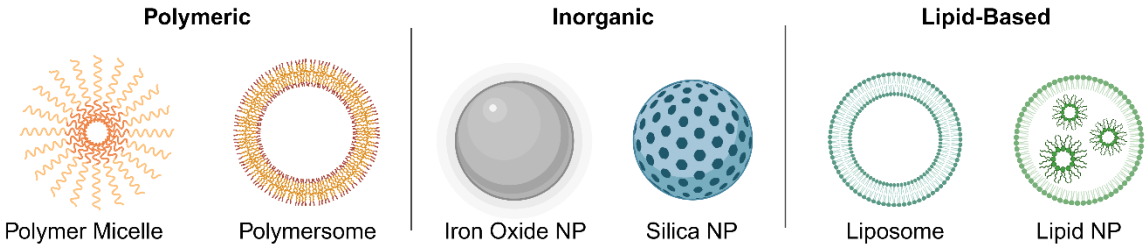

Figure 1.5. Polymeric, inorganic, and lipid-based nanoparticles for drug delivery applications. Nanocarriers for drug delivery include polymeric, inorganic and lipid-based nanoparticles, each with specific advantages in pharmacokinetics and the therapeutic type they best deliver.

1.4.2 Liposomes as Drug Delivery Platforms

Shortly after their discovery, the potential of liposomes as nanocarriers for therapeutic application was recognized by Gregoriadis and his experiments with liposomal enzyme delivery.[58] Since then, liposomes have become one of the most clinically validated nanoscale drug delivery platforms, with multiple FDA-approved formulations demonstrating improved safety and therapeutic outcomes compared to free drugs.[59] The first FDA-approved nanomedicine, Doxil®, encapsulates doxorubicin (Dox) in polyethylene glycol (PEG) coated liposomes and exhibits prolonged circulation, reduced cardiotoxicity, and altered biodistribution compared to the free therapeutic for improved treatment of ovarian cancer, Kaposi's sarcoma, and multiple myeloma. Other early liposomal formulations focused on cancer treatment as well, with Onivyde® for pancreatic

adenocarcinoma, AmBisome® for breast cancer, and DepoCyt® for lymphomatous meningitis. In the early 2000s however, therapeutic liposomal formulations expanded to include Visudyne® for macular degeneration, DepoDur® for pain management, Exparel® for anesthesia, Shingrix® for shingles, and most recently, Comirnaty® and Spikevax® for COVID-19. As of 2025, there are over 15 FDA-approved liposomal drug products.[59] Collectively, these systems demonstrate that lipid vesicles can significantly modify drug pharmacokinetics and toxicity profiles while maintaining or enhancing therapeutic efficacy.

A defining advantage of liposomes for improved therapeutic delivery is their dual-compartment architecture, which enables the encapsulation of both hydrophilic and hydrophobic cargos. This structural feature allows chemically diverse therapeutics to be formulated using a single carrier platform. When using liposomes as therapeutic carriers, there are key general characteristics that determine their effectiveness, including encapsulation efficiency, size, and surface charge. Encapsulation efficiency depends on lipid composition, vesicle size, lamellarity, and loading method. Passive loading with thin-film hydration is faster and yields low to modest encapsulation efficiency, whereas active loading methods are more involved but can generate higher and more reproducible encapsulation efficiency. Weakly basic drugs can further benefit from pH or ion gradient active loading measures, yielding near-quantitative encapsulation efficiency with long-term retention.[60,61]

While liposome structure is favorable for a wide range of therapeutic loading, particle size is a critical determinant of liposome circulation behavior and tissue distribution.

Clinically relevant liposomes typically range from 80-150 nm in diameter, which reduces rapid renal clearance for smaller liposomes and avoids uptake through the reticuloendothelial system (RES) for larger liposomes above 400 nm.[62] Liposomes of this size range also benefit from the enhanced permeation and retention (EPR) effect, where selective liposome accumulation into diseased tissues is enhanced due to leaky vasculature.[63] Liposome size also influences curvature stress, where enhanced fusion with cell membranes has been shown due to the increased curvature present in this size range.[64]

Surface charge and chemistry further modulate liposome interactions with biological systems. Neutral and zwitterionic liposomes generally exhibit lower non-specific protein adsorption and longer circulation times than charged systems but may suffer from increased aggregation. Cationic liposomes enhance cellular uptake through electrostatic interactions with negatively charged cell membranes whereas anionic liposomes can alter biodistribution and immune recognition depending on headgroup identity and surface density. Both charged types also sufficiently self-repel to prevent significant aggregation.[65,66] These differences in liposome charge highlight the importance of balancing surface charge to optimize stability, circulation, and cellular interactions, and lead directly into the effects of surface and composition modifications in this work.

1.4.3 Surface-Based Liposome Modifications

Surface modification of liposomes has been widely employed to improve circulation time, enhance targeting, and reduce nonspecific interactions *in vivo,* examples of which can be noted in Figure 1.6. RES-mediated removal of liposomes from circulation has limited liposomal treatment to liver, spleen, and lung systems, but surface modification

techniques have been developed to avoid RES clearance while also improving efficacy of these nanocarriers.

One of the most established approaches of surface modification is PEGylation, in which PEG chains are grafted onto the liposome surface to create a steric hydration layer around the liposome. This layer reduces protein adsorption and uptake by the mononuclear phagocyte system, while also improving storage ability and preventing aggregation.[67] PEGylated liposomes, or "stealth liposomes", exhibit prolonged circulation half-lives and improved pharmacokinetics compared to unmodified systems, allowing further enhancement of the EPR effect for increased liposome accumulation in diseased tissues.[68]

Beyond PEGylation, liposome surfaces can be functionalized with targeting ligands, including carbohydrates, antibodies, and peptides, to promote selective binding and uptake by diseased cells. These "actively targeted" systems rely on specific interactions between liposome-displayed targeting moieties and cell-surface receptors to enhance cellular association and internalization. Several cellular targeting receptors have been identified, including folate, mannose, and epidermal growth factor receptors (EGFR), each overexpressed in certain diseases.[69–71] Folic acid decorated liposomes take advantage of overexpressed folate receptors on cancer cells.[72] Decoration of liposome surfaces with carbohydrates focuses on glycan and mannose, as glycan binding protein receptors and mannose receptors are sufficiently overproduced on diseased cell surfaces to elicit significant selectivity.[73] Creation of immunoliposomes through antibody functionalization is another significant approach due to specificity to target ligands. These modified liposomes include antibodies attached by direct covalent bonds for significant stability.

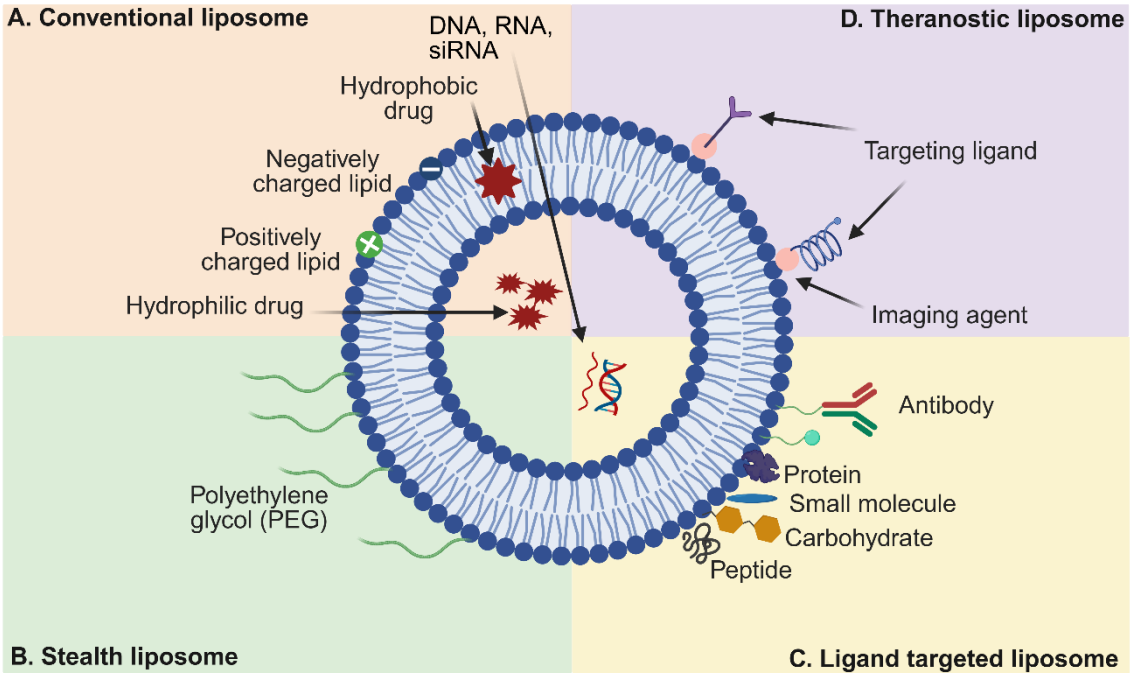

Figure 1.6. Representation of the different categories of liposomes for therapeutic delivery. Conventional liposomes represent the prototypical structure, with neutral, anionic, or cationic lipids in composition. Hydrophobic and hydrophilic cargo can be encapsulated within the bilayer or aqueous core, respectively. (B) Stealth liposomes are decorated with PEG polymers to prolong circulation time by shielding phagocyte uptake. (C) Ligand targeted liposomes are conjugated to antibodies, proteins, small molecules, carbohydrates, and peptides for targeted delivery and uptake of the liposomes. (D) Theranostic liposomes contain both active targeting groups and imaging agents for simultaneous delivery. Figure inspired by Sercombe et. al.[74]

Immunoliposomes specifically targeting EGFRs have an additional advantage as the protein bank of EGFR receptors is well-documented, allowing for a wide variety of possible immunoliposomes for the broad range of diseased cells expressing EGFRs. While surface modification can significantly alter biodistribution and cellular interactions, it does not directly regulate the internal membrane environment or control drug retention and release once the liposome reaches its target.

Despite their utility, surface modifications alone present notable limitations. PEGylation can hinder cellular uptake and endosomal escape, a phenomenon commonly referred to as the "PEG dilemma".[75] Targeting ligands may be masked by adsorbed serum proteins or fail to engage receptors efficiently in vivo.[76] Additionally, surface-functionalized liposomes often retain cargo through nonspecific membrane leakage rather than through a programmable release mechanism, limiting control over drug activation once at the target site. As a result, increasing attention has been directed toward composition-based modifications, which alter the internal physicochemical properties of the liposomal membrane itself.

1.5 Stimuli-Responsive and Triggered Liposomal Release

1.5.1 Passive and Active Triggered Release Strategies

While liposomes for therapeutic delivery have been established as an improvement to free therapeutic delivery, release of therapeutic cargo from liposomes remains difficult. Passive leakage of cargo from liposomes is minimal, where less than 5% of encapsulated cargo may be release before circulatory clearance or uptake of liposomes.[77] Thus, triggered release strategies have been developed to improve the spatial and temporal control of drug

delivery from liposomal carriers by promoting cargo release preferentially at diseased sites. Rather than relying on continuous, nonspecific leakage during circulation, these approaches apply external stimuli or exploit differences between healthy and diseased environments to destabilize liposomal membranes in a controlled manner while increasing the percentage of encapsulated cargo released.

Broadly, triggered release strategies can be categorized as active or passive, depending on whether release is initiated by externally applied triggers or endogenous biological conditions, respectively.[78] Active triggered release strategies require the application of an external stimulus to initiate cargo release from liposomes. Common external triggers include heat,[79] light,[80] ultrasound,[81] magnetic fields,[82] and electric fields,[83] which can be applied locally to induce membrane perturbation of phase transitions. Thermosensitive liposomes, for example, release cargo upon localized heating above a defined T_m, while light-responsive systems employ photoactivated components to disrupt membrane integrity. These approaches offer precise temporal control over release but require specialized equipment and careful localization of the applied stimulus.

In contrast, passive triggered release strategies rely on intrinsic physiological differences between healthy and diseased tissues to induce liposomal destabilization and cargo release. These differences include variations in pH,[84] enzyme expression,[85] redox potential,[86] and metabolite concentrations[87–90] that are characteristic of tumor microenvironments. Release with these triggers may also be achieved once liposomes enter specific intracellular compartments such as endosomes and lysosomes.[91] Liposomes designed for passive triggering incorporate membrane components that respond to these

conditions through protonation, enzymatic cleavage, or chemical transformation. Activation of these pathways results in cargo release through changes in membrane permeability or structural disruption. As these triggers are naturally present at target sites, passive systems do not require additional intervention once administered and can provide selective release based on biological conditions.

Both passive and active triggered release strategies have demonstrated promise for improving drug delivery outcomes, yet each presents inherent advantages and limitations. Active systems provide greater control over release timing and location but depend on effective stimulus delivery and penetration, which presents many technical challenges. Passive systems benefit from simplicity and biological selectivity but may exhibit variability due to heterogenous disease environments. These considerations have motivated continued development and improvement of liposomal platforms that respond selectively to endogenous biochemical signals.

1.5.2 Lipid Switches and Membrane Perturbation Mechanisms

Stimuli-responsive liposomal systems rely on molecular events that perturb membrane organization and promote cargo release. Independent of the specific trigger employed, effective cargo release requires translation of a localized chemical or structural change within individual lipids into a collective disruption of bilayer packing, curvature, or integrity. Across reported systems, lipid-based triggering mechanisms can be broadly categorized into headgroup modification, loss of acyl chains, and conformational lipid changes, each of which perturbs membranes through distinct but related physical mechanisms.[92–95]

One commonly employed strategy involves headgroup modification, in which chemical transformation of the lipid headgroup alters intermolecular interactions at the membrane surface. Changes in headgroup charge, size, or hydrogen-bonding capability can disrupt lipid-lipid interactions, modify surface hydration, and weaken electrostatic stabilization of the bilayer. Common headgroup modification strategies involve the modification of DOPE, a non-bilayer forming lipid.[96,97] With headgroup modification, such as *N*-acylation, the packing parameter of DOPE can be adjusted to favor bilayer formation. Subsequent introduction of the target trigger, however, removes the modified headgroup and converts DOPE back into a non-bilayer forming species, causing membrane perturbation.[98,99]

A second class of perturbation mechanisms relies on alteration or loss of hydrophobic acyl chains, which directly impacts bilayer packing and thickness. Cleavage or modification of lipid tails reduces hydrophobic volume and disrupts van der Waals interactions within the membrane core, generating packing defects and curvature stress. In particular, transformation of diacyl lipids into lysolipid species shifts lipid geometry from cylindrical to conical, favoring micelle formation and promoting membrane destabilization. Phospholipase A_2 (PLA_2) is an appealing target enzyme for these transformations as it can selectively cleave the *sn*-2 position of phospholipids, generating a membrane disrupting lysolipid.[100,101] Such hydrophobic-domain modifications often lead to pronounced permeability increases, transient pore formation, or phase separation due to the direct disruption of the bilayer interior.

A third and particularly versatile strategy involves conformationally active lipid

switches, in which a molecular interaction event induces a change in lipid geometry without covalent bond cleavage. In these systems, intramolecular rearrangements or binding interactions alter the effective cross-sectional areas of the headgroup and hydrophobic domains, driving transitions between cylindrical and conical geometries. With overall lipid integrity preserved, these systems offer the potential for tunable or reversible membrane perturbation.[88–90] Collectively, these three membrane perturbation mechanisms correspond to a wide range of passive, biologically triggered liposomal systems, and will be discussed further in the context of specific lipid designs in subsequent chapters.

1.6 Scope and Organization

Liposomes have demonstrated significant clinical success as drug delivery vehicles, but their broader therapeutic potential remains limited by a lack of precise control over cargo release. While several liposomal formulations are approved for clinical use, these systems function primarily as passive carriers rather than selectively triggered delivery platforms, leaving significant fractions of encapsulated cargo within liposomes as they are cleared from biological systems. The development of chemically responsive or "smart" liposomes capable of releasing cargo in response to defined biological signals therefore remains an important area of ongoing research, enhancing the amount and location of cargo release.

This dissertation explores the design and evaluation of stimuli-responsive lipid systems that enable controlled membrane perturbation and triggered release. Chapter 2 describes the development of a bis-triphenylphosphonium lipid switch that exhibits a tunable

triggered response to guanosine triphosphate (GTP) and inorganic tripolyphosphate (TPi) based on liposomal membrane composition. Chapter 3 focuses on a reactive oxygen species (ROS)-responsive Dox prodrug lipid utilizing a self-immolation mechanism for improved spatiotemporal control over therapeutic release. Chapter 4 presents exploratory syntheses and studies of alternate conformationally responsive lipid designs that further investigate how molecular switching events can be translated into membrane destabilization. Together, these studies aim to advance the development of programmable lipid systems that move liposomal cargo delivery beyond passive leakage toward site-selective, stimuli-responsive release.

CHAPTER 2.

ENGINEERING TUNABLE GTP/TPI-RESPONSIVE LIPOSOMES

A version of this chapter was originally published by Brooke E. Smith, et al.: Smith, Brooke E.; Russell, Caleb G.; Mustafa, Mayesha B.; Best, Michael D., Engineering tunable GTP/TPi-responsive liposomes through liposomal membrane modulation using a bis-triphenylphosphonium lipid switch. *RSC Pharmaceutics* **2026**, *3*, 256-264.

2.1 Project Overview

Liposomes are effective nanocarriers for targeted therapeutic delivery, yet challenges regarding the extent and specificity of cargo release persist. Many disease conditions result in metabolite concentration dysregulation, increasing the appeal to harness overly abundant metabolite concentrations as triggers for targeted delivery and cargo release. Here, we introduce a novel stimuli-responsive liposomal platform with a tunable response to either GTP or TPi that was achieved through incorporation of a novel bis-phosphonium-based lipid switch (BPLS) and strategic manipulation of liposome composition. This platform enables selective cargo release triggered by GTP, a metabolite upregulated in many fast-growing cancer cells. Fine-tuning of liposome composition also allows for TPi triggered release, a model phosphate compound to illustrate the dual response of this system. Hydrophobic and hydrophilic dye release assays, DLS, TEM, and kinetic cargo release studies confirmed metabolite-responsive membrane perturbation driven by BPLS, inciting controlled release of both polar and non-polar cargo. By fine-tuning liposome composition to control metabolite selectivity and release kinetics, this platform offers a versatile framework for addressing complex metabolite profiles in diseased cells, expanding the

stimuli-responsive liposome toolbox toward the potential of customized drug delivery.

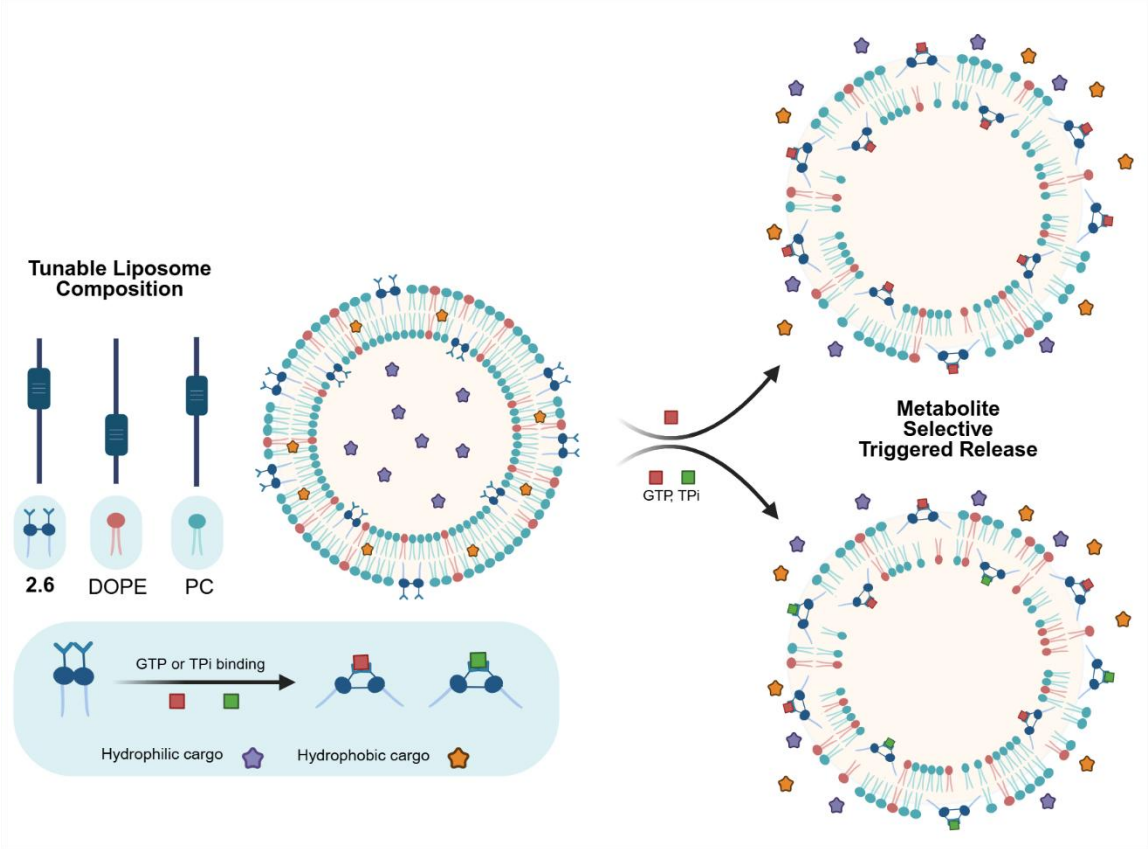

Figure 2.1. Overall system design graphic for BPLS 2.6 with tunable release. Liposomes containing BPLS **2.6** exhibit tunable triggered release based on the lipid content ratio of **2.6**, DOPE, and PC. GTP or TPi binding with BPLS are designed to incite a conformational change of the lipid, disturbing lipid membrane packing within BPLS liposomes in order to release both hydrophobic and hydrophilic cargo.

2.2 Introduction and Motivation

Liposomes are versatile nanocarriers that are capable of encapsulating a wide range of molecular cargo and are especially useful for applications in therapeutic drug delivery.[34,52] Therefore, liposomes have found widespread utility in clinical therapeutic applications.

While conventional liposomes offer improvements to therapeutic delivery, such as increased solubility and favorable pharmacokinetics, they also exhibit minimal cargo release and lack delivery specificity in the absence of a triggering mechanism.[52] These particular challenges have propelled recent advances in liposomal modifications to improve these properties, particularly through the development of stimuli-responsive liposomes. Liposome platforms utilizing both active (i.e. heat, ultrasound, light)[102–104] and passive (redox, pH, and enzyme expression)[105–107] release systems have been developed, but challenges remain for the clinical translation of each of these. For example, external stimuli that are commonly harnessed by active release systems can be toxic to healthy cells, while passive, internal release systems have historically targeted stimuli that only exhibit slight differences between healthy and diseased cells.[108,109]

Further expansion of this field has led to the recent development of metabolite-responsive liposomes, which exploit the benefits of passive release stimuli while addressing the challenges of diseased versus healthy cell differentiation due to the significant upregulation of metabolite concentrations that are common in diseased cells. These liposomes leverage chemical species specifically upregulated within disease states, such as zinc,[89] calcium,[110] GTP,[111] and adenosine triphosphate (ATP),[90] as internal triggers to selectively incite cargo release in the presence of the target stimulus.[112] This is achieved by incorporating synthetic lipid switches that undergo significant conformational changes upon metabolite binding, thereby disrupting liposomal membrane packing to release encapsulated contents.[113] While such innovations have the potential to enhance liposome delivery capabilities, fine-tuning these carriers to respond to multiple metabolites or

specific triggers by modulating liposome composition remains underexplored, limiting the ability to tailor delivery platforms to diverse disease profiles.

2.2.1 Biological Relevance of GTP

GTP is a central metabolite in cellular biology, serving essential roles in RNA transcription and DNA replication,[114] but also G-protein signaling,[115] protein biosynthesis,[116] gluconeogenesis,[117] and tubulin formation.[118] Alongside its tight coupling to regulation of cellular processes in intracellular signaling and cytoskeletal dynamics, it also serves as a nucleotide energy source with ATP. One of the most well-established roles of GTP is in signal transduction mediated by GTP-binding proteins, such as small GTPases and heterotrimeric G proteins.[119] These proteins act as molecular switches, cycling between active and inactive states depending on their GTP- or GDP-bound form. In addition to its signaling functions, GTP plays a critical role in protein biosynthesis, where it provides the energetic driving force for ribosomal translocation and translation fidelity. Protein synthesis is a highly energy-intensive process, and intracellular GTP levels are therefore sensitive to changes in cellular growth rate and metabolic demand.

To maintain GTP concentrations that are appropriate for the needs of the cell, it is produced through both nucleotide salvage and *de novo* biosynthesis pathways. The *de novo* biosynthesis involves a ten-step, 6-enzyme process, and as GTP demand within rapidly proliferating cells increases, enzymes along this pathway can become dysregulated.[120] While increased levels of GTP are noted for malignancies, enhanced GTP production is also tied to viral infection support.[121] These rapidly proliferating cells often exhibit altered nucleotide metabolism and elevated nucleotide turnover, resulting in distinct intracellular

nucleotide profiles compared to healthy tissue. Concentrations of GTP within various cancerous cell lines have been documented at 800 to 2400 μM, distinctly elevated from healthy cell concentrations.[122,123] Additionally, GTP is predominantly localized intracellularly.[124] This compartmentalization presents an opportunity for selective triggering strategies that exploit intracellular biochemical cues rather than non-specific extracellular conditions. Tight regulation of nucleotide concentrations and their direct link to cellular function make them attractive candidates for metabolite-responsive delivery systems.

Despite its clear biological relevance, GTP remains underexplored as a triggering signal for liposomal drug delivery. Most stimuli-responsive systems rely on general physicochemical differences between healthy and diseased tissues, rather than specific metabolic signals. The development of lipid-based systems capable of directly responding to GTP therefore represents a promising strategy for coupling liposomal release to biologically meaningful intracellular conditions.

2.2.2 Nucleotide-Responsive Liposomal Systems

Despite the biological relevance of nucleotides and phosphate-containing metabolites, relatively few liposomal systems have been developed that respond directly to these species. Compared to the more extensive body of work on enzyme,[99] pH,[125] light,[80] or metal-ion responsive liposomes such as zinc,[89] calcium,[110] or copper,[126] anion- and nucleotide-responsive systems remain underexplored. This disparity reflects both the chemical challenge of selectively recognizing highly solvated, multivalent anions and the difficulty of translating binding events into controlled membrane perturbation. To address

this challenge, a limited number of reported systems have begun to employ nucleotide-responsive strategies, primarily relying on binding, degradation, or conformational change to induce cargo release from nanomaterials.

Among metabolite-responsive delivery platforms, ATP-responsive systems represent the most developed class of nucleotide-triggered lipid-based nanomaterials. These include responsive materials such as phenylboronic acid modified LNPs for siRNA delivery,[127] G-quadruplex DNA-lipid conjugates with a hairpin DNA aptamer,[128] and HER2/ATP specific aptamers wrapped in nanostructured lipid carriers.[129] In these systems, ATP recognition is mediated through surface-bound aptamers or supramolecular complexation, resulting in changes to nanoparticle surface charge, stability, or assembly that indirectly promote cargo release. While effective, such approaches rely on auxiliary recognition elements external to the membrane rather than direct modulation of lipid packing within the particles.

In contrast, a limited number of reported systems employ ATP-responsive lipid switches embedded directly within the membrane, enabling nucleotide binding to be coupled more directly to membrane perturbation.[90] In these systems, ATP binding induces a conformational change in the lipid headgroup, altering effective molecular geometry and generating packing frustration that destabilizes the bilayer and promotes cargo release. Because the responsive element is an integral component of the membrane, this strategy provides a more direct translation of metabolite recognition into controlled membrane disruption. Building on this design strategy, related work has demonstrated that nucleotide selectivity within membrane-embedded lipid switches can be altered through modification of the recognition motif. In particular, exchange of the metal-dipicolylamine binding site

within an ATP-responsive lipid switch has been shown to shift selectivity toward GTP (Figure 2.2).[111] Such systems further support the feasibility of using conformational lipid switches to distinguish between closely related nucleotides and induce membrane perturbation through nucleotide binding.

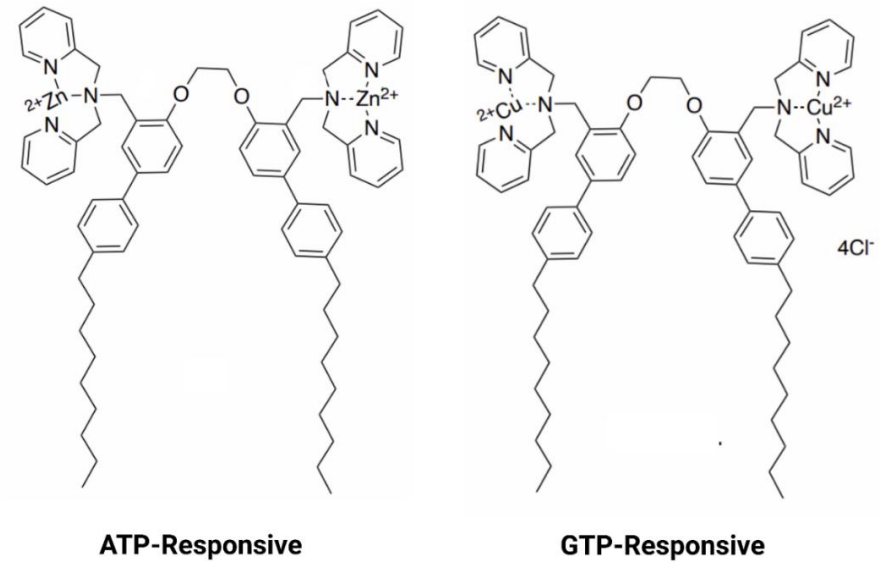

Figure 2.2. Previous ATP- and GTP-responsive lipid switches. Previous lipid switches with a matching scaffold exhibited triggered response to ATP or GTP depending on the particular metal chelated to dipicolylamine binding sites. Changes in the metal binding site alter the selectivity of response to either metabolite.

While lipid composition has been shown to modulate ATP selectivity and responsiveness within these systems, the broader applicability of this strategy to other biologically relevant nucleotides remains insufficiently explored. Systemic investigation of how membrane composition can be leveraged to tune responsiveness toward other biologically relevant nucleotides, such as GTP, and to more complex anionic environments, offers a promising route to tunable liposome systems. Further development

of tunable systems would enable selective coupling of biologically meaningful metabolite recognition to predictable membrane perturbation, providing a foundation for more programmable and responsive liposomal delivery platforms.

2.3 Design of Bis-Triphenylphosphonium Lipid Switch

The development of metabolite-responsive lipid switches capable of inducing controlled membrane perturbation requires integration of molecular recognition with a membrane environment. Previous ATP- and GTP-responsive lipid switches[90,111] have demonstrated that conformational changes within membrane-embedded lipids can be translated into curvature stress, packing frustration, and triggered cargo release. These systems established a general framework in which a conserved lipid scaffold can be paired with tunable headgroup functionality to modulate responsiveness toward specific nucleotide-derived signals. Building upon this foundation, the present work sought to explore how modification of lipid headgroup chemistry within a common membrane-active scaffold could influence responsiveness toward negatively charged and phosphorylated metabolites.

Initial design efforts focused on the incorporation of amine-based headgroups into the lipid switch architecture. This design was motivated by the potential for protonation-dependent behavior and electrostatic interactions with anionic metabolites. Molecular recognition of several nucleotides and phosphates has previously been noted with amine receptor-like molecules.[130–136] Incorporation of amine functionality into a scaffold previously shown to be compatible with phospholipid bilayers enables systemic evaluation of prospective lipid-anion interactions. However, during synthesis of these initial designs

in Scheme 2.1, the Staudinger reduction step intended to generate the target amine functionality instead resulted in formation of a bis-triphenylphosphonium (TPP) headgroup. Rather than discarding this outcome, preliminary screening in Figure 2.3 revealed that the resultant lipid exhibited a pronounced and semi-selective responsiveness toward highly charged phosphate-containing metabolites, particularly GTP, TPi, ATP, and uridine triphosphate (UTP). This unexpected observation motivated further investigation into the role of TPP headgroups in mediating phosphate-induced membrane perturbation.

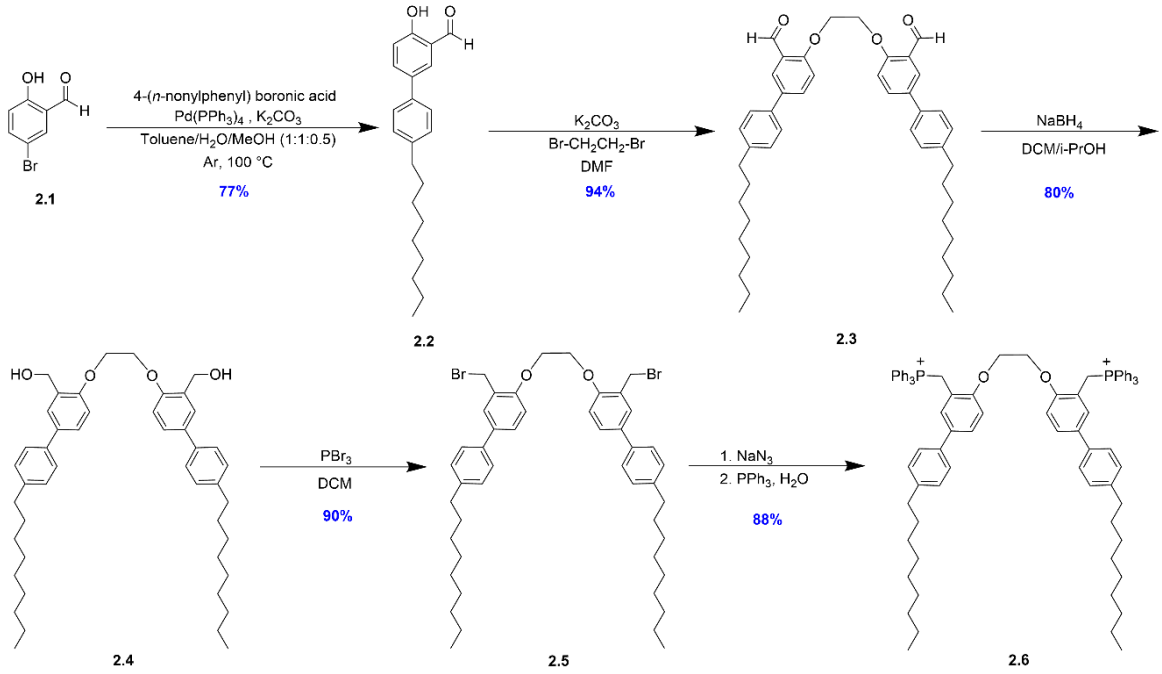

Scheme 2.1. Synthesis of bis-phosphonium lipid switch 2.6. A Suzuki coupling between **2.1** and 4-(n-nonylphenyl) boronic acid introduced the hydrophobic tail to form **2.2**. Dimerization with 1,2-dibromoethane yielded **2.3**, after which further head group modifications included reduction to **2.4**, bromination to **2.5**, and lastly Staudinger reduction conditions resulting in phosphine substitution to generate **2.6**.

The complete synthetic route to the BPLS is shown in Scheme 2.1, adapting a previously reported scaffold synthesis[90] prior to divergence at the headgroup modification stage. Synthesis begins with a Suzuki coupling between 5-bromo-2-hydroxybenzaldehyde (**2.1**) and 4-(*n*-nonylphenyl) boronic acid, which introduces the hydrophobic lipid tail to produce **2.2**. Subsequent dimerization with a 1,2-dibromoethane linker yielded compound **2.3**. Headgroup modification continued via reduction to **2.4** and bromination to **2.5**. Application of conditions intended to perform a Staudinger reduction in the final step instead resulted in substitution reactions with phosphine groups to generate the BPLS **2.6**.

2.4 Hydrophobic Dye Release Experiments

2.4.1 Initial Metabolite Selectivity Screening

With successful synthesis of BPLS **2.6**, we tested the initial capabilities of the switch with a fluorescence release assay. Liposomes were prepared with a fixed ratio of **2.6**, DOPE, and PC (35/30/25 mol%). Utilizing a Nile red (NR) dye release assay,[137] where NR fluorescence is activated within the hydrophobic interior of the liposomal membrane but deactivated upon escape into the aqueous buffer environment, we measured the extent of cargo release driven by bilayer perturbation through changes in fluorescence. Liposomes for these release experiments were prepared through standard thin-film hydration at 2 mM concentration in tris-buffered saline (TBS) and extruded through 200 nm polycarbonate membranes, followed by DLS analysis to confirm stable liposome formation.[138] Liposomes were incubated for 16 hours with 1, 5 or 10 mM concentrations of common phosphate- or carboxylate-containing anionic metabolites, including sodium phosphate (Pi), sodium pyrophosphate (PPi), adenosine 5'-diphosphate (ADP), ATP, D-fructose-6-phosphate

(FP), D-fructose-1,6-bisphosphate (FBP), TPi, cytidine 5'-triphosphate (CTP), GTP, UTP, adenosine 5'-monophosphate (AMP), malic acid (Mal), fumaric acid (Fum), oxaloacetic acid (Oxa), and succinic acid (Suc).

This metabolite selectivity screen in Figure 2.3 revealed that BPLS **2.6** liposomes exhibited significant cargo release in response to GTP and TPi (~70% and 72% NR fluorescence decrease, respectively), prompting our investigation into this lipid's capabilities and subsequent findings of tunable response. Some moderate metabolite driven release was also observed with ATP and UTP treated liposomes, although only at higher metabolite concentrations and resulting in less extensive cargo release. Conversely, CTP, an additional nucleotide triphosphate, yielded minimal release despite structural similarities to GTP. However, CTP has been noted as a weaker electron donor due to its pyrimidone functionality, which may account for its decreased binding affinity with **2.6**.[139] While data show some overlap in triggering by other nucleotide triphosphates, this is not expected to be problematic as increased concentrations of all nucleotide triphosphates are generally observed in cancer cells with rapid cell growth environments.[140] Several other anionic metabolites showed virtually no NR release under these conditions, showcasing partial selectivity with this liposomal triggered release platform.

2.4.2 Formulation Development and Identification of Tunable Metabolite Responses

The initial metabolite selectivity screening revealed that **2.6**-containing liposomes respond most strongly to highly charged triphosphate-derived anions, particularly GTP and TPi. However, the magnitude and selectivity of this response were found to depend strongly on membrane composition. After the initial metabolite selectivity screen revealed

responsiveness of **2.6** liposomes to GTP and TPi, a wider range of liposome formulations was tested with the same NR release assay, specifically focusing on GTP as the triggering metabolite, summarized in Table 2.1. Ultimately, two key liposome formulations exhibiting favorable GTP-triggered release were identified containing either 35% DOPE or 20% DOPE, with the remaining percentage shared in different ratios of **2.6** and PC.

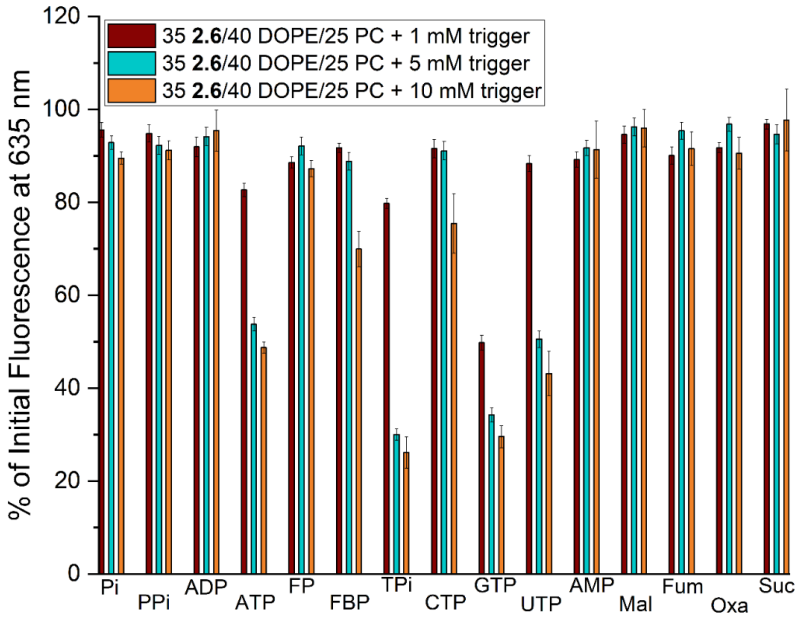

Figure 2.3. Metabolite selectivity screening for 2.6. NR release metabolite selectivity screen by treating 35/40/25 **2.6**/DOPE/PC liposomes with phosphate- or carboxylate-containing metabolites. Significant cargo release was noted with 5 and 10 mM GTP or TPi incubation, with moderate release noted from ATP and UTP. All other anionic metabolites tested showed virtually no response. Error bars denote standard errors from at least three biological replicates.

Further investigation into these formulation types while varying **2.6** concentrations yielded an interesting response. Liposomes containing 40/35/25 mol% of **2.6**/DOPE/PC

exhibited triggered release with both GTP and TPi, but lipid ratio adjustment to 45/20/35 mol% of **2.6**/DOPE/PC yielded enhanced cargo release selectivity with GTP, highlighted in Figure 2.4. This suggested that variation in membrane composition provided a means to modulate the energetic cost of bilayer perturbation, allowing responsiveness to be tuned without altering lipid switch chemistry.

2.4.3 Time-Dependent Fluorescence Release Assays for GTP/TPi

To further investigate the tunable metabolite selectivity of **2.6** and observe how lipid switch percentage and cargo release correlate, end-point NR release assays were next completed where DOPE percentages were held constant at 35 or 20% while **2.6** and PC percentages were varied, as shown in Figure 2.5. The inclusion of DOPE within liposome formulations promotes liposome destabilization,[141] priming liposomes for triggering and subsequent cargo release. However, with DOPE inclusion, inherent liposome leakiness can also arise due to excessive destabilization. While the two previous formulations exhibited tunable release, we expected that liposome leakiness could be improved from ~25% passive cargo release in Figure 2.4A.

For liposomes with 35% DOPE treated with TPi, our findings indicated a linear relationship between NR release and **2.6** percentage (Figure 2.5A), plateauing at ∼82% release with 35–45% **2.6**. However, destabilization of these liposomes to promote triggered cargo release also resulted in increased passive cargo leakage. Of this less-selective liposome type, formulations with 35/35/30 mol% **2.6**/DOPE/PC maintained the maximum cargo release while decreasing passive cargo release to ∼15%, balancing stability while maintaining metabolite triggered release capabilities.

Table 2.1. Summary of formulations explored for hydrophobic NR release. Fluorescence readings and cargo release of exploratory formulations for NR release.

% 2.6	% DOPE	% PC	Fluorescence Intensity Units	Cargo release % after 10 mM GTP Treatment	Passive Cargo Release %
25	0	75	456.587	37.651	38.147
50	0	50	372.343	64.417	39.836
75	0	25	344.867	86.467	64.105
100	0	0	212.111	94.306	82.268
30	20	50	521.147	59.464	3.192
30	25	45	715.701	34.412	29.131
30	30	40	786.063	57.316	39.884
30	35	35	1001.253	67.029	53.630
35	20	45	455.332	49.14	2.065
35	25	40	341.997	50.688	-3.511
35	30	35	424.055	61.696	1.816
35	35	30	362.236	94.821	1.016
40	20	40	383.981	95.405	22.474
40	25	35	333.625	91.177	11.789
40	30	30	388.229	93.163	6.065
40	35	25	373.523	97.647	20.878
45	20	35	380.592	92.091	0.551
45	25	30	483.852	93.836	9.281
45	30	25	516.105	95.489	16.719
45	35	20	471.885	96.451	26.314
50	20	30	392.503	94.659	12.022
50	25	25	439.322	95.581	15.321
50	30	20	432.84	96.59	15.573
50	35	15	351.183	96.995	25.877
55	20	25	308.921	96.799	8.518
55	25	20	300.966	95.931	25.567
55	30	15	265.128	95.766	53.310
55	35	10	192.878	94.568	80.499

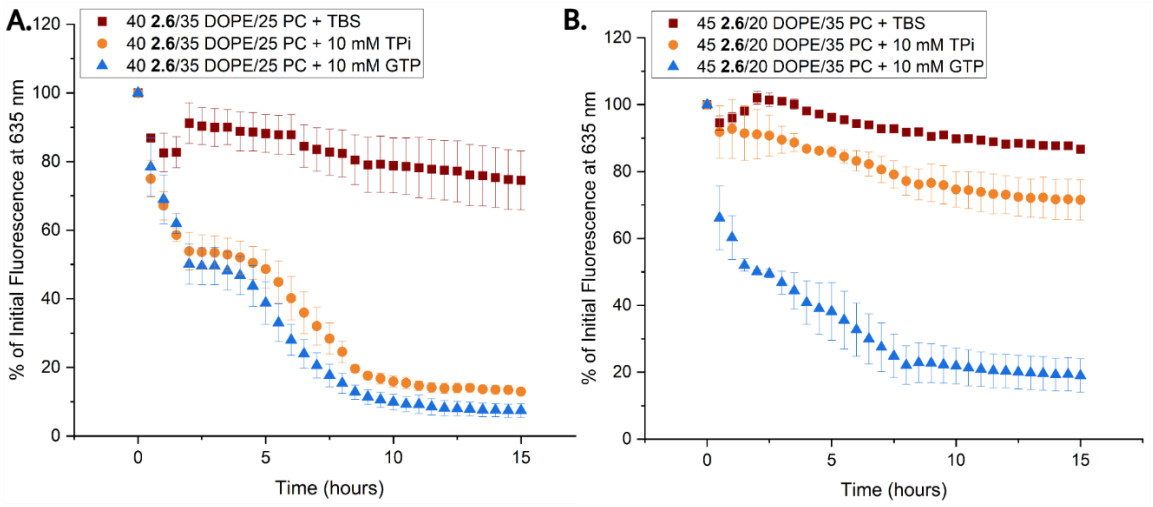

Figure 2.4. NR dye release highlighting tunable metabolite-triggered response through variation of membrane composition. NR dye release comparison of two liposome formulations treated with 10 mM GTP or TPi. Significant triggered release from each metabolite was observed for 40/35/25 **2.6**/DOPE/PC liposomes (A), but formulation adjustment to 45/20/35 **2.6**/DOPE/PC (B) promoted metabolite triggering selectivity by GTP. Error bars denote standard errors from at least three biological replicates.

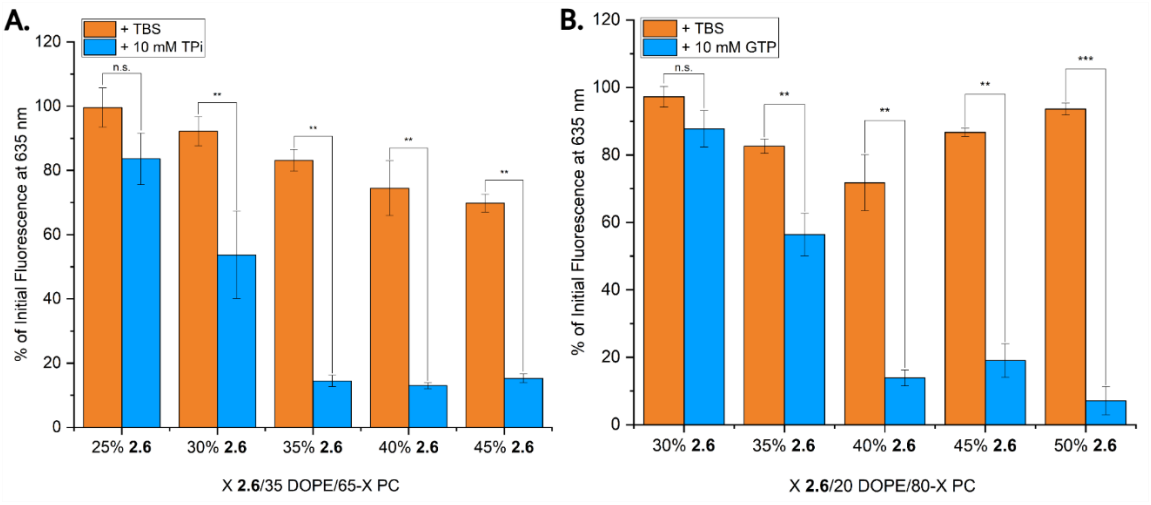

Figure 2.5. NR endpoint release assays comparing both formulation types with either TPi or GTP treatment. End-point NR release assay results for liposomes with varying BPLS **2.6** percentage but fixed DOPE (35% for A and 20% for B) treated with TPi (A) or GTP (B) after 16 hours. **2.6** percentage generally correlated to a linear relationship in triggered cargo release and passive cargo leakage for liposomes below 40-50% BPLS. Optimal formulations were found to contain 35/35/30 **2.6**/DOPE/PC (A) and 50/20/30 **2.6**/DOPE/PC (B). Error bars denote standard errors from at least three biological replicates. Statistical comparisons were performed between TBS and trigger (TPi, GTP) at each **2.6**% using unpaired two-tailed t-tests (Welch's correction), where n.s. ($p > 0.05$), * ($p < 0.05$), ** ($p < 0.01$), *** ($p < 0.001$).

For GTP-selective liposomes containing 20% DOPE, an initial linear trend in liposome destabilization was observed up to 30–40% **2.6** (Figure 2.5B). However, with higher concentrations of **2.6**, a re-stabilization effect appeared, where passive cargo leakage decreased while maximum cargo release was maintained. The optimal formulation of this type was determined as 50/20/30 **2.6**/DOPE/PC liposomes, which exhibited ~5% passive leakage and ~92% cargo release when treated with GTP.

We next explored an enhanced perspective of metabolite-driven release from **2.6** liposomes by studying the kinetics of NR release in Figure 2.6. Here, we selected The optimal and adjacent formulations from Figure 2.5 that exhibited cargo release. Liposomes were treated with either 10 mM TPi (X/35/65-X **2.6**/DOPE/PC) or 10 mM GTP (X/20/80-X **2.6**/DOPE/PC). The three liposome formulations treated with TPi (Figure 2.6A) showed similar kinetic release curves for NR release, plateauing at similar extents of cargo release and exhibiting ~40–50% cargo release within 2.5 hours. The GTP treated liposomes increased in release extent as **2.6** was increased (Figure 2.6B). Cargo release within the first 2.5 hours ranged from ~40–60%. Buffer treated controls indicated higher overall liposome stability with decreasing passive leakage as **2.6** was increased. Negative control liposomes without **2.6** exhibited minimal NR release after metabolite treatment, indicating NR release was facilitated through lipid switch and metabolite interaction. Rate constants and $t_{1/2}$ were also calculated for each of the GTP/TPi treated samples (Figure 2.7). The two key formulations determined from these experiments (35/35/30 and 50/20/30 **2.6**/DOPE/PC) were then lastly tested over a longer, untreated 7-day period to establish long-term stability, with minimal passive leakage noted in Figure 2.8.

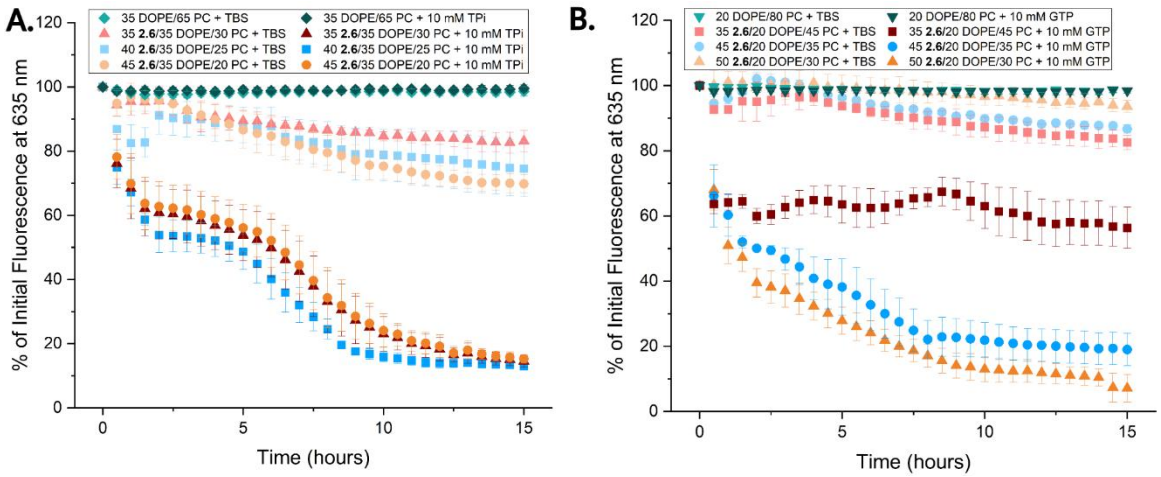

Figure 2.6. Kinetic NR release studies over 15 hours with TPi or GTP treatment. Kinetic NR release curves for BPLS **2.6** liposomes treated with 10 mM of TPi (A) or GTP (B) and monitored over 15 hours. Release curves indicate steady cargo release from liposomes, with minimal release from untreated controls. Error bars denote standard errors from at least three biological replicates.

Figure 2.7. Curve fittings of kinetic NR release curves for k_2 and $t_{1/2}$ calculations. (A) Fluorescence cargo release from 35 **2.6**/35 DOPE/30 PC liposomes + 10 mM TPi fit to a burst + first-order model. An initial burst ($\beta = 0.1817$) is followed by slower release ($k_2 = 0.11119$, $t_{1/2} = 6.2339$ hr). (B) Fluorescence cargo release from 40 **2.6**/35 DOPE/25 PC liposomes + 10 mM TPi fit to a burst + first-order model. An initial burst ($\beta = 0.21002$) is followed by slower release ($k_2 = 0.13429$, $t_{1/2} = 5.1616$ hr). (C) Fluorescence cargo release from 45 **2.6**/35 DOPE/25 PC liposomes + 10 mM TPi fit to a burst + first-order model. An initial burst ($\beta = 0.15935$) is followed by slower release ($k_2 = 0.10925$, $t_{1/2} = 6.3446$ hr). (D) Fluorescence cargo release from 35 **2.6**/20 DOPE/45 PC liposomes + 10 mM GTP fit to a burst + first-order model. An initial burst ($\beta = 0.34652$) is followed by slower release ($k_2 = 0.00676$, $t_{1/2} = 102.54$ hr). The model indicates the majority of the release for this formulation occurs within the initial burst, with minimal subsequent change. (E) Fluorescence cargo release from 45 **2.6**/20 DOPE/35 PC liposomes + 10 mM GTP fit to a burst + first-order model. An initial burst ($\beta = 0.36645$) is followed by slower release ($k_2 = 0.10295$, $t_{1/2} = 6.7329$ hr). (F) Fluorescence cargo release from 50 **2.6**/20 DOPE/35 PC liposomes + 10 mM GTP fit to a burst + first-order model. An initial burst ($\beta = 0.38749$) is followed by slower release ($k_2 = 0.15436$, $t_{1/2} = 4.4905$ hr). Error bars denote standard errors from at least three biological replicates.

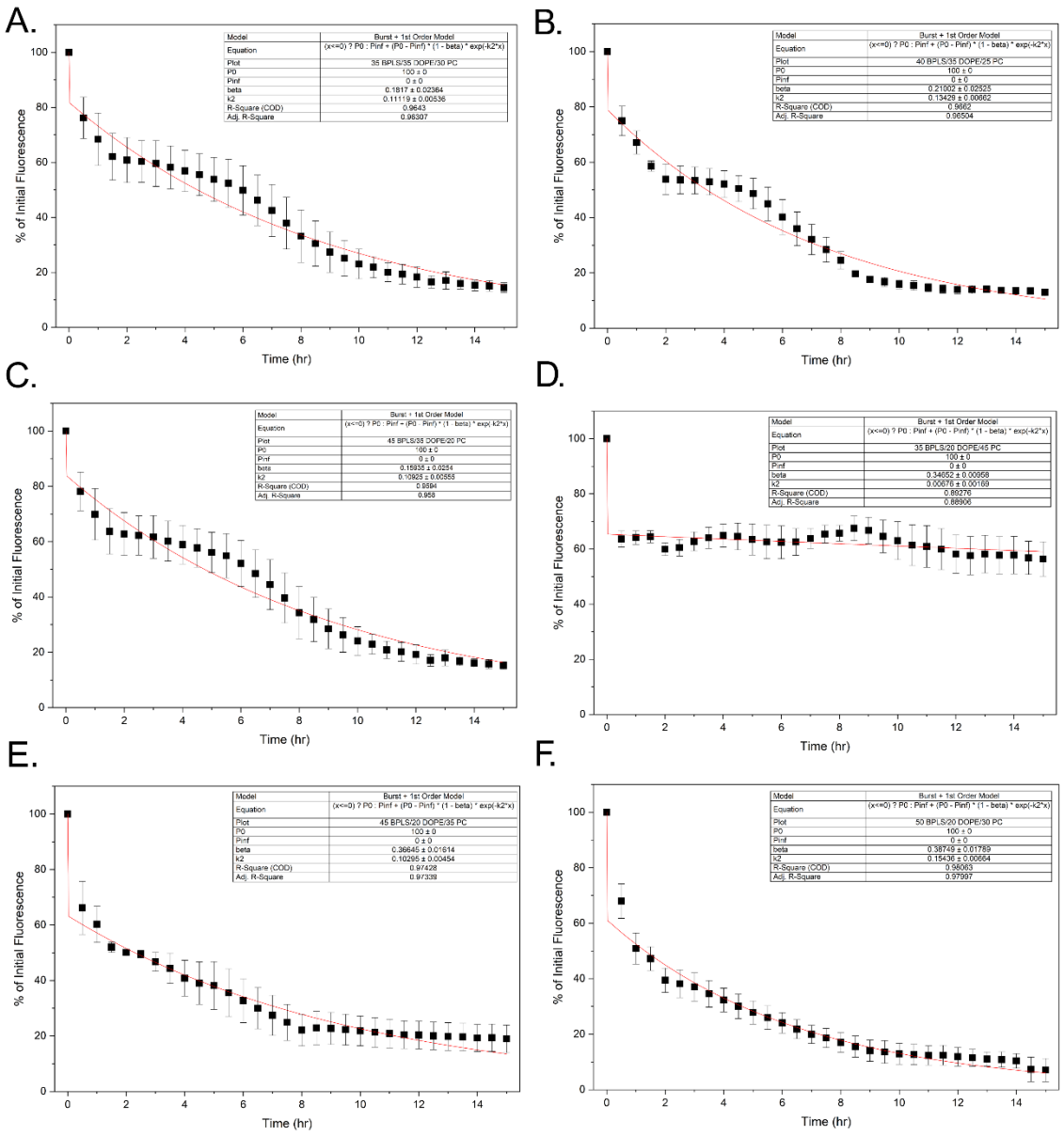
A.
Model | Burst + 1st Order Model
Equation | (x<=0) ? P0 : Pinf + (P0 - Pinf) * (1 - beta) * exp(-k2*x)
Plot | 35 BPLS/35 DOPE/30 PC
P0 | 100 ± 0
Pinf | 0 ± 0
beta | 0.1817 ± 0.02364
k2 | 0.11119 ± 0.00536
R-Square (COD) | 0.9643
Adj. R-Square | 0.96307
% of Initial Fluorescence
Time (hr)
B.
Model | Burst + 1st Order Model
Equation | (x<=0) ? P0 : Pinf + (P0 - Pinf) * (1 - beta) * exp(-k2*x)
Plot | 40 BPLS/35 DOPE/25 PC
P0 | 100 ± 0
Pinf | 0 ± 0
beta | 0.21002 ± 0.02525
k2 | 0.13429 ± 0.00662
R-Square (COD) | 0.9662
Adj. R-Square | 0.96504
% of Initial Fluorescence
Time (hr)
C.
Model | Burst + 1st Order Model
Equation | (x<=0) ? P0 : Pinf + (P0 - Pinf) * (1 - beta) * exp(-k2*x)
Plot | 45 BPLS/35 DOPE/20 PC
P0 | 100 ± 0
Pinf | 0 ± 0
beta | 0.15935 ± 0.0254
k2 | 0.10925 ± 0.00553
R-Square (COD) | 0.9694
Adj. R-Square | 0.968
% of Initial Fluorescence
Time (hr)
D.
Model | Burst + 1st Order Model
Equation | (x<=0) ? P0 : Pinf + (P0 - Pinf) * (1 - beta) * exp(-k2*x)
Plot | 35 BPLS/20 DOPE/45 PC
P0 | 100 ± 0
Pinf | 0 ± 0
beta | 0.34652 ± 0.00958
k2 | 0.00676 ± 0.00169
R-Square (COD) | 0.89276
Adj. R-Square | 0.88906
% of Initial Fluorescence
Time (hr)
E.
Model | Burst + 1st Order Model
Equation | (x<=0) ? P0 : Pinf + (P0 - Pinf) * (1 - beta) * exp(-k2*x)
Plot | 45 BPLS/20 DOPE/35 PC
P0 | 100 ± 0
Pinf | 0 ± 0
beta | 0.36645 ± 0.01614
k2 | 0.10295 ± 0.00454
R-Square (COD) | 0.97428
Adj. R-Square | 0.97339
% of Initial Fluorescence
Time (hr)
F.
Model | Burst + 1st Order Model
Equation | (x<=0) ? P0 : Pinf + (P0 - Pinf) * (1 - beta) * exp(-k2*x)
Plot | 50 BPLS/20 DOPE/30 PC
P0 | 100 ± 0
Pinf | 0 ± 0
beta | 0.38749 ± 0.01789
k2 | 0.15436 ± 0.00664
R-Square (COD) | 0.98003
Adj. R-Square | 0.97997
% of Initial Fluorescence
Time (hr)

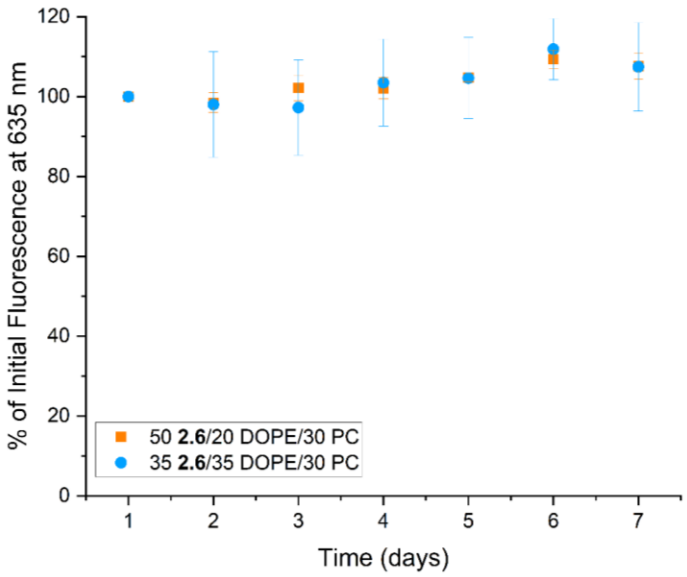

Figure 2.8. Long-term stability and leakage of liposomes over 7 days. Liposomal stability test with untreated liposomes monitored over 7 days for any passive dye leakage. Error bars denote standard errors from at least three biological replicates.

2.4.4 Fluorescence Release Assays in Competing Environments

Following identification of two optimized **2.6** formulations with distinct release profiles, an additional NR release study was conducted to directly compare their metabolite selectivity and evaluate tunable responsiveness relative to the initial screening. This focused screen examined the nucleotide triphosphates GTP, ATP, CTP, and UTP alongside TPi, enabling direct comparison between the original metabolites that showed partial triggering (Figure 2.9). For the 35/35/30 **2.6**/DOPE/PC formulation, triggered cargo release was observed following treatment with both TPi and GTP, consistent with its previously identified dual responsiveness. UTP treatment also resulted in moderate release, whereas ATP and CTP exhibited minimal membrane perturbation under the same conditions. These data indicate that this formulation remains responsive to multiple highly charged

triphosphates. In contrast, the 50/20/30 **2.6**/DOPE/PC formulation exhibited a markedly different selectivity profile. Under identical treatment conditions, significant cargo release was observed exclusively in response to GTP, while ATP, CTP, UTP, and TPi treatments resulted in minimal release comparable to buffer controls. This compositional shift therefore narrows responsiveness from a broader TPi/GTP profile to a more selective GTP-triggered release behavior. The divergence in selectivity between these two formulations demonstrates that membrane composition functions as an effective tuning parameter for **2.6**-mediated triggering. These data suggest that increasing the **2.6** fraction while reducing DOPE content alters the membrane's tolerance for headgroup-induced packing perturbation, effectively shifting the threshold at which nucleotide binding is translated into bilayer destabilization. Rather than altering lipid switch chemistry, modulation of the surrounding lipid environment alone is sufficient to refine selectivity among closely related nucleotide triphosphates.

With extensive release indicated within a TBS environment, we next investigated the function and tunability of BPLS **2.6** within more complex environments. Because phosphate-containing species are abundant in physiological fluids and intracellular compartments, evaluating lipid responsiveness in buffers and media that more closely approximate biological conditions is essential for assessing selectivity and robustness of the triggered release behavior.[142,143] Liposomes hydrated in 1x PBS still exhibited minimal cargo leakage in a phosphate-rich environment, and additional changes in the phosphate environment with PBS(+)(+) treatment maintained passive cargo leakage below ~15%. Changes in osmolarity of the surrounding buffer were also assessed with 10 mM NaCl

treatment, where passive cargo leakage was maintained below ~20% (Figure 2.10)

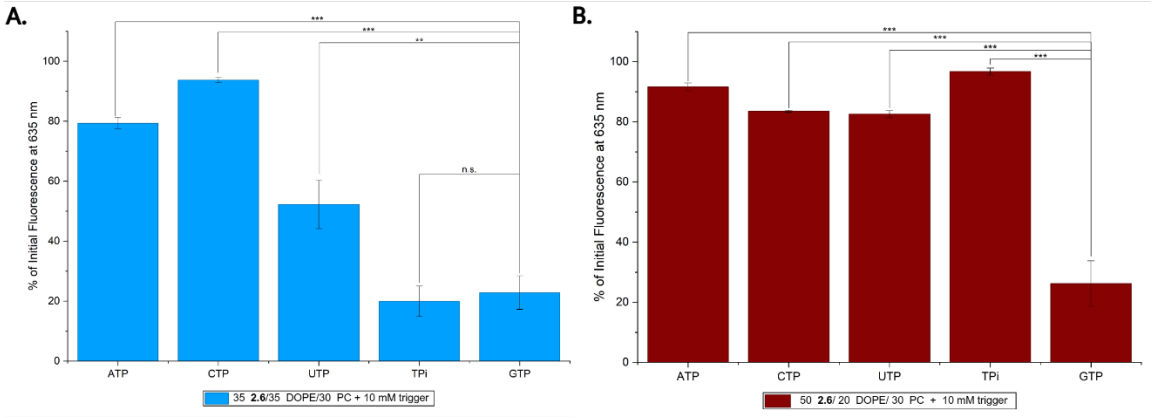

Figure 2.9. Additional metabolite selectivity screen with optimized 2.6 formulations. Additional metabolite selectivity experiments highlight the tunable selectivity of BPLS **2.6** with optimized liposome formulations determined from the previous kinetic NR release curves. (A) 35/35/30 **2.6**/DOPE/PC liposomes incubated with nucleotide triphosphates or TPi exhibited triggered cargo release with GTP and TPi, while NR release from UTP and ATP incubation was attenuated when compared to the initial selectivity screen. (B) 50/20/30 **2.6**/DOPE/PC liposomes incubated with the nucleotide triphosphates or TPi exhibited triggered cargo release by GTP incubation only, verifying the tunable selectivity of BPLS **2.6** against similar metabolites. Error bars denote standard errors from at least three biological replicates. Statistical analysis was performed using a two-way ANOVA (factors: formulation and trigger) followed by Tukey's post-hoc multiple comparison test. Significance between triggers within each formulation is shown where n.s. ($p > 0.05$), * ($p < 0.05$), ** ($p < 0.01$), *** ($p < 0.001$). The two-way ANOVA also confirmed a significant formulation x trigger interaction ($p < 0.0001$).

After confirming liposome stability in phosphate-rich buffer conditions, NR release assays were next performed in competitive metabolite environments to evaluate whether BPLS **2.6**-mediated triggering could be preserved in the presence of multiple anionic species, as noted in Figure 2.11. Liposomes were treated with a mixed metabolite solution containing equimolar concentrations of common phosphate- and carboxylate-containing metabolites at final concentrations of either 12 mM total metabolites, or 6 mM total metabolites supplemented with 6 mM of either TPi or GTP. Under these conditions, 35/35/30 **2.6**/DOPE/PC liposomes exhibited no statistically significant cargo release relative to buffer controls. In contrast, 50/20/30 **2.6**/DOPE/PC liposomes displayed a significant decrease in NR fluorescence only upon treatment with GTP-containing samples, indicating that GTP-selective release is retained in a competitive environment.

To assess the influence of serum proteins and media components on BPLS **2.6**-mediated membrane perturbation, NR release assays were also performed in cell culture media. Liposomes formulated as the GTP-responsive 50/20/30 **2.6**/DOPE/PC were incubated in phenol-red free DMEM supplemented with 10% fetal bovine serum (FBS) and 1% penicillin-streptomycin (pen/strep) (Figure 2.12). Under these conditions, GTP-treated liposomes exhibited time-dependent cargo release, reaching a plateau corresponding to about 44% NR release after 24 hours. In contrast, untreated liposomes subjected to TPi or PBS(+)(+) exhibited minimal passive leakage over the same period. Although the overall extent of release was reduced relative to buffer-based experiments, preservation of GTP-selective triggering in this environment demonstrates that **2.6**-mediated membrane perturbation remains operative in complex biological conditions.

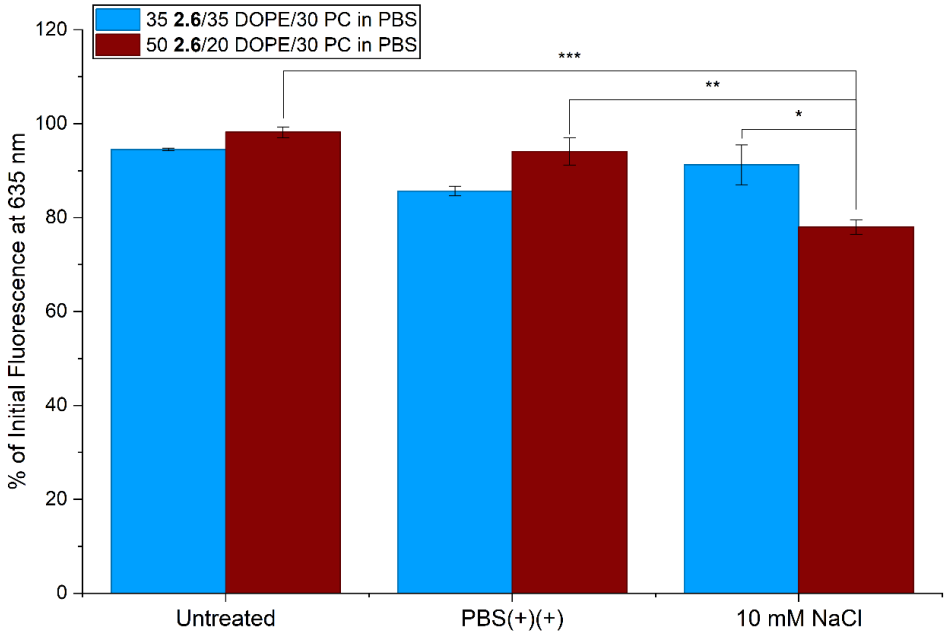

Figure 2.10. Passive leakage of PBS-hydrated liposomes in phosphate rich and altered osmolarity environments. NR release studies were completed for liposomes hydrated with 1x PBS buffer, treated with 10 mM NaCl or an equivalent volume of 1x PBS(+)(+), and measured after 48 hours. Error bars denote standard errors from at least three biological replicates. Statistical analysis was performed using a two-way ANOVA (factors: formulation and trigger) followed by Tukey's post-hoc multiple comparison test. Significance between triggers within each formulation is shown where n.s. ($p > 0.05$), * ($p < 0.05$), ** ($p < 0.01$), *** ($p < 0.001$). The two-way ANOVA confirmed no statistical significance was observed between any treated 35/35/30 2.6/DOPE/PC liposomes, whereas significance was observed for NaCl treated 50/20/30 2.6/DOPE/PC liposomes. This indicates some cargo leakage from liposomes occurs when osmolarity of the surrounding environment is increased, but minimal leakage is observed in the presence of increased phosphate from the buffer solution.

Figure 2.11. NR release from liposomes in complex metabolite environments. NR release studies were completed for liposomes treated with TBS buffer, a mixed metabolite solution for a final concentration of 12 mM, a mixed metabolite solution with a final concentration of 6 mM plus 6 mM TPi, and a mixed metabolite solution with a final concentration of 6 mM plus 6 mM of GTP. The mixed metabolite solution stock was made up of equal concentrations of Pi, PPi, ADP, ATP, FP, FBP, CTP, UTP, AMP, Mal, Fum, and Oxa for a total final concentration of 300 mM of all metabolites (25 mM for each metabolite), and diluted to a final concentration of either 6 mM or 12 mM when treating liposomes. Liposomes were treated and measured after 16 hours. Error bars denote standard errors from at least three biological replicates. Statistical analysis was performed using a two-way ANOVA (factors: formulation and trigger) followed by Tukey's post-hoc multiple comparison test. Significance between triggers within each formulation is shown where n.s. ($p > 0.05$), * ($p < 0.05$), ** ($p < 0.01$), *** ($p < 0.001$). The two-way ANOVA confirmed no statistical significance was observed between any treated 35/35/30 2.6/DOPE/PC liposomes, whereas significance was observed for GTP treated 50/20/30 2.6/DOPE/PC liposomes when compared to buffer or TPi treatment of the same liposomes, and GTP treatment of the 35/35/30 liposomes. The 35/35/30 liposomes did not yield significant cargo release from exposure to control buffer treatments versus metabolites, whereas 50/20/30 liposomes exhibited significant cargo release from liposomes treated with 6 mM mixed metabolites plus 6 mM GTP.

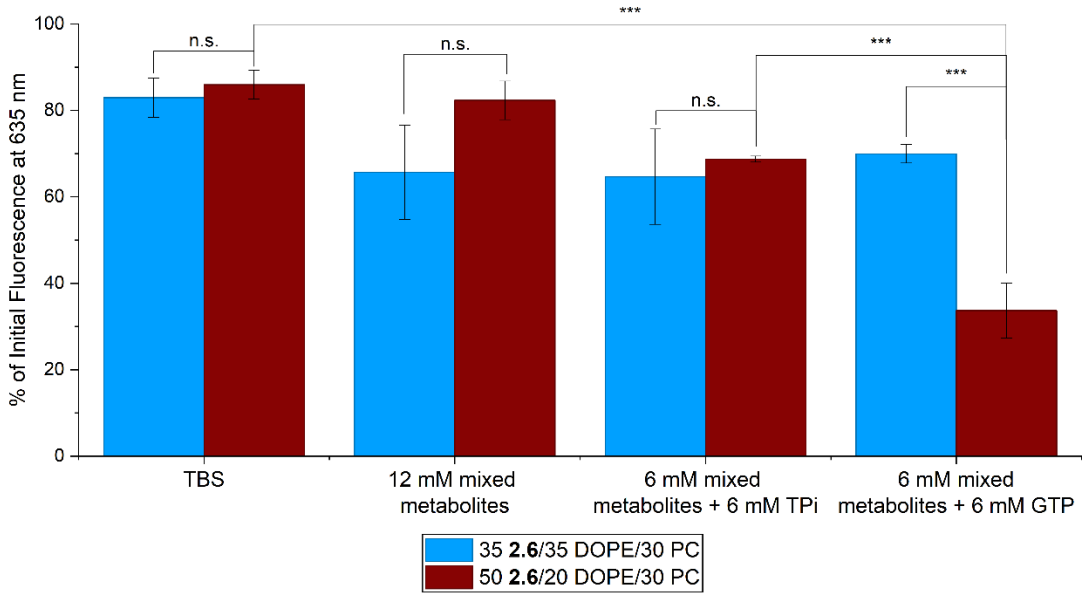
***
n.s.
n.s.
***
n.s.
***
100
80
60
40
20
0
% of Initial Fluorescence at 635 nm
TBS
12 mM mixed metabolites
6 mM mixed metabolites + 6 mM TPi
6 mM mixed metabolites + 6 mM GTP
35 **2.6**/35 DOPE/30 PC
50 **2.6**/20 DOPE/30 PC

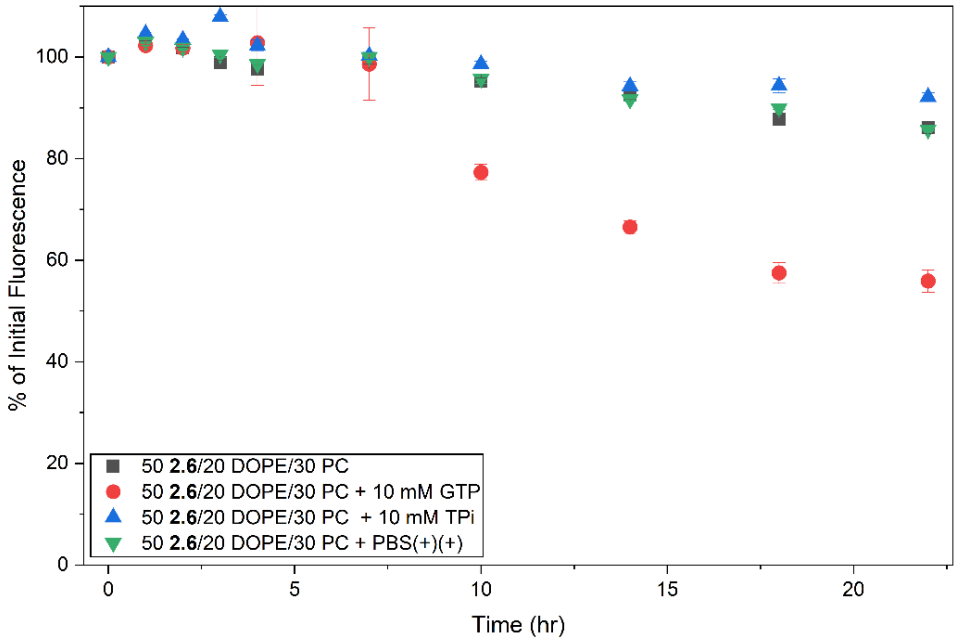

Figure 2.12. NR release from liposomes in DMEM + 10% FBS. Fluorescence studies for release of NR from 50/20/30 **2.6**/DOPE/PC liposomes were performed in phenol-red free DMEM media with 10% FBS, 1% pen/strep. GTP treated liposomes plateaued at 44% NR release while untreated, TPi treated, and PBS(+)(+) treated samples minimized passive leakage. Error bars denote standard errors from at least three biological replicates.

2.5 Size and Morphology Change Studies

2.5.1 GTP/TPi-Lipid Binding Studies

While BPLS **2.6** exposure to TPi and GTP elicits hydrophobic cargo release, we next investigated binding, size, and morphology behaviors and changes with **2.6** alone and **2.6** liposomes. To first determine the molecular basis of metabolite-triggered membrane perturbation, fluorescence titration studies were performed to quantify direct binding interactions between BPLS **2.6** and GTP or TPi. These experiments were conducted in solution to isolate headgroup-anion interactions independent of bilayer organization. Titration with either metabolite to stock solutions of **2.6** revealed changes in fluorescence intensity that could be plotted into binding isotherms (Figure 2.13). A dissociation constant (K_d) between **2.6** and GTP was determined to be 0.150 ± 0.010 mM. In contrast, titration with TPi resulted in a weaker apparent interaction, with K_d = 1.225 ± 0.081 mM. These results demonstrate that BPLS **2.6** binds GTP more strongly than TPi in solution, consistent with the enhanced GTP-triggered cargo release observed for compositionally optimized liposomes.

2.5.2 Dynamic Light Scattering Studies

To determine whether metabolite-triggered release was accompanied by structural changes in vesicle morphology, particle size was monitored by DLS before and after treatment with GTP or TPi (Figure 2.14). DOPE percentages were kept constant to match optimized formulations determined, while **2.6** and thus PC concentrations were adjusted. All formulations initially exhibited uniform diameters, confirming stable liposome formation following extrusion.

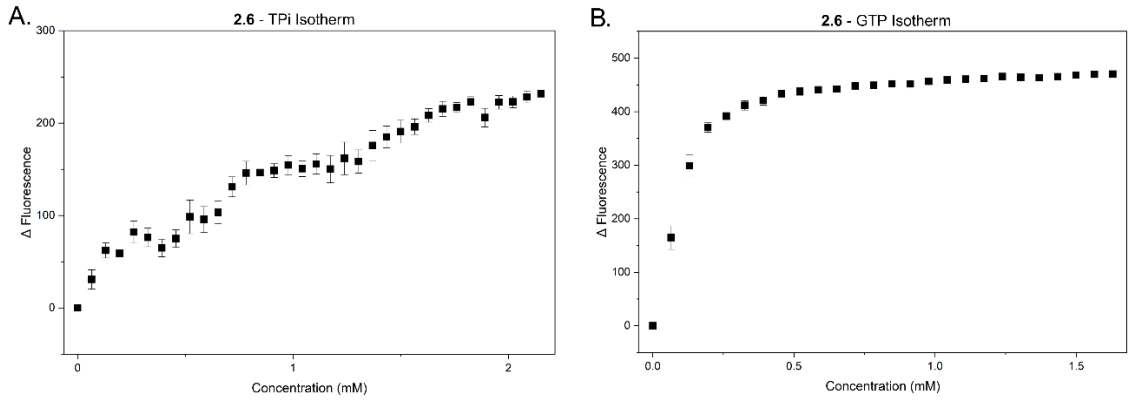

Figure 2.13. Binding isotherms for 2.6-TPi and 2.6-GTP. 2.6-TPi solution binding study was completed through fluorescence titration. Fluorescence titration for the **2.6**-TPi interaction was fitted to a single-site Langmuir binding isotherm, $\theta = \theta_0 + \Delta\theta([L] / (K_d + [L])$, using nonlinear least-squares regression. Both unweighted and weighted fits (weighted by the standard error of each measurement) were performed. The unweighted fit, assuming uniform variance across data points, yielded $K_d = 0.417$ (±0.026 mM). The weighted fit, accounting for heteroscedasticity in the fluorescence data, provided a more statically robust estimate of $K_d = 1.225$ (±0.081 mM). Weighted regression reduced the influence of high-variance points and more accurately captured the mid-range curvature of the binding isotherm consistent with a single-site, non-cooperative binding model. (B) GTP solution binding study was completed through fluorescence titration. Binding of GTP to **2.6** was quantified by fitting to a single-site Langmuir isotherm, $\theta = [L] / (K_d + [L])$, where [L] is the free GTP concentration and K_d is the equilibrium dissociation constant. Nonlinear least-squares fitting of the titration data yielded $K_d = 0.150$ mM (±0.010 mM). Error bars denote standard errors from at least three biological replicates.

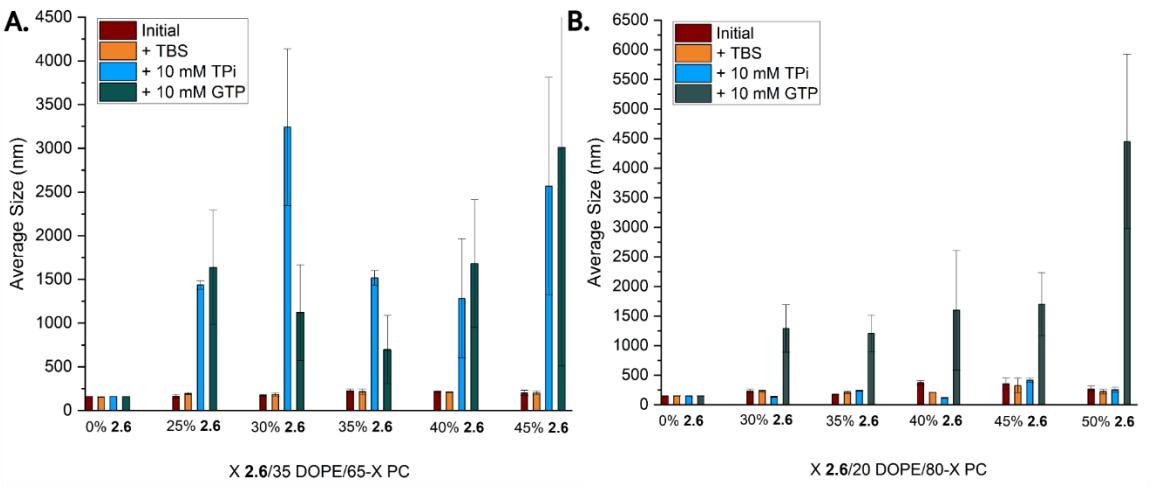

Figure 2.14. DLS comparisons of both 2.6 liposome formulations treated with TPi and GTP. DLS analysis of liposomes with varying **2.6** percentage and fixed DOPE, before and after (16 hours) treatment with TBS, 10 mM GTP, or 10 mM TPi. Liposomes showed uniform sizes in the expected range before metabolite treatment, with minimal changes after buffer treatment. Significant size increases were observed for **2.6** liposomes treated with GTP (A-B) or TPi (A). Error bars denote standard errors from at least three biological replicates.

Liposomes lacking BPLS **2.6** (0% control) showed no significant size changes after treatment with either metabolite. Likewise, buffer-treated **2.6** liposomes remained largely unchanged. In contrast, **2.6**-containing formulations displayed pronounced size increases following metabolite exposure. For the 35% DOPE formulation type, both GTP and TPi treatment produced substantial size changes, suggesting aggregation, fusion, or membrane reorganization (Figure 2.14A). The 20% DOPE formulations behaved differently. Here, significant size changes were observed primarily after GTP treatment, while TPi-treated samples measured by Mayesha Mustafa remained comparable to test controls (Figure

2.14B). Raw DLS data also indicated a split population for the GTP treated liposomes, with some particles retaining the original size and others shifted to larger diameters (Figure 2.15). This can be clearly contrasted with more uniformly large aggregates from TPi-triggered liposomes in the same study. While these liposomes release cargo in the presence of either metabolite, the liposomal response and reorganization differed. Together, the sets of DLS data confirm that triggered release corresponds to measurable changes in vesicle structure. More importantly, they reinforce that membrane composition governs how BPLS **2.6** binding is translated into bilayer destabilization.

2.5.3 Zeta Potential Studies

To further probe how metabolite-binding alters membrane surface properties, ZP measurements were performed before and after treatment with 4-(2-hydroxyethyl)piperazine-1-ethane-sulfonic acid (HEPES) buffer, TPi, or GTP. Initial measurements confirmed that both formulations possessed positive surface charge, consistent with incorporation of the cationic BPLS **2.6** along with net neutral egg PC and DOPE. Treatment with HEPES buffer alone produced minimal changes, indicating that ionic strength effects were not responsible for subsequent charge variations. For the 35/35/30 **2.6**/DOPE/PC formulation, addition of 10 mM TPi resulted in a pronounced shift in surface potential, producing an overall charge inversion from positive to negative (Figure 2.16A). This behavior was not observed for GTP -treated samples, which remained positively charged. The charge reversal induced by TPi suggests strong surface association, providing a plausible explanation for the broader, less selective membrane response observed in this formulation.

Figure 2.15. Raw DLS curves of 2.6 liposomes from both formulations. Raw DLS curves of 35/35/30 **2.6**/DOPE/PC liposomes, before (A) and after treatment with TBS (B), GTP (C), and TPi (D). Raw DLS curves of 50/20/30 **2.6**/DOPE/PC liposomes, before (E) and after treatment with TBS (F), GTP (G), and TPi (H).

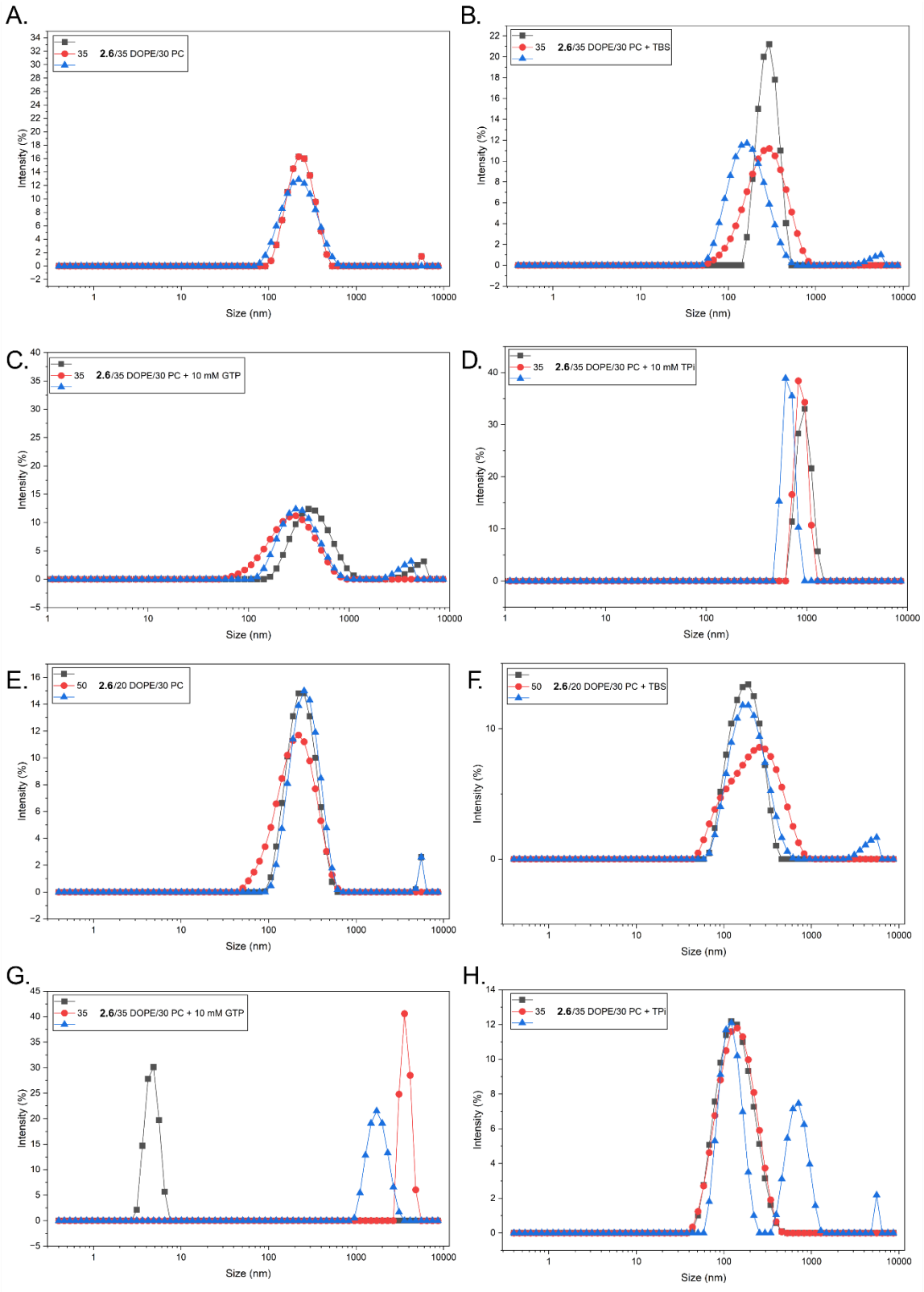
A.
35 2.6/35 DOPE/30 PC
Intensity (%)
Size (nm)
B.
35 2.6/35 DOPE/30 PC + TBS
Intensity (%)
Size (nm)
C.
35 2.6/35 DOPE/30 PC + 10 mM GTP
Intensity (%)
Size (nm)
D.
35 2.6/35 DOPE/30 PC + 10 mM TPi
Intensity (%)
Size (nm)
E.
50 2.6/20 DOPE/30 PC
Intensity (%)
Size (nm)
F.
50 2.6/20 DOPE/30 PC + TBS
Intensity (%)
Size (nm)
G.
35 2.6/35 DOPE/30 PC + 10 mM GTP
Intensity (%)
Size (nm)
H.
35 2.6/35 DOPE/30 PC + TPi
Intensity (%)
Size (nm)

In contrast, the 50/20/30 **2.6**/DOPE/PC formulation exhibited a different response profile (Figure 2.16B). While TPi treatment produced a measurable decrease in surface potential, all samples remained positively charged. GTP-treated liposomes likewise showed a reduced but still positive ZP. The absence of charge inversion with this formulation is consistent with its narrower, GTP-selective triggering behavior. Together, the ZP measurements support direct interaction between BPLS **2.6** and TPi/GTP.

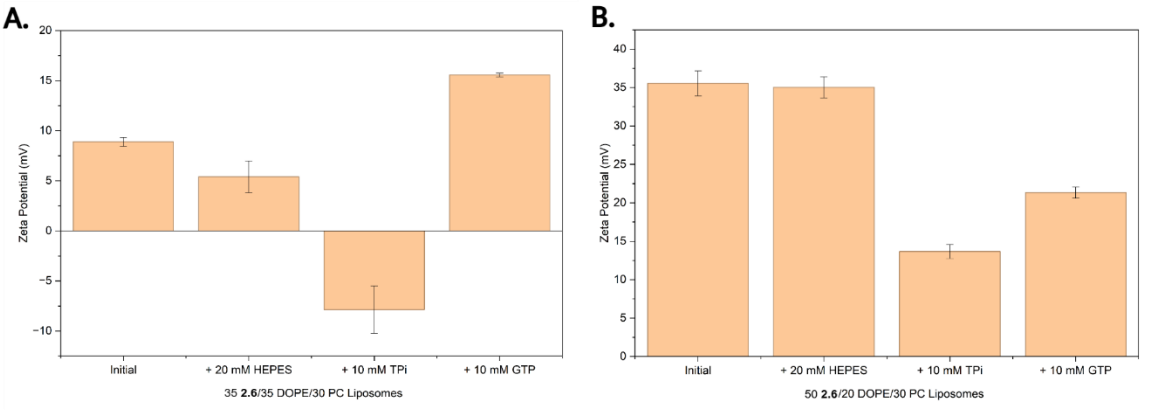

Figure 2.16. ZP of both liposome formulations with buffer, TPi or GTP treatment. ZP studies with 35/35/30 **2.6**/DOPE/PC liposomes with initial measurements and samples treated with HEPES, TPi, or GTP. Treatment with 10 mM TPi resulted in an overall charge flip to negative, which is not observed in the other measured samples. Studies with 50/320/30 **2.6**/DOPE/PC liposomes with initial measurements and samples treated with HEPES, TPi, or GTP. Treatment with 10 mM TPi resulted in a larger charge decrease, but all samples remained positive overall. Error bars denote standard errors from at least three biological replicates.

2.5.4 Transmission Electron Microscopy Imaging

To directly visualize morphology changes associated with metabolite-triggered release,

negatively stained TEM imaging was performed on 35/35/30 **2.6**/DOPE/PC liposomes before and after treatment. While certain untreated liposomes had difficulty surviving stain treatment, we were able to image several examples of unilamellar, uniform liposomes (Figure 2.17A,B). TEM images of the liposomes after one minute of incubation with 10 mM GTP (Figure 2.17C,D), 30 mM GTP (Figure 2.17E,F), 10 mM TPi (Figure 2.17G) or 30 mM TPi (Figure 2.17H) highlighted drastic morphology changes within the liposomes. Multivesicular aggregates were noted for all metabolite treatment conditions, but an interesting shift in aggregate morphology from 10 mM to 30 mM treatment was noted. Liposomes treated with 10 mM GTP or TPi showed multivesicular aggregates with more spherical vesicles identifiable within the larger aggregate. Increasing metabolite treatment to 30 mM shifted the captured morphology where individual spherical vesicles were much more difficult to identify, indicating more extensive membrane perturbations resulting from **2.6** triggering. These images corroborate the DLS data showing substantial size increases after metabolite treatment and support the interpretation that BPLS **2.6** binding induces large-scale membrane reorganization. Rather than simple pore formation, the triggered response appears to involve vesicle fusion, aggregation, and structural destabilization, consistent with curvature stress proposed for the lipid switch.

2.6 Hydrophilic Cargo Release Experiments

2.6.1 Formulation Development for GTP/TPi Release

While the prior studies primarily investigated NR hydrophobic dye release using **2.6**, the unique bilayer structure of liposomes also allows for encapsulation of hydrophilic cargo within the aqueous liposome core for delivery. Release of polar,

hydrophilic cargo is of particular interest due to the recent rise in RNA treatment strategies including CRISPR/Cas9 gene editing or mRNA sequence delivery.[65,144,145] Eliciting polar cargo release from liposomes can present additional challenges as this cargo must escape through the non-polar membrane bilayer, requiring more extreme membrane perturbation, necessitating a fine balance of liposome stability before and after encountering the stimulus. Therefore, inclusion of additional membrane-destabilizing lipids such as DOPE and PA can enhance triggered release but require formulation testing to ensure that passive cargo leakage remains low.

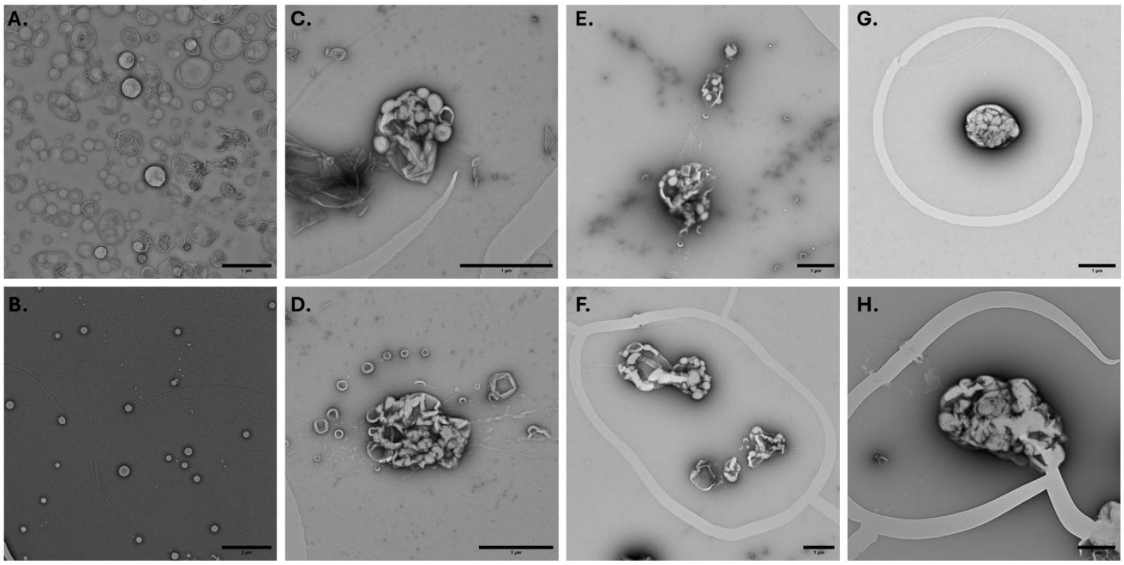

Figure 2.17. TEM images of 35/35/30 2.6/DOPE/PC liposomes before and after GTP and TPi treatment. Negatively stained TEM images of 35/35/30 **2.6**/DOPE/PC liposomes before treatment (A,B) highlighted unilamellar, uniform vesicles. After treatment with 10 mM GTP (C,D), 30 mM GTP (E,F), 10 mM TPi (G), or 30 mM TPi (H), multivesicular aggregates formed with more extensive vesicle degradation after 30 mM treatments (E,F,H). All scale bars represent 1 μm.

To extend BPLS **2.6**-mediated triggering into hydrophilic cargo systems, release studies were performed using hydrophilic fluorescent dyes encapsulated within the aqueous core of liposomes. While NR provided insight into membrane perturbation within the bilayer, evaluation of hydrophilic cargo release is necessary to assess translational relevance for therapeutic delivery applications. Encapsulation of aqueous dyes is inherently more sensitive to membrane defects and passive leakage, and early formulations that performed well in hydrophobic dye studies often exhibited either negligible hydrophilic release or excessive passive leakage. Achieving a balance between membrane stability and trigger responsiveness therefore required systematic compositional tuning. Several dye systems were initially screened, including a fluorophore/quencher pair 8-aminonaphthalene-1,3,6-trisulfonic acid (ANTS)/1,1'-(1,4-phenylenebis(methylene)) bis(pyridin-1-ium) bromide (DPX) and fluorescent dyes calcein and sulforhodamine B (SRB). Differences in dye charge and electrostatic interactions with the cationic TPP headgroups of **2.6** significantly influenced encapsulation efficiency and passive leakage behavior. ANTS and calcein, which possess higher net negative charge at physiological pH, exhibited increased background leakage and reduced formulation stability, likely due to stronger electrostatic interactions within the liposomal interior. In contrast, SRB carries a lower overall negative charge and demonstrated improved encapsulation stability with reduced passive leakage while still enabling clear detection of triggered release. For these reasons, SRB was selected for subsequent optimization studies.

Formulation development then focused on fine-tuning lipid ratios to achieve selective GTP- or dual GTP/TPi-responsive behavior while minimizing baseline leakage. Initial

compositions often resulted in either insufficient release upon metabolite treatment or excessive destabilization that led to significant passive cargo leakage. To address this, lipid compositions were adjusted incrementally, including half-percentage variations in **2.6** incorporation and modulation of membrane curvature stress through changes in DOPE content or incorporation of additional destabilizing lipids such as PA. Through iterative optimization, two key formulations were identified that balanced membrane integrity with metabolite-triggered responsiveness. These optimized systems were subsequently evaluated in time-dependent kinetic release studies and therapeutic cargo assays.

2.6.2 Time-Dependent Fluorescence Release Assays for GTP/TPi

Following formulation optimization, time-dependent fluorescence assays were conducted to quantify hydrophilic cargo release from **2.6**-containing liposomes. SRB was selected as a polar model cargo due to its high aqueous solubility and self-quenching behavior at elevated concentrations. When encapsulated at high concentration within the liposomal core, SRB fluorescence is suppressed through collisional quenching but release into surrounding buffer increases fluorescence intensity for quantitative cargo escape.

Liposomes were hydrated with SRB-containing Tris–HCl buffer and subsequently purified by size-exclusion chromatography (SEC) to remove unencapsulated dye. To minimize osmotic stress–induced leakage, buffer osmolarity was corrected to isotonic conditions prior to experimentation. Release was monitored over 16 hours and normalized to total encapsulated dye, determined by detergent-mediated disruption of liposomes with Triton X-100 at the conclusion of each experiment. Two optimized formulations containing 37.5% **2.6** were evaluated, differing in DOPE/PA/PC ratios. Liposomes composed of

37.5/32.5/2/28 **2.6**/DOPE/PA/PC exhibited gradual SRB release reaching approximately 15% and 20% upon treatment with 10 mM GTP and 10 mM TPi, respectively (Figure 2.18A). In contrast, liposomes formulated as 37.5/36.5/2/24 **2.6**/DOPE/PA/PC demonstrated altered responsiveness, releasing ~10% of encapsulated cargo in response to GTP and ~25% in response to TPi (Figure 2.18B). Thus, even within destabilized systems designed to facilitate polar cargo escape, modest compositional changes resulted in measurable shifts in selectivity and release magnitude.

Hydrophilic cargo release was less extensive than the previously observed NR release, consistent with the requirement that polar molecules traverse the entire bilayer rather than redistribute within the membrane core. Importantly, passive leakage remained below ~5% for both formulations, indicating that membrane integrity was largely preserved in the absence of metabolite stimulus. Release curves approached release plateaus near 15 hours, and kinetic parameters including rate constants and half-lives were extracted from fitted models (Figure 2.19) to enable quantitative comparison of trigger-dependent behavior.

2.6.3 Therapeutic Release Assays for GTP/TPi

To evaluate whether **2.6**-mediated membrane perturbation could be extended beyond model dyes to clinically relevant therapeutics, both optimized formulations were loaded with Dox. Consistent with trends observed in NR and SRB studies, metabolite-triggered Dox release reflected formulation-dependent selectivity. The partially selective 35% **2.6** formulation exhibited significant Dox release upon treatment with both 10 mM TPi and 10 mM GTP (Figure 2.20). In contrast, the more selective 50% **2.6** formulation demonstrated pronounced release only in response to GTP, and minimal release following TPi exposure.

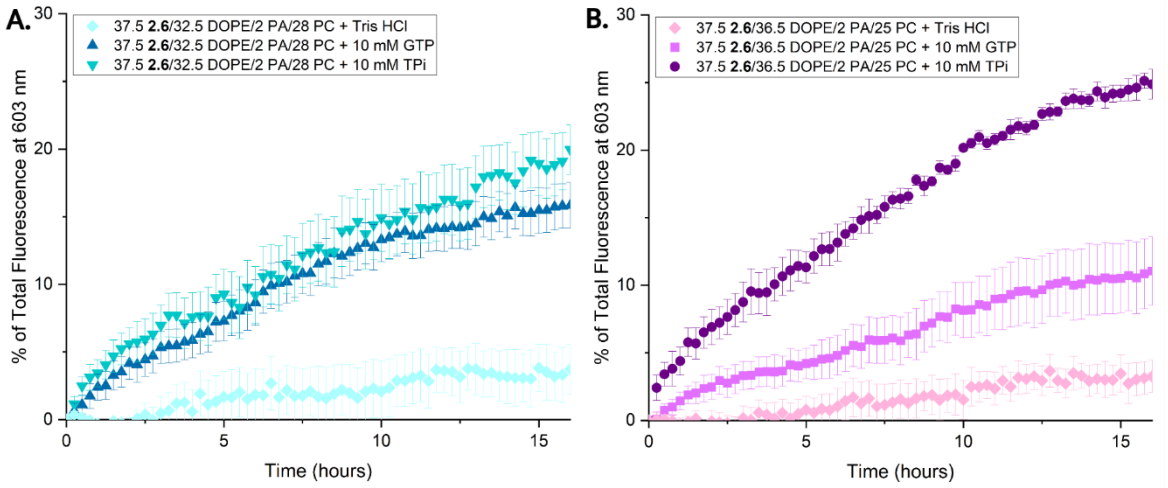

Figure 2.18. Kinetic SRB studies investigating both formulations over 16 hours with either TPi or GTP treatment. Kinetic SRB release curves for **2.6** liposomes treated with 10 mM of either TPi or GTP and monitored over 16 hours. Release plateaus were observed near the 15-hour mark, indicating steady release of cargo from liposomes. Release from 37.5/32.5/2/28 **2.6**/DOPE/PA/PC liposomes (A) was noted at ~15 and ~20% for 10 mM GTP and 10 mM TPi treatment respectively. Release from 37.5/36.5/2/24 **2.6**/DOPE/PA/PC liposomes (B) exhibited some tunability, with 10% and 25% release from 10 mM GTP and 10 mM TPi treatment, respectively. Error bars denote standard errors from at least three biological replicates.

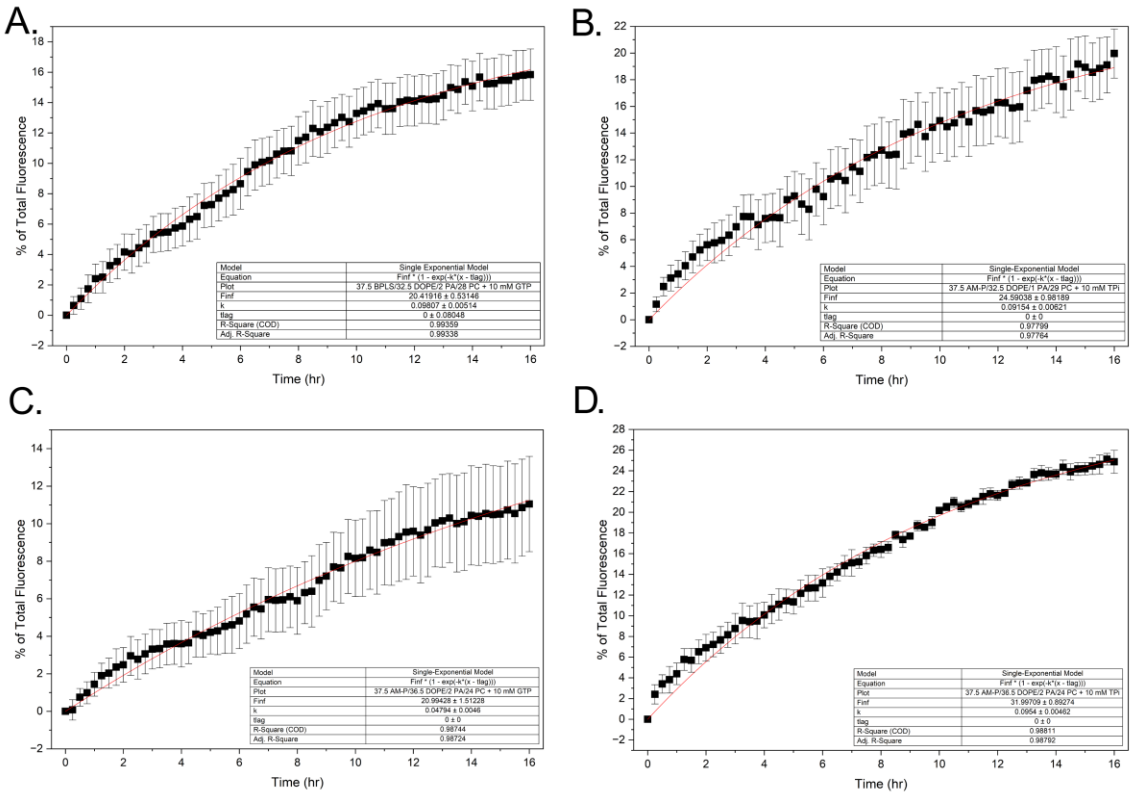

Figure 2.19. Curve fittings of kinetic SRB release curves for k2 and t1/2 calculations. (A) Fluorescence cargo release from 37.5/32.5/2/28 **2.6**/DOPE/PA/PC liposomes + 10 mM GTP fit to a single-exponential model, where k = 0.09807, t1/2 = 7.0679 hr. (B). Fluorescence cargo release from 37.5/32.5/2/28 **2.6**/DOPE/PA/PC liposomes + 10 mM TPi fit to a single-exponential model, where k = 0.09154, t1/2 = 7.5721 hr. (C) Fluorescence cargo release from 37.5/36.5/2/24 **2.6**/DOPE/PA/PC liposomes + 10 mM GTP fit to a single-exponential model, where k = 0.04794, t1/2 = 14.459 hr. (D) Fluorescence cargo release from 37.5/36.5/2/24 **2.6**/DOPE/PA/PC liposomes + 10 mM TPi fit to a single-exponential model, where k = 0.0954, t1/2 = 7.266 hr. Error bars denote standard errors from at least three biological replicates.

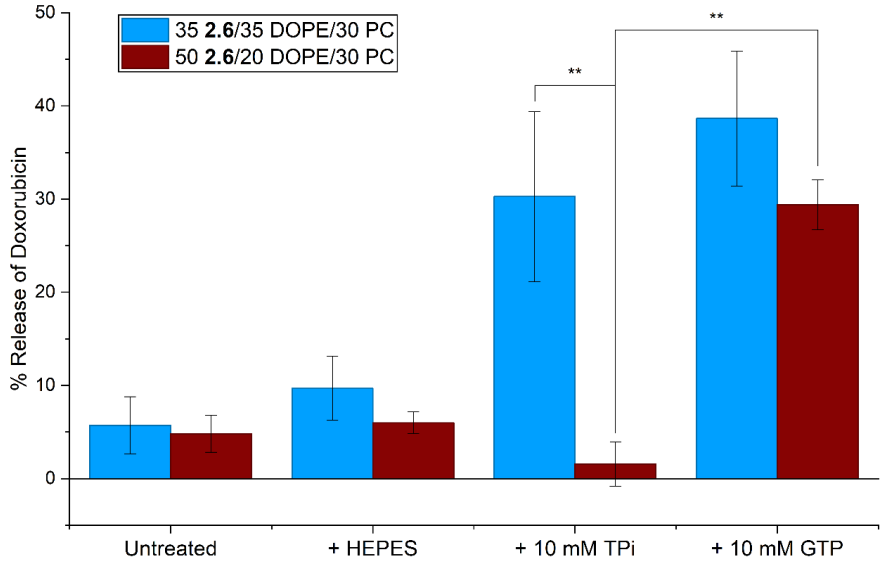

Figure 2.20. Release of Dox from 2.6 liposomes treated with TPi or GTP. Fluorescence studies for release of Dox from 50/20/30 and 35/35/30 **2.6**/DOPE/PC liposomes were performed where liposomes were left untreated, or treated with HEPES buffer, 10 mM TPi, or 10 mM GTP and measured after 16 hours. Error bars denote standard errors from at least three biological replicates. Statistical analysis was performed using a two-way ANOVA (factors: formulation and trigger) followed by Tukey's post-hoc multiple comparison test. Significance between triggers within each formulation is shown where n.s. ($p > 0.05$), * ($p < 0.05$), ** ($p < 0.01$), *** ($p < 0.001$). 50% **2.6** liposomes exhibited significant GTP selective release of Dox whereas the less selective 35% **2.6** liposomes exhibited significant release of Dox with both TPi and GTP treatment. Passive cargo leakage from untreated and buffer treated samples was minimized and determined as statistically significant when compared to GTP treatment (50 and 35% **2.6**) and TPi treatment (35% **2.6**).

Additionally, passive leakage from untreated or HEPES-treated samples remained low for both formulations over the 16-hour incubation period. This behavior closely parallels the hydrophobic and hydrophilic dye release data, reinforcing the conclusion that membrane composition governs trigger specificity. These results further validate that metabolite-induced membrane perturbation can be translated to therapeutic cargo release and further demonstrate that compositional tuning of **2.6**-containing membranes enables modulation of nucleotide selectivity even in drug-loaded systems.

2.7 Miscellaneous Experiments

2.7.1 Cargo Encapsulation Efficiency Studies and Calculations

Encapsulation efficiencies for hydrophobic and hydrophilic cargos were determined using calibration curves constructed from known concentrations of each dye (Figure 2.21). All measurements were performed following purification to remove unencapsulated cargo, and values are reported as mean ± standard error from at least three independent preparations. For NR, encapsulation efficiencies were determined to be (19.2 ± 0.4)% and (63.3 ± 0.8)% for 35/35/30 and 50/20/30 **2.6**/DOPE/PC liposomes, respectively. The higher encapsulation efficiency observed in the 50% **2.6** formulation is consistent with increased hydrophobic character or enhanced bilayer stability, which promotes enhanced partitioning of NR into the bilayer. Encapsulation efficiencies for the hydrophilic dye SRB were substantially lower, as expected for passive aqueous loading during thin-film hydration. Calculated efficiencies and dye-to-lipid ratios were 0.201 ± 0.005% (12.1 ± 0.3 nmol SRB per μmol lipid) for 37.5/32.5/2/28 **2.6**/DOPE/PA/PC liposomes and 0.075 ± 0.004% (4.51 ± 0.2 nmol SRB per μmol lipid) for 37.5/36.5/2/24 formulations. Passive entrapment of

polar cargo during vesicle formation is random, limited by the internal aqueous volume of the liposomes, and loaded in excess, resulting in low encapsulation efficiencies.[146]

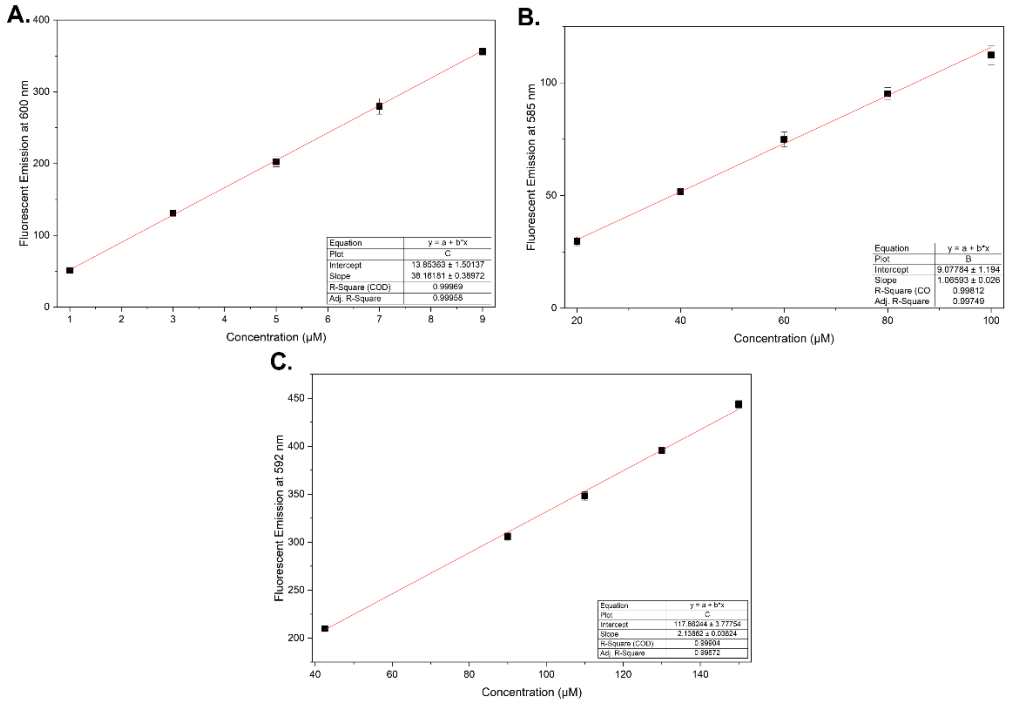

Figure 2.21. Fluorescence calibration curves of NR, SRB, and Dox for encapsulation efficiency calculations. (A) Fluorescence calibration curve for NR in chloroform used to measure encapsulation efficiency. The linear fit equation was determined to be y = (38.16181± 0.38972)x + (13.85363 ± 1.50137). (B) Fluorescence calibration curve for SRB in MilliQ water used to measure encapsulation efficiency with hydrophilic liposomes. The linear fit equation was determined to be y = (1.06593 ± 0.0146)x + (9.07784 ± 1.194). (C) Fluorescence calibration curve for Dox in MilliQ water used to measure encapsulation efficiency with Dox loaded liposomes. Error bars denote standard errors from at least three biological replicates. The linear fit equation was determined to be y = 2.13862 ± 0.03824)x + (117.86244 ± 3.77754).

In contrast, Dox loading efficiencies were significantly higher, at (5.93 ± 0.4)% and (5.12 ± 0.4)% for 35/35/30 and 50/20/30 **2.6**/DOPE/PC liposomes, respectively. Unlike SRB, Dox was incorporated using an active loading strategy, which exploits transmembrane gradients to drive drug accumulation into preformed vesicles. Active loading methods generally yield higher and more reproducible encapsulation efficiencies compared to passive hydration approaches, explaining the observed difference in drug incorporation despite both cargos being hydrophilic.

2.7.2 Alternate Synthetic Routes for Triphenylphosphonium Addition

Formation of the bis-triphenylphosphonium headgroup in **2.6** was initially unexpected, as the synthetic route was designed to yield an amine-functionalized lipid via Staudinger reduction of the corresponding azide precursor. Upon observing spectral data inconsistent with the anticipated amine product, additional control reactions were conducted to clarify the transformation pathway and confirm the identity of the resulting headgroup. To evaluate whether the reaction was terminating at the iminophosphorane intermediate stage, a dry Staudinger reaction was performed under anhydrous conditions. However, NMR analysis of the resulting material did not match that of the isolated product **2.6**, suggesting that the observed structure did not correspond to a trapped iminophosphorane species. This conclusion was further supported by electrospray ionization mass spectrometry (ESI-MS), which did not indicate formation of the expected intermediate. We next investigated whether nucleophilic substitution of the brominated intermediate (2.5) by triphenylphosphine could be occurring under the reaction conditions. Direct treatment of 2.5 with Staudinger reduction conditions was performed to probe potential phosphonium

formation through displacement of bromide. While this reaction produced phosphorus-containing species, the resulting NMR spectra did not fully reproduce the distinct features observed in **2.6**, indicating that simple substitution at the brominated position was unlikely to account for the final structure. Additionally, NR release data from liposomes formed with this switch product also did not match the stability of **2.6.**

Although the most chemically plausible pathway involves transformation of the azide intermediate under Staudinger conditions to ultimately yield a phosphonium-functionalized product, definitive mechanistic assignment was complicated by the inability to isolate and fully characterize the azide intermediate. As no purification step was performed between azide formation and Staudinger conditions, a combination of sequential substitution and phosphine-mediated transformations may contribute to the observed outcome. To further probe this possibility, a model reaction was conducted using benzyl bromide under analogous Staudinger conditions. In this simplified system, formation of a benzyl triphenylphosphonium species was confirmed by the appearance of a characteristic methylene doublet arising from phosphorus–proton coupling in the ^{1}H NMR spectrum. This diagnostic splitting pattern closely resembled the methylene doublet observed in the headgroup region of **2.6**, supporting assignment of the TPP structure (Figure 2.22). These control experiments confirmed that the final synthetic step resulted in formation of phosphonium-functionalized lipid **2.6** rather than the originally targeted amine derivative.

2.8 Conclusions

We have developed a novel liposomal platform that exhibits tunable responsiveness to GTP and TPi through strategic modulation of lipid compositions. By incorporating our

TPP-based BPLS **2.6** lipid switch, we achieved tunable, semi-selective and controlled cargo release with both hydrophobic and hydrophilic dye cargos. These results were confirmed using NR release assays, kinetic cargo release curves, DLS, metabolite selectivity screening, TEM imaging, and SRB kinetic release assays.

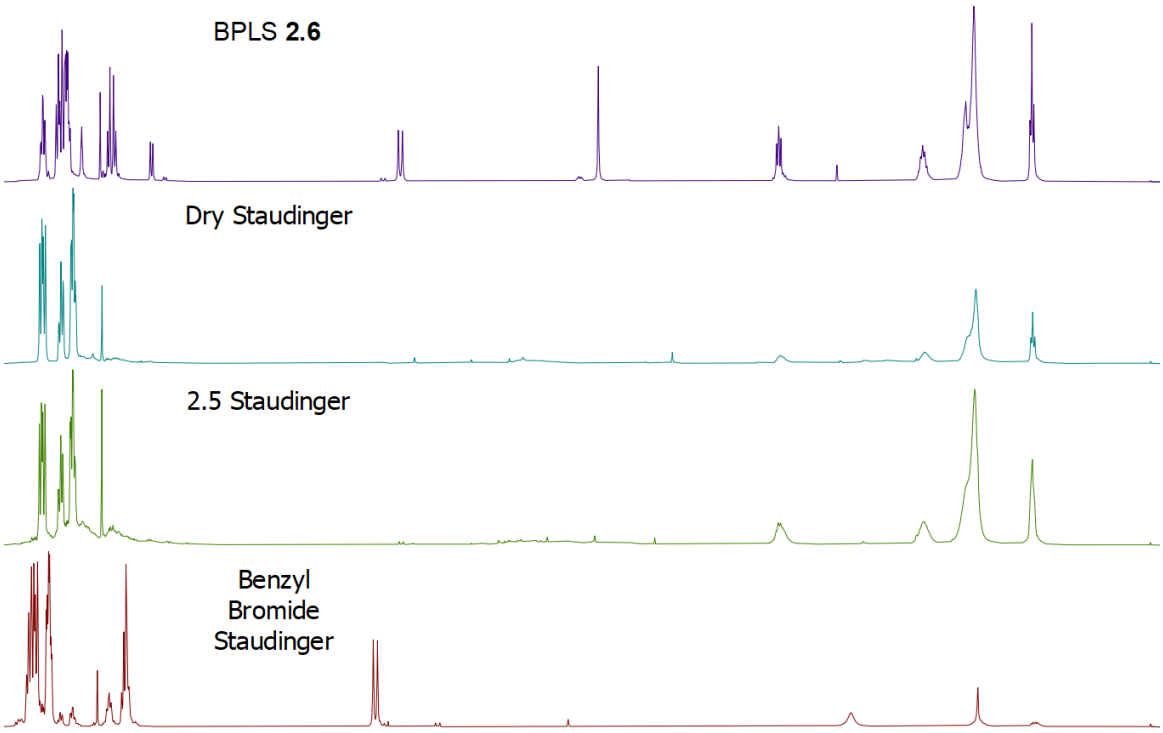

Figure 2.22. NMR comparison of Staudinger reduction products for experimental reactions. NMR comparison of the original and model reactions to verify **2.6** headgroup identity and possible formation pathway. Characteristic methylene doublet split by phosphorous was observed for BPLS **2.6** and the benzyl bromide test reaction.

Further development of this work is necessary for translation into clinical application, including optimization of trigger concentration sensitivity and release kinetics. Pharmacological evaluations completed through studies such as biodistribution,

biodegradability, and toxicity analysis will additionally be necessary for further translation of the system. However, our chemical proof-of-concept results do highlight the critical role of liposome composition in fine-tuning metabolite triggered selectivity and release kinetics. While the structure of the lipid switch is important for metabolite selectivity and subsequent switch triggering, the percentage of the lipid switch in relation to other bulk lipids within liposomes also plays a key role in triggered release activity. By leveraging GTP upregulation in diseased states and exploring TPi as a model phosphate to investigate liposome platform tunability, this work provides the foundation towards a versatile approach for complex metabolic profiles in diseased cells. Together, the discovery and rationalization of the BPLS system illustrate how unexpected chemical outcomes can be transformed into programmable membrane behavior through careful mechanistic analysis and compositional control. With this adaptable framework, a modular toolbox of lipid switches could be envisaged to eventually target a wide range of disease conditions with various upregulated metabolites. Instead of utilizing one unique lipid switch per metabolite of interest, strategically modifying liposome composition may allow a smaller number of unique switches to selectively respond to a wider range of metabolites through tuning. In the long term, liposomes that respond to targeted metabolites show promise for enhancing the selectivity of delivery to diseased cells in which those particular metabolites are upregulated. Toward that end, this work expands the stimuli-responsive liposome toolbox and paves the way for exploration of multi-metabolite responsive systems.

2.9 Synthesis and Experimental Procedures

Reagents and solvents were generally purchased from Sigma-Aldrich or Fisher

Scientific and used without further purification. PC (L-α-Phosphatidylcholine, mixed isomers from chicken egg), PA (L-α-phosphatidic acid, mixed isomers from chicken egg), and 18:1 (Δ9-Cis) PE (1,2-dioleoyl-*sn*-glycero-3-phosphoethanolamine) were purchased from Avanti Polar Lipids, Inc (Alabaster, AL). Dry solvents were obtained from a Pure Solv MD-7 solvent purification system purchased from Innovative Technology, Inc (Newburyport, MA). Column chromatography was performed using 230-400 mesh silica gel purchased from Sorbent Technologies. NMR spectra were obtained using a Bruker 500 MHz NMR spectrometer. Mass spectra were obtained with JEOL DART-Accustom mass spectrometer. Liposome extruder and polycarbonate membranes were obtained from Avanti Polar Lipids, Inc (Alabaster, AL). Ultrapure water was purified via a Millipore water system (≥ 18 MW·cm triple water purification system). Small quantities (< 5 mg) were weighed on a Mettler Toledo XS105 dual range analytical balance. Osmotic pressure was measured with Wescor Vapor Pressure Osmometer 5520. Fluorescence studies were performed using a Cary Eclipse Fluorescence Spectrophotometer from Agilent Technologies. DLS analyses were carried out with a Malvern Zetasizer Nano ZS instrument equipped with a 4.0 mW laser operating at l = 633 nm. Plots were generated using Origin Pro 2025b. All error bars in plots indicate the standard errors of at least three experimental replicates. Compounds **2.2**-**2.5** were synthesized as previously reported.[90]

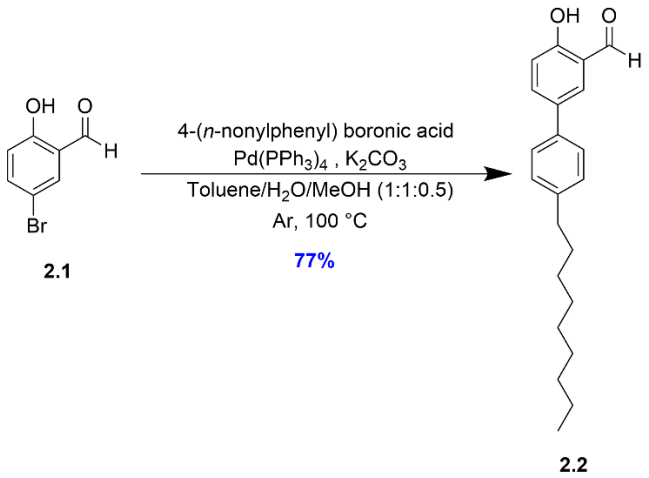

4-Hydroxy-4'-nonyl-[1,1'-biphenyl]-3-carbaldehyde (2.2)

5-Bromo-2-hydroxybenzaldehyde (**2.1**, 0.5649 g, 2.81 mmol), 4-(*n*-nonylphenyl) boronic acid (1.0450 g 4.21 mmol), tetrakis(triphenylphosphine)palladium(0) (0.0325 g, 0.0281 mmol) and potassium carbonate (K_2CO_3, 0.5818 g, 4.21 mmol) were combined in a 100 mL RBF under argon. After being dissolved with 25 mL toluene/H_2O/MeOH (2/2/1, v/v), the reaction mixture was heated at 100 ºC overnight (10.5 hours). After completion, the reaction was cooled to rt, and the solvent was removed using a rotary evaporator. The residue was re-dissolved in 25 mL DCM and washed with 10 mL of 0.5 M HCl, followed by the addition of 50 mL water. The aqueous layer was extracted with 3 x 25 mL DCM. The combined organic layer was further washed with 1 x 50 mL water and 1 x 50 mL brine, respectively, before being dried over Na_2SO_4 , filtered, and concentrated under reduced pressure. The crude was next loaded onto silica gel and subjected to column chromatography. Gradient elution from hexanes to 10% ethyl acetate in hexanes yielded the product as a slight yellow solid (0.7028 g, 2.17 mmol, 77% yield). R_f = 0.63 (10% EtOAc/hexanes).

^{1}H NMR (500 MHz, $CDCl_3$) δ 10.98 (s, 1H), 9.97 (s, 1H), 7.75 (d, J = 8.5 Hz, 2H), 7.46 (d, J = 8.0 Hz, 2H), 7.27 (d, J = 8.0 Hz, 2H), 7.06 (d, J = 8.5 Hz, 1H), 2.65 (t, J = 8.0 Hz, 2H), 1.65 (p, J = 7.5 Hz, 2H), 1.34 (m, 6H),1.27 (m, 6 H), 0.88 (t, J = 7.0 Hz, 3H).^{13}C NMR (126 MHz, $CDCl_3$) δ 196.70, 160.76, 142.33, 136.64, 135.64, 133.35, 131.64, 129.03, 126.42, 120.70, 118.04, 35.57, 31.88, 31.49, 29.51, 29.32, 22.66, 14.10. HRMS-DART: $[M+H]^+$ calcd for $C_{22}H_{29}O_2$: 325.2166, Found: 325.21463

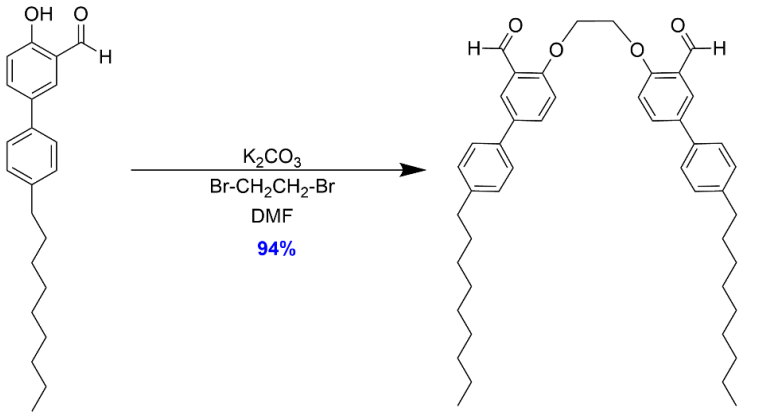

2.2 2.3

4,4''-(Ethane-1,2-diylbis(oxy))bis(4'-nonyl-[1,1'-biphenyl]-3-carbaldehyde) (2.3)

Compound **2.2** (0.1095 g, 0.3364 mmol) and K_2CO_3 (0.1273 g, 0.9211 mmol) were combined in a 50-mL RBF under argon and were dissolved with 5 mL of dry DMF. After the addition of 1,2-dibromoethane (13.27 µL, 0.1535 mmol), the reaction was heated to 80 °C. Reaction progress was monitored via TLC (25% EtOAc-hexanes) until starting materials were consumed after 42 hours, with equivalent additions of 1,2-dibromoethane at the reaction times 18 and 24.5 hours to ensure reaction completion. After completion, the mixture was cooled to rt, and the solvent was removed via rotary evaporator. The brown-orange mixture was added to 100 mL of 0.5 M HCl and extracted with 3 x 25 mL DCM. The combined organic layer was then washed with 5 x 50 mL H_2O and 1 x 50 mL

brine. After being dried over Na_2SO_4, filtered and concentrated under reduced pressure, the crude orange product was purified via silica gel column chromatography with a gradient elution of hexanes to 25 % ethyl acetate in hexanes, yielding the product as a yellow-orange solid (**2.3**, 0.1068 g, 0.1581 mmol, 94% yield). R_f = 0.41 (25% EtOAc/hexanes). ^{1}H NMR (500 MHz, $CDCl_3$) δ 10.51 (s, 2H), 8.09 (d, J = 2.5 Hz, 2H), 7.81 (dd, J = 8.5, 2.5 Hz, 2H), 7.51 (d, J = 8.0 Hz, 4H), 7.26 (d, J = 7.0 Hz, 4H), 7.13 (d, J = 7.0 Hz, 2H), 4.58 (s, 4H), 2.56 (t, J = 8.0 Hz, 4H), 1.56 (p, J = 7.5 Hz, 4H), 1.31 (m, 24H), 0.89 (t, J = 7.0 Hz, 6H).^{13}C NMR (126 MHz, $CDCl_3$) δ 189.30, 159.88, 142.38, 136.59, 134.67, 134.10, 128.96, 126.75, 126.56, 125.27, 113.18, 67.21, 35.58, 31.89, 31.48, 29.55, 29.52, 29.34, 29.33, 22.67, 14.11. HRMS-DART: $[M+H]^+$ calcd for $C_{46}H_{59}O_4$: 675.441335, Found: 675.46768

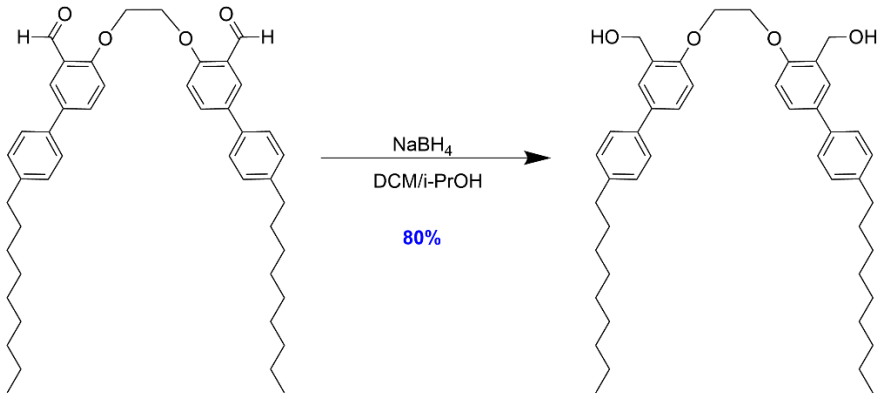

2.3 2.4

((Ethane-1,2-diylbis(oxy))bis(4'-nonyl-[1,1'-biphenyl]-4,3-diyl))dimethanol (2.4)

Compound **2.3** (0.0803 g, 0.1189 mmol) was dissolved in 12 mL of DCM/*i*-PrOH (3/1 v/v) under argon in a 50 mL RBF at 0°C. Sodium borohydride ($NaBH_4$, 0.0135 g, 0.3567 mmol) was slowly added while stirring. The mixture was then warmed to room temperature, stirred for 6 hours, and then re-cooled to 0°C. To quench the reaction, 10%

citric acid solution was added dropwise until no gas evolution was observed, followed by 20 minutes of stirring. The organic layer was collected and the aqueous was extracted with 2 x 25 mL DCM. The combined organic layer was then washed with 1 x 50 mL water, 1 x 50 mL brine, and dried over $MgSO_4$. After filtering and concentrating, the crude was purified via column chromatography with a gradient elution of hexanes to 25% EtOAc/hexanes. For larger scale reactions, solubility issues require the use of a DCM/hexanes eluent. The product was obtained as a yellow-white solid (0.06457 g, 0.09510 mmol, 80% yield). R_f = 0.30 (25% EtOAc/hexanes).

^{1}H NMR (500 MHz, $CDCl_3$) δ 7.54 (d, J = 2.5 Hz, 2H), 7.50 (dd, J = 8.5, 2.5 Hz, 2H), 7.48 (d, J = 8.0 Hz, 2H), 7.24 (d, J = 8.0 Hz, 4H), 7.00 (d, J = 8.5 Hz, 2H), 4.73 (s, 4H), 4.45 (s, 4H), 2.64 (t, J = 8.0 Hz, 4H), 1.65 (p, J = 7.5 Hz, 4h), 1.29 (m, 24H), 0.90 (t, J = 7.0 Hz, 6H).^{13}C NMR (126 MHz, $CDCl_3$) δ 155.70, 141.74, 137.82, 134.70, 130.00, 128.81, 128.19, 127.24, 126.65, 112.15, 67.04, 61.77, 35.60, 31.91, 31.53, 29.58, 29.55, 29.39, 29.35, 22.69, 14.12. HRMS-DART: $[M + H - H_2O]^+$ calcd for $C_{46}H_{61}O_3$: 661.46152, Found: 661.44322

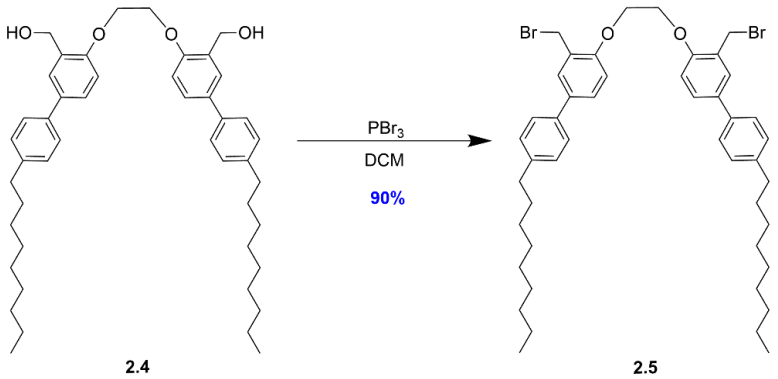

2.4 2.5

1,2-bis((3-(bromomethyl)-4'-nonyl-[1,1'-biphenyl]-4-yl)oxy)ethane (2.5)

Compound **2.4** (0.0500 g, 0.0736 mmol) was dissolved in 20 mL of dry DCM under

argon in a 100 mL RBF and cooled to 0°C. Phosphorus tribromide (PBr_3, 208 µL, 2.208 mmol) was added dropwise while stirring. The mixture was then warmed to rt and stirred for 6 hours, followed by a re-cooling to 0°C to quench any unreacted PBr_3 with dropwise additions of MeOH. After quenching, the mixture was added to a separatory funnel with 100 mL of water. The aqueous layer was extracted with 2 x 20 mL DCM, and the combined organic layer was washed with 1 x 50 mL water and 1 x 50 mL brine. The crude was then dried over $MgSO_4$, filtered, concentrated under pressure, and purified via a short silica column with a gradient elution of hexanes to 10% ethyl acetate/hexanes. The product was yielded as a yellow-white solid (0.0533 g, 0.0662 mmol, 90% yield). R_f = 0.80 (25% EtOAc/hexanes).

^{1}H NMR (500 MHz, $CDCl_3$) δ 7.57 (d, J = 2.5, 2H), 7.54 (dd, J = 8.5, 2.5 Hz, 2H), 7.48 (d, J = 8.0 Hz, 4H), 7.25 (d, J = 8.0 Hz, 4H), 7.06 (d, J = 8.5 Hz, 2H), 4.61 (s, 4H), 4.53 (s, 4H), 2.64 (t, J = 8.0 Hz, 4H), 1.64 (p, J = 7.5, 4H), 1.27 (m, 24H), 0.89 (t, J = 7.0, 6H).^{13}C NMR (126 MHz, $CDCl_3$) δ 155.83, 141.87, 137.47, 134.45, 129.61, 128.84, 128.52, 126.86, 126.59, 112.60, 67.29, 35.58, 31.90, 31.52, 29.70, 29.56, 29.36, 29.11, 22.68, 14.11. HRMS-DART: $[M - Br]^+$ calcd for $C_{46}H_{60}BrO_2$: 723.37712, Found: 723.50699

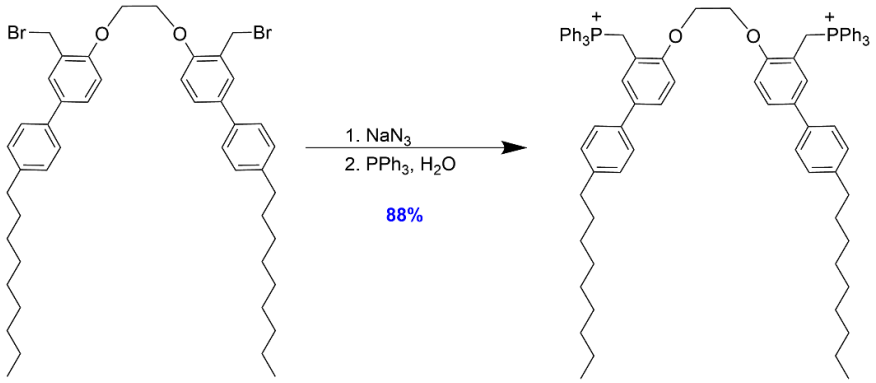

2.5 **2.6**

Methyl((4'-nonyl-4-(2-((4'-nonyl-3-((triphenylphosphonio)methyl)-[1,1'-biphenyl]-4-yl)oxy)ethoxy)-[1,1'-biphenyl]-3-yl)methyl)diphenylphosphonium (2.6)

Compound **2.5** (0.0600 g, 0.0790 mmol) was dissolved in 50 mL of a 1:4 v/v water acetone mixture. While stirring, NaN_3 (0.0077 g, 0.1185 mmol) was added, and the suspension was stirred vigorously for 24 hours. To separate the suspension, 10 mL of DCM and water were added. The aqueous layer was then extracted with 3 x 10 mL of DCM, and the combined organic layers were washed with water and then dried over $MgSO_4$. The solution was filtered and concentrated under pressure, yielding the white crude R_f= 0.72 (25% EtOAc/hexanes). This crude was then dissolved in 8 mL of THF:H_2O (3:1, v/v) under Ar. While stirring, triphenylphosphine (PPh_3, 0.1094 g, 0.4163 mmol) was added and the mixture was allowed to stir at rt for 24 hours. The mixture was concentrated under reduced pressure and purified on an alumina column with a 0 to 10% MeOH gradient in DCM, yielding a solid (0.0876 g, 0.0749 mmol, 88%). R_f = 0.22 (10% MeOH/DCM). ^{1}H NMR (500 MHz, $CDCl_3$) δ 7.60 (t, J = 8.0 Hz, 6H), 7.44-7.50 (m, 16H), 7.42-7.44 (m, 12 H), 7.33 (t, J = 2.5 Hz, 4H), 7.13 (dd, J = 12.0, 8.5 Hz, 4H), 6.86 (d, J = 8.5 Hz, 2H), 5.14 (d, J = 14.0 Hz, 4H), 3.7 (s, 4H), 2.55 (t, J = 2.5 Hz, 4H), 1.55 (p, J = 8.0 Hz, 4H), 1.21 (m, 24 H), 0.81 (t, J = 7.0 Hz, 6H). ^{13}C NMR (126 MHz, $CDCl_3$) δ 156.39, 142.16, 136.48, 134.95, 134.27, 134.00, 133.92, 130.14, 130.04, 128.91, 126.33, 118.38, 117.70, 116.69, 113.61, 68.11, 35.56, 31.90, 31.50, 29.58, 29.54, 29.34, 26.24, 25.86, 22.68, 14.11. ESI-MS: [M/2] calcd for $C_{82}H_{90}O_2P_2^{2+}$: 584.3203, Found 584.3207

Preparation of liposomes for NR release assays

Stock solutions of **2.6** were prepared at 19.93 mM in $CHCl_3$/MeOH solution (1/1, v/v),

32.46 mM PC, 33.60 mM DOPE, and 5 mM Nile red (NR) solutions were prepared in chloroform. All the stock solutions were kept in a -20 °C freezer after preparation. To prepare liposomes through thin film hydration, appropriate volumes of each stock solution were pipetted in 0.5 dr vials to reach a total lipid concentration of 2 mM, with desired percentages of each lipid type. NR was added as an extra 5% of the total lipid content. The organic solvents were then evaporated under a nitrogen stream, and the resulting lipid films were kept under vacuum for at least one hour. The films were then hydrated with proper volumes of 1x TBS buffer, (pH = 7.4) in a 60 °C water bath for 1 hr. The vials were vortexed every 15 minutes while incubating. Next, 10 freeze-thaw cycles were performed in a dry ice-acetone bath and 60 °C water bath. Lastly, the liposome solutions were extruded through a 200 nm polycarbonate membrane for 21 passes with an extruder purchased from either Avestin or Avanti. The resulting liposomes were then studied immediately.

Phosphorylated and carboxylate metabolite selectivity screen for liposome NR release

50 mM stock solutions of each metabolite were prepared by dissolving the reagents (sodium phosphate dibasic heptahydrate (Pi, $Na_2HPO_4 \cdot 7H_2O$); sodium pyrophosphate dibasic (PPi, $Na_2H_2P_2O_7$); ADP; adenosine 5’-triphosphate disodium salt, hydrate (ATP); D-fructose-6-phosphate disodium salt (FP); D-fructose-1,6-bisphosphate trisodium salt (FBP); sodium tripolyphosphate (TPi); cytidine-5'-triphosphate disodium salt (CTP); guanosine-5’- triphosphate trisodium salt (GTP); uridine 5′-triphosphate trisodium salt hydrate (UTP), AMP, malic acid (Mal), fumaric acid (Fum), oxaloacetic acid (Oxa), succinic acid (Suc)); with MilliQ water. For each study, 56 μL of liposome solution

encapsulating NR was first added into a sub-micro quartz cuvette. After an initial scan, 14 μL of 50 mM stock solution of the metabolite under study was added to the cuvette (final concentration = 10 mM). Samples were incubated for 16 hours at rt and fluorescence intensities were recorded after incubation (excitation wavelength = 552 nm, excitation slit = 5 nm, emission slit = 5 nm). Control experiments were run by adding 14 μL of 1x TBS. When processing the data, the fluorescence intensities at 635 nm were selected and converted to percentage of the initial fluorescence before metabolite addition. Experiments were run at least three times with different batches of liposomes. Averaged data were reported with error bars denoting standard error.

Nucleotide triphosphate and TPi metabolite selectivity screen for liposome NR release

300 mM stock solutions of each metabolite were prepared by dissolving the same reagents previously described (ATP, GTP, CTP, UTP, TPi) in MilliQ water. For each study, 68 μL of liposome solution encapsulating NR was first added into a sub-micro quartz cuvette. After an initial scan, 2.33 μL of the 300 mM stock solution of the metabolite under study was added to the cuvette (final concentration = 10 mM). Samples were incubated for 16 hours at rt and fluorescence intensities were recorded after incubation (excitation wavelength = 552 nm, excitation slit = 5 nm, emission slit = 5 nm). Control experiments were run by adding 2.33 μL of 1x TBS buffer. When processing the data, the fluorescence intensities at 635 nm were selected and converted to percentage of initial fluorescence before metabolite addition. Experiments were run at least three times with different batches of liposomes. Averaged data were reported with error bars denoting standard error.

NR kinetic release assays

The same 300 mM stock solutions of TPi and GTP were prepared as previously mentioned. For each study, 68 μL of liposome solution encapsulating NR was first added into a sub-micro quartz cuvette. After an initial scan, 2.33 μL of the 300 mM stock solution of the metabolite under study was added to the cuvette (final concentration = 10 mM). Samples were then capped, sealed, and measured continuously for 16 hours with measurements every 15 or 30 minutes. Control experiments were run by adding 2.33 μL of 1x TBS buffer, or by treating 0% **2.6** liposomes with 2.33 μL of the stock solutions. When processing the data, the fluorescence intensities at 635 nm were selected and converted to percentage of initial fluorescence before metabolite addition. Experiments were run at least three times with different batches of liposomes. Averaged data were reported with error bars denoting standard error.

Preparation of liposomes for sulforhodamine B release assays

The same stock solutions of **2.6**, PC, and DOPE prepared for the NR release assay were used. An additional stock of PA was prepared at 5 mM in $CHCl_3$/MeOH solution (1/1, v/v). 30 mM sulforhodamine B (SRB) stock solutions were prepared by dissolving SRB with 25 mM Tris-HCl buffer (298 mOsm/L) and the pH was then adjusted to 7.4 by adding 1 N NaOH droplets. The osmolality of the solution was determined to be 291 mOsm/L. To prepare liposomes through thin film hydration, appropriate volumes of each stock solution were pipetted in 0.5 dr vials to reach a total lipid concentration of 5 mM, with desired percentages of each lipid type. The organic solvents were then evaporated under a nitrogen stream, and the resulting lipid films were kept under vacuum for at least one hour. The films were then hydrated with proper volumes of 30 mM SRB in a 60 °C water bath for 1

hr. The vials were vortexed every 15 minutes while incubating. Next, 10 freeze-thaw cycles were performed by cycling in a dry ice-acetone bath and 60 °C water bath. The liposome solutions were then extruded through a 200 nm polycarbonate membrane for 21 passes with an extruder purchased from either Avestin or Avanti. Lastly, the unencapsulated SRB dye was removed by size-exclusion chromatography. A micro-column (5 ¾" glass pipette) was packed with Sephadex G-50 (pre-saturated with isotonic 25 mM Tri-HCl buffer). The fractions were collected in 3 key color change transition (clear, pink, and magenta, Figure S1). Pink fractions with some turbidity were collected and used in the following release assays. Confirmation of liposome formation was assessed by treating liposomes with Triton X-100 detergent while measuring fluorescence before and after treatment, where an increase in fluorescence intensity confirmed liposome presence.

Sulforhodamine B kinetic release assays

A 68 μL aliquot of liposomes encapsulating SRB prepared as previously described was added into a sub-micro quartz cuvette. After an initial scan, 2.33 μL of the 300 mM stock solution of the metabolite under study was added to the cuvette (final concentration = 10 mM). Samples were capped and sealed and then measured continuously for 16 hours with measurements every 15 or 30 minutes (excitation wavelength = 550 nm, excitation slit = 2.5 nm, emission slit = 2.5 nm). Control experiments were run by adding 2.33 μL of 25 mM Tris-HCl buffer, or by treating 0% **2.6** liposomes with 2.33 μL of the stock solutions. To calibrate the assay, samples were treated with 2 μL of 20% Triton X-100 detergent to lyse liposomes and induce 100% dye release. When processing the data, the fluorescence intensities at 603 nm were selected and converted to percentage of the fluorescence after

Triton X-100 treatment. Experiments were run at least three times with different batches of liposomes. Averaged data were reported with error bars denoting standard error.

DLS analysis of liposomes before and after triggered release

DLS measurements were performed with a Malvern Zetasizer Nano ZS instrument with a 4.0 mW laser at I = 633 nm. Samples were prepared by diluting liposomes by 10x (5 μL liposomes, 45 μL buffer). All measurements were taken at a scattering angle of 173° at 20 °C. Bar graphs were made by averaging at least three experiments, with error bars denoting standard error.

Transmission electron microscope analysis

Liposomes were prepared at 4 μg/mL without any dye encapsulation using the standard thin film hydration procedure described above. For TEM studies, droplets of the liposome solution were placed on parafilm (10 μL). For treated liposomes, appropriate volumes of 300 mM GTP or TPi stocks were added to the liposome solutions before droplets were placed on the parafilm. Thin carbon films supported by 200 mesh copper grids were placed face down onto the droplets and allowed to soak for 1 minute. The grids were then removed from the droplet and blotted. Droplets of dH_2O were then placed on the parafilm, where the grids were briefly placed (10 seconds) to rinse before removal and blotting. Droplets of 1% uranyl acetate were next placed on the parafilm sheet, followed by another 1-minute soak of the grids and blotting. Grids were allowed to air dry for 2 hours. Images were taken using a JOEL 1400 Flash microscope with a beam energy of 80 keV. Images were taken with a Gaten One View camera and processed with ImageJ software.

Fluorescence titration 2.6-GTP and 2.6-TPi binding experiment

2.6 stock prepared in MeOH/$CHCl_3$ at 19.93 mM and 300 mM GTP and TPi stocks prepared in MilliQ water used for previous studies were utilized for these experiments. 7.53 uL of **2.6** stock was diluted to 50 μM to 3 mL in DMSO. An additional reference solution was prepared with 7.53 uL of MeOH/$CHCl_3$ diluted to 3 mL in DMSO. Each solution was added to a quartz cuvette and 1 uL of either GTP or TPi stocks were added with spectra recorded after each addition. When processing the data, intensities at 335 nm were selected. The decreases in fluorescence were plotted against the concentrations of GTP or TPi. Binding of GTP to **2.6** was quantified by fitting to a single-site Langmuir isotherm, $\theta = [L] / (K_d + [L])$, where [L] is the free GTP concentration and K_d is the equilibrium dissociation constant. Nonlinear least-squares fitting of the titration data yielded $K_d = 0.150$ mM (±0.010 mM). Fluorescence titration for the **2.6**-TPi interaction was also fitted to a single-site Langmuir binding isotherm, $\theta = \theta_0 + \Delta\theta([L] / (K_d + [L])$, using nonlinear least-squares regression. Both unweighted and weighted fits (weighted by the standard error of each measurement) were performed. The unweighted fit, assuming uniform variance across data points, yielded $K_d = 0.417$ (±0.026 mM). The weighted fit, accounting for heteroscedasticity in the fluorescence data, provided a more statically robust estimate of $K_d = 1.225$ (±0.081 mM).

Kinetic Fluorescence Release Curve Fitting

Fluorescence kinetic release profiles in Figure 4 were analyzed using nonlinear regression in OriginPro 2025b. Data were expressed as % of initial fluorescence (P_0=100) over time and fit to kinetic models describing either biphasic or burst-type release. Initial evaluation using a bi-exponential model:

$$P(t) = P_\infty + (P_0 - P_\infty)\,[\phi e^{-k_1 t} + (1-\phi)e^{-k_2 t}]$$

revealed large uncertainties in the fast rate constant (k_1) due to the limited temporal resolution at early time points. As the fast release process occurred within the sampling interval, a simplified burst-plus-first-order model was adopted.

$$P(t) = P_\infty + (P_0 - P_\infty)(1-\beta)e^{-k_2 t}$$

where β represents the fraction of fluorescence quenched within the first measurement ("burst" release) and k_2 describes the subsequent slower first-order decay. Parameters P_0 and P_∞ were fixed to 100 and 0, respectively. The burst model provided statistically comparable fits to the biexponential with fewer free parameters and random residuals. Fluorescence kinetic release profiles in Figure 7 were also analyzed using nonlinear regression in OriginPro 2025b and were fit to a single-exponential association model:

$$P(t) = F_\infty(1 - e^{-k\,t})$$

where F_∞ is the plateau fraction of released dye and $k$is the first-order rate constant.

Nile red encapsulation efficiency

Fluorescence scans were used to assess cargo encapsulation, where first a Nile red calibration curve in chloroform was generated. Liposomes used in NR release assays (35/35/30 and 50/20/30 **2.6**/DOPE/PC) were prepared as previously described. After liposome formation, an aliquot of 300 µL of liposomes was added to a 4 dr vial and water was removed under reduced pressure. The film was then re-dissolved with 3 mL chloroform, followed by sonication and filtration through a 0.2 µm PTFE filter. The solution was then transferred to a quartz cuvette for fluorescent measurements and the fluorescent intensities at 600 nm were used to calculate the NR encapsulation efficiency.

Sulforhodamine B encapsulation efficiency

Fluorescence scans were used to assess cargo encapsulation, where first a sulforhodamine B calibration curve in MilliQ + 2% Triton X-100 was generated. Liposomes used in SRB release assays (37.5/32.5/2/28 and 37.5/36.5/2/24 **2.6**/DOPE/PA/PC) were prepared as previously described. After liposome formation, samples were treated with Triton X-100 for a final concentration of 2%. All samples and stocks were diluted 10x to mitigate signal self-quenching. The solutions were then transferred to a quartz cuvette for fluorescent measurements and the fluorescent intensities at 585 nm were used to calculate the SRB encapsulation efficiency.

Preparation of liposomes for Dox release assays

The same stock solutions of **2.6**, PC, and DOPE prepared for the NR/SRB release assays were used. Fresh 10 mg/mL solutions of Dox were prepared in MilliQ water for each study and protected from light. Citrate buffer (150 mM, pH 4.0) and HEPES buffer (20 mM, pH 7.4) were prepared and their osmolarities corrected to 303 and 297 mOsm/L respectively. To prepare liposomes through thin film hydration, appropriate volumes of each stock solution were pipetted in 0.5 dr vials to reach a total lipid concentration of 5 mM, with desired percentages of each lipid type. The organic solvents were then evaporated under a nitrogen stream, and the resulting lipid films were kept under vacuum for at least one hour. The films were then hydrated with proper volumes of 150 mM citrate buffer in a 60 °C water bath for 1 hr. The vials were vortexed every 15 minutes while incubating. Next, 10 freeze-thaw cycles were performed by cycling in a dry ice-acetone bath and 60 °C water bath. The liposome solutions were then extruded through a 200 nm

polycarbonate membrane for 21 passes with an extruder purchased from either Avestin or Avanti. Extruded liposome solutions were then loaded into Slide-A-Lyzer Mini cassettes (10 kDa, 0.1-0.5 mL) and dialyzed against 100 mL 20 mM HEPES buffer at 4°C while stirring. Buffer was changed every 30 minutes until 3 exchanges were completed. Liposomes were then added to a 1 dr vial with Dox added to a final concentration of 1 mM. Liposomes and Dox were incubated in a 60 °C water bath for 20 minutes with gentle mixing every 5 minutes. Solutions were then cooled on ice for 5 minutes before loading into an additional Slide-A-Lyzer Mini cassette (10 kDa, 0.1-0.5 mL) and exchanged against 100 mL 20 mM HEPES buffer at 4°C while stirring again. Buffer was changed every 30 minutes until 3 exchanges were completed. Liposomes were then recovered from cassettes and used for release studies. Confirmation of liposome formation was assessed by treating liposomes with Triton X-100 detergent while measuring fluorescence before and after treatment, where an increase in fluorescence intensity confirmed liposome presence.

Dox encapsulation efficiency

Fluorescence scans were used to assess cargo encapsulation, where first a Dox calibration curve in MilliQ + 2% Triton X-100 was generated. Liposomes used in Dox release assays (35/35/30 and 50/20/30 **2.6**/DOPE/PC) were prepared as previously described. After liposome formation, samples were treated with Triton X-100 for a final concentration of 2%. The solutions were then transferred to a quartz cuvette for fluorescent measurements and the fluorescent intensities at 592 nm were used to calculate the Dox encapsulation efficiency.

Dox fluorescence release assays

Liposomes were prepared as previously described for Dox release assays. Initial liposome samples were lysed with 2% Triton X-100 and initial maximum fluorescence values were recorded. Fresh liposome samples were then left untreated or treated with 300 mM stock solution of TPi or GTP, or an equivalent volume of 20 mM HEPES buffer. Sample fluorescence was re-measured after 16 hours, followed by lysing with 2% Triton X-100 and final fluorescence values were recorded. When processing the data, the fluorescence intensities at 592 nm were selected and converted to percentage of Dox released after metabolite/buffer addition.

NR kinetic release assays in media

Liposomes were prepared as previously described for NR kinetic release assays, with concentration increased to 5 mM. Phenol red-free Dulbecco's modified eagle medium (DMEM) was supplemented with 10% (v/v) fetal bovine serum (FBS, Gibco) and 50 U mL^{-1} penicillin/streptomycin (pen/strep)Gibco). To each microplate well, 100 uL of DMEM and 40 uL of prepared liposome solution was added for a final liposome concentration of 1.42 mM per well. After an initial fluorescence scan, 4.66 μL of TPi, GTP or PBS (+Mg, +Ca) was added to the appropriate wells, and measurements were taken at sequential time points. When processing the data, the fluorescence intensities at 635 nm were selected and converted to percentage of initial fluorescence before metabolite/buffer addition.

NR release assays with mixed metabolite treatment

Liposomes were prepared as previously described for NR release assays at 2 mM concentration. Mixed metabolite solutions were made in MilliQ water with sodium

phosphate (Pi), sodium pyrophosphate (PPi), ADP, ATP, D-fructose-6-phosphate (FP), D-fructose-1,6-bisphosphate (FBP), TPi, cytidine-5'-triphosphate (CTP), GTP, uridine 5'-triphosphate (UTP), AMP, malic acid (Mal), fumaric acid (Fum), and oxaloacetic acid (Oxa) for a total final concentration of 300 mM of all metabolites (25 mM for each metabolite). Alternate mixed metabolite solutions were made with the same metabolites at half the concentration (12.5 mM each metabolite, 150 mM total), with 150 mM TPi or GTP added. Prepared liposomes were treated with buffer, the 300 mM mixed metabolite solution, the TPi containing mixed metabolite solution or the GTP containing mixed metabolite solution for a final concentration of either 12 mM mixed metabolites, 6 mM mixed metabolites and 6 mM TPi, or 6 mM mixed metabolites and 6 mM GTP. When processing the data, the fluorescence intensities at 635 nm were selected and converted to percentage of initial fluorescence before metabolite/buffer addition.

NR release assays with phosphate-buffered saline hydrated liposomes

Liposomes were prepared as previously described for NR release assays at 2 mM concentration, but were hydrated with 1x PBS (pH 7.4). Initial fluorescence was measured, then liposomes were left untreated, or treated with NaCl or an equivalent volume of PBS(+)(+) for a final concentration of 10 mM. After 48 hours, sample fluorescence was re-measured. When processing the data, the fluorescence intensities at 635 nm were selected and converted to percentage of initial fluorescence before salt/buffer addition.

CHAPTER 3.

REACTIVE OXYGEN SPECIES-RESPONSIVE LIPID-PRODRUG LIPOSOMES FOR DOXORUBICIN DELIVERY

A version of this chapter is in progress for publication submission by Brooke E. Smith, et al.: Smith, Brooke E.; Lou, Jinchao.; Phillips, Miranda A.; Sagar, Ruhani; Qualls, Megan; McBee, Dillon P.; Turner, Robert F.; Baccile, Joshua A.; Best, Michael D.

3.1 Project Overview

Many clinically used chemotherapeutics, including Dox, suffer from dose-limiting toxicities, poor biodistribution, and limited control over intracellular activation. To mitigate these challenges, two primary delivery strategies have been widely explored: prodrug design and liposomal encapsulation. Prodrugs can improve solubility, pharmacokinetics, and site-selective activation, while liposomes enhance circulation time and reduce off-target exposure. However, each approach presents limitations when employed independently. Prodrugs may introduce stability or solubility concerns and can undergo premature activation, whereas liposomal formulations often rely on passive release mechanisms and may exhibit incomplete or non-specific cargo leakage. In the current work, we sought to develop a synergistic delivery approach that integrates a chemically responsive prodrug directly within the liposomal membrane. We report a reactive oxygen species-responsive Dox lipid prodrug conjugate ROSDoxL, which is integrated within the liposomal bilayer, enabling membrane-embedded therapeutic loading rather than aqueous core encapsulation. The prodrug design features a boronate caging group that undergoes oxidation in the presence of elevated ROS, triggering a self-immolative release of Dox. A non-responsive control Dox lipid DoxL, lacking the boronate moiety, was used to evaluate the specific ROS-mediated uncaging mechanism. ESI-MS studies confirmed this ROS-dependent cleavage of the ROSDoxL, while liposomal

characterization and cellular studies demonstrated functional delivery and concentration-dependent cytotoxicity in A375 melanoma cells comparable to free Dox. Our membrane-integrated liposomal prodrug approach provides a modular strategy for coupling disease-associated biochemical signals to controlled drug activation, advancing liposomal systems beyond passive carriers towards stimulus-responsive therapeutic delivery.

3.2 Introduction and Motivation

3.2.1 Biological Relevance of ROS

Reactive oxygen species (ROS) have emerged as attractive endogenous triggers for stimulus-responsive drug delivery due to their dysregulated production in numerous pathological states.[147–150] ROS encompass a range of chemically reactive oxygen-derived species, such as superoxide ($O_2^{\bullet-}$), hydroxyl radical (•OH), hydrogen peroxide (H_2O_2), and singlet oxygen ($^1O_2$). At controlled, low concentrations, these species serve essential physiological roles in cell signaling, oxygen sensing, vascular regulation, and immune defense.[151] However, disruption of redox homeostasis leads to oxidative stress, characterized by excessive ROS accumulation that damages lipids, proteins, and nucleic acids.

The majority of intracellular ROS are generated as byproducts of mitochondrial electron transport chain (ETC) activity. Dysregulation of mitochondrial respiration increases superoxide production and leakage, while heightened protein folding demands within the endoplasmic reticulum (ER) contribute to elevated H_2O_2 generation.[152] In cancer and other proliferative or inflammatory diseases, metabolite reprogramming, mitochondrial dysfunction, and hypoxic stress frequently result in ROS overproduction.

Elevated ROS levels have been implicated in tumor progression, hypertension, diabetes, and neurodegenerative disorders such as Alzheimer's and Parkinson's disease.[153]

Among endogenous ROS, H_2O_2 is particularly relevant for prodrug activation strategies. Compared to superoxide and hydroxyl radicals, H_2O_2 exhibits greater membrane permeability, lower intrinsic reactivity, and longer intracellular half-life, enabling it to function as a diffusible redox signaling molecule.[154–156] Because boronate-based caging groups are selectively oxidized by H_2O_2, this species represents a practical and biologically meaningful trigger for controlled drug release. Importantly, ROS concentrations differ substantially between healthy and diseased tissues, with reported basal levels in healthy cells on the order of ~20 nM compared to concentrations approaching ~100 μM in certain diseased environments.[157] This disparity provides a potential biochemical window for selective activation of ROS-responsive therapeutics. However, ROS abundance is not uniform across all cancer types or disease states. For example, highly metabolic tumor cells and regions of hypoxia or necrosis often exhibit elevated ROS, whereas cancer stem cells may maintain comparatively lower ROS levels to preserve genomic integrity.[158,159] In inflammatory settings, immune cell activation can generate transient ROS bursts, while neighboring healthy tissue remains less oxidative.[160] Furthermore, ROS levels fluctuate dynamically depending on cell cycle stage, therapeutic stress, and antioxidant feedback mechanisms.[161–164] These complexities underscore both the promise and the challenge of ROS-responsive delivery systems. While redox dysregulation provides a compelling endogenous trigger, effective design must account for variability in ROS abundance across disease states and cellular subpopulations. Consequently, ROS-responsive platforms

should aim for sensitivity within physiologically relevant oxidative windows while maintaining stability under normal redox conditions.

3.2.2 ROS-Responsive Prodrug Strategies

A variety of ROS-responsive cargo delivery systems have been previously developed, utilizing specific ROS-responsive chemical bonds for the desired effect. These include sulfur-based thioethers, thioketal attachments, selenium/tellurium-based, and boronic ester/boronic acid derivatives.[165] Of particular interest for a ROS-prodrug approach are cleavable, ROS-responsive linkers utilizing these bonds, including thioketal, diselenide, peroxalate ester, vinyldithioether, and phenylboronic acid variants.[166] Numerous ROS-responsive anticancer prodrugs have been reported that validate the translational potential of ROS-triggered activation. Thioketal linkers incorporated into paclitaxel conjugates enabled oxidative cleave within tumor microenvironments,[167] while selenium-containing systems underwent oxidation-triggered elimination reactions to release active agents under elevated ROS conditions.[168] Nitrogen mustard derivatives masked with arylboronate triggers demonstrated selective DNA crosslinking in ROS-rich cancer environments. The cytotoxicity of the nitrogen mustard was initially masked with an electron withdrawing linker unit (quaternary ammonia, carboxyamide, or carbonate) attached to an arylboronate mask. Exposure of the arylboronate to a ROS-rich environment though triggers its removal, converting the electron withdrawing linker into an electron donating group and revealing nitrogen mustard cytotoxicity.[169] Histone deacetylase inhibitors have also been successfully converted into ROS-activated prodrugs by masking the hydroxamic acid pharmacophores with phenylboronate-containing self-immolative linkers. For example,

ROS-responsive suberoylanilide hydroxamic acid[170] and belinostat[171] derivatives demonstrated reduced off-target toxicity and improved *in vivo* tumor suppression compared to the parent compounds. These studies emphasize the utility of boronate triggers in modulating both potency and selectivity.

The Lewis acidity of boron makes it particularly susceptible to nucleophilic attack by H_2O_2, and when coupled to a linker and a parent drug to construct a prodrug structure, an electronic cascade can be utilized to cleave the linker and release the parent drug upon H_2O_2 exposure (Figure 3.1).[147,172] Among the various linker strategies employed for arylboronate containing ROS-responsive prodrugs, carbonate ester[173] or carbamate[147] self-immolative linkers have proven to be the fastest and most efficient as the hydrolysis is accompanied and accelerated by the thermodynamics of CO_2 release. While many alternate ROS-responsive systems exist utilizing these cleavable bonds, ROS-activated Dox prodrugs utilizing boronate esters and boronic acid moieties are of particular interest.[174,175] These arylboronate-caged Dox derivatives have been reported in which the amino group of Dox was masked through a self-immolative linker, enabling H_2O_2 triggered release of the active therapeutic. These prodrug assemblies demonstrated comparable *in vitro* cytotoxicity to free Dox in ROS-elevated cancer cells while offering reduced systemic toxicity in preliminary models.

This previous work establishes arylboronate triggers as one of the most well-characterized and clinically promising ROS-responsive motifs. However, these systems were primarily investigated as small-molecule prodrugs and often rely on nanoparticle carriers or polymeric assemblies for cellular delivery. Integration of a ROS-responsive

prodrug directly into a liposomal bilayer represents a comparatively underexplored strategy, offering the potential to combine membrane stability with intracellular redox-triggered activation.

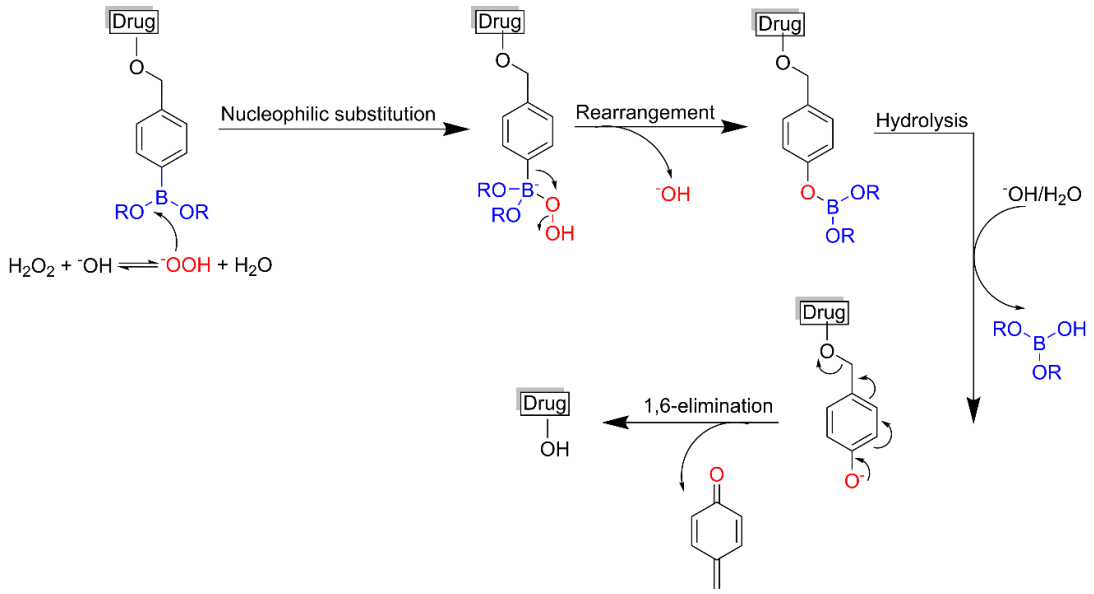

Figure 3.1. Drug release mechanism for arylboronate containing ROS-responsive prodrugs. Oxidation with hydrogen peroxide and subsequent rearrangement leads to hydrolysis of the phenylboronate, initiating an electron cascade to break the cleavable drug linker, generating a quinone-methide by-product and releasing the target drug.[147]

3.2.3 ROS-Responsive Lipids and Liposomal Delivery Systems

ROS-responsive liposomal systems have emerged as promising platforms for redox-triggered drug delivery, leveraging oxidative stress associated with cancer and inflammatory disease. Unlike small-molecule prodrugs alone, liposomes provide a membrane architecture capable of amplifying localized oxidative events into broader bilayer destabilization, permeability changes, or nanoparticle disassembly. Arylboronate-containing lipids, especially boronic acids and boronate esters, represent one of the most

widely utilized ROS-sensitive motifs due to their rapid oxidation by hydrogen peroxide. Upon conversion to phenols, boronate groups can initiate self-immolative cleavage when coupled to carbonate or carbamate linkers, setting up the potential for self-immolating lipids for membrane destabilization.[147,173]

Several such boronate-functionalized lipids have been designed to induce membrane destabilization following oxidation. In one common approach, boronate groups are appended to modified phospholipids to suppress their intrinsic non-bilayer-forming behavior, such as DOPE.[98] Upon oxidation, cleavage of the boronate moiety regenerates DOPE or related conical lipids, increasing negative curvature stress and promoting bilayer disruption. This strategy translates a localized oxidative event into collective membrane perturbation, enabling release of encapsulated hydrophobic or hydrophilic cargo. Beyond headgroup-triggered destabilization, boronate chemistry has also been used to construct ROS-cleavable lipid–drug conjugates within nanoparticle systems. In these cases, oxidation of the boronate moiety releases the active therapeutic via a self-immolative cascade, while the lipid scaffold contributes to nanoparticle stability and delivery. Examples of these boronate-caged, ROS responsive prodrugs include the attachment of epigallocatechin gallate,[176] 5-fluorouracil,[177] ciprofloxacin, bortezomib, or miconazole[178] to various lipid scaffolds via boronic acid linkage. Such systems demonstrate that boronate oxidation can function either as a membrane destabilization mechanism or as a direct prodrug activation trigger. Continued incorporation of clinically relevant therapeutics into boronate-responsive lipid scaffolds will further advance this emerging strategy and may offer significant improvements over free prodrug administration.

3.3 Design of ROS-Responsive Dox Lipid Prodrug and Control

To expand upon prior work in Dox prodrug development,[179–181] we sought to integrate prodrug activation and liposomal delivery within a single molecular architecture by covalently linking Dox to a lipid scaffold via an arylboronate-based self-immolative linker (SIL). Incorporation of the prodrug directly into the liposomal bilayer enables membrane-integrated delivery while minimizing premature leakage associated with non-covalent encapsulation.[77] The design centers on a diglyceride lipid scaffold conjugated to Dox through a boronate-containing linker positioned between the lipid and drug. Upon exposure to elevated H_2O_2 levels characteristic of diseased cells, oxidation of the boronate group generates a phenolic intermediate that initiates a self-immolative cascade, ultimately releasing free Dox from **3.5** (Scheme 3.1). This mechanism couples intracellular ROS recognition to controlled drug liberation, providing a strategy to enhance spatial selectivity while preserving the pharmacokinetic advantages of liposomal delivery.

To evaluate whether ROSDoxL **3.5** (Scheme 3.2) responds to ROS specifically via the boronate cage, a non-responsive control compound **3.9** was also synthesized, lacking the boronate functionality for comparison experiments (Scheme 3.3). In both compounds, a triazole linkage between the lipid scaffold and ROS-responsive Dox was introduced to facilitate a modular synthesis through the copper-catalyzed azide-alkyne cycloaddition (CuAAC) reaction while maintaining favorable membrane compatibility.[182]

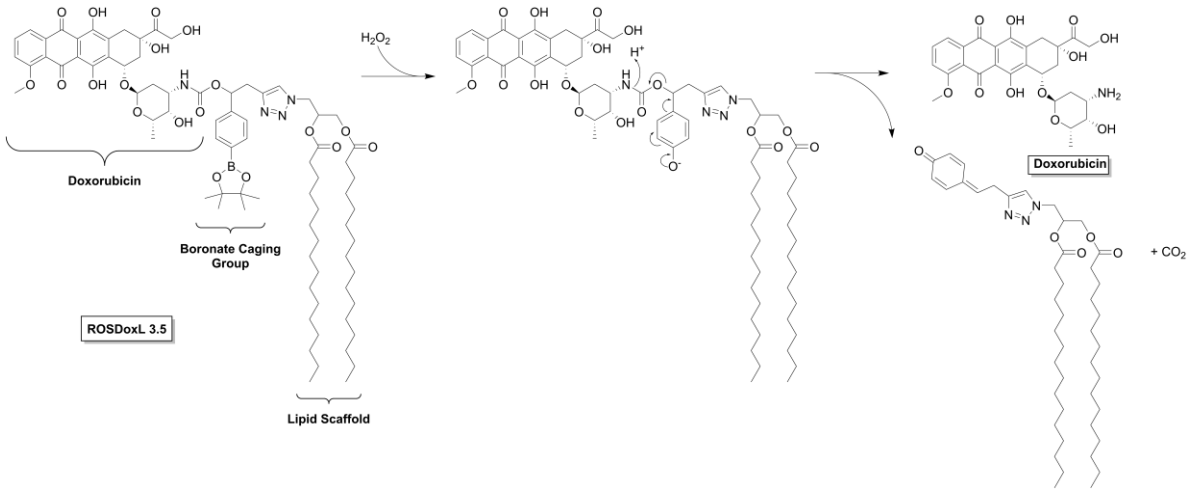

Scheme 3.1. ROS-triggered cleavage of ROSDoxL 3.5 for release of Dox. Oxidation of the boronate caging group of ROSDoxL by H_2O_2 reveals a phenolic hydroxyl, initiating the self-immolation of the lipid scaffold linker to release Dox along with CO_2 and a quinone-methide lipid byproduct.

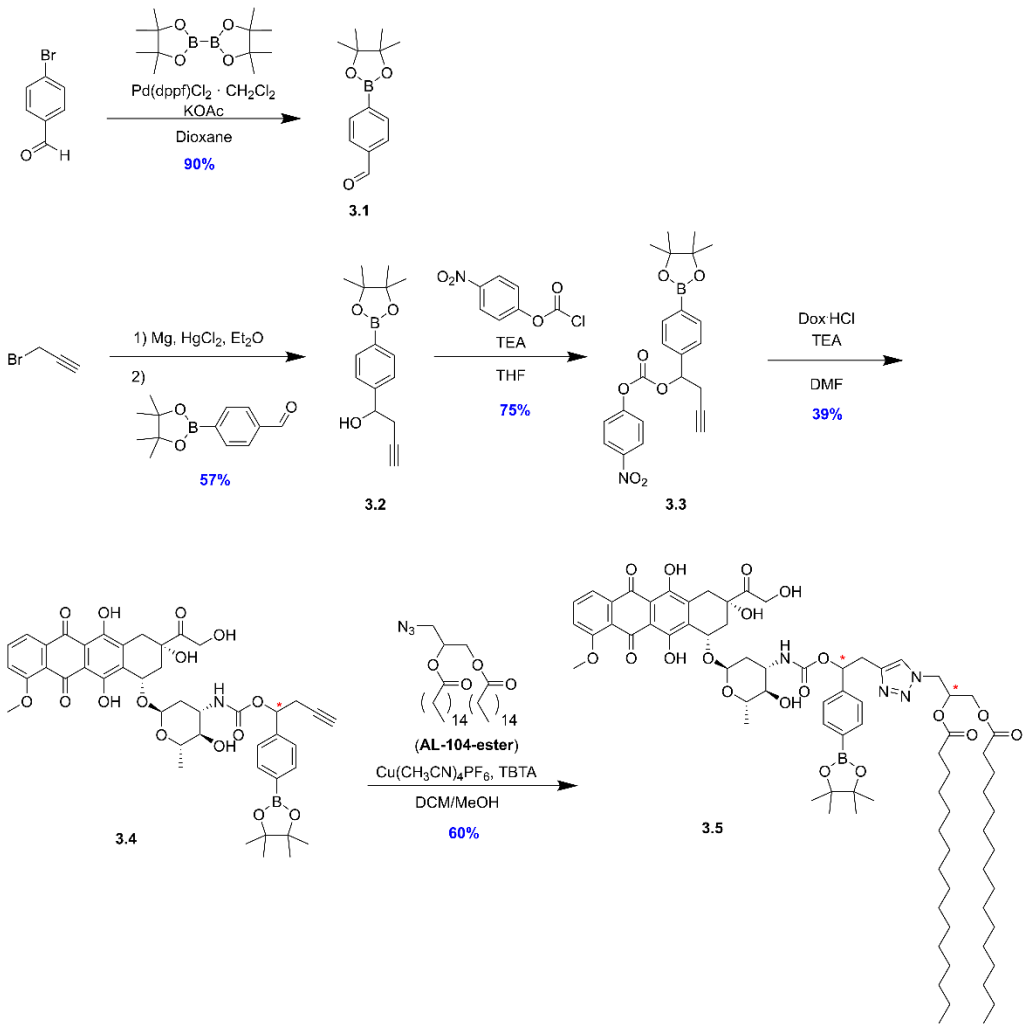

Scheme 3.2. Synthetic route for ROSDoxL 3.5. Synthetic route to ROSDoxL **3.5** first converted *p*-bromobenzaldehyde into boronate **3.2**, followed by a Grignard reaction for **3.2**. Carbonate ester linkage was achieved through nucleophilic acyl substitution with 4-nitrophenyl chloroformate for **3.3** formation, followed by carbamate linkage to attach Dox for **3.4** and ending with CuAAC clicking to attach the AL-104-ester tails for ROSDoxL **3.5.**

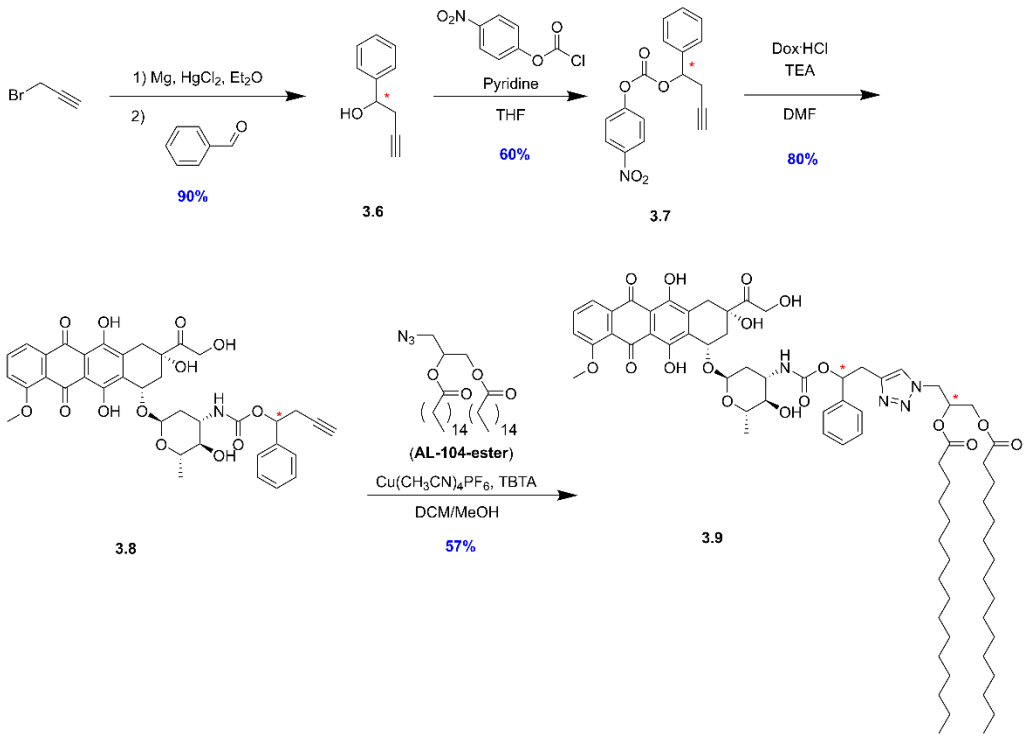

Scheme 3.3. Synthetic route for DoxL 3.9. Synthetic route to DoxL **3.9** first utilized a Grignard reaction for **3.6**. Carbonate ester linkage was achieved through nucleophilic acyl substitution with 4-nitrophenyl chloroformate for **3.7** formation, followed by carbamate linkage to attach Dox for **3.8** and ending with CuAAC clicking to attach the AL-104-ester tails for DoxL **3.9.**

For the former, *p*-bromobenzaldehyde was first converted to boronate **3.1**, followed by generation of **3.2** through a Grignard reaction and formation of the *p*-nitrophenyl carbonate group of **3.3**. Dox was then attached through a carbamate linkage to yield **3.4**, after which CuAAC was used to attach Dox to the azido- diglyceride AL-104-ester to generate ROSDoxL **3.5**. DoxL **3.9** was synthesized in a similar fashion, with the exclusion of the boronate group in the initial Grignard reaction to prevent ROS-triggered self-immolation in the subsequent studies. All synthesis in this section was performed by Dr. Jinchao Lou.

3.4 Electrospray Ionization Mass Spectrometry Experiments

To confirm ROS-triggered boronate oxidation and release of free Dox, ESI-MS experiments were performed on ROSDoxL **3.5** and the non-responsive negative control DoxL **3.9**. These studies were designed to demonstrate that the boronate cage is a necessary design element to facilitate the cleavage of the linker and release of Dox. Without boronate cage inclusion, a lack of the responsive moiety will block release of Dox. Figure 3.2 shows the full spectra of both compounds (Figure 3.2A,C) where the parent ion peaks were observed for **3.5** and **3.9** at m/z 1435.8320 and 1309.7466 respectively. Upon treatment of the 50 μM lipid samples with 20 mM H_2O_2 (diluted in dH_2O), a new peak corresponding to Dox was found at m/z 544.1810 in Figure 3.2B, confirming Dox release from ROSDoxL **3.5**. This signal was absent in spectra obtained from DoxL **3.9** (Figure 3.2D), indicating that oxidative cleavage did not occur in the absence of the boronate cage. These results confirm that the boronate moiety is essential for ROS-responsive linker self-immolation and demonstrate that these oxidative conditions selectivity liberate Dox from the lipid-prodrug scaffold.

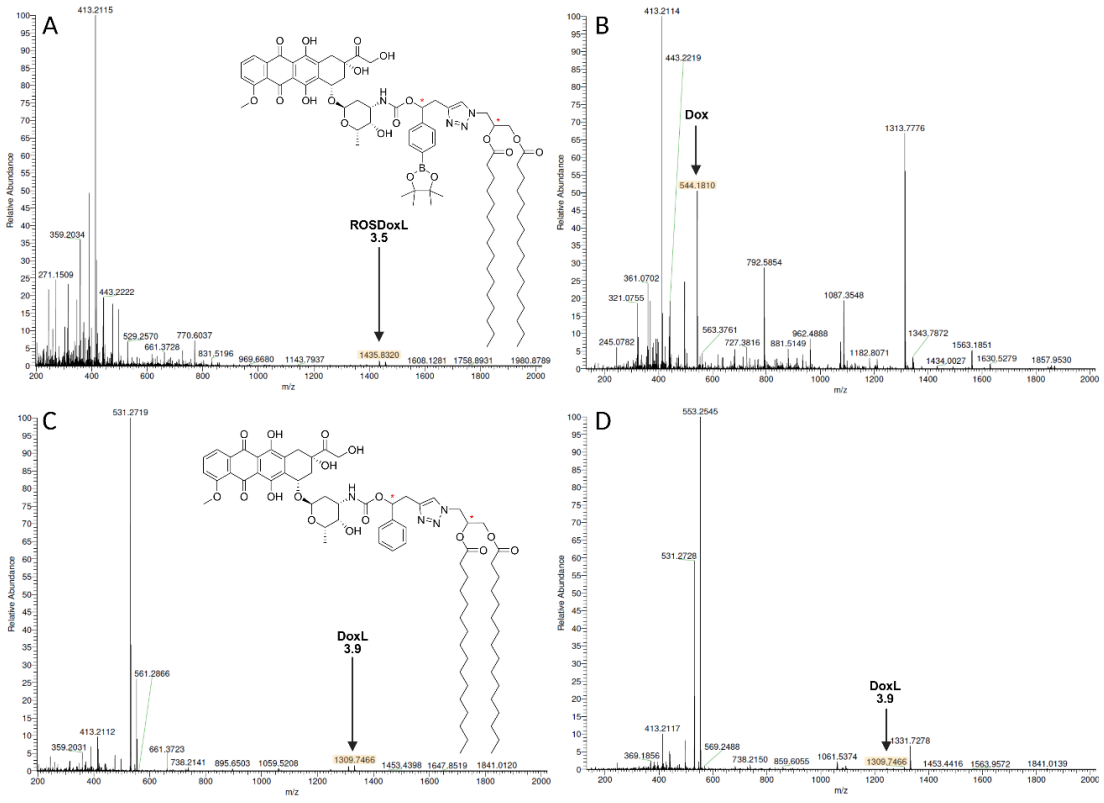

Figure 3.2. ESI-MS study highlighting Dox release from 3.5 while 3.9 remains uncleaved. ESI-MS spectra illustration with initial ROSDoxL **3.5** and DoxL **3.9** full spectra (A, C) and spectra after 20 mM H_2O_2 treatment (B, D) showing the release of Dox from ROSDoxL **3.5**. Quinone methide byproduct (+ 3 H_2O) was also observed at 792.5854.

3.5 Size and Morphology Change Studies

3.5.1 Dynamic Light Scattering Studies

With oxidative cleavage and release of Dox confirmed, we next constructed liposomes containing these compounds and completed DLS studies to evaluate whether the oxidative cleavage of **3.5** resulted in measurable changes in liposome structure (Figure 3.3). Liposomes composed of 20% lipid-prodrug (**3.5** or **3.9**) doped into 80% PC formed uniform vesicles with diameters near 145 nm under untreated conditions, consistent with

stable nanoscale assemblies. Buffer treatment alone (+PBS) did not significantly alter particle size for either formulation, confirming stability in non-oxidative environments. Upon exposure to H_2O_2 (2:1 molar ratio H_2O_2:lipid), **3.9** liposomes exhibited no meaningful size change, where in contrast, **3.5** liposomes displayed a small but meaningful increase in hydrodynamic diameter. Although the size increase is modest, the selective expansion only observed in **3.5**-containing liposomes is consistent with the oxidation of the boronate cage and local membrane perturbation following Dox release. Importantly, the absence of large-scale aggregation suggests that ROS activation promotes structural reorganization sufficient for Dox release while preserving overall nanoparticle integrity, further supported by consistent PDI values below 0.20 for all samples (Figure 3.4).

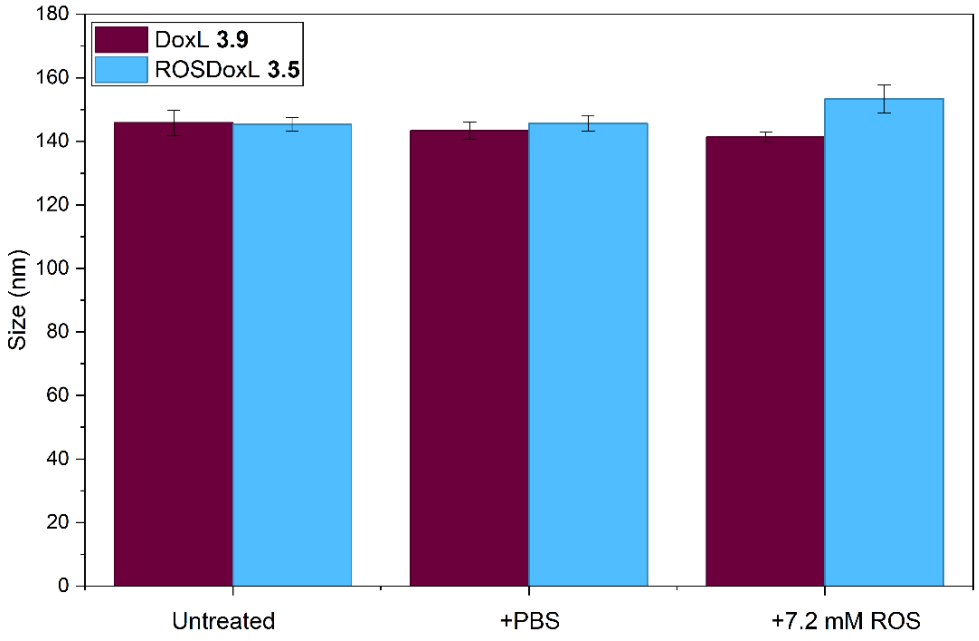

Figure 3.3. DLS of untreated and ROS-treated ROSDoxL 3.5 and DoxL 3.9 liposomes. DLS size data of 20% ROSDoxL **3.5** or DoxL **3.9**, 80% PC liposomes before treatment, after buffer treatment, and after ROS treatment (treated 2:1 mol/mol H2O2:**3.5** or **3.9**).

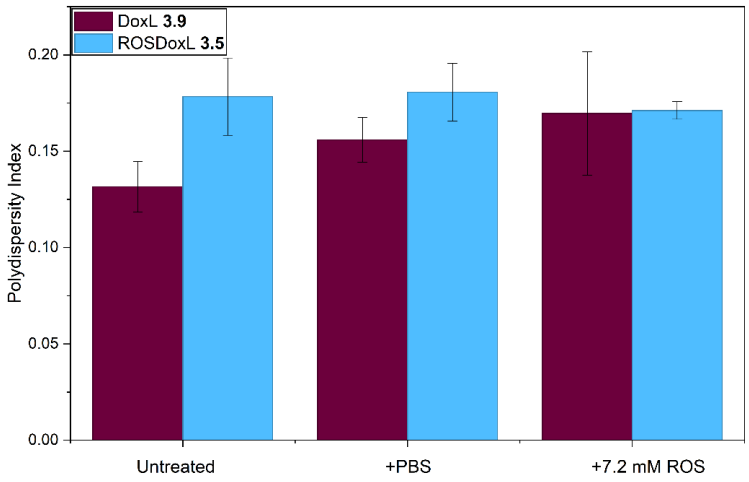

Figure 3.4. PDI of untreated and treated ROSDoxL 3.5 and DoxL 3.9 liposomes. PDI values of 20% ROSDoxL **3.5** or DoxL **3.9**, 80% PC liposomes before treatment, after buffer treatment, and after ROS treatment (treated in a 2:1 mole ratio of H_2O_2:**3.5** or **3.9**).

3.5.2 Zeta Potential Studies

ZP potential measurements were performed to assess whether ROS exposure induced significant changes in liposome surface charge that could contribute to liposome destabilization (Figure 3.5). Both DoxL **3.9** and ROSDoxL **3.5** liposomes exhibited mildly negative surface potentials under all treatment conditions, ranging from approximately -6 to -9 mV. Treatment with PBS or H_2O_2 resulted in only modest shifts in surface charge for either formulation. Notably, ROS exposure did not produce charge inversion or substantial electrostatic collapse for **3.5** liposomes, despite confirmed Dox release by ESI-MS. These results indicate that ROS-mediated activation of **3.5** does not induce large-scale surface composition modification, further supporting a mechanism of drug release driven by chemical cleavage of the boronate-containing self-immolative linker rather than through global liposome destabilization.

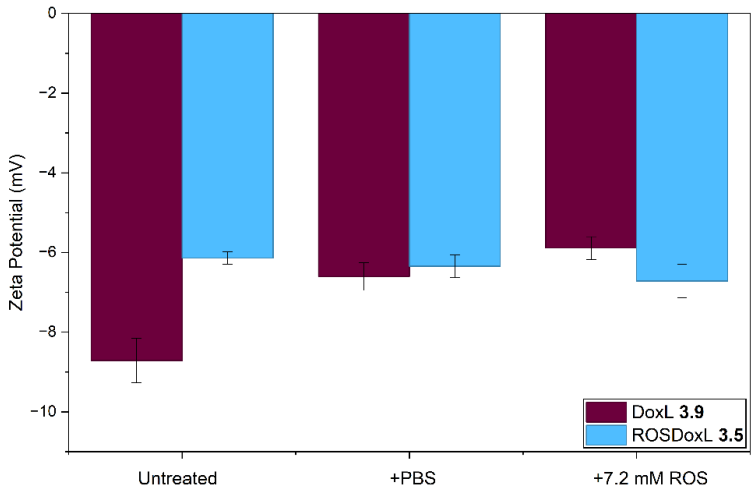

Figure 3.5. ZP of untreated and treated ROSDoxL 3.5 and DoxL 3.9 liposomes. ZP of 20% ROSDoxL **3.5** or DoxL **3.9**, 80% PC liposomes before treatment, after buffer treatment, and after ROS treatment (treated in a 2:1 mole ratio of H_2O_2:**3.5** or **3.9**).

3.6 Cell Viability Experiments

3.6.1 Concentration-Dependent Cell Viability Assays with A375 Cells

After confirming H_2O_2 triggered release of Dox from ROSDoxL **3.5** via ESI-MS, we evaluated the cytotoxic capabilities of the prodrug *in vitro*. To evaluate endogenous ROS-mediated activation, we compared the biological activity of **3.5** with the non-responsive control **3.9**, in both free and liposomal form, to treatment with free Dox. A375 melanoma cells were treated with increasing concentrations of **3.5**, **3.9**, or Dox, with cellular viability assessed after 48 hours using a colorimetric 3-(4,5-dimethylthiazol-2-yl)-5-(3-carboxymethoxyphenyl)-2-(4-sulfophenyl)-2H-tetrazolium (MTS) assay (Figure 3.6). Cells were seeded at 8×10^3 cells per well by Dr. Dillon McBee or Robert Turner, and treated in DMSO/DMEM solutions under standard culture conditions. The absence of the boronate moiety in **3.9** was expected to prevent ROS-triggered release of Dox, serving

again as a mechanistic control.

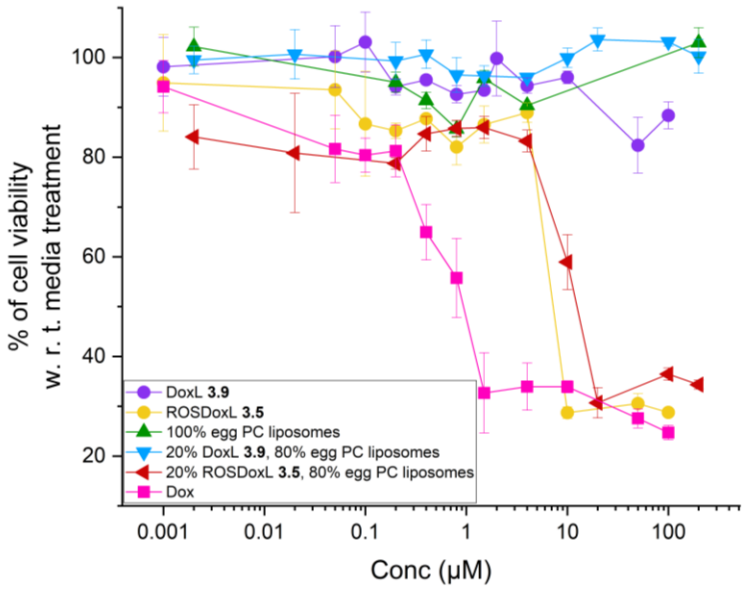

Figure 3.6. MTS cell viability studies with free and liposomal ROSDoxL 3.5 and DoxL 3.9, free Dox, and control PC liposomes over a range of concentrations. MTS cellular viability study for A375 cells treated with free ROSDoxL **3.5** or DoxL **3.9**, liposomal ROSDoxL **3.5** or DoxL **3.9**, negative control (PC) liposomes, and free Dox. Results show that ROSDoxL **3.5** exhibited anti-cancer activity, while DoxL **3.9** did not, both in free form and 20% liposomes. Free DoxL **3.9**, 20% DoxL **3.9** liposomes, and egg-PC liposomes were found to be non-toxic when compared to free ROSDoxL **3.5** (100 μM, 71.247% cell death), 20% ROSDoxL **3.5** liposomes (200 μM, 65.667% cell death), and Dox treatment (100 μM, 75.275% cell death).

Liposomes were prepared in 1 x PBS buffer (pH 7.4) with PC (100 or 80%) along with 0 or 20% **3.5** or **3.9** and then diluted with DMEM. Free **3.5**, **3.9**, and Dox solutions were prepared in 0.5% v/v DMSO/DMEM in a range of concentrations from 1 nM – 200 μM. A375 cells were seeded at 8 × 10^3 cells per well and incubated with treatments for 48h

prior to MTS analysis. As shown in Figure 3.6, clear mechanistic differences emerged between ROS-responsive and non-responsive systems. Free **3.9** and 20% **3.9** liposomes maintained cell viabilities above 90% across nearly all concentrations, confirming that removal of the boronate cage stifles cytotoxic activity. Likewise, control egg-PC liposomes exhibited no measurable toxicity. These results demonstrate that the lipid scaffold itself is not inherently cytotoxic under the tested conditions.

In contrast, both free **3.5** and 20% **3.5** liposomes produced dose-dependent reductions in cell viability, particularly at concentrations above 0.1 μM. At higher concentrations, treatment with 100 μM free **3.5** resulted in 71.25% cell death, while 200 μM **3.5** incorporated within liposomes resulted in 65.67% cell death. For comparison, 100 μM free Dox yielded 75.28% cell death. These data indicate that **3.5** retains substantial therapeutic activity both in free form and when embedded within a lipid bilayer. With these results, we can conclude that our **3.5** prodrug responds to endogenous H_2O_2 levels to undergo cleavage and release Dox, both in free form and integrated within liposomes. While the **3.5** prodrug was less potent than free Dox under these *in vitro* conditions, it still exhibited dose-dependent cytotoxicity. Importantly, the liposomal platform preserves ROS responsiveness while maintaining minimal background toxicity, reinforcing the translational potential of this hybrid lipid–prodrug strategy.

3.6.2 Testing of ROS Concentration on Free Lipid-Prodrug

We next evaluated the effects of increasing ROS concentrations on free prodrug **3.5** function. To probe whether exogenous oxidative stress enhanced prodrug activation, parallel treatment groups were supplemented with 25 or 100 μM H_2O_2. Control treatments

containing 0.5% v/v DMSO and 50–500 μM H_2O_2 alone maintained expected cell viabilities (Figure 3.8), confirming that the observed changes in cell viabilities were not due to solvent or oxidant toxicity under these conditions.

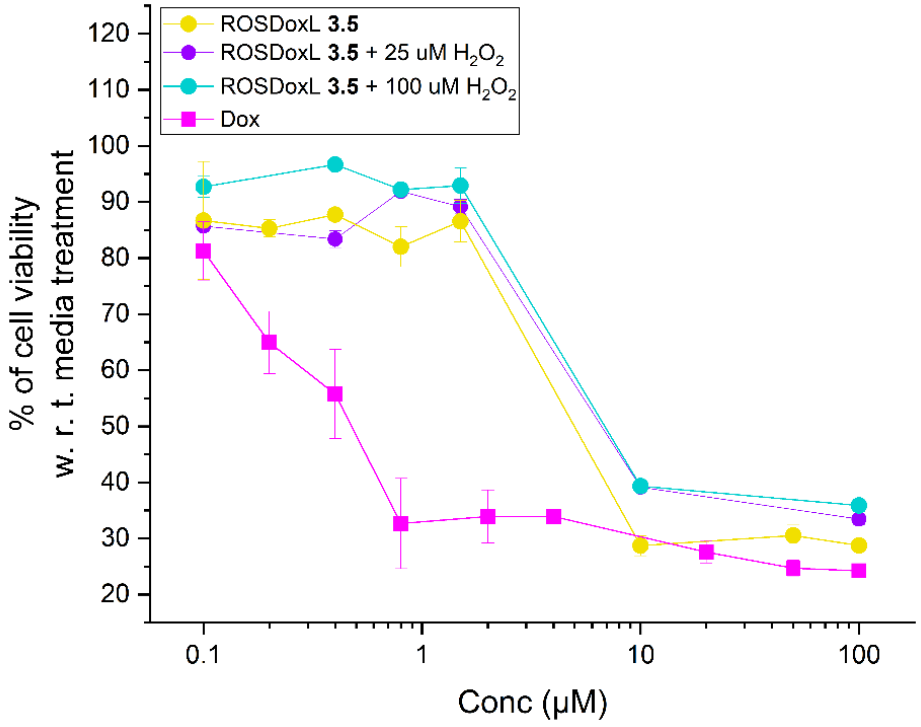

Figure 3.7. MTS cell viability studies with free 3.5 with and without H_2O_2. MTS cellular viability studies for lipid prodrug ROSDoxL **3.5** in DMSO/DMEM solutions 48 h after treatment. Differences in cell viability decay curves were noted for ROSDoxL **3.5** and Dox treated cells. Additionally, no difference in cell viability was found for cells treated with and without H_2O_2 after ROSDoxL **3.5** incubation.

Both Dox and **3.5** were active when comparing the decay curves, with free Dox resulting in greater potency during these *in vitro* experiments. The decreased potency of **3.5** is consistent with its requirement for oxidative prodrug activation prior to Dox release.

Importantly though, ROSDoxL **3.5** maintained substantial cytotoxic activity, indicating that conjugation to the lipid scaffold did not abolish therapeutic function.

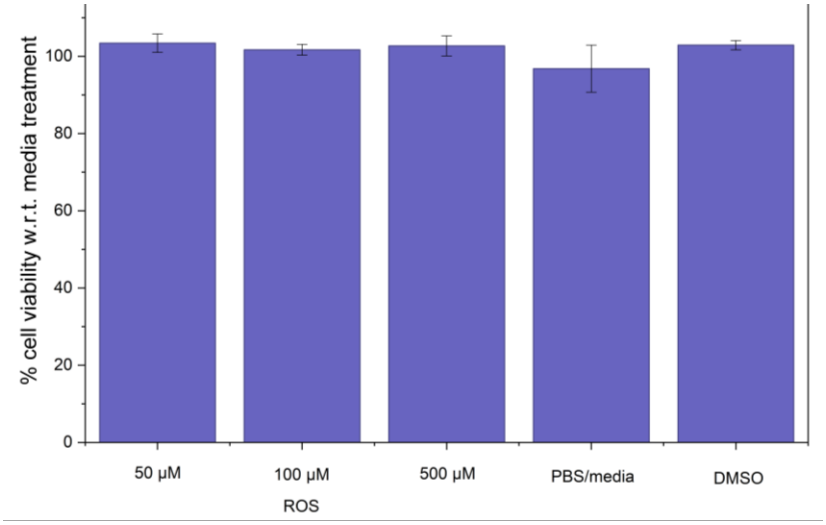

Figure 3.8. MTS cell viability controls with ROS, buffer, and DMSO treatments. Cell viability study controls where minimal cell death was observed for cells treated with 50-500 µM H_2O_2, PBS(-)(-) (1:4 v/v buffer/media), or DMSO (0.5% v/v DMSO/DMEM) with respect to (w.r.t.) plain media treatment (phenol-red free DMEM, 10% FBS, 1% pen/strep).

3.6.3 ROS Quantification Among Cancerous Cell Lines

To contextualize the ROS-responsive behavior of **3.5** across different tumor environments, intracellular ROS levels were compared in three cancer cell lines: A375 (melanoma), HeLa (cervical carcinoma), and Hep-G2 (hepatocellular carcinoma). Lines were compared with a fluorescence assay using 2′,7′-dichlorodihydrofluorescein diacetate (DCF-DA) by Miranda Phillips. DCF-DA, a cell-permeable probe that is deacetylated intracellularly and subsequently oxidized by reactive oxygen species to generate fluorescent DCF, enabling relative comparison of basal oxidative stress between cell lines (Figure 3.9).

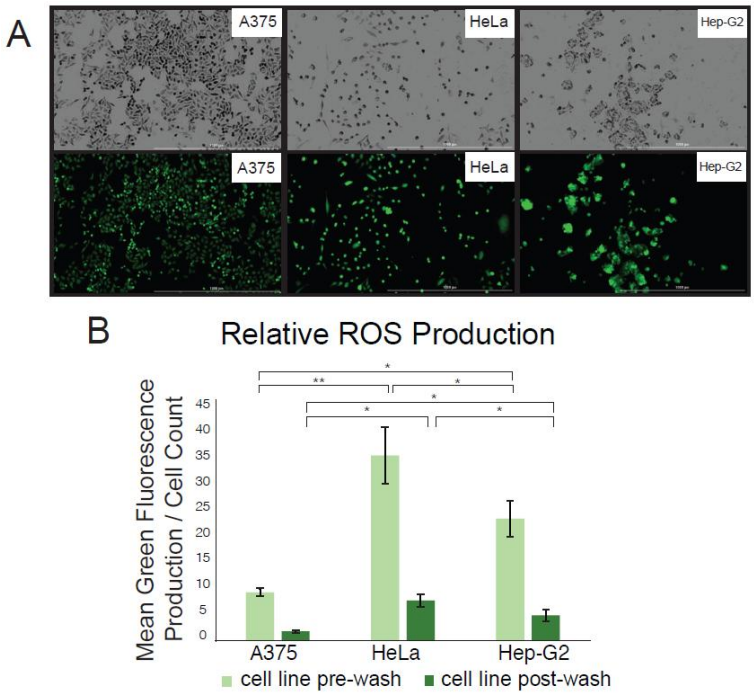

Figure 3.9. Relative ROS production comparison of A375, HeLa, and Hep-G2. (A) Representative brightfield images and fluorescence (Ex 469/35, Em 525/39) of A375, HeLa, and Hep-G2cells before washing. (B) Intracellular ROS measured using a DCF-DA fluorescence assay, where ROS-mediated cleavage of DCF-DA generates the fluorescent DCF in proportion to ROS levels. Across experiments, fluorescence production per cell was highest in HeLa cells and lowest in A375 cells, in both pre-wash and post-wash conditions. Statistical significance is denoted by * ($p < 0.05$) and ** ($p < 0.01$).Figured generated by Miranda Phillips.

Measurements were taken before and after cell washing with warmed DMEM to compare initial ROS secreted and within cells to ROS levels within cells after excess ROS around the cell was removed. While DCF-DA reports general oxidative activity, it is not ROS-species specific.[183] Measurements revealed differential ROS abundance across the

three cancer lines, with A375 cells exhibiting the lowest basal ROS levels of the three on a per cell basis, both before and after cell washes (Figure 3.9B). HeLa cells exhibited the highest basal ROS levels of the three on a per cell basis, again both before and after cell washes. Despite the lower oxidative environment, **3.5** retained significant biological activity in A375 cells, indicating that the boronate self-immolative linker is sufficiently sensitive to trigger drug release even under modest endogenous ROS conditions for diseased cells. These findings suggest that ROSDoxL **3.5** activation does not require extreme oxidative stress and may therefore function across a broader range of tumor redox and development states.

It is possible that the endogenous ROS triggering of ROSDoxL **3.5** could occur either in the surrounding media or within the cells depending on the ROS residence in prevalent diseased cells. ROS levels identified from the DCF-DA assay indicate higher ROS levels after 48 hours of incubation for all lines prior to media removal and washing. Subsequent measurements of ROS after washing also indicate significant ROS levels but these are significantly lower than the initial measurements in media. In both scenarios, A375 cells exhibited the lowest ROS abundance. Prodrug triggering could occur from both media residing ROS and ROS within cells, which may be a promising indicator of prodrug **3.5**'s function within both a tumor microenvironment as well as individual cancerous cells.

3.7 Conclusions

Through this work, we have successfully developed and validated a ROS-responsive Dox lipid prodrug for controlled therapeutic release in diseased cell environments. ROS-mediated cleavage of Dox from the prodrug scaffold was achieved through the introduction

of an aryl-boronate cage and SIL in **3.5** to release Dox after a cascade cleavage event. This design coupled intracellular redox dysregulation directly to therapeutic activation, enabling this stimulus-responsive drug release rather than simply passive therapeutic release. ESI-MS studies confirmed selective H_2O_2-mediated cleavage of **3.5** and release of free Dox, while the non-responsive control compound **3.9** demonstrated that removal of the boronate moiety abolishes oxidative activation. Liposomal formulations incorporating **3.5** formed stable nanoscale assemblies with minimal changes in size, polydispersity, or surface charge following ROS exposure, indicating that drug release is driven by chemical self-immolation rather than global nanoparticle destabilization. Cellular studies further validated functional prodrug activation. Compound **3.5** exhibited concentration-dependent cytoxicity in A375 melanoma cells both in free form and when embedded within liposomes, while the non-responsive control remained inactive. Importantly, supplemental H_2O_2 did not significantly enhance potency, demonstrating that endogenous ROS levels in cancer cells are sufficient to trigger drug release. Comparative ROS quantification and viability studies across multiple cancer cell lines further suggest that the boronate-based linker operates effectively within physiologically relevant oxidative windows, maintaining activity even in tumor models with comparatively modest ROS abundance observed in A375 cells . While ROSDoxL **3.5** is less potent than Dox, presumably due to the need for activation, this approach shows a promising development for achieving diseased-cell selectivity by targeting stimuli that are overexpressed in disease, of which ROS are particularly exciting targets. In addition to diseased-cell selectivity, the integration of this ROS-responsive prodrug system into a synergistic liposomal-prodrug system adds further

potential benefits, including improved pharmacokinetics and tumor accumulation of liposomes. Using similar design strategies as noted in this work, we envision that other important therapeutic molecules can be constructed into lipid-based prodrugs for similar control and disease-cell selective release applications.

3.8 Synthesis and Experimental Procedures

PC (L-α-Phosphatidylcholine, mixed isomers from chicken egg) was purchased from Avanti Polar Lipids, Inc (Alabaster, AL). Liposome extruder and polycarbonate membranes were obtained from Avanti Polar Lipids, Inc (Alabaster, AL). Ultrapure water was purified via a Millipore water system (≥ 18 MW·cm triple water purification system). Small quantities (< 5 mg) were weighed on a Mettler Toledo XS105 dual range analytical balance. Gibco^{TM} medias and buffers were purchased from Fischer Scientific. Column. CellTiter 96® AQueous One Solutions Cell Proliferation Assay (MTS reagent) was purchased from Promega. ROS Detection Assay Kit was purchased from Oz Biosciences. Fluorometric analysis was performed using Gen5 software and Cytation 1 Cell Imaging Multimode Microplate Reader)BioTek Instruments, Winooski, VT) with an RFP filter (λ_{ex} = 531, λ_{em} = 593 nm) and DAPI filter (λ_{ex} = 377, λ_{em} = 447 nm). Plots were generated using Origin Pro 2025b. All error bars in plots indicate the standard errors of at least three experimental replicates.

Preparation of liposomes for cell viability assays

Stock solutions of ROSDoxL **3.5** and DoxL **3.9** were prepared at 5.00 mM in $CHCl_3$/MeOH solution (1/1, v/v), and a stock solution of PC was prepared at 32.46 mM in chloroform. All the stock solutions were kept in a -20 °C freezer after preparation. To

prepare liposomes through thin film hydration, appropriate volumes of each stock solution were pipetted in 0.5 dr vials to reach a total lipid concentration of 4 mM, with desired percentages of each lipid type. The organic solvents were then evaporated under a nitrogen stream, and the resulting lipid films were kept under vacuum for at least one hour. The films were then hydrated with proper volumes of 1 x Dulbecco's phosphate buffered saline without calcium or magnesium (PBS(-)(-), pH = 7.4) in a 60 °C water bath for 1 hr. The vials were vortexed every 15 minutes while incubating. Next, 10 freeze-thaw cycles were performed in a dry ice-acetone bath and 60 °C water bath. Lastly, the liposome solutions were extruded through a 200 nm polycarbonate membrane for 21 passes with an extruder purchased from either Avestin or Avanti. The resulting liposomes were then studied immediately.

A375 cell culture

Melanoma A375 cells, obtained from ATCC® (Manassas, VA) were grown in 100 mm plates and then plated at 8 x 10^3 cells per well in a 96-well plate (clear bottom) for cell delivery experiments. Cells were grown for 48 h to reach 80% confluency in Dulbecco's modified eagle medium (DMEM) + Glutamax, supplemented with 10% (v/v) fetal bovine serum (FBS, Gibco) and 1% penicillin/streptomycin (pen/strep)Gibco). Incubation was performed at 37 °C under 5% CO_2 with 95% humidity.

Cellular viability studies for ROSDoxL 3.5 and DoxL 3.9 with H_2O_2

Standard Dox drug and ROSDoxL **3.5** were prepared in stock solutions at 20 mM in DMSO, serially diluted further with DMSO, followed by dilution with DMEM (phenol red-free, (+) 4.5g/L D-glucose, (+) L-glutamine, (+) 25 mM HEPES, (-) sodium pyruvate,

10% (v/v) FBS and 1% pen/strep) to obtain final 0.5% v/v DMSO/DMEM solutions. Samples from the ROSDoxL **3.5** solution were aliquoted and left plain or treated with appropriate amounts of H_2O_2 to generate final concentrations of 25 μM or 100 μM of H_2O_2 and incubated for 12 hours. A375 cells were plated at a density of 8 x 10^3 cells per well and were treated with 100 μL of the prepared samples of Dox or ROSDoxL **3.5** with and without H_2O_2. Cells were then incubated at 37 °C for 48 hours. After incubation, media was removed and cells were washed 2x with 200 μL of 1 x Dulbecco's phosphate buffered saline with calcium and magnesium (PBS++, warmed to 37 °C). A mixture of the MTS reagent and DMEM was prepared with 10 mL of media and 1.5 mL of MTS reagent (per 96-well plate used). Through reverse pipetting, 115 μL of the MTS mixture was added to each well. Absorbance was measured at 490 nm on a Cytation 1 Cell Imaging Multimode Microplate Reader, with readings taken every 30 minutes starting at 0 hours until 3.5 hours or until absorbance measurements plateaued.

Cellular viability studies for free and liposomal ROSDoxL 3.5 and DoxL 3.9

Standard Dox drug, ROSDoxL **3.5,** and DoxL **3.9,** were prepared in stock solutions at 20 mM in DMSO, serially diluted further with DMSO, followed by dilution with DMEM (phenol red-free, (+) 4.5g/L D-glucose, (+) L-glutamine, (+) 25 mM HEPES, (-) sodium pyruvate, 10% (v/v) FBS and 1% pen/strep) to obtain final 0.5% v/v DMSO/DMEM solutions from 1 nM to 100 μM. PC based liposomes with 0-20% of either **3.5** or **3.9** were prepared per the previous protocol at 4 mM. Liposomes were then serially diluted with PBS(-)(-) from 4 mM to 0.080 μM. Buffer diluted liposomes were then diluted (1:4, v/v, liposome/media) with DMEM (phenol red-free, (+) 4.5g/L D-glucose, (+) L-glutamine, (+)

25 mM HEPES, (-) sodium pyruvate, 10% (v/v) FBS and 1% pen/strep) to produce a range of samples from 20 nM to 200 μM. A375 cells previously plated at a density of 8 x 10^3 cells per well and incubated for 48 hours were treated with 100 μL of the prepared samples of Dox, **3.5**, **3.9**, 20% **3.5** liposomes, 20% **3.9** liposomes, or 100% PC liposomes. Cells were then incubated at 37 °C for 48 hours. After incubation, media was removed and cells were washed 2x with 200 μL PBS++ (warmed to 37 °C). A mixture of the MTS reagent and DMEM was prepared with 10 mL of media and 1.5 mL of MTS reagent (per 96-well plate used). Through reverse pipetting, 115 μL of the MTS mixture was added to each well. Absorbance was measured at 490 nm on a Cytation 1 Cell Imaging Multimode Microplate Reader, with readings taken every 30 minutes starting at 0 hours until 3.5 hours or until absorbance measurements plateaued.

A375, HeLa, and Hep-G2 Cultures for ROS Comparison Studies

A375, HeLa, and Hep-G2 cells, obtained from ATCC® (Manassas, VA) were grown in 100 mm plates. Cell lines A375 and HeLa were grown in DMEM + Glutamax (10% FBS, 1% pen/strep), and Hep-G2 was grown in EMEM with L-glutamine (10% FBS, 1% pen/strep). Incubation was performed at 37 °C under 5% CO2 with 95% humidity.

Preparation of DCF-DA Kit for ROS Detection

DCF-DA solutions were prepared using the ROS detection assay kit (Oz Biosciences). ROS buffer (1x) was prepared by diluting the 10x ROS buffer within the kit 1:10 with DMEM (without FBS or pen/strep). The DCF-DA solution was prepared by diluting the kit DCF-DA (25 mM) solution into 1x ROS buffer, using 10 μL of 25 mM DCF-DA and 10 mL of ROS buffer per 96-well plate tested.

Cellular ROS Comparison Studies with A375, HeLa, and Hep-G2

Cultured cells were plated at 5 x 103 cells per well in a 96-well plate (clear bottom) for ROS comparison studies and were grown for 48 h to reach confluency. Culture media was removed from each cell containing well and transferred to empty wells, following the plate layout indicated in Table S5. Cells were then washed with 1x DMEM (phenol red-free, (+) 4.5g/L D-glucose, (+)L-glutamine, (+) 25 mM HEPES, (-) sodium pyruvate, without FBS and pen/strep), followed by transfer of the wash media to additional empty wells. DCF-DA solution (100 μL) was then added to all wells, followed by a 30-minute incubation period without light exposure. Cells were then imaged on a Cytation 1 Cell Imaging Multimode Microplate Reader, on both the green channel (469 excitation, 525 emission) and fluorescence channel. Media from the 30-minute incubation period with DCF-DA was then removed and placed in a new, empty row of wells. Cells were washed again with 1x DMEM (without FBS and pen/strep) and the supernatant placed in an additional empty row of wells. Cell and media fluorescence was then measured and cells were imaged again on the same channels. Cell counts were obtained using Gen5 software, and fluorescence production was normalized to total cell count to optimize comparisons across cell lines. Cell morphology and count were determined by measuring object sizes ranging from 10 μm to 100 μm.

CHAPTER 4.

DEVELOPMENT AND MECHANISTIC EVALUATION OF ADDITIONAL SUCCINATE-RESPONSIVE LIPID SWITCHES

4.1 Project Overview

The development of additional metabolite-responsive lipid switches designed to respond selectively to dicarboxylate metabolites, such as succinate, was explored through various anion-binding headgroups. Succinate has emerged as an important signaling molecule in cancer and inflammatory disease, where dysregulated metabolic pathways can lead to elevated intracellular concentrations. Targeting succinate as an endogenous trigger represents an opportunity to expand the lipid switch platform beyond nucleotide and phosphate-responsive systems toward recognition of tricarboxylic acid (TCA) cycle intermediates. A conserved membrane-active lipid scaffold was modified by systematically varying the headgroup functionality to introduce cationic and hydrogen-bond–donating motifs capable of interacting with dicarboxylate species. Several nitrogen-containing headgroups were investigated, including guanidinium, ammonium, and thiourea derivatives. The switches successfully synthesized and incorporated into liposomes were first evaluated through metabolite selectivity screenings, and formulations demonstrating significant activity were further assessed using hydrophobic dye release assays, DLS, TEM, and confocal microscopy. Among the systems examined, the cyclic guanidinium switch initially exhibited the most pronounced membrane response toward succinate. However, subsequent mechanistic evaluation and synthetic reproducibility challenges prompted further investigation into structural assignment and headgroup identity.

Additional headgroup variants were therefore developed to probe structure–function relationships and to better define the molecular features necessary for selective dicarboxylate recognition within lipid bilayers, including quaternary ammonium, guanidinium, and thiourea.

4.2 Introduction and Motivation

Metabolite-responsive lipid switches provide a strategy for coupling endogenous biochemical signals to membrane perturbation and controlled cargo release. While prior work in this dissertation focused on nucleotide- and phosphate-responsive systems, expanding this platform toward additional classes of metabolites is necessary to broaden biological applicability. In particular, targeting intermediates of central carbon metabolism offers an opportunity to leverage disease-associated metabolic reprogramming as a trigger for responsive delivery. Succinate, a four-carbon dicarboxylate intermediate of the TCA cycle, has emerged as an important metabolic signaling molecule in cancer and inflammatory disease.[184,185] Under normal physiological conditions, succinate is tightly regulated within mitochondrial metabolism. However, mutations in succinate dehydrogenase (SDH) or dysregulation of mitochondrial respiration can result in intracellular succinate accumulation.[186] This accumulation leads to distinct concentration differences between healthy (0.015 to 0.026 mM)[187] and disease state (1-30 mM)[188] cells, making it a promising stimulus to selectively target. These elevated succinate levels have been implicated in oncogenesis through stabilization of hypoxia-inducible factor (HIF-1α), promotion of angiogenesis, and alteration of epigenetic regulation via inhibition of α-ketoglutarate–dependent dioxygenases.[184] In inflammatory settings, extracellular succinate

can act as a signaling metabolite through activation of the SUCNR1 receptor, contributing to immune modulation and disease progression. These findings highlight succinate not only as a metabolic intermediate but as an oncometabolite with disease-specific elevation and signaling consequences.

From a chemical design perspective, dicarboxylates such as succinate are attractive targets for recognition by cationic nitrogen-based headgroups. However, their simple structure presents a unique recognition challenge in terms of achieving selective recognition over other aliphatic dicarboxylates (e.g., malonate, fumarate, malate, oxaloacetate). Guanidinium and ammonium functionalities are well known to form strong electrostatic and hydrogen-bonding interactions with carboxylate anions in both biological and synthetic systems. Anslyn and co-workers reported on the thermodynamics of guanidinium and boronic acid interactions with carboxylates like succinate, where sensors containing guanidinium groups exhibited a higher affinity for carboxylate guests than the boronic acid versions (Figure 4.1A).[189] Kilburn and co-workers reported guanidiniums and ammoniums as also having high affinity for carboxylates (Figure 4.1B) due to hydrogen-bonding and charge-induced electrostatic effects (Figure 4.1C).[190] Cyclic guanidinium motifs in particular provide preorganized charge distribution and directional hydrogen-bond donors that may enhance binding affinity and selectivity toward dicarboxylates. Thiourea motifs represent an alternative recognition strategy based primarily on dual hydrogen-bond donation, where bis-thioureas specifically have been shown to have higher selectivity for dicarboxylate anions (Figure 4.1D).[191] Martí et al. demonstrated that thiourea-functionalized gold nanoparticles selectively aggregate in the presence of

succinate, producing a visible colorimetric response, whereas structurally similar dicarboxylates induced minimal effects.[192] In that system, succinate uniquely promoted interparticle cross-linking via simultaneous coordination of its terminal carboxylates to thiourea donors on adjacent nanoparticle surfaces, highlighting the importance of analyte geometry and multivalent interactions. These findings suggest that hydrogen-bond–rich motifs such as thiourea may provide enhanced discrimination among structurally similar dicarboxylates.

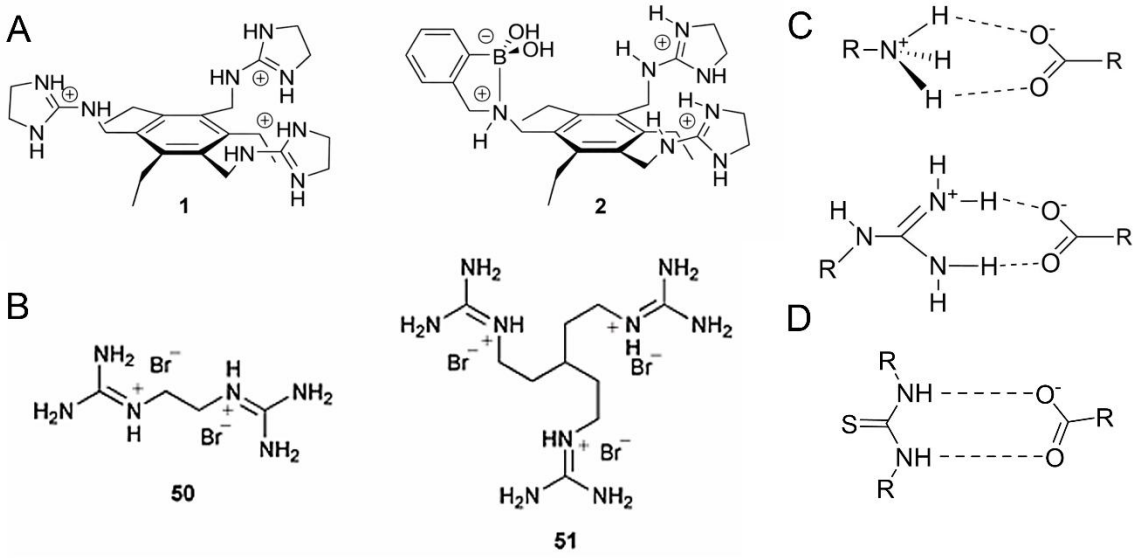

Figure 4.1. Previously developed carboxylate sensors and their potential interactions. (A) Guandinium-based sensors developed by Anslyn and co-workers exhibiting high carboxylate affinity.[189] (B) Guanidinium sensors developed by Kilburn and co-workers with high carboxylate affinity.[190] (C) Ammonium and guanidinium interactions with carboxylate show that guanidinium-carboxylate interactions benefit from a more favorable spatial alignment. (D) Thiourea and carboxylate interactions also possess favorable spatial alignment for electrostatic and H-bonding interactions.

Despite these advances in molecular recognition and nanoparticle sensing, translation of succinate recognition into membrane-active lipid systems remains comparatively unexplored. Incorporating dicarboxylate-binding motifs into amphiphilic scaffolds introduces additional mechanistic complexity. Along with specific headgroup-metabolite interactions, incorporation of positively charged headgroups into membrane-embedded lipids offers the potential to translate localized anion binding into bilayer packing perturbation, curvature stress, or domain formation. Building upon the conserved membrane-active scaffold developed in Chapter 2, this chapter explores systematic variation of anion-binding headgroups to evaluate structure–function relationships governing dicarboxylate recognition. Through this approach, we sought to determine whether succinate accumulation could serve as an endogenous trigger for lipid switch activation and to define the molecular features required for selective dicarboxylate-responsive membrane perturbation.

4.3 Design and Development of a Cyclic Guanidinium Lipid Switch

4.3.1 Synthetic Design of a Cyclic Guanidinium Lipid Switch

The cyclic guanidinium (CG) lipid switch was designed to introduce a preorganized, multidentate cationic binding motif capable of selectively interacting with dicarboxylate metabolites such as succinate. Unlike phosphate- or nucleotide-responsive systems described in earlier chapters, recognition of succinate requires accommodation of a dianionic, linear C4 dicarboxylate with a defined charge spacing. Succinate exists predominantly as a doubly deprotonated species at physiological pH, presenting two carboxylate groups separated by approximately 4–5 Å. Effective recognition therefore

demands a headgroup capable of strong electrostatic attraction combined with directional hydrogen bonding and an appropriately sized binding space.

Guanidinium groups are well established in supramolecular chemistry as robust anion-binding motifs due to their planar geometry, delocalized positive charge, and ability to donate multiple hydrogen bonds simultaneously.[193–196] Prior solution-phase receptor studies have demonstrated enhanced affinity of guanidinium-containing scaffolds for dicarboxylates, including succinate, through cooperative electrostatic and hydrogen-bonding interactions. The cyclic guanidinium architecture was selected to further enhance this effect by constraining the binding site into a rigid, preorganized geometry. Compared to acyclic guanidinium or simple ammonium headgroups, the cyclic structure was anticipated to reduce entropic penalties upon binding and improve spatial complementarity to the succinate dianion.

To evaluate this concept within a membrane context, the CG headgroup was appended to the conserved membrane-active scaffold previously employed for the BPLS-based switch. Retaining the same hydrophobic framework allowed isolation of headgroup effects while maintaining comparable bilayer insertion and packing behavior. The synthetic route to the cyclic guanidinium lipid paralleled that of earlier scaffold derivatives (Scheme 4.1) through formation of the aryl–ether–linked lipid backbone and installation of the terminal bromine intermediate (analogous to **2.5** in Chapter 2)**.** Azide substitution was performed on **2.5** to yield azide **4.1**, followed by purification and standard Staudinger reduction conditions to generate the amine **4.2.** A Boc-protected imidazoline reagent was then formed and melted with **4.2** to form the protected guanidine headgroup before Boc deprotection

generated the final cyclic guanidinium switch **4.3.** However, subsequent synthetic attempts though failed to reproduce matched spectra of **4.3**, leading to reproducibility and characterization concerns for **4.3** discussed in later sections.

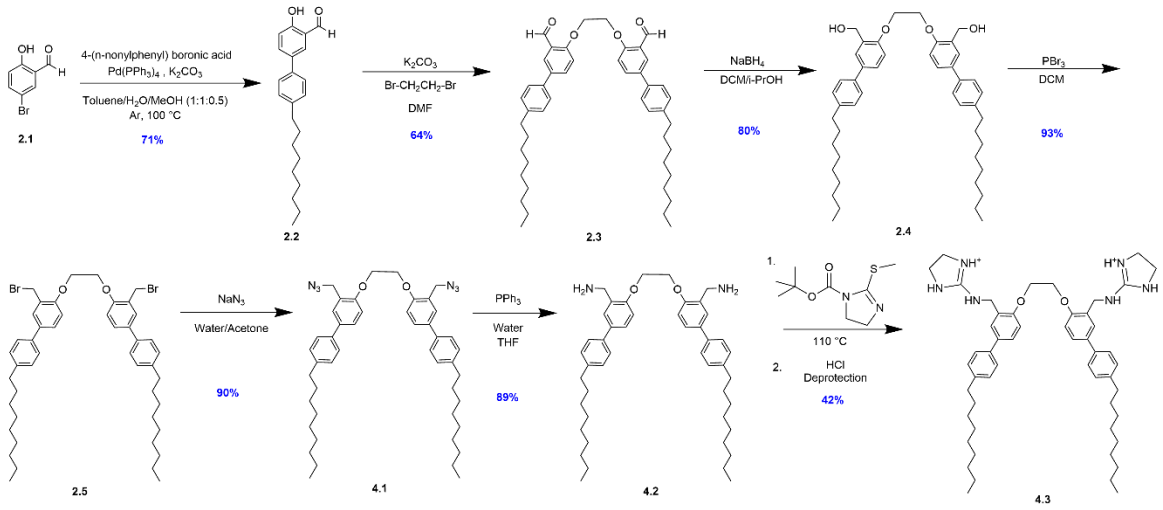

Scheme 4.1. Synthetic reaction scheme for CG 4.3. A Suzuki coupling between **1.1** and 4-(*n*-nonylphenyl) boronic acid introduces hydrophobic tail to form **2.2**. Dimerization with 1,2-dibromoethane yields **2.3**, where further head group modifications include reduction to **2.4**, bromination to **2.5**, azide substitution to **4.1**, Staudinger reduction conditions to generate **4.2**, and lastly reaction with a Boc-protected imidazoline reagent and subsequent deprotection to generate suspected CG **4.3** before reproducibility and characterization concerns were identified.

The CG functionality was installed at the lipid headgroup position, oriented toward the aqueous interface to maximize accessibility to extracellular or cytosolic succinate. Mechanistically, succinate binding was hypothesized to alter headgroup electrostatic interactions at the membrane surface. Because the scaffold was designed to balance bilayer stability with headgroup responsiveness, binding of a dianionic metabolite could increase

local charge density, modify interfacial packing, and induce curvature stress through a conformational change of the switch (Scheme 4.2). Such perturbations were expected to translate into collective membrane destabilization, promoting cargo release in a manner analogous to previously described metabolite-responsive systems, but driven by selective recognition of a TCA cycle intermediate.

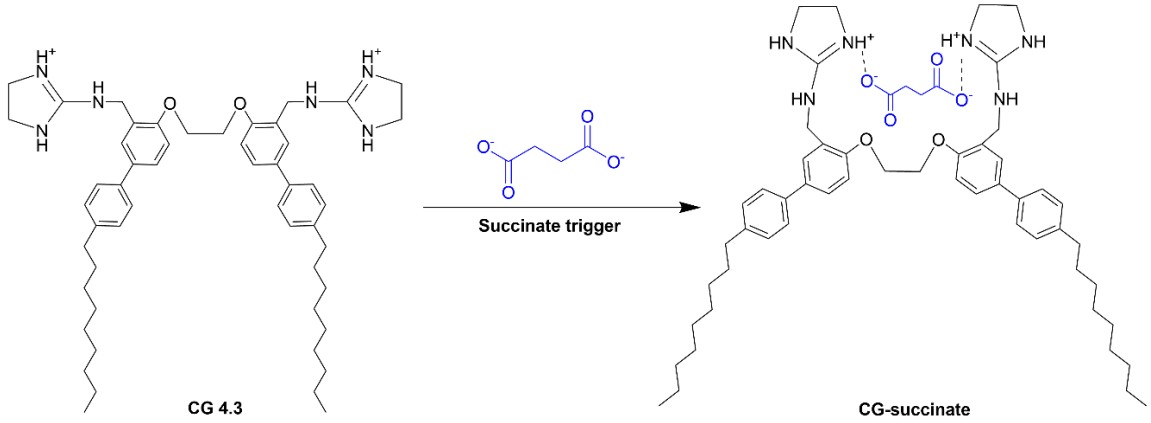

Scheme 4.2. CG 4.3 proposed binding to succinate with potential conformational change. Hypothesized fitting of succinate into CG 4.3 headgroup pocket for conformational lipid shape change through binding.

4.3.2 Hydrophobic Dye Release and Kinetic Evaluation

We next evaluated the function of the putative CG switch **4.3** and determined if the CG headgroup could translate succinate exposure/binding into membrane perturbation and subsequent hydrophobic dye release. NR release assays previously described were performed using liposomes composed of **4.3**, DOPE, and PC. After establishing baseline concentrations of the three lipids that formed relatively stable liposomes with detectable dye encapsulation, we performed a series of studies probing the effects of ratio adjustment. Initial studies first examined the influence of CG lipid **4.3** and its mol% effect on the

membrane. Liposomes were formulated with varying percentages of CG from 20-35 mol%, DOPE held constant at 40 mol%, and PC constituting the remaining mol%. Liposomes were treated with 8.7 mM succinate and incubated for 24 hours while monitoring NR release through changes in fluorescence (Figure 4.2).

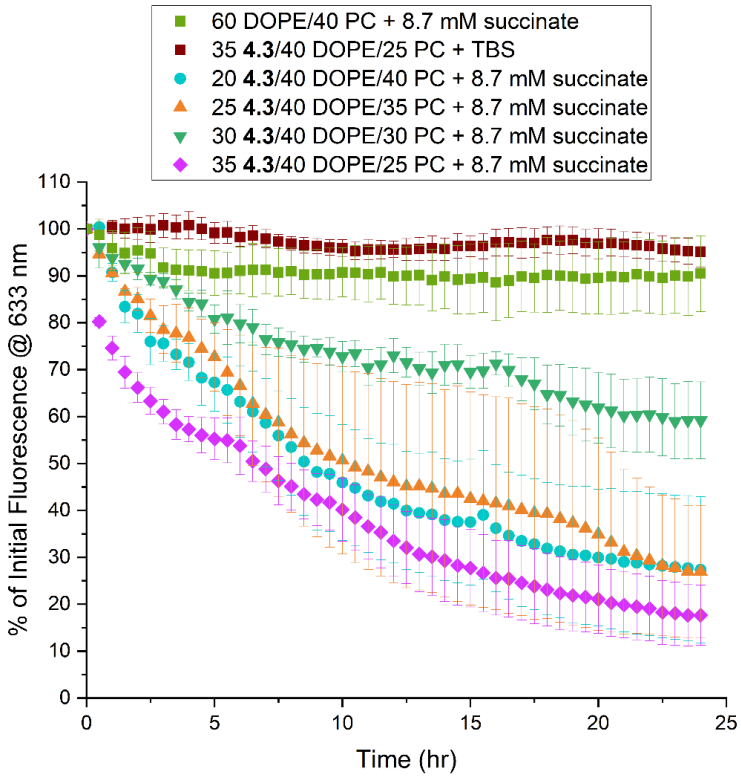

Figure 4.2. NR release from liposomes with varying CG 4.3%. NR release from liposomes with varying concentrations of CG **4.3**. Liposomal cargo release is highly sensitive to **4.3** percent, resulting in variable release patterns as **4.3** percentage increases, culminating in optimal release with 35% **4.3**. Buffer treated **4.3** liposomes and succinate treated DOPE/PC liposomes tested as controls show minimal release as expected.

Minimal passive leakage was observed in buffer-treated controls and succinate treated controls with **4.3** across formulations, confirming baseline membrane stability. Upon

succinate exposure, however, formulations containing CG **4.3** exhibited measurable NR release. A general trend between release and **4.3** mol% was expected but comparing the release curves of 30% and 35% **4.3**, drastic differences in cargo release were observed. This non-linear response suggests that membrane behavior is not governed solely by headgroup abundance, but rather by collective membrane dynamics that emerge once a critical threshold of switch incorporation is reached.

These findings highlight the importance of lateral organization within the bilayer.[197] At higher mol% incorporation, CG lipids may cluster within the membrane, forming locally enriched domains that alter interfacial charge density and packing stress.[198] Because the CG headgroup is cationic at physiological pH, electrostatic interactions with dianionic succinate could promote localized charge neutralization or transient cross-linking between neighboring switch molecules. Such interactions may induce domain formation or microphase separation within the bilayer, even prior to large-scale curvature changes.[199–202] Once a threshold concentration of switch–succinate complexes is achieved, these localized perturbations may propagate into collective membrane destabilization sufficient to promote NR release. Importantly, this behavior also suggests that membrane perturbation may not require a discrete conformational "switching" event but could instead arise from electrostatic reorganization and altered headgroup packing at the aqueous interface. In this context, the CG lipid acts as both a binding motif and a membrane-active unit whose spatial distribution critically influences release behavior. These results indicate the presence of an optimal compositional window in which succinate-induced membrane perturbation could be maximized, with 35/40/25 **4.3**/DOPE/PC representing the most

responsive formulation within the tested range. To further refine membrane responsiveness, the proportion of DOPE was then also systematically varied from 30 to 45 mol% (Figure 4.3).

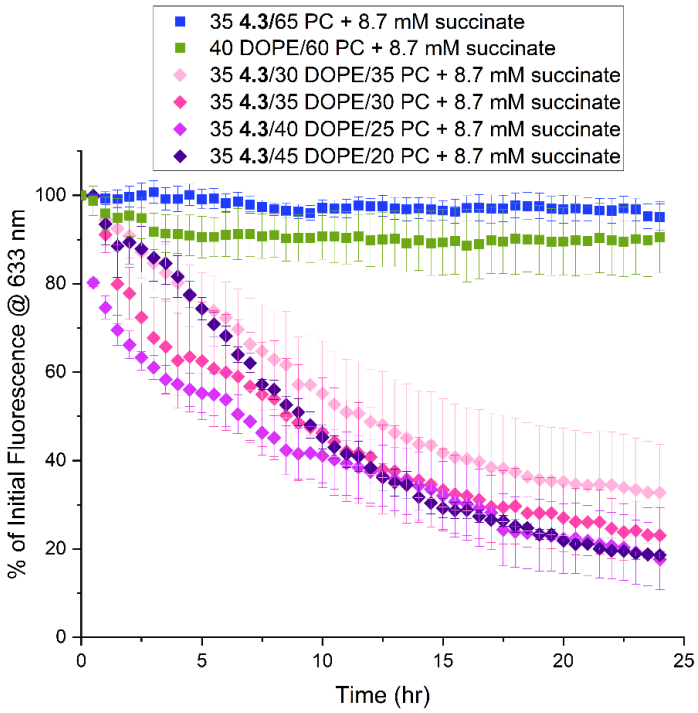

Figure 4.3. NR release from liposomes with varying DOPE%. NR release from liposomes with varying concentrations of DOPE, where larger amounts of DOPE incite slightly more extensive release but yield poorer dye encapsulation. Liposomes without DOPE show no release, indicating the necessity of including a destabilizing lipid in the formulation to aid in release.

As DOPE favors negative curvature and non-bilayer phases, increasing DOPE content was anticipated to amplify perturbations arising from headgroup binding events.[203] Indeed, formulations containing elevated DOPE percentages demonstrated enhanced NR release upon succinate treatment compared to lower-DOPE counterparts, with an overall increase

of ~15% NR release plateauing at 35% DOPE incorporation. These observations reinforce the concept that membrane responsiveness arises from a balance between headgroup-mediated binding interactions and pre-existing curvature stress within the bilayer. Given the potential role of electrostatic interactions in succinate binding, additional destabilizing lipids were evaluated. Incorporation of small percentages of negatively charged PA in combination with zwitterionic DOPE, further modulated release behavior (Figure 4.4).

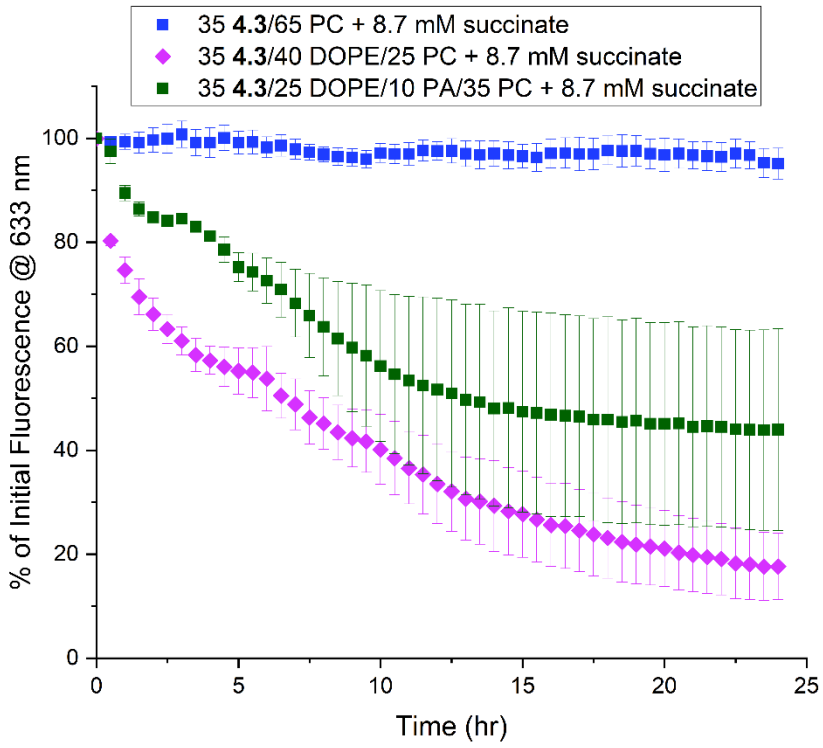

Figure 4.4. NR release from liposomes with varying destabilizing lipids. A comparison of Nile red release from liposomes with increasing types of non-bilayer-forming lipids included. Inclusion of DOPE enables release of cargo from liposomes once treated with succinate whereas addition of DOPE and PA does not yield as efficient release but produces highly variable release patterns.

In selected formulations containing only DOPE, succinate-triggered NR release was amplified relative to DOPE-PA systems, while passive leakage remained within an acceptable range. In contrast, PA-containing liposomes exhibited widely varied, but overall lower release. These data suggest that surface charge density and membrane elasticity collectively influences the ability of the CG headgroup to translate metabolite recognition into membrane disruption, where negative PA incorporation disrupts effective triggering or NR release.[204] However, incorporation of a cyclic guanidinium headgroup could promote succinate-responsive membrane perturbation within a defined compositional window and careful formulation tuning.. Membrane sensitivity was strongly dependent on both CG mol% and the relative proportions of DOPE, PC and PA, underscoring the importance of composition-driven tuning in metabolite-responsive lipid systems.

4.3.3 Structural Characterization Studies

DLS was next performed to evaluate if succinate exposure produced measurable changes in vesicle size consistent with the membrane perturbation observed in NR release assays (Figure 4.5). Untreated liposomes displayed average diameters consistent with stable nanoscale assemblies, under 200 nm, with the exception of 45% **4.3** liposomes, indicating stable liposomes did not form for this formulation. Upon treatment with increasing concentrations of succinate, size increases were observed for formulations containing 25 to 40% **4.3**. The most pronounced changes in diameter were observed for liposomes with 35% **4.3**, the optimized formulation from the kinetic NR release studies. With this optimized formulation, the liposomes exhibited significant response to all tested concentrations of succinate. Liposomes with lower **4.3** percentages were not as

significantly altered when treated with lower concentrations of succinate, indicating that lipid switch percentage and formulation optimization may also affect triggering sensitivity. The observed increases in size, though, suggest aggregation or membrane reorganization events consistent with succinate-induced perturbation.

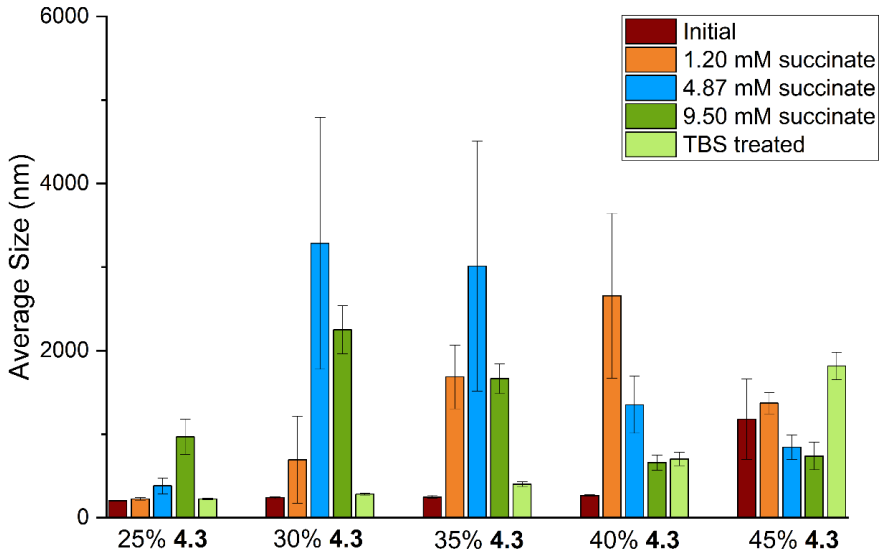

Figure 4.5. DLS studies with varying concentrations of CG 4.3. DLS studies with varying lipid switch and succinate concentrations (X **4.3**/40 DOPE/60-X PC). Liposomes with 40% **4.3** indicate the highest succinate sensitivity whereas 30% and 35% **4.3** liposomes indicate the largest response by size change to higher succinate concentrations. Error bars represent standard errors from at least three replicates.

TEM was subsequently employed to visualize these morphological changes (Figure 4.6). Untreated CG-containing liposomes exhibited spherical, unilamellar vesicles with relatively uniform size distribution, confirming successful liposome formation. Following succinate treatment, distinct, well-defined vesicle fusion events such as those observed in prior BPLS systems were not consistently resolved. Instead, TEM images revealed

irregular lipid masses and clustered structures suggestive of aggregation or membrane reorganization. While these features are less morphologically distinct than classical vesicle bursting or multivesicular structures, they are consistent with DLS data indicating significant size increases at higher succinate concentrations. It is important to note that negatively stained TEM can exaggerate or obscure subtle bilayer perturbations, particularly in systems undergoing electrostatically driven aggregation. Therefore, while TEM supports the presence of structural reorganization, the precise morphological pathway of succinate-triggered perturbation in the CG system remains less clearly defined than in previously characterized phosphate-responsive switches.

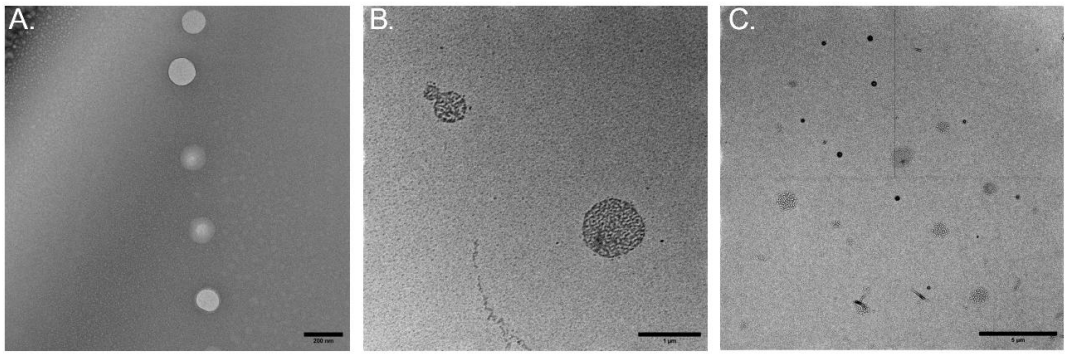

Figure 4.6. TEM images of 35 4.3/40 DOPE/25 PC liposomes before and after treatment with succinate. Liposomes were prepared and stained with uranyl acetate prior to any metabolite treatment. Uniform, unilamellar vesicles are observed before treatment (A) but fusion and aggregation of liposomes appear after treatment with 10 mM succinate (B,C).

4.3.4 Metabolite Selectivity Screening

To assess whether membrane perturbation induced by CG switch **4.3** was selective toward succinate, a metabolite screening study was performed using a panel of structurally

and functionally diverse small molecules (Figure 4.7). Liposomes composed of 35/40/25 **4.3**/DOPE/PC were treated with increasing concentrations (1, 5, and 10 mM) of inorganic phosphate species, nucleotides, sugar phosphates, and TCA cycle metabolites. NR fluorescence was monitored after 24 hours and reported as percent of initial fluorescence.

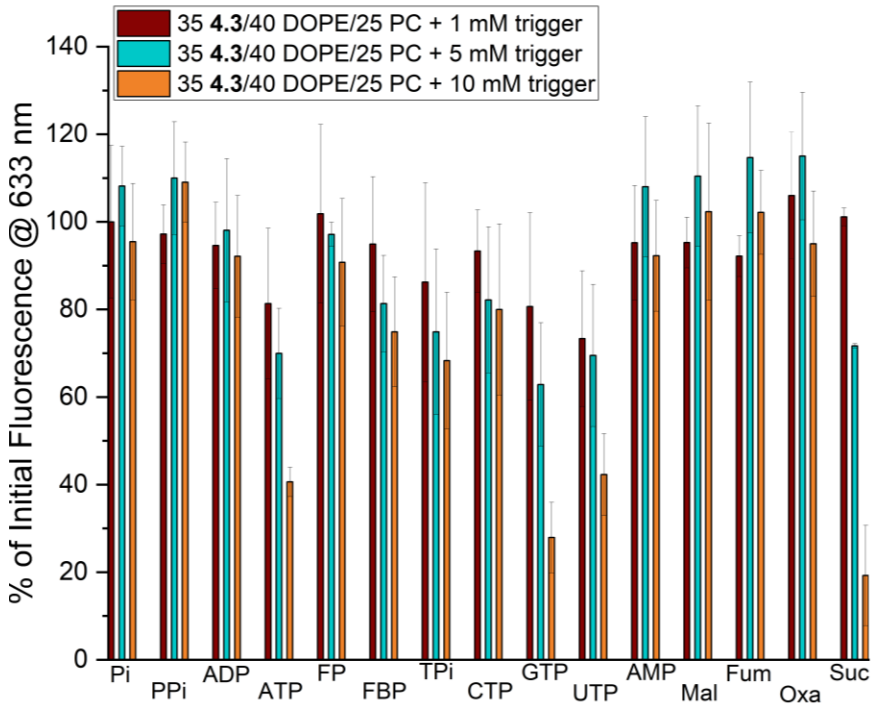

Figure 4.7. Metabolite selectivity screening through NR release for 4.3 liposomes. Nile red release assay with CG **4.3** liposomes for selectivity screening over 24 hours with 1 mM, 5 mM, and 10 mM metabolite concentrations. Notable release was observed with ATP, GTP, UTP and Suc.

At lower metabolite concentrations (1 mM), minimal perturbation was observed across most analytes, indicating baseline membrane stability under dilute conditions. ATP, GTP, and UTP were exceptions where more than 20% NR release was observed. At 5 mM and particularly at 10 mM, differential responses emerged. Phosphate-containing species such

as ATP, TPi, GTP and UTP produced moderate decreases in fluorescence, consistent with partial membrane perturbation at higher ionic strength. However, among the TCA cycle metabolites tested, succinate induced one of the most pronounced decreases in NR fluorescence at 10 mM, suggesting enhanced membrane disruption relative to monocarboxylates and certain structurally similar dicarboxylates. Importantly, fumarate, malate, and oxaloacetate exhibited comparatively smaller effects under identical conditions. Given their structural similarity to succinate, this observation initially suggested a degree of preferential interaction between the CG headgroup and the specific charge spacing and flexibility of the succinate dianion. The absence of strong responses to AMP and other singly charged metabolites further supports a mechanism dependent on dianionic engagement rather than nonspecific ionic screening alone.

The screening also revealed measurable responses to several highly charged phosphate metabolites at elevated concentrations. These findings indicate that electrostatic interactions contribute significantly to membrane perturbation in this system. While succinate produced one of the strongest responses within the TCA metabolite panel, the overall selectivity window was not absolute. Instead, the data suggest a combination of charge density, multivalency, and specific headgroup–metabolite interactions govern the extent of membrane disruption. These findings supported the working hypothesis that cyclic guanidinium incorporation could translate dicarboxylate recognition into membrane destabilization. However, the contribution of general electrostatic effects versus discrete succinate-specific binding would require further mechanistic evaluation in subsequent studies.

4.3.5 Fluorescence Microscopy Studies

To further visualize succinate-induced structural perturbations suggested by DLS analysis, confocal fluorescence microscopy experiments were performed using 35/40/25 **4.3**/DOPE/PC liposomes incorporating 0.08% rhodamine-PE (Rd-PE) as a membrane fluorescent marker. Liposomes were treated with succinate and monitored over time to observe potential aggregation or morphological transitions at the micron scale (Figure 4.8). Succinate-treated samples displayed the progressive appearance of bright, punctate, red, fluorescent structures over time. These fluorescent structures increased in both size and intensity, indicating aggregation or reorganization of Rd-PE–labeled liposomes into larger assemblies detectable by confocal microscopy. The emergence of these micron-scale aggregates correlates with the substantial hydrodynamic diameter increase observed by DLS at elevated succinate concentrations. Rather than simple vesicle swelling, the microscopy data suggest that succinate binding to the cyclic guanidinium headgroups promotes liposome–liposome interactions and higher-order assembly, also observed in the collected TEM images. Electrostatic complexation between dianionic succinate and multiple cationic CG headgroups may reduce interfacial repulsion and facilitate cross-linking between adjacent vesicles. This process could drive clustering, membrane fusion events, or transitions toward non-bilayer lipid phases. Importantly, buffer-treated liposomes and liposomes without CG switch **4.3** did not exhibit comparable aggregation over the same time period, supporting the conclusion that the observed structural reorganization is triggered by succinate exposure to **4.3** rather than spontaneous instability. Together with NR release and DLS findings, these fluorescence microscopy studies

reinforce the hypothesis that succinate binding induces collective membrane reorganization in CG-containing liposomes, translating metabolite recognition into supramolecular structural change.

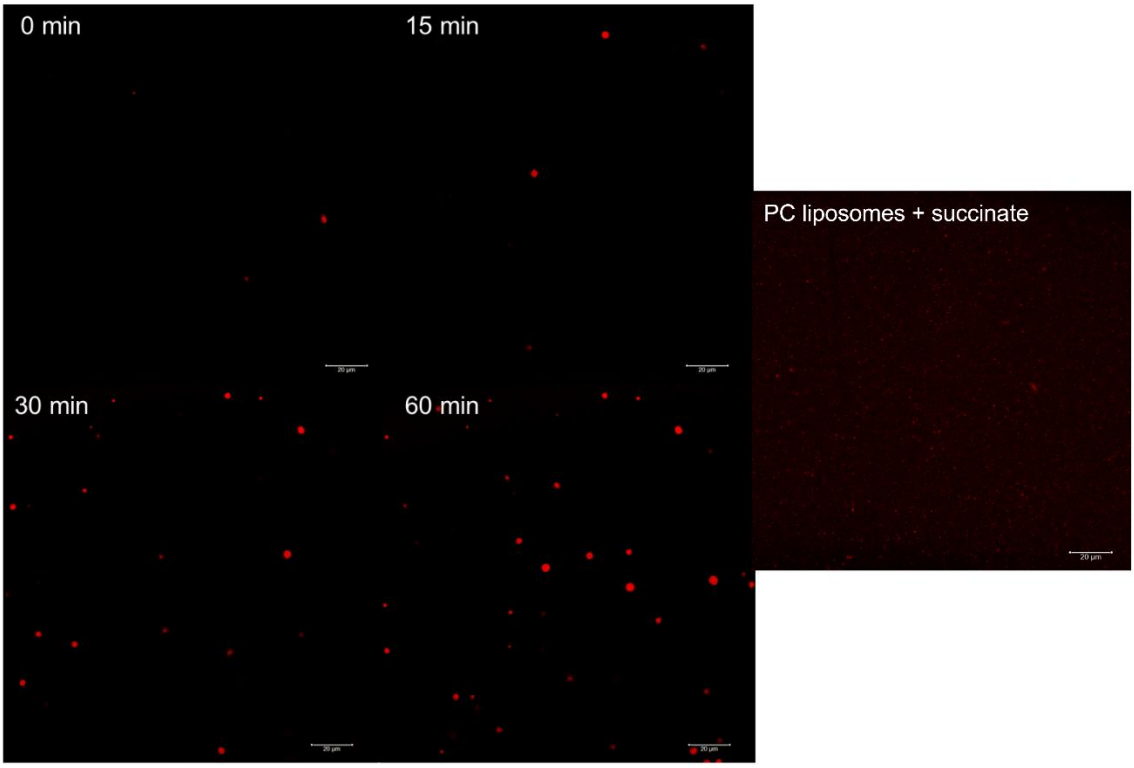

Figure 4.8. Confocal microscopy aggregation study of 4.3 liposomes treated with succinate and imaged over 60 minutes. A confocal microscopy aggregation study was performed with 35/40/25 **4.3**/DOPE/PC liposomes tagged with Rd-PE, treated with 50 mM succinate, and monitored over 60 minutes for aggregation or fusion of liposomes as **4.3** interacts with succinate. PC liposomes without **4.3** did not exhibit this same aggregation.

4.3.6 Mechanistic Reassessment and Structural Considerations

Although the CG lipid **4.3** initially demonstrated promising succinate-responsive membrane behavior, subsequent attempts to reproduce the synthesis and extend

hydrophilic cargo release studies prompted a mechanistic reassessment of the headgroup structure. Early characterization of **4.3** was consistent with formation of the intended cyclic guanidinium species, with mass spectrometry matching the calculated molecular weight and $^{1}H/^{13}C$ NMR spectra largely supporting the proposed structure. However, closer inspection revealed subtle inconsistencies, including the absence of an expected methylene doublet in the headgroup region, which instead appeared as a singlet. Because cyclic guanidinium formation would be expected to preserve diagnostic splitting patterns associated with adjacent protons, this observation raised the possibility of structural deviation.

Subsequent synthetic attempts failed to consistently reproduce the originally observed mass and NMR features. Notably, mass spectrometry from later batches did not match the expected cyclic guanidinium molecular ion. These discrepancies suggest that the guanidinylation step may not have proceeded as intended in all preparations. One plausible explanation is that unintended headgroup modification occurred at the amine intermediate stage. Given the prior observation of phosphonium substitution in related systems (Chapter 2), formation of a bis-triphenylphosphonium-like structure at the amine stage cannot be excluded. Such substitution would alter the electronic environment of the headgroup and prevent subsequent guanidinylation, thereby producing a structurally distinct lipid capable of exhibiting membrane activity but lacking the designed cyclic guanidinium motif. If partial or competing pathways occurred during synthesis, it is conceivable that the initial batch contained either the intended cyclic guanidinium lipid or a mixture of cationic headgroup species, whereas subsequent preparations diverged due to subtle variations in

reaction conditions. The inability to definitively confirm cyclic guanidinium formation by advanced structural methods (e.g., ^{31}P NMR or 2D NMR) further complicates assignment. Importantly, however, the membrane activity observed in early dye release and aggregation studies indicates that a cationic, membrane-active species was indeed formed, even if its precise structural identity remains ambiguous.

Hydrophilic cargo release experiments performed during later stages of this work were complicated by increased passive leakage across formulations, preventing clear identification of succinate-triggered behavior. Because bilayer permeability is highly sensitive to headgroup charge density and packing interactions, even modest structural changes at the headgroup could significantly alter membrane stability. Thus, variations in synthetic outcome may explain both the altered physical characterization data and the difficulty in reproducing controlled release behavior. While the cyclic guanidinium concept remains mechanistically compelling, the precise structure of the membrane-active species responsible for the observed succinate responsiveness requires further clarification.

4.4 Alternate Nitrogen-Based Lipid Switches

To further interrogate the structural features required for succinate-responsive membrane perturbation, additional nitrogen-containing headgroups were incorporated onto the conserved lipid scaffold. These designs aimed to decouple the roles of permanent charge, hydrogen-bond donation, and conformational preorganization in dicarboxylate recognition within a bilayer environment. Two variants were prepared from the common amine intermediate **4.2**, a quaternary ammonium lipid (QA) **4.4** and a guanidinium lipid **4.5** (Scheme 4.3).

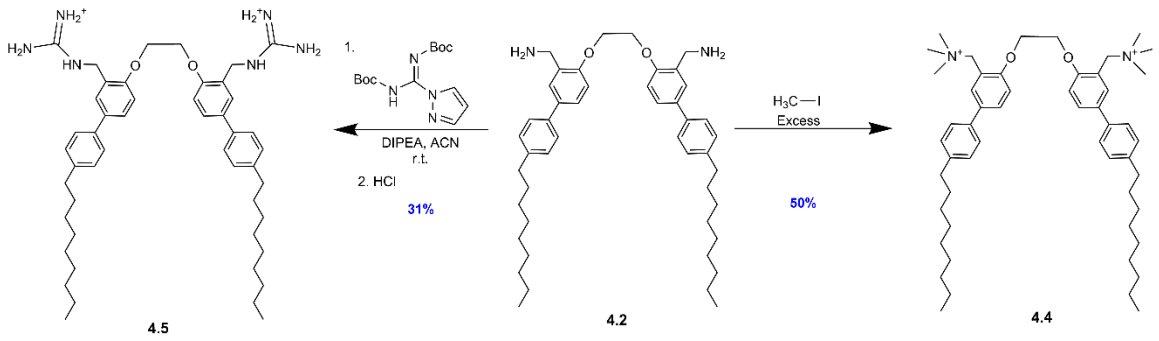

Scheme 4.3. Synthesis of QA 4.4 and guanidinium 4.5. Synthesis of both **4.4** and **4.5** start with amine precursor **4.2**. For **4.4** synthesis, **4.2** was reacted with excess iodomethane until conversion. For **4.5** synthesis, **4.2** was refluxed with a protected-carboxamidine precursor until addition, followed by Boc-deprotection to generate **4.5**.

The QA headgroup provides a permanently charged cationic center but lacks hydrogen-bond donating capability. This design allowed evaluation of whether simple electrostatic attraction to the dianionic succinate would be sufficient to induce membrane perturbation. Liposomes incorporating QA **4.4** formed stable vesicles and were subjected to metabolite selectivity screening (Figure 4.9). However, only minimal hydrophobic dye release was observed across tested metabolites, and no pronounced succinate selectivity emerged. The lack of response from QA **4.4** indicated charge–charge interactions alone are insufficient to translate succinate binding into collective membrane destabilization within this scaffold.

To assess whether hydrogen-bond donation without cyclic preorganization could restore responsiveness, a flexible, acyclic guanidinium lipid **4.5** was also synthesized. While guanidinium groups are well-established anion binders in solution due to their planar charge distribution and multidentate hydrogen-bonding capacity, incorporation of **4.5** into liposomal formulations resulted in poor bilayer stability and elevated passive leakage.

Stable vesicles suitable for metabolite screening could not be reproducibly obtained under conditions comparable to those used for the cyclic guanidinium system.

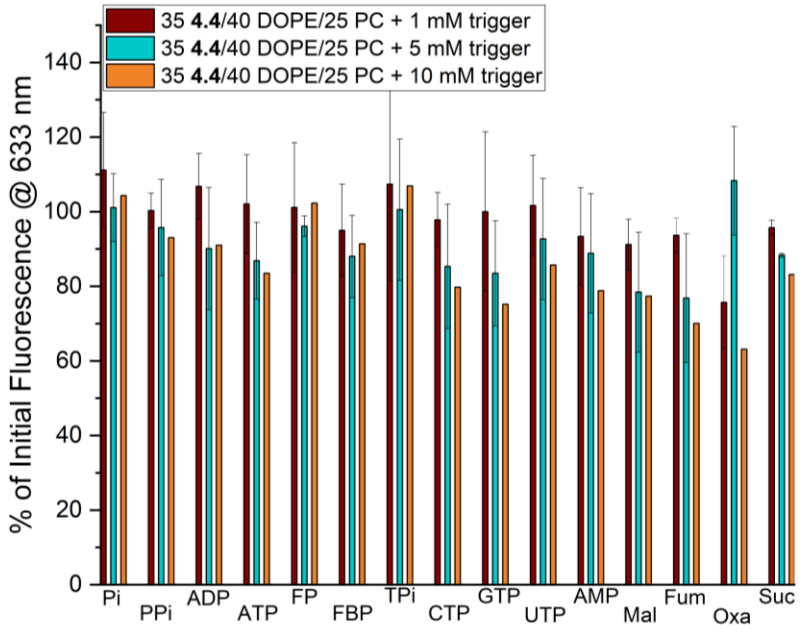

Figure 4.9. Metabolite selectivity screening through NR release for QA 4.4. Nile red release with **4.4** liposomes for selectivity screening over 24 hours with 1 mM, 5 mM, and 10 mM metabolite concentrations. No notable release was observed with any metabolites but rather generally increased cargo release with higher metabolite concentrations.

Both of these tested lipids highlight the importance of structural organization in membrane-active recognition motifs. Permanent positive charge without hydrogen bonding (QA **4.4**) failed to produce succinate-responsive behavior, while flexible guanidinium functionality compromised bilayer integrity. In contrast to these variants, the cyclic guanidinium design uniquely combined multidentate hydrogen bonding with conformational constraint, suggesting that both binding geometry and membrane compatibility are critical parameters for translating dicarboxylate recognition into lipid

bilayer perturbation.

4.5 Design of Thiourea Lipid Switch

In addition to the previous nitrogen-based headgroups, an additional nitrogen-based hydrogen-bond donor motif was explored as an alternative strategy for succinate recognition in the form of thiourea functionalization. Thiourea functional groups are well established in supramolecular chemistry as effective anion-binding motifs due to their ability to donate two directional hydrogen bonds to carboxylate and other oxyanion species.[205] Previous receptor systems have demonstrated selective recognition of dicarboxylate metabolites through thiourea-based binding pockets capable of stabilizing carboxylate pairs through cooperative hydrogen-bonding interactions.[192,206] These properties suggested that incorporation of a thiourea headgroup could provide an alternative mechanism for succinate-responsive membrane perturbation.

To investigate this possibility, a thiourea-functionalized lipid switch was designed using the same membrane-active scaffold employed throughout this chapter, allowing comparison of headgroup effects while maintaining consistent bilayer insertion and packing behavior. The synthetic route to the thiourea lipid is outlined in Scheme 4.4. Conversion of 5-bromosalicylaldehyde to intermediate **4.6** was achieved through oxime formation followed by Zn/HCl reduction. Subsequent Boc protection and selective deprotection produced **4.7**, which underwent Suzuki coupling with 4-(n-nonylphenyl)boronic acid to introduce the hydrophobic tail. Subsequent Williamson ether dimerization with 1,2-dibromoethane is planned to generate the dimeric lipid scaffold **4.9**. The final modification will involve Boc deprotection and reaction with 4-nitrophenyl

isothiocyanate to install the thiourea headgroup and yield thiourea lipid (TUL) switch **4.10**.

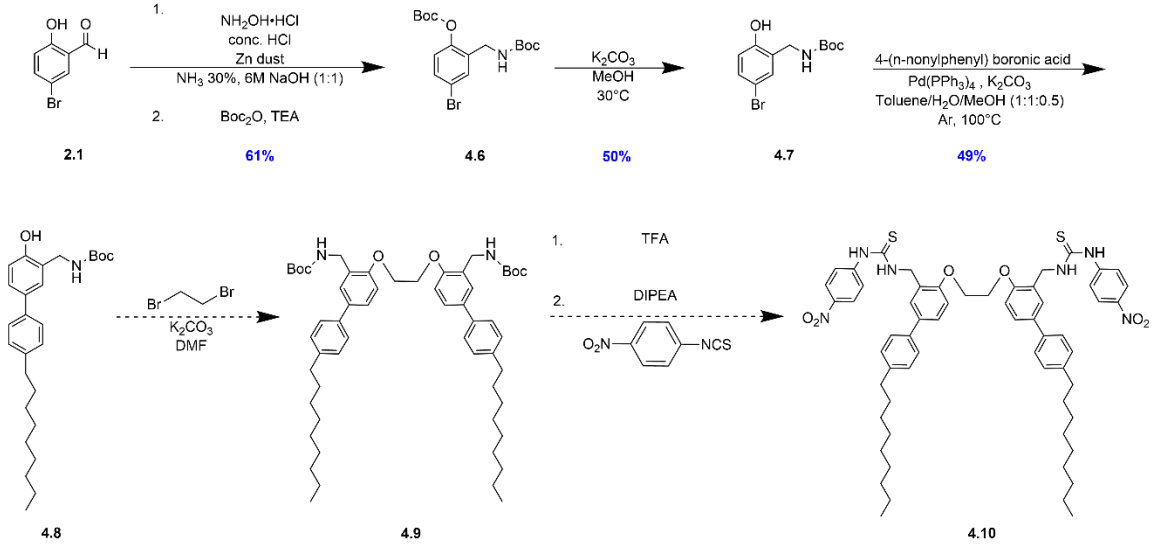

Scheme 4.4. Synthetic reaction scheme for TUL 4.10. Reduction of **2.1** was achieved through oxime formation by $NH_2OH \cdot HCl$ followed by reduction using Zn/HCl. Subsequent Boc protection generated **4.6**, where selective Boc deprotection of the benzyl alcohol was achieved with K2CO3 for **4.7**. A Suzuki coupling with 4-(n-nonylphenyl)boronic acid introduced the hydrophobic tail to yield **4.8**. Williamson ether dimerization using 1,2-dibromoethane is predicted to generate scaffold **4.9**. Subsequent headgroup modification including Boc deprotection with TFA to produce free amine before reacting with 4-nitrophenyl isothiocyanate is then planned to form the thiourea lipid switch **4.10**.

The thiourea lipid scaffold is still being actively developed and further evaluation of its membrane behavior and succinate responsiveness will be explored. As with the previously described headgroup variants, the design of this switch was motivated by the hypothesis that selective metabolite binding at the membrane interface could induce local changes in

packing interactions and membrane curvature. In the case of thiourea motifs, hydrogen-bonding interactions with dicarboxylate metabolites such as succinate may provide a complementary recognition mechanism to the electrostatic binding strategies explored with ammonium and guanidinium headgroups. Future studies evaluating liposome formulation, metabolite selectivity, and cargo release behavior will be necessary to determine whether thiourea-based headgroups can effectively translate dicarboxylate recognition into membrane perturbation.

4.6 Conclusions

This chapter explored the development of additional anion-binding, nitrogen-based lipid switches designed to expand metabolite responsiveness toward succinate and related dicarboxylates. By maintaining the conserved membrane-active scaffold and systematically varying headgroup functionality, we sought to begin isolating the structural features necessary to translate succinate recognition into membrane perturbation. Initial hydrophobic dye NR release studies suggested that incorporation of a CG headgroup could induce succinate-dependent membrane destabilization. Release behavior was sensitive to switch mol% and DOPE content, emphasizing that membrane organization and curvature stress play a critical role alongside headgroup binding interactions. Structural characterization with DLS and TEM supported the formation of stable liposomes prior to treatment and revealed succinate-induced aggregation and reorganization consistent with perturbation of bilayer packing. Subsequent synthetic reproducibility challenges, however, complicated definitive assignment of the cyclic guanidinium structure. Variations in spectroscopic data and difficulty reproducing the originally characterized material raised

the possibility that the active species may not have corresponded to the initially proposed headgroup.

Evaluation of alternative nitrogen-based headgroups such as quaternary ammonium and thiourea motifs further demonstrated that changes in charge distribution and hydrogen-bonding capacity significantly influence bilayer stability and release profiles. The results suggest that dicarboxylate-responsive membrane systems require precise geometric and electrostatic complementarity that may be more difficult to achieve within the dynamic bilayer environment than in solution-phase receptors. While a fully validated succinate-selective lipid switch was not conclusively established, the studies presented here clarify key design considerations for translating small-molecule anion recognition motifs into membrane-integrated systems. These insights provide a framework for future refinement of succinate and carboxylate-responsive lipid platforms.

4.7 Synthesis and Experimental Procedures

Reagents and solvents were generally purchased from Sigma-Aldrich or Fisher Scientific and used without further purification. PC (L-α-Phosphatidylcholine, mixed isomers from chicken egg), PA (L-α-phosphatidic acid, mixed isomers from chicken egg), and 18:1 (Δ9-Cis) PE (1,2-dioleoyl-*sn*-glycero-3-phosphoethanolamine) were purchased from Avanti Polar Lipids, Inc (Alabaster, AL). Dry solvents were obtained from a Pure Solv MD-7 solvent purification system purchased from Innovative Technology, Inc (Newburyport, MA). Column chromatography was performed using 230-400 mesh silica gel purchased from Sorbent Technologies. NMR spectra were obtained using a Bruker 500 MHz NMR spectrometer. Mass spectra were obtained with JEOL DART-Accustom mass

spectrometer. Liposome extruder and polycarbonate membranes were obtained from Avanti Polar Lipids, Inc (Alabaster, AL). Ultrapure water was purified via a Millipore water system (≥ 18 MW·cm triple water purification system). Small quantities (< 5 mg) were weighed on a Mettler Toledo XS105 dual range analytical balance. Osmotic pressure was measured with Wescor Vapor Pressure Osmometer 5520. Fluorescence studies were performed using a Cary Eclipse Fluorescence Spectrophotometer from Agilent Technologies. DLS analyses were carried out with a Malvern Zetasizer Nano ZS instrument equipped with a 4.0 mW laser operating at l = 633 nm. Confocal microscopy images were acquired using a Leica SP8 White Light Laser Confocal microscope (Wetzlar, Germany). Plots were generated using Origin Pro 2026b. All error bars in plots indicate the standard errors of at least three experimental replicates. Compounds **2.2**-**2.5** were synthesized as previously mentioned.

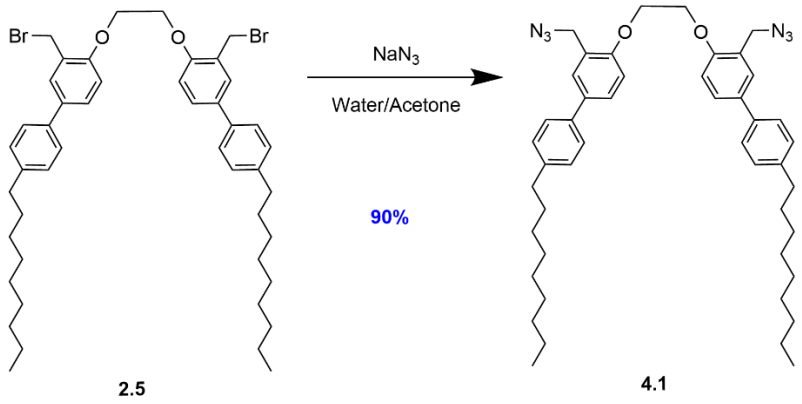

2.5 **4.1**

1,2-Bis((3-(azidomethyl)-4'-nonyl-[1,1'-biphenyl]-4-yl)oxy)ethane (4.1)

Compound **2.5** (0.0600 g, 0.0790 mmol) was dissolved in 50 mL of a 1:4 v/v water acetone mixture. While stirring, NaN_3 (0.0077 g, 0.1185 mmol) was added and the suspension was stirred vigorously for 24 hours. To separate the suspension, 10 mL of DCM

and 10 mL water were added. The aqueous layer was then extracted with 3 x 10 mL of DCM and the combined organic layers were washed with water and then dried over $MgSO_4$. The solution was filtered and concentrated under pressure, yielding the white azide product as sufficiently pure without further purification (0.0607 g, 0.0833 mmol, 90%). R_f = 0.72 (25% EtOAc-hexanes).

^{1}H NMR (500 MHz, $CDCl_3$) δ 7.57 (m, 3H), 7.47 (d, J = 8.3Hz, 3H), 7.25 (d, J = 9.0 Hz, 3H), 7.06 (d, J = 8.1 Hz, 1H), 4.62 (s, 2H),4.53 (s, 2H), 2.65 (t, J = 9.2 Hz, 3H), 1.65 (m, 4H), 1.35 (m, 7H), 1.29 (m, 16H), 0.90 (t, J = 7.2 Hz, 6H). ^{13}C NMR (126 MHz, CDCl3) δ 167.75, 155.84, 141.88, 137.47, 134.45, 129.61, 128.85, 128.53, 126.60, 112.61, 68.16, 67.30, 50.27, 38.74, 35.60, 31.91, 31.53, 29.55, 22.69, 14.06, 10.97. HRMS-DART: [M-$2N_2$ + $2H^+$]$^+$ calcd for $C_{46}H_{66}N_2O_2$: 679.04490, Found: 679.39773

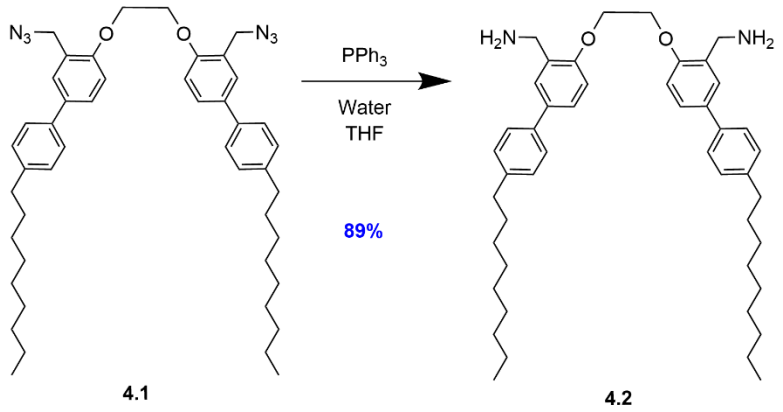

4.1 4.2

((Ethane-1,2-diylbis(oxy))bis(4'-nonyl-[1,1'-biphenyl]-4,3-diyl))dimethanamine (4.2)

Compound **4.1** (0.1611 g, 0.2210 mmol) was dissolved in 8 mL of THF:H_2O (3:1 v/v) under Ar. While stirring, PPh_3 (0.2900 g, 1.104 mmol) was added and the mixture was allowed to stir at rt for 24 hours. The mixture was concentrated under reduced pressure and purified via flash chromatography on an alumina column with a 0 to 100% MeOH gradient

in DCM, yielding the pale-yellow amine (0.1330 g, 0.1967 mmol, 89%). R_f = 0.22 (10% MeOH-DCM).

^{1}H NMR (500 MHz, $CDCl_3$) δ 7.82 (t, J = 7.6 Hz, 4H), 7.64-7.53 (m, 12H), 7.31 (t, J = 2.2 Hz, 2H), 6.95 (d, J = 8.9 Hz, 2 H), 4.87 (s, 4H), 3.62 (s, 3H), 2.62 (t, J = 7.5 Hz, 4H), 1.63 (t, J = 6.5 Hz, 4H), 1.33 (m, 8H), 1.29 (m, 16H), 0.88 (t, J = 7.5 Hz, 6H). ^{13}C NMR (126 MHz, CDCl3) δ 142.27, 136.60, 135.05, 134.07, 130.23, 130.13, 129.02, 126.43, 118.49, 117.81, 77.39, 77.13, 76.88, 68.09, 35.66, 32.00, 31.62, 29.80, 29.68, 29.65, 29.45, 22.78, 14.22, 0.09. HRMS-DART: [M- $2N_2$ + $2H^+$]$^+$ calcd for $C_{46}H_{66}N_2O_2$: 679.04490, Found: 679.39773

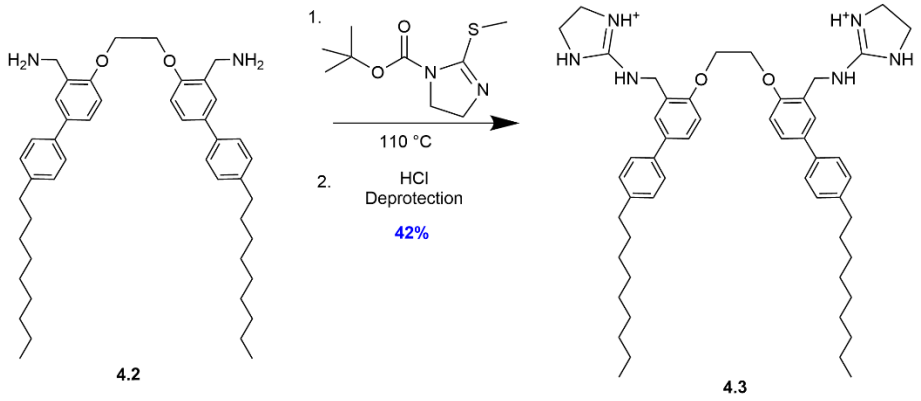

2,2'-((((ethane-1,2-diylbis(oxy))bis(4'-nonyl-[1,1'-biphenyl]-4,3-diyl))bis(methylene))bis(azanediyl))bis(4,5-dihydro-1H-imidazol-3-ium) (4.3)

2-Methylthio-2-imidazoline (MTI) was protected with di-tert-butyl dicarbonate (Boc) in THF:H_2O (1:1 v/v) at ambient temperature. The solution was stirred for 20 hours until starting material was consumed. Compound **4.2** (0.0500 g, 0.07390 mmol) and protected MTI (0.0639 g, .2954 mmol) were added to an Ar purged pressure reactor and heated to melting while stirring at 110 °C, later increased to 130° C two hours later. Melted

compounds were left to stir at 130 °C for 24 hours before redissolving material in DCM. The dissolved compounds were then concentrated under reduced pressure and purified via column chromatography on an alumina column with a 0 to 10% MeOH in DCM gradient to yield protected **4.3**. Protected **4.3** was then deprotected with 6 mL of 1:1 v/v conc. HCl and MeOH, stirring 24-48 hours until fully deprotected. Sample was then concentrated under reduced pressure to yield **4.3** (0.0251g, 0.0308 mmol, 42%). R_f = 0.62 in 10% MeOH in DCM.

^{1}H NMR (500 MHz, $CDCl_3$) δ 7.70 (m, 2H), 7.50 (m, 8H), 7.12 (m, 4H), 4.88 (s, 2H), 4.12 (s, 8H), 3.56 (m, 2H), 3.27 (m, 2H), 2.56 (t, J = 7.7 Hz, 2H), 1.26 (m, 8H), 1.20 (m, 16H), 0.80 (t, J = 7.2 Hz, 6H). ^{13}C NMR (126 MHz, $CDCl_3$) δ 167.74, 156.31, 142.15, 136.45, 135.07, 134.07, 132.46, 130.88, 130.31, 128.91, 126.37, 118.42, 117.74, 113.71, 68.15, 38.74, 35.56, 31.89, 31.50, 30.37, 29.57, 29.33, 28.92, 23.75, 22.97, 22.67, 14.11, 10.95. HRMS DART: $[M/2]^+$ calcd for $C_{52}H_{74}N_6O_2^{+2}$: 407.2931, Found: 407.2902

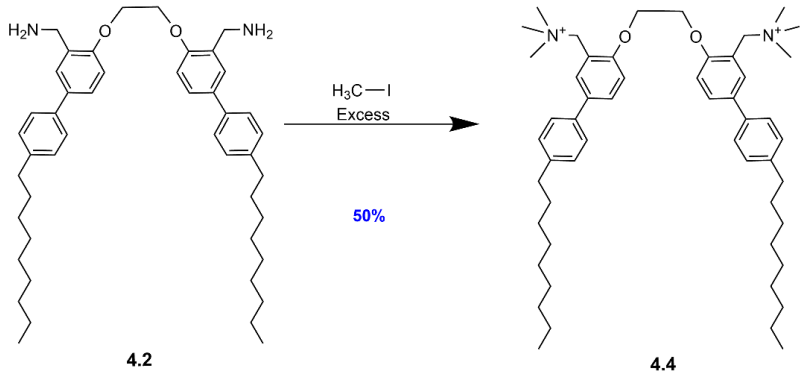

4.2 4.4

1,1'-((Ethane-1,2-diylbis(oxy))bis(4'-nonyl-[1,1'-biphenyl]-4,3-diyl))bis(N,N,N-trimethylmethanaminium) (4.4)

Compound **4.2** (0.0200 g, 0.02956 mmol) and iodomethane (0.0504 g, 0.3547mmol) were added to a 50 mL RBF under Ar, dissolved in 10 mL of MeOH, and stirred for 24

hours, followed by additions of iodomethane until reaction completion was determined by TLC. Iodomethane was then quenched with NaOH, followed by washing the aqueous layer with 10 mL DCM until TLC confirmed all product was removed. The organic layer was then concentrated under reduced pressure to yield **4.4** (0.0120 g, 0.0157 mmol, 50%). Rf = 0.80 (10% EtOAc/hexanes), alumina.

^{1}H NMR (500 MHz, $CDCl_3$) δ 7.56-7.51 (m, 14H), 7.44-7.39 (m, 11H), 7.31 (s, 2H), 7.15 (d, J = 8.4 Hz), 4.33 (s, 2H), 4.18 (s, 16H), 3.28 (m, 2H), 2.55 (t, J = 7.6 Hz, 2H), 2.21 (s, 4H), 1.86 (s, 2H), 1.23 (m, 28H), 0.80 (t, J = 6.7 Hz, 6H). ^{13}C NMR (126 MHz, $CDCl_3$) δ 136.31, 135.89, 135.81, 134.89, 133.29, 132.67, 132.57, 130.42, 129.02, 115.76, 71.09, 53.00, 52.83, 52.66, 52.49, 52.32, 52.15, 39.41, 35.75, 35.39, 33.52, 33.40, 33.19, 26.51, 20.13, 17.81. HRMS-DART: [M/2 – $2CH_3$+$2H^+$]: calcd for $C_{50}H_{74}N_2O_2^{+2}$: 367.2870, Found: 367.3552

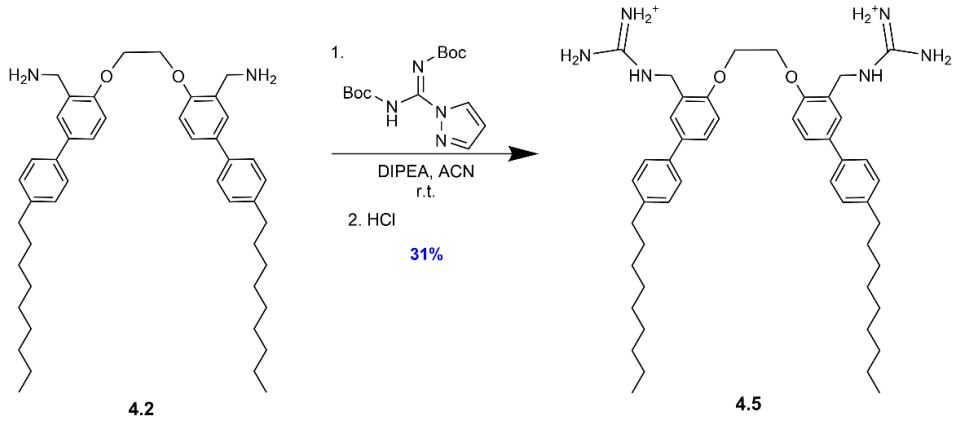

((((Ethane-1,2-diylbis(oxy))bis(4'-nonyl-[1,1'-biphenyl]-4,3-diyl))bis(methylene))bis(azanediyl))bis(aminomethaniminium) (4.5)

N,N'-Di-Boc-1*H*-pyrazole-1-carboxamidine (0.5734 g, 0.1848 mmol) and DIPEA (32.19 µL, 0.1848 mmol) were added to an Ar purged RBF and dissolved in 5 mL of ACN.

Compound **4.2** (0.0500 g, 0.07391 mmol) was then added and solution was stirred at rt for 28 hours. Heat was then increased to 60°C and refluxed for 72 hours. The solution was then concentrated under reduced pressure and purified via column chromatography on silica with a 0 to 25% gradient of EtOAc in hexanes to yield **4.5**-Boc. R_f = 0.54 (10% EtOAc/hexanes). All **4.5**-Boc was then dissolved in 6 mL of 1:1 (v/v) conc. HCl:MeOH for 24-48 hours until deprotection was complete. The solution was then concentrated under reduced pressure, yielding **4.5** (0.0175 g, 0.02293 mmol, 31%). R_f = 0.73 (25% EtOAc/hexanes)**.**

^{1}H NMR (500 MHz, $CDCl_3$) δ 7.56-7.50 (m, 4H), 7.42 (t, 7.0 Hz, 2H), 7.08 (s, 1H), 6.94 (s, 1H), 6.83 (d, J = 16.1 Hz, 2H), 6.61 (s, 1H), 6.50 (s, 1H), 3.77 (s, 4H), 3.71 (s, 4H), 2.18 (s, 4H), 2.13 (d, J = 7.9 Hz, 8H), 1.34 (s, 16H), 1.30 (s, 24H), 1.18 (s, 24H), 0.8 (m, 6H), 0.64 (m, 4H). ^{13}C NMR (126 MHz, $CDCl_3$) δ 142.23, 141.95, 137.32, 136.37, 135.89, 135.82, 132.69, 132.59, 132.41, 131.36, 130.22, 38.70, 38.42, 35.55, 34.22, 34.15, 33.79, 33.63, 33.59, 33.51, 26.50, 24.59. HRMS-DART: $[M/2 + 2H^+]^+$ calcd for $C_{48}H_{70}N_6O_2^{+2}$: 383.57495, Found: 383.92243

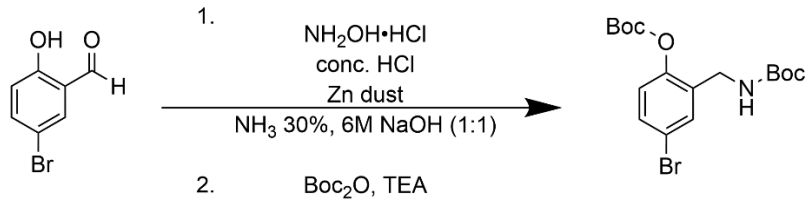

2.1 **61%** **4.6**

Tert-butyl (5-bromo-2-((tert-butoxycarbonyl)oxy)benzyl)carbamate (4.6)

5-bromo-2-hydroxybenzaldehyde (0.200 g, 0.9949 mmol) and hydroxylamine hydrochloride (0.0830 g, 1.19 mmol) were added to an Ar purged RBF and dissolved in 5

mL of ethanol at rt for 2 hours. Concentrated HCl (0.3416 mL, 4.13 mmol) and zinc dust (0.1626 g, 2.487 mmol) were then slowly added and the resulting slurry was stirred for 30 minutes. Ammonia (30%, 0.3 mL, 4.40 mmol) and NaOH (6M, 0.3 mL, 1.80 mmol) were mixed and slowly added to the reaction, followed by stirring for an additional 30 minutes. The reaction solution was then concentrated under reduced pressure, redissolved with ethyl acetate and 1 mL H_2O, with aqueous layer extracted 3x with ethyl acetate. The organic layer was then dried with Na_2SO_4, filtered, and concentrated under reduced pressure. The resulting crude was then redissolved in 10 mL DCM with di-tert-butyl dicarbonate (0.6270 g, 3.872 mmol) and TEA (0.416 mL, 2.985 mmol) and stirred for 2 hours. Water was then added to the reaction, followed by extraction of the aqueous with DCM. Brine (50 mL) was then added and the organic was dried over Na_2SO_4 and filtered. The solution was then concentrated under reduced pressure and purified via column chromatography on silica with a 0 to 25% gradient of EtOAc in hexanes to yield **4.6** (0.2337 g, 0.6069 mmol, 61%). R_f = 0.28 (10% EtOAc/hexanes). ^{1}H NMR (500 MHz, $CDCl_3$) δ 7.41 (s, 1H), 7.29 (d, J = 8.5 Hz, 1H), 6.92 (d, J = 8.4 Hz, 1H), 4.96 (s, 1H), 4.16 (s, 2H), 1.46 (s, 9H), 1.36 (s, 9H). ^{13}C NMR (126 MHz, $CDCl_3$) δ 155.74, 151.41, 148.05, 133.26, 132.20, 131.42, 123.78, 119.30, 84.15, 79.64, 39.26, 28.36, 27.61. HRMS-DART: $[M - 2C_4H_9 - CO]^-$ calcd for $C_1H_{24}BrNO_5$: 227.9665, Found: 227.83130

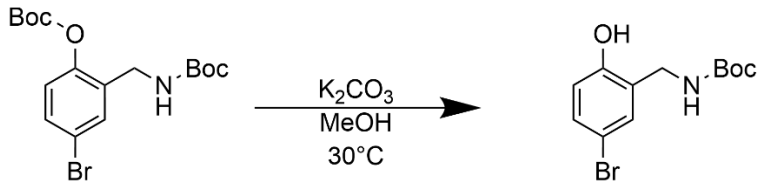

4.6 **50%** **4.7**

Tert-butyl (5-bromo-2-hydroxybenzyl)carbamate (4.7)

4.6 (0.9796 g, 2.543 mmol) and K_2CO_3 (1.758 g, 12.72 mmol) were added to an Ar purged RBF and dissolved in 10 mL of ethyl acetate at 30°C overnight. 50 mL of H_2O was then added, followed by extraction of the aqueous with ethyl acetate. Brine was then added to the organic, followed by drying over Na_2SO_4 and filtered. The solution was then concentrated under reduced pressure and purified via column chromatography on silica with a 0 to 25% gradient of EtOAc in hexanes to yield **4.7** (0.3843 g, 1.272 mmol, 50%). R_f = 0.16 (10% EtOAc/hexanes).

^{1}H NMR (500 MHz, $CDCl_3$) δ 9.04 (s, 1H), 7.19 (d, J = 8.5 Hz, 1H), 7.17 (s, 1H), 6.73 (d, J = 8.4 Hz, 1H), 5.32 (s, 1H), 4.09 (d, J = 6.8 Hz, 2H), 1.36 (s, 9H). ^{13}C NMR (126 MHz, $CDCl_3$) δ 158.49, 154.90, 132.96, 132.37, 127.10, 119.56, 111.45, 81.53, 40.79, 28.30. HRMS-DART: $[M- CO_2C(CH_3)_3-H]^+$ calcd for $C_{12}H_{16}BrNO_3$: 199.9717, Found: 199.6959.

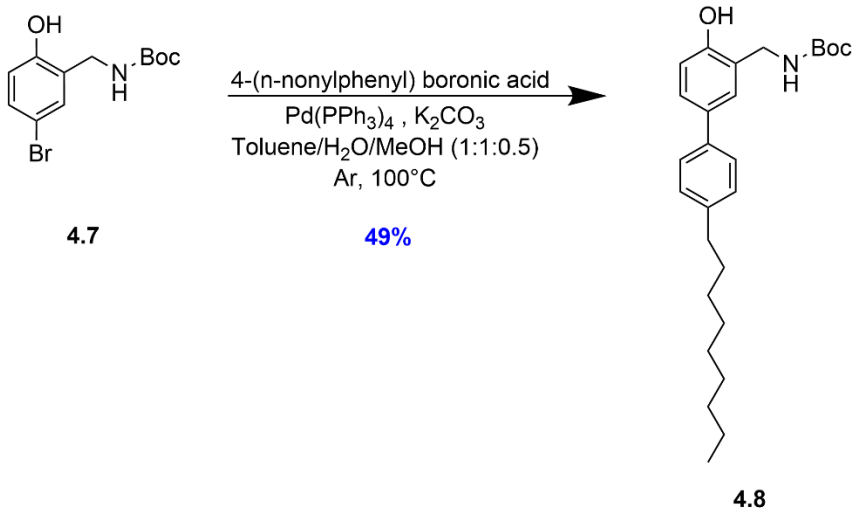

4.7 **49%** **4.8**

Tert-butyl ((4-hydroxy-4'-nonyl-[1,1'-biphenyl]-3-yl)methyl)carbamate (4.8)

4.7 (0.250 g, 2.65 mmol), 4-(*n*-nonylphenyl) boronic acid (0.3080 g, 2.48 mmol), tetrakis(triphenylphosphine)palladium(0) (0.0095 g, 0.0165 mmol) and potassium

carbonate (0.1715 g, 2.48 mmol) were combined in a 100 mL RBF under argon. After being dissolved with 25 mL toluene/H_2O/MeOH (2/2/1, v/v), the reaction mixture was heated at 100 ºC overnight (10.5 hours). After completion, the reaction was cooled to rt and concentrated under reduced pressure. The residue was re-dissolved in 25 mL DCM and washed with 10 mL of 0.5 M HCl, followed by the addition of 50 mL water. The aqueous layer was extracted with 3x DCM. The combined organic layer was further washed with 1 x 50 mL water and 1 x 50 mL brine, respectively, before being dried over Na_2SO_4 , filtered, and concentrated under reduced pressure. The crude was next loaded onto silica gel and subjected to column chromatography. Gradient elution from hexanes to 20% ethyl acetate in hexanes yielded **4.8** as a white solid (0.1719 g, 0.4042 mmol, 49%). R_f = 0.61 (25% EtOAc/hexanes).

^{1}H NMR (500 MHz, $CDCl_3$) δ 8.90 (s, 1H), 7.34 (d, J = 8.0 Hz, 3H), 7.17 (s, 1H), 7.11 (d, J = 8.0 Hz, 2H), 6.90 (d, J = 7.7 Hz, 1H), 5.24 (s, 1H), 4.17 (d, J = 6.8 Hz, 2H), 2.53 (t, J = 7.5 Hz, 2H), 1.53 (p, J = 6.7 Hz, 2H), 1.36 (s, 9H), 1.21 (m, 12H), 0.80 (t, J = 7.0 Hz, 3H). ^{13}C NMR (126 MHz, $CDCl_3$) δ 158.50, 155.12, 141.43, 138.06, 133.08, 129.18, 128.79, 128.29, 126.49, 125.12, 118.05, 81.30, 41.49, 35.61, 31.94, 31.55, 29.60, 29.37, 28.34, 22.71, 14.15. HRMS-DART: $[M-H]^-$ calcd for $C_{27}H_{39}NO_3$: 424.2857, Found: 424.3397

Preparation of liposomes for NR release assays

Stock solutions of **4.3, 4.4** or **4.5** were prepared at 19.93 mM, 5mM, and 5 mM, respectively, in $CHCl_3$/MeOH solution (1/1, v/v), along with stock solutions of 32.46 mM PC, 33.60 mM DOPE, and 5 mM Nile red (NR) solutions prepared in chloroform. All the

stock solutions were kept in a -20 °C freezer after preparation. To prepare liposomes through thin film hydration, appropriate volumes of each stock solution were pipetted in 0.5 dr vials to reach a total lipid concentration of 2 mM, with desired percentages of each lipid type. NR was added as an extra 5% of the total lipid content. The organic solvents were then evaporated under a nitrogen stream, and the resulting lipid films were kept under vacuum for at least one hour. The films were then hydrated with proper volumes of 1x TBS buffer, (pH = 7.4) in a 60 °C water bath for 1 hr. The vials were vortexed every 15 minutes while incubating. Next, 10 freeze-thaw cycles were performed in a dry ice-acetone bath and 60 °C water bath. Lastly, the liposome solutions were extruded through a 200 nm polycarbonate membrane for 21 passes with an extruder purchased from either Avestin or Avanti. The resulting liposomes were then studied immediately.

Phosphorylated and carboxylate metabolite selectivity screen for liposome NR release

50 mM stock solutions of each metabolite were prepared by dissolving the reagents Pi, $Na_2HPO_4 \cdot 7H_2O$; PPi, $Na_2H_2P_2O_7$; ADP; ATP; FP; FBP; TPi; CTP; GTP; UTP, AMP, Mal, Fum, Oxa, Suc; with MilliQ water. For each study, 56 μL of liposome solution encapsulating NR was first added into a sub-micro quartz cuvette. After an initial scan, 14 μL of 50 mM stock solution of the metabolite under study was added to the cuvette (final concentration = 10 mM). Samples were incubated for 16 hours at rt, and fluorescence intensities were recorded after incubation (excitation wavelength = 552 nm, excitation slit = 5 nm, emission slit = 5 nm). Control experiments were run by adding 14 μL of 1x TBS. When processing the data, the fluorescence intensities at 635 nm were selected and converted to percentage of the initial fluorescence before metabolite addition. Experiments

were run at least three times with different batches of liposomes. Averaged data were reported with error bars denoting standard error.

NR kinetic release assays

A 300 mM stock solution of Suc was prepared. For each study, 68 μL of liposome solution encapsulating NR was first added into a sub-micro quartz cuvette. After an initial scan, 2.03 μL of the 300 mM stock solution of the metabolite under study was added to the cuvette (final concentration = 10 mM). Samples were then capped, sealed, and measured continuously for 16 hours with measurements every 15 or 30 minutes. Control experiments were run by adding 2.03 μL of 1x TBS buffer, or by treating 0% **4.3** liposomes with 2.03 μL of the stock solutions. When processing the data, the fluorescence intensities at 635 nm were selected and converted to percentage of initial fluorescence before metabolite addition. Experiments were run at least three times with different batches of liposomes. Averaged data were reported with error bars denoting standard error.

DLS analysis of liposomes before and after triggered release

DLS measurements were performed with a Malvern Zetasizer Nano ZS instrument with a 4.0 mW laser at I = 633 nm. Samples were prepared by diluting liposomes by 10x (5 μL liposomes, 45 μL buffer). All measurements were taken at a scattering angle of 173° at 20 °C. Bar graphs were made by averaging at least three experiments, with error bars denoting standard error.

Transmission electron microscope analysis

Liposomes were prepared at 4 μg/mL without any dye encapsulation using the standard thin film hydration procedure described above. For TEM studies, droplets of the liposome

solution were placed on a sheet of parafilm (10 μL). For treated liposomes, appropriate volumes of 300 mM Suc stock were added to the liposome solutions before droplets were placed on the parafilm. Thin carbon films supported by 200 mesh copper grids were placed face down onto the droplets and allowed to soak for 1 minute. The grids were then removed from the droplet and blotted. Droplets of dH_2O were then placed on the parafilm, where the grids were briefly placed (10 seconds) to rinse before removal and blotting. Droplets of 1% uranyl acetate were next placed on the parafilm sheet, followed by another 1-minute soak of the grids and blotting. Grids were allowed to air dry for 2 hours. Images were taken using a JOEL 1400 Flash microscope with a beam energy of 80 keV. Images were taken with a Gaten One View camera and processed with ImageJ software.

Confocal Microscopy Fluorescence Studies

Liposomes with 35/40/25 **4.3**/DOPE/PC labelled with 0.08% Rd-PE in 1x TBS buffer (pH = 7.4, 25 mM Tris/Tris-HCl, 0.13 M NaCl, 0.0027 M KCl) were prepared using the same thin-film hydration procedures described above. An aliquot of the liposome solutions (200 μL) was first added into a FluoroDish Cell Cultures Dish and allowed to settle for 15 minutes before imaging using a 63x 1.4NA oil objective. Rd-PE was excited using a 561 nm laser line and the emission was collected between 566-620 nm. After imaging initial liposomes for 15m, 50 mM Suc was added to the cell culture dish from a corner. We then generated a time-course video and still images from the experiment.

CHAPTER 5.

CONCLUSIONS

This dissertation examines the design of chemically responsive lipid systems that convert molecular recognition into membrane perturbation and controlled cargo release. Although liposomal formulations have reached clinical use, most rely on passive leakage or externally applied triggers. The work presented here moves beyond that framework by embedding chemical responsiveness directly within membrane components, allowing liposomes to react to endogenous biochemical signals associated with disease.

In Chapter 2, a metabolite-responsive lipid switch was integrated into DOPE/PC bilayers to couple nucleotide binding with measurable membrane disruption. Incorporation of the BPLS headgroup enabled GTP- and TPi-dependent changes in size, surface charge, and cargo release. Selectivity did not arise from binding affinity alone, but instead, membrane composition proved to be a decisive factor. Adjusting BPLS and DOPE content altered curvature stress and lateral organization, ultimately tuning responsiveness between structurally similar metabolites. These findings highlight that molecular recognition may be amplified through bilayer mechanics to produce functional cargo release.

A different strategy was pursued in Chapter 3. Rather than relying on conformational switching, a boronate-containing self-immolative linker was embedded within a lipid–Dox conjugate to achieve ROS-triggered cleavage directly inside the liposomal membrane. This design enabled covalent drug loading while preserving liposomal stability under non-oxidative conditions. ESI-MS confirmed oxidative release of Dox and liposomal characterization showed that activation did not require large-scale membrane

destabilization. Cellular studies further demonstrated that endogenous ROS levels were sufficient to trigger prodrug activation, even in A375 cells with comparatively modest basal oxidative stress. These results illustrate how membrane-integrated prodrugs can merge liposomal pharmacokinetics with chemically selective activation.

Chapter 4 shifted the focus towards the development of lipid switches with dicarboxylate recognition, particularly succinate. A conserved membrane scaffold was retained while anion-binding headgroups were systematically varied to probe structure–function relationships. The cyclic guanidinium variant initially showed succinate-responsive aggregation and dye release behavior. However, difficulties in synthetic reproducibility and structural assignment required careful mechanistic reassessment. These experiments highlight the challenges of translating supramolecular binding motifs into membrane-embedded systems. Even where ambiguity remained, the work clarified how headgroup chemistry and membrane composition intersect to govern metabolite-triggered perturbation.

Across all chapters, several principles emerge. Membrane composition acts as a programmable parameter that can amplify or suppress binding events. Head group interactions must couple to curvature stress or packing frustration to achieve release. Chemical activation strategies embedded within lipid scaffolds allow selective therapeutic liberation while preserving nanoparticle stability. Finally, successful design of responsive systems requires careful alignment between trigger sensitivity and physiologically relevant concentration windows, as endogenous metabolite and ROS levels vary across disease states and cellular contexts.

Overall, these studies support the use of lipid membranes as responsive materials rather than passive carriers. Through integration of supramolecular binding, self-immolative chemistry, and bilayer mechanics, this work advances the design of liposomal systems capable of selective activation in diseased environments. Continued refinement of headgroup chemistry, improved structural validation, and *in vivo* evaluation will further define the translational potential of these systems. Through rational molecular design paired with systematic membrane-level analysis, this work contributes to the development of programmable lipid platforms for selective therapeutic delivery.

LIST OF REFERENCES

(1) Marsh, D. Thermodynamics of Phospholipid Self-Assembly. *Biophys J* **2012**, *102* (5), 1079–1087. https://doi.org/10.1016/j.bpj.2012.01.049.

(2) Serhan, C. N.; Haeggström, J. Z.; Leslie, C. C. Lipid Mediator Networks in Cell Signaling: Update and Impact of Cytokines[1]. *The FASEB Journal* **1996**, *10* (10), 1147–1158. https://doi.org/10.1096/fasebj.10.10.8751717.

(3) Gurr, M. I.; Harwood, J. L. Lipids as Energy Stores. In *Lipid Biochemistry: An Introduction*; Gurr, M. I., Harwood, J. L., Eds.; Springer US: Boston, MA, 1991; pp 119–161. https://doi.org/10.1007/978-1-4615-3862-2_4.

(4) van Meer, G.; Voelker, D. R.; Feigenson, G. W. Membrane Lipids: Where They Are and How They Behave. *Nat Rev Mol Cell Biol* **2008**, *9* (2), 112–124. https://doi.org/10.1038/nrm2330.

(5) Welte, M. A.; Gould, A. P. Lipid Droplet Functions beyond Energy Storage. *Biochimica et Biophysica Acta (BBA) - Molecular and Cell Biology of Lipids* **2017**, *1862* (10, Part B), 1260–1272. https://doi.org/10.1016/j.bbalip.2017.07.006.

(6) Jové, M.; Mota-Martorell, N.; Obis, È.; Sol, J.; Martín-Garí, M.; Ferrer, I.; Portero-Otín, M.; Pamplona, R. Lipid Adaptations against Oxidative Challenge in the Healthy Adult Human Brain. *Antioxidants (Basel)* **2023**, *12* (1), 177. https://doi.org/10.3390/antiox12010177.

(7) Moullé, V. S.; Cansell, C.; Luquet, S.; Cruciani-Guglielmacci, C. The Multiple Roles of Fatty Acid Handling Proteins in Brain. *Front. Physiol.* **2012**, *3*. https://doi.org/10.3389/fphys.2012.00385.

(8) Fahy, E.; Cotter, D.; Sud, M.; Subramaniam, S. Lipid Classification, Structures and Tools. *Biochimica et Biophysica Acta (BBA) - Molecular and Cell Biology of Lipids* **2011**, *1811* (11), 637–647. https://doi.org/10.1016/j.bbalip.2011.06.009.

(9) Fahy, E.; Subramaniam, S.; Brown, H. A.; Glass, C. K.; Merrill Jr., A. H.; Murphy, R. C.; Raetz, C. R. H.; Russell, D. W.; Seyama, Y.; Shaw, W.; Shimizu, T.; Spener, F.; van Meer, G.; VanNieuwenhze, M. S.; White, S. H.; Witztum, J. L.; Dennis, E. A. A Comprehensive Classification System for Lipids. *European Journal of Lipid Science and Technology* **2005**, *107* (5), 337–364. https://doi.org/10.1002/ejlt.200405001.

(10) Demel, R. A.; De Kruyff, B. The Function of Sterols in Membranes. *Biochimica et Biophysica Acta (BBA) - Reviews on Biomembranes* **1976**, *457* (2), 109–132. https://doi.org/10.1016/0304-4157(76)90008-3.

(11) Cooper, G. M. Structure of the Plasma Membrane. In *The Cell: A Molecular Approach. 2nd edition*; Sinauer Associates, 2000.

(12) Blanco, A.; Blanco, G. Chapter 11-Membranes. In *Medical Biochemistry*; 2017; pp 215–250. https://doi.org/10.1016/B978-0-12-803550-4.00011-2.

(13) Alberts, B.; Johnson, A.; Lewis, J.; Raff, M.; Roberts, K.; Walter, P. The Lipid Bilayer. In *Molecular Biology of the Cell. 4th edition*; Garland Science, 2002.

(14) Eibl, H. Phospholipids as Functional Constituents of Biomembranes. *Angewandte Chemie International Edition in English* **1984**, *23* (4), 257–271. https://doi.org/10.1002/anie.198402573.

(15) van der Veen, J. N.; Kennelly, J. P.; Wan, S.; Vance, J. E.; Vance, D. E.; Jacobs, R. L. The Critical Role of Phosphatidylcholine and Phosphatidylethanolamine Metabolism in Health and Disease. *Biochimica et Biophysica Acta (BBA) - Biomembranes* **2017**, *1859* (9, Part B), 1558–1572. https://doi.org/10.1016/j.bbamem.2017.04.006.

(16) Cockcroft, S. Mammalian Lipids: Structure, Synthesis and Function. *Essays Biochem* **2021**, *65* (5), 813–845. https://doi.org/10.1042/EBC20200067.

(17) Madrid, E.; Horswell, S. L. Effect of Headgroup on the Physicochemical Properties of Phospholipid Bilayers in Electric Fields: Size Matters. *Langmuir* **2013**, *29* (5), 1695–1708. https://doi.org/10.1021/la304455d.

(18) Janmey, P. A.; Stossel, T. P. Gelsolin-Polyphosphoinositide Interaction. *Journal of Biological Chemistry* **1989**, *264* (9), 4825–4831. https://doi.org/10.1016/S0021-9258(18)83665-1.

(19) Pande, A. H.; Qin, S.; Tatulian, S. A. Membrane Fluidity Is a Key Modulator of Membrane Binding, Insertion, and Activity of 5-Lipoxygenase. *Biophysical Journal* **2005**, *88* (6), 4084–4094. https://doi.org/10.1529/biophysj.104.056788.

(20) Seu, K. J.; Cambrea, L. R.; Everly, R. M.; Hovis, J. S. Influence of Lipid Chemistry on Membrane Fluidity: Tail and Headgroup Interactions. *Biophysical Journal* **2006**, *91* (10), 3727–3735. https://doi.org/10.1529/biophysj.106.084590.

(21) Komura, S.; Andelman, D. Physical Aspects of Heterogeneities in Multi-Component Lipid Membranes. *Advances in Colloid and Interface Science* **2014**, *208*, 34–46. https://doi.org/10.1016/j.cis.2013.12.003.

(22) Starke, L. J.; Allolio, C.; Hub, J. S. Pore Formation in Complex Biological Membranes: Torn between Evolutionary Needs. bioRxiv May 8, 2024, p 2024.05.06.592649. https://doi.org/10.1101/2024.05.06.592649.

(23) Israelachvili, J. N.; Mitchell, D. J.; Ninham, B. W. Theory of Self-Assembly of Lipid Bilayers and Vesicles. *Biochimica et Biophysica Acta (BBA) - Biomembranes* **1977**, *470* (2), 185–201. https://doi.org/10.1016/0005-2736(77)90099-2.

(24) Sun, C.; Hanasaka, A.; Kashiwagi, H.; Ueno, M. Formation and Characterization of Phosphatidylethanolamine/Lysophosphatidylcholine Mixed Vesicles. *Biochimica et Biophysica Acta (BBA) - Biomembranes* **2000**, *1467* (1), 18–26. https://doi.org/10.1016/S0005-2736(00)00192-9.

(25) Watson, H. Biological Membranes. *Essays Biochem* **2015**, *59*, 43–69. https://doi.org/10.1042/bse0590043.

(26) Kumar, V. V. Complementary Molecular Shapes and Additivity of the Packing Parameter of Lipids. *Proceedings of the National Academy of Sciences* **1991**, *88* (2), 444–448. https://doi.org/10.1073/pnas.88.2.444.

(27) Finer, E. G.; Phillips, M. C. Factors Affecting Molecular Packing in Mixed Lipid Monolayers and Bilayers. *Chemistry and Physics of Lipids* **1973**, *10* (3), 237–252. https://doi.org/10.1016/0009-3084(73)90004-2.

(28) Khalil, R. A.; Zarari, A. A. Theoretical Estimation of the Critical Packing Parameter of Amphiphilic Self-Assembled Aggregates. *Applied Surface Science* **2014**, *318*, 85–89. https://doi.org/10.1016/j.apsusc.2014.01.046.

(29) Larsen, J. B.; Kennard, C.; Pedersen, S. L.; Jensen, K. J.; Uline, M. J.; Hatzakis, N. S.; Stamou, D. Membrane Curvature and Lipid Composition Synergize To Regulate N-Ras Anchor Recruitment. *Biophys J* **2017**, *113* (6), 1269–1279. https://doi.org/10.1016/j.bpj.2017.06.051.

(30) Mouritsen, O. G. Lipids, Curvature, and Nano-Medicine. *Eur J Lipid Sci Technol* **2011**, *113* (10), 1174–1187. https://doi.org/10.1002/ejlt.201100050.

(31) Lasic, D. Liposomes. *American Scientist* **1992**, *80* (1), 20–31.

(32) Bozzuto, G.; Molinari, A. Liposomes as Nanomedical Devices. *International Journal of Nanomedicine* **2015**, *10*, 975–999. https://doi.org/10.2147/IJN.S68861.

(33) Montes, L.-R.; Alonso, A.; Goñi, F. M.; Bagatolli, L. A. Giant Unilamellar Vesicles Electroformed from Native Membranes and Organic Lipid Mixtures under Physiological Conditions. *Biophys J* **2007**, *93* (10), 3548–3554. https://doi.org/10.1529/biophysj.107.116228.

(34) Akbarzadeh, A.; Rezaei-Sadabady, R.; Davaran, S.; Joo, S. W.; Zarghami, N.; Hanifehpour, Y.; Samiei, M.; Kouhi, M.; Nejati-Koshki, K. Liposome: Classification, Preparation, and Applications. *Nanoscale Res Lett* **2013**, *8* (1), 102. https://doi.org/10.1186/1556-276X-8-102.

(35) Doskocz, J.; Dałek, P.; Foryś, A.; Trzebicka, B.; Przybyło, M.; Mesarec, L.; Iglič, A.; Langner, M. The Effect of Lipid Phase on Liposome Stability upon Exposure to the Mechanical Stress. *Biochimica et Biophysica Acta (BBA) - Biomembranes* **2020**, *1862* (9), 183361. https://doi.org/10.1016/j.bbamem.2020.183361.

(36) Wunderlich, B.; Leirer, C.; Idzko, A.-L.; Keyser, U. F.; Wixforth, A.; Myles, V. M.; Heimburg, T.; Schneider, M. F. Phase-State Dependent Current Fluctuations in Pure Lipid Membranes. *Biophys J* **2009**, *96* (11), 4592–4597. https://doi.org/10.1016/j.bpj.2009.02.053.

(37) De Gier, J.; Mandersloot, J. G.; Van Deenen, L. L. M. Lipid Composition and Permeability of Liposomes. *Biochimica et Biophysica Acta (BBA) - Biomembranes* **1968**, *150* (4), 666–675. https://doi.org/10.1016/0005-2736(68)90056-4.

(38) Kranenburg, M.; Smit, B. Phase Behavior of Model Lipid Bilayers. *J. Phys. Chem. B* **2005**, *109* (14), 6553–6563. https://doi.org/10.1021/jp0457646.

(39) Dua, J. S.; Rana, A. C.; Bhandari, D. A. K. LIPOSOME: METHODS OF PREPARATION AND APPLICATIONS.

(40) Nambiar, N. R.; Gaur, S.; Ramachandran, G.; Pandey, R. S.; M, S.; Nath, L. R.; Dutta, T.; Sudheesh, M. S. Remote Loading in Liposome: A Review of Current Strategies and Recent Developments. *Journal of Liposome Research* **2024**, *34* (4), 658–670. https://doi.org/10.1080/08982104.2024.2315449.

(41) Yamazaki, T.; Kamada, K.; Nakabayashi, K.; Sotoma, S.; Maeda, K.; Yoshida, Y. Active Loading and Release of Cationic Drugs into/from Cationic Liposomes by Utilizing a Concentration Gradient of NaCl. *Langmuir* **2025**, *41* (33), 22357–22364. https://doi.org/10.1021/acs.langmuir.5c02647.

(42) Haran, G.; Cohen, R.; Bar, L. K.; Barenholz, Y. Transmembrane Ammonium Sulfate Gradients in Liposomes Produce Efficient and Stable Entrapment of Amphipathic

Weak Bases. *Biochim Biophys Acta* **1993**, *1151* (2), 201–215. https://doi.org/10.1016/0005-2736(93)90105-9.

(43) Niu, G.; Cogburn, B.; Hughes, J. Preparation and Characterization of Doxorubicin Liposomes. *Methods Mol Biol* **2010**, *624*, 211–219. https://doi.org/10.1007/978-1-60761-609-2_14.

(44) Lombardo, D.; Kiselev, M. A. Methods of Liposomes Preparation: Formation and Control Factors of Versatile Nanocarriers for Biomedical and Nanomedicine Application. *Pharmaceutics* **2022**, *14* (3), 543. https://doi.org/10.3390/pharmaceutics14030543.

(45) Saunders, L.; Perrin, J.; Gammack, D. Ultrasonic Irradiation of Some Phospholipid Sols. *Journal of Pharmacy and Pharmacology* **1962**, *14* (1), 567–572. https://doi.org/10.1111/j.2042-7158.1962.tb11141.x.

(46) Du, G.; Sun, X. Ethanol Injection Method for Liposome Preparation. *Methods Mol Biol* **2023**, *2622*, 65–70. https://doi.org/10.1007/978-1-0716-2954-3_5.

(47) Wehrle, N.; Tran, L. M.; Zheng, A.; Pissay, R.; Park, Y. C. Effect of Solvent and Cholesterol on Liposome Production by the Reverse-Phase Evaporation (RPE) Method. *Langmuir* **2024**, *40* (44), 23521–23528. https://doi.org/10.1021/acs.langmuir.4c03322.

(48) Yu, B.; Lee, R. J.; Lee, L. J. Microfluidic Methods for Production of Liposomes. *Methods Enzymol* **2009**, *465*, 129–141. https://doi.org/10.1016/S0076-6879(09)65007-2.

(49) Franzé, S.; Selmin, F.; Samaritani, E.; Minghetti, P.; Cilurzo, F. Lyophilization of Liposomal Formulations: Still Necessary, Still Challenging. *Pharmaceutics* **2018**, *10* (3), 139. https://doi.org/10.3390/pharmaceutics10030139.

(50) Müller, M.; Mackeben, S.; Müller-Goymann, C. C. Physicochemical Characterisation of Liposomes with Encapsulated Local Anaesthetics. *Int J Pharm* **2004**, *274* (1–2), 139–148. https://doi.org/10.1016/j.ijpharm.2004.01.015.

(51) Fröhlich, M.; Brecht, V.; Peschka-Süss, R. Parameters Influencing the Determination of Liposome Lamellarity by 31P-NMR. *Chem Phys Lipids* **2001**, *109* (1), 103–112. https://doi.org/10.1016/s0009-3084(00)00220-6.

(52) Pattni, B. S.; Chupin, V. V.; Torchilin, V. P. New Developments in Liposomal Drug Delivery. *Chem Rev* **2015**, *115* (19), 10938–10966. https://doi.org/10.1021/acs.chemrev.5b00046.

(53) Lôbo, G. C. N. B.; Paiva, K. L. R.; Silva, A. L. G.; Simões, M. M.; Radicchi, M. A.; Báo, S. N. Nanocarriers Used in Drug Delivery to Enhance Immune System in Cancer Therapy. *Pharmaceutics* **2021**, *13* (8), 1167. https://doi.org/10.3390/pharmaceutics13081167.

(54) Mazdaei, M.; Asare-Addo, K. A Mini-Review of Nanocarriers in Drug Delivery Systems. *British Journal of Pharmacy* **2022**, *7* (1). https://doi.org/10.5920/bjpharm.780.

(55) Anselmo, A. C.; Mitragotri, S. Nanoparticles in the Clinic: An Update. *Bioeng Transl Med* **2019**, *4* (3), e10143. https://doi.org/10.1002/btm2.10143.

(56) Arias, L. S.; Pessan, J. P.; Vieira, A. P. M.; de Lima, T. M. T.; Delbem, A. C. B.; Monteiro, D. R. Iron Oxide Nanoparticles for Biomedical Applications: A Perspective on Synthesis, Drugs, Antimicrobial Activity, and Toxicity. *Antibiotics (Basel)* **2018**, *7* (2), 46. https://doi.org/10.3390/antibiotics7020046.

(57) Fenton, O. S.; Olafson, K. N.; Pillai, P. S.; Mitchell, M. J.; Langer, R. Advances in Biomaterials for Drug Delivery. *Advanced Materials* **2018**, *30* (29), 1705328. https://doi.org/10.1002/adma.201705328.

(58) Gregoriadis, G.; Ryman, B. E. Liposomes as Carriers of Enzymes or Drugs: A New Approach to the Treatment of Storage Diseases. *Biochem J* **1971**, *124* (5), 58P. https://doi.org/10.1042/bj1240058p.

(59) Gatto, M. S.; Johnson, M. P.; Najahi-Missaoui, W. Targeted Liposomal Drug Delivery: Overview of the Current Applications and Challenges. *Life (Basel)* **2024**, *14* (6), 672. https://doi.org/10.3390/life14060672.

(60) Liu, J.-J.; Hong, R.-L.; Cheng, W.-F.; Hong, K.; Chang, F.-H.; Tseng, Y.-L. Simple and Efficient Liposomal Encapsulation of Topotecan by Ammonium Sulfate Gradient: Stability, Pharmacokinetic and Therapeutic Evaluation. *Anticancer Drugs* **2002**, *13* (7), 709–717. https://doi.org/10.1097/00001813-200208000-00005.

(61) Fenske, D. B.; Cullis, P. R. Encapsulation of Drugs Within Liposomes by pH-Gradient Techniques.

(62) Machy, P. *Liposomes in Cell Biology and Pharmacology*; Paris, France : Editions INSERM ; London : John Libbey Eurotext, 1987.

(63) Gabizon, A.; Papahadjopoulos, D. Liposome Formulations with Prolonged Circulation Time in Blood and Enhanced Uptake by Tumors. *Proc Natl Acad Sci U S A* **1988**, *85* (18), 6949–6953. https://doi.org/10.1073/pnas.85.18.6949.

(64) Gaber, B. P.; Sheridan, J. P. Kinetic and Thermodynamic Studies of the Fusion of Small Unilamellar Phospholipid Vesicles. *Biochimica et Biophysica Acta (BBA) - Biomembranes* **1982**, *685* (1), 87–93. https://doi.org/10.1016/0005-2736(82)90038-4.

(65) Tenchov, R.; Bird, R.; Curtze, A. E.; Zhou, Q. Lipid Nanoparticles─From Liposomes to mRNA Vaccine Delivery, a Landscape of Research Diversity and Advancement. *ACS Nano* **2021**, *15* (11), 16982–17015. https://doi.org/10.1021/acsnano.1c04996.

(66) Miller, C. R.; Bondurant, B.; McLean, S. D.; McGovern, K. A.; O'Brien, D. F. Liposome−Cell Interactions in Vitro: Effect of Liposome Surface Charge on the Binding and Endocytosis of Conventional and Sterically Stabilized Liposomes. *Biochemistry* **1998**, *37* (37), 12875–12883. https://doi.org/10.1021/bi980096y.

(67) Nosova, A. S.; Koloskova, O. O.; Nikonova, A. A.; Simonova, V. A.; Smirnov, V. V.; Kudlay, D.; Khaitov, M. R. Diversity of PEGylation Methods of Liposomes and Their Influence on RNA Delivery. *Medchemcomm* **2019**, *10* (3), 369–377. https://doi.org/10.1039/c8md00515j.

(68) Gaston, J. P.; Meepat, S.; Islam, M. S.; Li, J.; Daljit Singh, J. K.; Booth, M. J.; Wickham, S. FJ.; Baker, M. AB. The Effect of PEGylation on Surface Tethering of

Liposomes via DNA Nanotechnology. *Journal of Lipid Research* **2026**, *67* (1), 100940. https://doi.org/10.1016/j.jlr.2025.100940.

(69) Danhier, F.; Feron, O.; Préat, V. To Exploit the Tumor Microenvironment: Passive and Active Tumor Targeting of Nanocarriers for Anti-Cancer Drug Delivery. *Journal of Controlled Release* **2010**, *148* (2), 135–146. https://doi.org/10.1016/j.jconrel.2010.08.027.

(70) Lopes, S. C. de A.; Giuberti, C. dos S.; Rocha, T. G. R.; Ferreira, D. dos S.; AmaralLeite, E.; Oliveira, M. C.; Lopes, S. C. de A.; Giuberti, C. dos S.; Rocha, T. G. R.; Ferreira, D. dos S.; AmaralLeite, E.; Oliveira, M. C. Liposomes as Carriers of Anticancer Drugs. In *Cancer Treatment - Conventional and Innovative Approaches*; IntechOpen, 2013. https://doi.org/10.5772/55290.

(71) Li, X.; Ding, L.; Xu, Y.; Wang, Y.; Ping, Q. Targeted Delivery of Doxorubicin Using Stealth Liposomes Modified with Transferrin. *Int J Pharm* **2009**, *373* (1–2), 116–123. https://doi.org/10.1016/j.ijpharm.2009.01.023.

(72) Kumar, P.; Huo, P.; Liu, B. Formulation Strategies for Folate-Targeted Liposomes and Their Biomedical Applications. *Pharmaceutics* **2019**, *11* (8), 381. https://doi.org/10.3390/pharmaceutics11080381.

(73) Raju, A.; Muthu, M. S.; Feng, S.-S. Trastuzumab-Conjugated Vitamin E TPGS Liposomes for Sustained and Targeted Delivery of Docetaxel. *Expert Opin Drug Deliv* **2013**, *10* (6), 747–760. https://doi.org/10.1517/17425247.2013.777425.

(74) Sercombe, L.; Veerati, T.; Moheimani, F.; Wu, S. Y.; Sood, A. K.; Hua, S. Advances and Challenges of Liposome Assisted Drug Delivery. *Front Pharmacol* **2015**, *6*, 286. https://doi.org/10.3389/fphar.2015.00286.

(75) Zalba, S.; ten Hagen, T. L. M.; Burgui, C.; Garrido, M. J. Stealth Nanoparticles in Oncology: Facing the PEG Dilemma. *Journal of Controlled Release* **2022**, *351*, 22–36. https://doi.org/10.1016/j.jconrel.2022.09.002.

(76) Li, J.; Yu, J.; Song, J.; Zhang, Y.; Li, N.; Wang, Z.; Qin, M.; Zhao, M.; Zhang, B.; Huang, R.; Zhou, S.; Liu, Y.; He, Z.; Liu, H.; Dan Liu; Wang, Y. Galloylated Liposomes Enable Targeted Drug Delivery by Overcoming Protein Corona Shielding. *Nat Commun* **2025**, *16*, 7926. https://doi.org/10.1038/s41467-025-63198-4.

(77) Russell, L. M.; Hultz, M.; Searson, P. C. Leakage Kinetics of the Liposomal Chemotherapeutic Agent Doxil: The Role of Dissolution, Protonation, and Passive Transport, and Implications for Mechanism of Action. *J Control Release* **2018**, *269*, 171–176. https://doi.org/10.1016/j.jconrel.2017.11.007.

(78) Aizik, G.; Waiskopf, N.; Agbaria, M.; Ben-David-Naim, M.; Levi-Kalisman, Y.; Shahar, A.; Banin, U.; Golomb, G. Liposomes of Quantum Dots Configured for Passive and Active Delivery to Tumor Tissue. *Nano Lett.* **2019**, *19* (9), 5844–5852. https://doi.org/10.1021/acs.nanolett.9b01027.

(79) Ta, T.; Porter, T. M. Thermosensitive Liposomes for Localized Delivery and Triggered Release of Chemotherapy. *J Control Release* **2013**, *169* (1–2), 112–125. https://doi.org/10.1016/j.jconrel.2013.03.036.

(80) Agiba, A. M.; Arreola-Ramírez, J. L.; Carbajal, V.; Segura-Medina, P. Light-Responsive and Dual-Targeting Liposomes: From Mechanisms to Targeting Strategies. *Molecules* **2024**, *29* (3), 636. https://doi.org/10.3390/molecules29030636.

(81) Kim, Y.-S.; Ko, M. J.; Moon, H.; Sim, W.; Cho, A. S.; Gil, G.; Kim, H. R. Ultrasound-Responsive Liposomes for Targeted Drug Delivery Combined with Focused Ultrasound. *Pharmaceutics* **2022**, *14* (7), 1314. https://doi.org/10.3390/pharmaceutics14071314.

(82) Vlasova, K. Yu.; Piroyan, A.; Le-Deygen, I. M.; Vishwasrao, H. M.; Ramsey, J. D.; Klyachko, N. L.; Golovin, Y. I.; Rudakovskaya, P. G.; Kireev, I. I.; Kabanov, A. V.; Sokolsky-Papkov, M. Magnetic Liposome Design for Drug Release Systems Responsive to Super-Low Frequency Alternating Current Magnetic Field (AC MF). *J Colloid Interface Sci* **2019**, *552*, 689–700. https://doi.org/10.1016/j.jcis.2019.05.071.

(83) Silbaugh, A.; Vallin, J.; Pelaez, F.; Kim, M.; Shao, Q.; Lee, H. S.; Bischof, J. C.; Azarin, S. M. Enhancing Electroporation-Induced Liposomal Drug Release in Suspension and Solid Phases. *International Journal of Pharmaceutics* **2023**, *635*, 122744. https://doi.org/10.1016/j.ijpharm.2023.122744.

(84) Rustad, E. A. L.; von Hofsten, S.; Kumar, R.; Lænsman, E. A.; Berge, G.; Škalko-Basnet, N. The pH-Responsive Liposomes—The Effect of PEGylation on Release Kinetics and Cellular Uptake in Glioblastoma Cells. *Pharmaceutics* **2022**, *14* (6), 1125. https://doi.org/10.3390/pharmaceutics14061125.

(85) Wei, Y.; Lv, J.; Zhu, S.; Wang, S.; Su, J.; Xu, C. Enzyme-Responsive Liposomes for Controlled Drug Release. *Drug Discovery Today* **2024**, *29* (7), 104014. https://doi.org/10.1016/j.drudis.2024.104014.

(86) Zhao, Y.; Peng, Y.; Yang, Z.; Lu, J.; Li, R.; Shi, Y.; Du, Y.; Zhao, Z.; Hai, L.; Wu, Y. pH-Redox Responsive Cascade-Targeted Liposomes to Intelligently Deliver Doxorubicin Prodrugs and Lonidamine for Glioma. *European Journal of Medicinal Chemistry* **2022**, *235*, 114281. https://doi.org/10.1016/j.ejmech.2022.114281.

(87) Lou, J.; Hudson, M. M.; Ancajas, C. F.; Best, M. D. Development of GTP-Responsive Liposomes by Exchanging the Metal-DPA Binding Site in a Synthetic Lipid Switch. *Chem. Commun.* **2023**, *59* (22), 3285–3288. https://doi.org/10.1039/D3CC00288H.

(88) Lou, J.; Best, M. D. Calcium-Responsive Liposomes: Toward Ion-Mediated Targeted Drug Delivery. *Methods Enzymol* **2020**, *640*, 105–129. https://doi.org/10.1016/bs.mie.2020.04.005.

(89) Sagar, R.; Lou, J.; Watson, A. J.; Best, M. D. Zinc Triggered Release of Encapsulated Cargo from Liposomes via a Synthetic Lipid Switch. *Bioconjugate Chem.* **2021**, *32* (12), 2485–2496. https://doi.org/10.1021/acs.bioconjchem.1c00425.

(90) Lou, J.; Schuster, J. A.; Barrera, F. N.; Best, M. D. ATP-Responsive Liposomes via Screening of Lipid Switches Designed to Undergo Conformational Changes upon Binding Phosphorylated Metabolites. *J. Am. Chem. Soc.* **2022**, *144* (8), 3746–3756. https://doi.org/10.1021/jacs.2c00191.

(91) Burnouf, P.-A.; Su, Y.-C.; Yang, S.-H. Safe and Efficient Intracellular Release of SN38 via Lysosomal-Responsive SN38-G Loaded Liposomes. *ACS Appl. Bio Mater.* **2025**, *8* (7), 6231–6242. https://doi.org/10.1021/acsabm.5c00722.

(92) Lou, J.; Best, M. D. Strategies for Altering Lipid Self-Assembly to Trigger Liposome Cargo Release. *Chem Phys Lipids* **2020**, *232*, 104966. https://doi.org/10.1016/j.chemphyslip.2020.104966.

(93) Thamphiwatana, S.; Gao, W.; Pornpattananangkul, D.; Zhang, Q.; Fu, V.; Li, J.; Li, J.; Obonyo, M.; Zhang, L. Phospholipase A2-Responsive Antibiotic Delivery via Nanoparticle-Stabilized Liposomes for the Treatment of Bacterial Infection. *Journal of Materials Chemistry B* **2014**, *2* (46), 8201–8207. https://doi.org/10.1039/C4TB01110D.

(94) Davidsen, J.; Jørgensen, K.; Andresen, T. L.; Mouritsen, O. G. Secreted Phospholipase A2 as a New Enzymatic Trigger Mechanism for Localised Liposomal Drug Release and Absorption in Diseased Tissue. *Biochimica et Biophysica Acta (BBA) - Biomembranes* **2003**, *1609* (1), 95–101. https://doi.org/10.1016/S0005-2736(02)00659-4.

(95) Pak, C. C.; Ali, S.; Janoff, A. S.; Meers, P. Triggerable Liposomal Fusion by Enzyme Cleavage of a Novel Peptide–Lipid Conjugate. *Biochimica et Biophysica Acta (BBA) - Biomembranes* **1998**, *1372* (1), 13–27. https://doi.org/10.1016/S0005-2736(98)00041-8.

(96) Heyes, J. A.; Niculescu-Duvaz, D.; Cooper, R. G.; Springer, C. J. Synthesis of Novel Cationic Lipids: Effect of Structural Modification on the Efficiency of Gene Transfer. *J Med Chem* **2002**, *45* (1), 99–114. https://doi.org/10.1021/jm010918g.

(97) Ermilova, I.; Swenson, J. DOPC versus DOPE as a Helper Lipid for Gene-Therapies: Molecular Dynamics Simulations with DLin-MC3-DMA. *Phys. Chem. Chem. Phys.* **2020**, *22* (48), 28256–28268. https://doi.org/10.1039/D0CP05111J.

(98) Lou, J.; Best, M. D. Reactive Oxygen Species-Responsive Liposomes via Boronate-Caged Phosphatidylethanolamine. *Bioconjugate Chemistry* **2020**. https://doi.org/10.1021/acs.bioconjchem.0c00397.

(99) Lou, J.; Best, M. D. A General Approach to Enzyme-Responsive Liposomes. *Chemistry – A European Journal* **2020**, *26* (39), 8597–8607. https://doi.org/10.1002/chem.202000529.

(100) Vermehren, C.; Kiebler, T.; Hylander, I.; Callisen, T. H.; Jørgensen, K. Increase in Phospholipase A2 Activity towards Lipopolymer-Containing Liposomes. *Biochimica et Biophysica Acta (BBA) - Biomembranes* **1998**, *1373* (1), 27–36. https://doi.org/10.1016/S0005-2736(98)00084-4.

(101) Pedersen, P. J.; Viart, H. M.-F.; Melander, F.; Andresen, T. L.; Madsen, R.; Clausen, M. H. Synthesis of Tocopheryl Succinate Phospholipid Conjugates and Monitoring of Phospholipase A2 Activity. *Bioorganic & Medicinal Chemistry* **2012**, *20* (13), 3972–3978. https://doi.org/10.1016/j.bmc.2012.05.024.

(102) Yuba, E. Development of Functional Liposomes by Modification of Stimuli-Responsive Materials and Their Biomedical Applications. *J. Mater. Chem. B* **2020**, *8* (6), 1093–1107. https://doi.org/10.1039/C9TB02470K.

(103) Lee, Y.; Thompson, D. h. Stimuli-Responsive Liposomes for Drug Delivery. *WIREs Nanomedicine and Nanobiotechnology* **2017**, *9* (5), e1450. https://doi.org/10.1002/wnan.1450.

(104) Yoon-Seok Kim; Ko, M. J.; Moon, H.; Sim, W.; Cho, A. S.; Gil, G.; Kim, H. R. Ultrasound-Responsive Liposomes for Targeted Drug Delivery Combined with Focused Ultrasound. *Pharmaceutics* **2022**, *14* (7), 1314. https://doi.org/10.3390/pharmaceutics14071314.

(105) Ong, W.; Yang, Y.; Cruciano, A. C.; McCarley, R. L. Redox-Triggered Contents Release from Liposomes. *J. Am. Chem. Soc.* **2008**, *130* (44), 14739–14744. https://doi.org/10.1021/ja8050469.

(106) AlSawaftah, N. M.; Awad, N. S.; Pitt, W. G.; Husseini, G. A. pH-Responsive Nanocarriers in Cancer Therapy. *Polymers* **2022**, *14* (5), 936. https://doi.org/10.3390/polym14050936.

(107) Fouladi, F.; Steffen, K. J.; Mallik, S. Enzyme-Responsive Liposomes for the Delivery of Anticancer Drugs. *Bioconjug Chem* **2017**, *28* (4), 857–868. https://doi.org/10.1021/acs.bioconjchem.6b00736.

(108) Webb, B. A.; Chimenti, M.; Jacobson, M. P.; Barber, D. L. Dysregulated pH: A Perfect Storm for Cancer Progression. *Nat Rev Cancer* **2011**, *11* (9), 671–677. https://doi.org/10.1038/nrc3110.

(109) Fisher, G. J.; Wang, Z.; Datta, S.; Varani, J.; Kang, S.; Voorhees, J. Pathophysiology of Premature Skin Aging Induced by Ultraviolet Light | New England Journal of Medicine. *N Engl J Med* **1997**, *337* (20), 1419–1429. https://doi.org/10.1056/NEJM199711133372003.

(110) Lou, J.; Carr, A. J.; Watson, A. J.; Mattern-Schain, S. I.; Best, M. D. Calcium-Responsive Liposomes via a Synthetic Lipid Switch. *Chemistry – A European Journal* **2018**, *24* (14), 3599–3607. https://doi.org/10.1002/chem.201705810.

(111) Lou, J.; Hudson, M. M.; Ancajas, C. F.; Best, M. D. Development of GTP-Responsive Liposomes by Exchanging the Metal-DPA Binding Site in a Synthetic Lipid Switch. *Chem. Commun.* **2023**, *59* (22), 3285–3288. https://doi.org/10.1039/D3CC00288H.

(112) Lou, J.; Sagar, R.; Best, M. D. Metabolite-Responsive Liposomes Employing Synthetic Lipid Switches Driven by Molecular Recognition Principles. *Acc. Chem. Res.* **2022**, *55* (20), 2882–2891. https://doi.org/10.1021/acs.accounts.2c00446.

(113) Frolov, V. A.; Shnyrova, A. V.; Zimmerberg, J. Lipid Polymorphisms and Membrane Shape. *Cold Spring Harb Perspect Biol* **2011**, *3* (11), a004747. https://doi.org/10.1101/cshperspect.a004747.

(114) Lane, A. N.; Fan, T. W.-M. Regulation of Mammalian Nucleotide Metabolism and Biosynthesis. *Nucleic Acids Res* **2015**, *43* (4), 2466–2485. https://doi.org/10.1093/nar/gkv047.

(115) Syrovatkina, V.; Alegre, K. O.; Dey, R.; Huang, X.-Y. Regulation, Signaling, and Physiological Functions of G-Proteins. *J Mol Biol* **2016**, *428* (19), 3850–3868. https://doi.org/10.1016/j.jmb.2016.08.002.

(116) Maracci, C.; Rodnina, M. V. Review: Translational GTPases. *Biopolymers* **2016**, *105* (8), 463–475. https://doi.org/10.1002/bip.22832.

(117) Grasmann, G.; Smolle, E.; Olschewski, H.; Leithner, K. Gluconeogenesis in Cancer Cells - Repurposing of a Starvation-Induced Metabolic Pathway? *Biochim Biophys Acta Rev Cancer* **2019**, *1872* (1), 24–36. https://doi.org/10.1016/j.bbcan.2019.05.006.

(118) Vale, R. D.; Coppin, C. M.; Malik, F.; Kull, F. J.; Milligan, R. A. Tubulin GTP Hydrolysis Influences the Structure, Mechanical Properties, and Kinesin-Driven Transport of Microtubules. *J Biol Chem* **1994**, *269* (38), 23769–23775.

(119) Tuteja, N. Signaling through G Protein Coupled Receptors. *Plant Signal Behav* **2009**, *4* (10), 942–947. https://doi.org/10.4161/psb.4.10.9530.

(120) Kofuji, S.; Sasaki, A. T. GTP Metabolic Reprogramming by IMPDH2: Unlocking Cancer Cells' Fuelling Mechanism. *J Biochem* **2020**, *168* (4), 319–328. https://doi.org/10.1093/jb/mvaa085.

(121) Harrus, D.; Ahmed-El-Sayed, N.; Simister, P. C.; Miller, S.; Triconnet, M.; Hagedorn, C. H.; Mahias, K.; Rey, F. A.; Astier-Gin, T.; Bressanelli, S. Further Insights into the Roles of GTP and the C Terminus of the Hepatitis C Virus Polymerase in the Initiation of RNA Synthesis. *J Biol Chem* **2010**, *285* (43), 32906–32918. https://doi.org/10.1074/jbc.M110.151316.

(122) Kopra, K.; Mahran, R.; Yli-Hollo, T.; Tabata, S.; Vuorinen, E.; Fujii, Y.; Vuorinen, I.; Ogawa-Iio, A.; Hirayama, A.; Soga, T.; Sasaki, A. T.; Härmä, H. Homogeneous Luminescent Quantitation of Cellular Guanosine and Adenosine Triphosphates (GTP and ATP) Using QT-LucGTP&ATP Assay. *Anal Bioanal Chem* **2023**, *415* (27), 6689–6700. https://doi.org/10.1007/s00216-023-04944-9.

(123) Bianchi-Smiraglia, A.; Rana, M. S.; Foley, C. E.; Paul, L. M.; Lipchick, B. C.; Moparthy, S.; Moparthy, K.; Fink, E. E.; Bagati, A.; Hurley, E.; Affronti, H. C.; Bakin, A. V.; Kandel, E. S.; Smiraglia, D. J.; Feltri, M. L.; Sousa, R.; Nikiforov, M. A. Internally Ratiometric Fluorescent Sensors for Evaluation of Intracellular GTP Levels and Distribution. *Nat Methods* **2017**, *14* (10), 1003–1009. https://doi.org/10.1038/nmeth.4404.

(124) Chavrier, P.; Parton, R. G.; Hauri, H. P.; Simons, K.; Zerial, M. Localization of Low Molecular Weight GTP Binding Proteins to Exocytic and Endocytic Compartments. *Cell* **1990**, *62* (2), 317–329. https://doi.org/10.1016/0092-8674(90)90369-P.

(125) Tang, T.; Gong, Y.; Gao, Y.; Pang, X.; Liu, S.; Xia, Y.; Liu, D.; Zhu, L.; Fan, Q.; Sun, X. A pH-Responsive Liposomal Nanoplatform for Co-Delivery of a Pt(IV) Prodrug and Cinnamaldehyde for Effective Tumor Therapy. *Front. Bioeng. Biotechnol.* **2023**, *11*. https://doi.org/10.3389/fbioe.2023.1191534.

(126) Sagar, R.; Jaremba, E. A.; Lou, J.; Best, M. D. Copper-Responsive Liposomes for Triggered Cargo Release Employing a Picolinamide−lipid Conjugate. *Org. Biomol. Chem.* **2023**, *21* (5), 955–959. https://doi.org/10.1039/D2OB01977A.

(127) ATP-Responsive Tumor Targeted Lipid Nanoparticle for Enhanced siRNA Delivery and Improved Treatment Efficacy in Melanoma. *Journal of Controlled Release* **2025**, *382*, 113622. https://doi.org/10.1016/j.jconrel.2025.113622.

(128) Cozzoli, L.; Gjonaj, L.; Stuart, M. C. A.; Poolman, B.; Roelfes, G. Responsive DNA G-Quadruplex Micelles. *Chem. Commun.* **2018**, *54* (3), 260–263. https://doi.org/10.1039/C7CC07899D.

(129) Liang, T.; Yao, Z.; Ding, J.; Min, Q.; Jiang, L.; Zhu, J.-J. Cascaded Aptamers-Governed Multistage Drug-Delivery System Based on Biodegradable Envelope-Type Nanovehicle for Targeted Therapy of HER2-Overexpressing Breast Cancer. *ACS Appl. Mater. Interfaces* **2018**, *10* (40), 34050–34059. https://doi.org/10.1021/acsami.8b14009.

(130) Brand, G.; Hosseini, M. W.; Ruppert, R. Synthesis of Selectively Substituted Lipocyclopolyamines. *Helvetica Chimica Acta* **1992**, *75* (3), 721–728. https://doi.org/10.1002/hlca.19920750307.

(131) Kimura, E.; Koike, T. Dynamic Anion Recognition by Macrocyclic Polyamines in Neutral pH Aqueous Solution: Development from Static Anion Complexes to an Enolate Complex. **1998**. https://doi.org/10.1039/A802285B.

(132) Dietrich, B.; Hosseini, M. W.; Lehn, J. M.; Sessions, R. B. Anion Receptor Molecules. Synthesis and Anion-Binding Properties of Polyammonium Macrocycles. *J. Am. Chem. Soc.* **1981**, *103* (5), 1282–1283. https://doi.org/10.1021/ja00395a077.

(133) Hosseini, M. W.; Blacker, A. J.; Lehn, J.-M. Multiple Molecular Recognition and Catalysis. Nucleotide Binding and ATP Hydrolysis by a Receptor Molecule Bearing an Anion Binding Site, an Intercalator Group, and a Catalytic Site. *J. Chem. Soc., Chem. Commun.* **1988**, No. 9, 596–598. https://doi.org/10.1039/C39880000596.

(134) Hosseini, M. W.; Lehn, J.-M. Binding of AMP, ADP, and ATP Nucleotides by Polyammonium Macrocycles. *Helvetica Chimica Acta* **1987**, *70* (5), 1312–1319. https://doi.org/10.1002/hlca.19870700512.

(135) Hosseini, M. W.; Lehn, J.-M.; Mertes, M. P. Efficient Molecular Catalysis of ATP-Hydrolysis by Protonated Macrocyclic Polyamines. *Helvetica Chimica Acta* **1983**, *66* (8), 2454–2466. https://doi.org/10.1002/hlca.19830660811.

(136) Anda, C.; Llobet, A.; Salvado, V.; Martell, A. E.; Motekaitis, R. J. A Systematic Evaluation of Molecular Recognition Phenomena. 2. Interaction between Phosphates and Nucleotides with Hexaazamacrocyclic Ligands Containing Diethylic Ether Spacers. *Inorg. Chem.* **2000**, *39* (14), 3000–3008. https://doi.org/10.1021/ic9908468.

(137) Greenspan, P.; Fowler, S. D. Spectrofluorometric Studies of the Lipid Probe, Nile Red. *J Lipid Res* **1985**, *26* (7), 781–789.

(138) Zhang, H. Thin-Film Hydration Followed by Extrusion Method for Liposome Preparation. In *Liposomes: Methods and Protocols*; D'Souza, G. G. M., Ed.; Springer: New York, NY, 2017; pp 17–22. https://doi.org/10.1007/978-1-4939-6591-5_2.

(139) Jose, D. A.; Mishra, S.; Ghosh, A.; Shrivastav, A.; Mishra, S. K.; Das, A. Colorimetric Sensor for ATP in Aqueous Solution. *Org. Lett.* **2007**, *9* (10), 1979–1982. https://doi.org/10.1021/ol0705797.

(140) Mullen, N. J.; Singh, P. K. Nucleotide Metabolism: A Pan-Cancer Metabolic Dependency. *Nat Rev Cancer* **2023**, *23* (5), 275–294. https://doi.org/10.1038/s41568-023-00557-7.

(141) Johnsson, M.; Edwards, K. Phase Behavior and Aggregate Structure in Mixtures of Dioleoylphosphatidylethanolamine and Poly(Ethylene Glycol)-Lipids. *Biophysical Journal* **2001**, *80* (1), 313–323. https://doi.org/10.1016/S0006-3495(01)76016-X.

(142) Qadeer, H. A.; Bashir, K. Physiology, Phosphate. In *StatPearls*; StatPearls Publishing: Treasure Island (FL), 2025.

(143) Kaur, J.; Castro, D. Hypophosphatemia. In *StatPearls*; StatPearls Publishing: Treasure Island (FL), 2025.

(144) Aldosari, B. N.; Alfagih, I. M.; Almurshedi, A. S. Lipid Nanoparticles as Delivery Systems for RNA-Based Vaccines. *Pharmaceutics* **2021**, *13* (2), 206. https://doi.org/10.3390/pharmaceutics13020206.

(145) Zhen, S.; Li, X. Liposomal Delivery of CRISPR/Cas9. *Cancer Gene Ther* **2020**, *27* (7), 515–527. https://doi.org/10.1038/s41417-019-0141-7.

(146) Eloy, J. O.; Claro de Souza, M.; Petrilli, R.; Barcellos, J. P. A.; Lee, R. J.; Marchetti, J. M. Liposomes as Carriers of Hydrophilic Small Molecule Drugs: Strategies to Enhance Encapsulation and Delivery. *Colloids and Surfaces B: Biointerfaces* **2014**, *123*, 345–363. https://doi.org/10.1016/j.colsurfb.2014.09.029.

(147) Wang, P.; Gong, Q.; Hu, J.; Li, X.; Zhang, X. Reactive Oxygen Species (ROS)-Responsive Prodrugs, Probes, and Theranostic Prodrugs: Applications in the ROS-Related Diseases. *J. Med. Chem.* **2021**, *64* (1), 298–325. https://doi.org/10.1021/acs.jmedchem.0c01704.

(148) Murphy, M. P.; Holmgren, A.; Larsson, N.-G.; Halliwell, B.; Chang, C. J.; Kalyanaraman, B.; Rhee, S. G.; Thornalley, P. J.; Partridge, L.; Gems, D.; Nyström, T.; Belousov, V.; Schumacker, P. T.; Winterbourn, C. C. Unravelling the Biological Roles of Reactive Oxygen Species. *Cell Metab* **2011**, *13* (4), 361–366. https://doi.org/10.1016/j.cmet.2011.03.010.

(149) Chu, B.; Qu, Y.; He, X.; Hao, Y.; Yang, C.; Yang, Y.; Hu, D.; Wang, F.; Qian, Z. ROS-Responsive Camptothecin Prodrug Nanoparticles for On-Demand Drug Release and Combination of Chemotherapy and Photodynamic Therapy. *Advanced Functional Materials* **2020**, *30* (52), 2005918. https://doi.org/10.1002/adfm.202005918.

(150) Tang, Q.; Chen, Y.; Zhang, Y.; Wang, K.; Liu, L.; Pan, D.; Liu, Q.; Jiang, C. ROS-Responsive Prodrug Micelle Co-Delivery System for Synergistic Antiatherosclerotic Therapy. *Mol. Pharmaceutics* **2023**, *20* (9), 4478–4490. https://doi.org/10.1021/acs.molpharmaceut.3c00127.

(151) Alfadda, A. A.; Sallam, R. M. Reactive Oxygen Species in Health and Disease. *J Biomed Biotechnol* **2012**, *2012*, 936486. https://doi.org/10.1155/2012/936486.

(152) Tu, B. P.; Weissman, J. S. Oxidative Protein Folding in Eukaryotes : Mechanisms and Consequences. *Journal of Cell Biology* **2004**, *164* (3), 341–346. https://doi.org/10.1083/jcb.200311055.

(153) Umeno, A.; Biju, V.; Yoshida, Y. In Vivo ROS Production and Use of Oxidative Stress-Derived Biomarkers to Detect the Onset of Diseases Such as Alzheimer's Disease, Parkinson's Disease, and Diabetes. *Free Radic Res* **2017**, *51* (4), 413–427. https://doi.org/10.1080/10715762.2017.1315114.

(154) Rhee, S. G. H2O2, a Necessary Evil for Cell Signaling. *Science* **2006**, *312* (5782), 1882–1883. https://doi.org/10.1126/science.1130481.

(155) Stone, J. R.; Yang, S. Hydrogen Peroxide: A Signaling Messenger. *Antioxid Redox Signal* **2006**, *8* (3–4), 243–270. https://doi.org/10.1089/ars.2006.8.243.

(156) Murphy, M. P.; Holmgren, A.; Larsson, N.-G.; Halliwell, B.; Chang, C. J.; Kalyanaraman, B.; Rhee, S. G.; Thornalley, P. J.; Partridge, L.; Gems, D.; Nyström, T.; Belousov, V.; Schumacker, P. T.; Winterbourn, C. C. Unraveling the Biological Roles of Reactive Oxygen Species. *Cell Metabolism* **2011**, *13* (4), 361–366. https://doi.org/10.1016/j.cmet.2011.03.010.

(157) Szatrowski, T. P.; Nathan, C. F. Production of Large Amounts of Hydrogen Peroxide by Human Tumor Cells. *Cancer Res* **1991**, *51* (3), 794–798.

(158) Chu, Y.; Sun, T.; Jiang, C. Emerging Landscapes of Nanosystems Based on Pre-Metastatic Microenvironment for Cancer Theranostics. *Chinese Chemical Letters* **2022**, *33* (9), 4157–4168. https://doi.org/10.1016/j.cclet.2022.02.051.

(159) Kobayashi, C. I.; Suda, T. Regulation of Reactive Oxygen Species in Stem Cells and Cancer Stem Cells. *Journal of Cellular Physiology* **2012**, *227* (2), 421–430. https://doi.org/10.1002/jcp.22764.

(160) Chelombitko, M. A. Role of Reactive Oxygen Species in Inflammation: A Minireview. *Moscow Univ. Biol.Sci. Bull.* **2018**, *73* (4), 199–202. https://doi.org/10.3103/S009639251804003X.

(161) Burhans, W. C.; Heintz, N. H. The Cell Cycle Is a Redox Cycle: Linking Phase-Specific Targets to Cell Fate. *Free Radical Biology and Medicine* **2009**, *47* (9), 1282–1293. https://doi.org/10.1016/j.freeradbiomed.2009.05.026.

(162) Boonstra, J.; Post, J. A. Molecular Events Associated with Reactive Oxygen Species and Cell Cycle Progression in Mammalian Cells. *Gene* **2004**, *337*, 1–13. https://doi.org/10.1016/j.gene.2004.04.032.

(163) Dharmaraja, A. T. Role of Reactive Oxygen Species (ROS) in Therapeutics and Drug Resistance in Cancer and Bacteria. *J. Med. Chem.* **2017**, *60* (8), 3221–3240. https://doi.org/10.1021/acs.jmedchem.6b01243.

(164) Snezhkina, A. V.; Kudryavtseva, A. V.; Kardymon, O. L.; Savvateeva, M. V.; Melnikova, N. V.; Krasnov, G. S.; Dmitriev, A. A. ROS Generation and Antioxidant Defense Systems in Normal and Malignant Cells. *Oxidative Medicine and Cellular Longevity* **2019**, *2019* (1), 6175804. https://doi.org/10.1155/2019/6175804.

(165) Chi, T.; Sang, T.; Wang, Y.; Ye, Z. Cleavage and Noncleavage Chemistry in Reactive Oxygen Species (ROS)-Responsive Materials for Smart Drug Delivery.

Bioconjugate Chem. **2024**, *35* (1), 1–21. https://doi.org/10.1021/acs.bioconjchem.3c00476.

(166) Yao, Y.; Zhang, H.; Wang, Z.; Ding, J.; Wang, S.; Huang, B.; Ke, S.; Gao, C. Reactive Oxygen Species (ROS)-Responsive Biomaterials Mediate Tissue Microenvironments and Tissue Regeneration. *J. Mater. Chem. B* **2019**, *7* (33), 5019–5037. https://doi.org/10.1039/C9TB00847K.

(167) Li, J.; Sun, C.; Tao, W.; Cao, Z.; Qian, H.; Yang, X.; Wang, J. Photoinduced PEG Deshielding from ROS-Sensitive Linkage-Bridged Block Copolymer-Based Nanocarriers for on-Demand Drug Delivery. *Biomaterials* **2018**, *170*, 147–155. https://doi.org/10.1016/j.biomaterials.2018.04.015.

(168) Pan, Z.; Zhang, J.; Ji, K.; Chittavong, V.; Ji, X.; Wang, B. Organic CO Prodrugs Activated by Endogenous ROS. *Org. Lett.* **2018**, *20* (1), 8–11. https://doi.org/10.1021/acs.orglett.7b02775.

(169) Chen, W.; Han, Y.; Peng, X. Aromatic Nitrogen Mustard-Based Prodrugs: Activity, Selectivity, and the Mechanism of DNA Cross-Linking. *Chemistry – A European Journal* **2014**, *20* (24), 7410–7418. https://doi.org/10.1002/chem.201400090.

(170) Bhagat, S. D.; Singh, U.; Mishra, R. K.; Srivastava, A. An Endogenous Reactive Oxygen Species (ROS)-Activated Histone Deacetylase Inhibitor Prodrug for Cancer Chemotherapy. *ChemMedChem* **2018**, *13* (19), 2073–2079. https://doi.org/10.1002/cmdc.201800367.

(171) Zheng, S.; Guo, S.; Zhong, Q.; Zhang, C.; Liu, J.; Yang, L.; Zhang, Q.; Wang, G. Biocompatible Boron-Containing Prodrugs of Belinostat for the Potential Treatment

of Solid Tumors. *ACS Med. Chem. Lett.* **2018**, *9* (2), 149–154. https://doi.org/10.1021/acsmedchemlett.7b00504.

(172) Peiró Cadahía, J.; Previtali, V.; Troelsen, N. S.; Clausen, M. H. Prodrug Strategies for Targeted Therapy Triggered by Reactive Oxygen Species. *Medchemcomm* **2019**, *10* (9), 1531–1549. https://doi.org/10.1039/c9md00169g.

(173) Jourden, J. L. M.; Daniel, K. B.; Cohen, S. M. Investigation of Self-Immolative Linkers in the Design of Hydrogen Peroxide Activated Metalloprotein Inhibitors. *Chem. Commun.* **2011**, *47* (28), 7968–7970. https://doi.org/10.1039/C1CC12526E.

(174) Jafari, M.; Sriram, V.; Premnauth, G.; Merino, E.; Lee, J.-Y. Modified Peroxamide-Based Reactive Oxygen Species (ROS)-Responsive Doxorubicin Prodrugs. *Bioorganic Chemistry* **2022**, *127*, 105990. https://doi.org/10.1016/j.bioorg.2022.105990.

(175) Skarbek, C.; Serra, S.; Maslah, H.; Rascol, E.; Labruère, R. Arylboronate Prodrugs of Doxorubicin as Promising Chemotherapy for Pancreatic Cancer. *Bioorg Chem* **2019**, *91*, 103158. https://doi.org/10.1016/j.bioorg.2019.103158.

(176) Li, Y.; Chen, Z.; Lu, Z.; Yang, Q.; Liu, L.; Jiang, Z.; Zhang, L.; Zhang, X.; Qing, H. "Cell-Addictive" Dual-Target Traceable Nanodrug for Parkinson's Disease Treatment via Flotillins Pathway. *Theranostics* **2018**, *8* (19), 5469–5481. https://doi.org/10.7150/thno.28295.

(177) Xiao, W.; Geng, R.; Bi, D.; Luo, Y.; Zhang, Z.; Gan, Q.; Liu, Y.; Zhu, J. pH/H2O2 Cascade-Responsive Nanoparticles of Lipid-Like Prodrugs through Dynamic-

Covalent and Coordination Interactions for Chemotherapy. *Small* **2024**, *20* (30), 2308790. https://doi.org/10.1002/smll.202308790.

(178) Ding, Y.; Hu, X.; Piao, Y.; Huang, R.; Xie, L.; Yan, X.; Sun, H.; Li, Y.; Shi, L.; Liu, Y. Lipid Prodrug Nanoassemblies via Dynamic Covalent Boronates. *ACS Nano* **2023**, *17* (7), 6601–6614. https://doi.org/10.1021/acsnano.2c12233.

(179) Yang, S.; Shim, M. K.; Kim, W. J.; Choi, J.; Nam, G.-H.; Kim, J.; Kim, J.; Moon, Y.; Kim, H. Y.; Park, J.; Park, Y.; Kim, I.-S.; Ryu, J. H.; Kim, K. Cancer-Activated Doxorubicin Prodrug Nanoparticles Induce Preferential Immune Response with Minimal Doxorubicin-Related Toxicity. *Biomaterials* **2021**, *272*, 120791. https://doi.org/10.1016/j.biomaterials.2021.120791.

(180) Ibsen, S.; Zahavy, E.; Wrasdilo, W.; Berns, M.; Chan, M.; Esener, S. A Novel Doxorubicin Prodrug with Controllable Photolysis Activation for Cancer Chemotherapy. *Pharm Res* **2010**, *27* (9), 1848–1860. https://doi.org/10.1007/s11095-010-0183-x.

(181) Tang, L.; Jiang, W.; Wu, L.; Yu, X.; He, Z.; Shan, W.; Fu, L.; Zhang, Z.; Zhao, Y. TPGS2000-DOX Prodrug Micelles for Improving Breast Cancer Therapy. *Int J Nanomedicine* **2021**, *16*, 7875–7890. https://doi.org/10.2147/IJN.S335405.

(182) Losey, E. A.; Smith, M. D.; Meng, M.; Best, M. D. Microplate-Based Analysis of Protein-Membrane Binding Interactions via Immobilization of Whole Liposomes Containing a Biotinylated Anchor. *Bioconjug Chem* **2009**, *20* (2), 376–383. https://doi.org/10.1021/bc800414k.

(183) Ng, N. S.; Ooi, L. A Simple Microplate Assay for Reactive Oxygen Species Generation and Rapid Cellular Protein Normalization. *Bio Protoc* **2021**, *11* (1), e3877. https://doi.org/10.21769/BioProtoc.3877.

(184) Zhao, T.; Mu, X.; You, Q. Succinate: An Initiator in Tumorigenesis and Progression. *Oncotarget* **2017**, *8* (32), 53819–53828. https://doi.org/10.18632/oncotarget.17734.

(185) Pollard, P. J.; Brière, J. J.; Alam, N. A.; Barwell, J.; Barclay, E.; Wortham, N. C.; Hunt, T.; Mitchell, M.; Olpin, S.; Moat, S. J.; Hargreaves, I. P.; Heales, S. J.; Chung, Y. L.; Griffiths, J. R.; Dalgleish, A.; McGrath, J. A.; Gleeson, M. J.; Hodgson, S. V.; Poulsom, R.; Rustin, P.; Tomlinson, I. P. M. Accumulation of Krebs Cycle Intermediates and Over-Expression of HIF1α in Tumours Which Result from Germline FH and SDH Mutations. *Human Molecular Genetics* **2005**, *14* (15), 2231–2239. https://doi.org/10.1093/hmg/ddi227.

(186) Hobert, J. A.; Mester, J. L.; Moline, J.; Eng, C. Elevated Plasma Succinate in PTEN, SDHB, and SDHD Mutation-Positive Individuals. *Genet Med* **2012**, *14* (6), 616–619. https://doi.org/10.1038/gim.2011.63.

(187) Beloborodova, N.; Pautova, A.; Sergeev, A.; Fedotcheva, N. Serum Levels of Mitochondrial and Microbial Metabolites Reflect Mitochondrial Dysfunction in Different Stages of Sepsis. *Metabolites* **2019**, *9* (10), 196. https://doi.org/10.3390/metabo9100196.

(188) Connors, J.; Dawe, N.; Van Limbergen, J. The Role of Succinate in the Regulation of Intestinal Inflammation. *Nutrients* **2018**, *11* (1), 25. https://doi.org/10.3390/nu11010025.

(189) Wiskur, S. L.; Lavigne, J. J.; Metzger, A.; Tobey, S. L.; Lynch, V.; Anslyn, E. V. Thermodynamic Analysis of Receptors Based on Guanidinium/Boronic Acid Groups for the Complexation of Carboxylates, α-Hydroxycarboxylates, and Diols: Driving Force for Binding and Cooperativity. *Chemistry – A European Journal* **2004**, *10* (15), 3792–3804. https://doi.org/10.1002/chem.200305737.

(190) Fitzmaurice, R. J.; Kyne, G. M.; Douheret, D.; Kilburn, J. D. Synthetic Receptors for Carboxylic Acids and Carboxylates. *J. Chem. Soc., Perkin Trans. 1* **2002**, No. 7, 841–864. https://doi.org/10.1039/B009041G.

(191) Liu, Y.; Liu, Y.; Liang, Z.; Li, X.; Liu, S.; Yu, J. Enhanced Sensitivity and Selectivity of Chemosensor for Malonate by Anchoring on Gold Nanoparticles. *Chinese Journal of Chemistry* **2011**, *29* (3), 531–538. https://doi.org/10.1002/cjoc.201190118.

(192) Martí, A.; Costero, A. M.; Gaviña, P.; Parra, M. Selective Recognition and Sensing of Succinate vs. Other Aliphatic Dicarboxylates by Thiourea-Functionalized Gold Nanoparticles. *ChemistrySelect* **2016**, *1* (5), 1057–1060. https://doi.org/10.1002/slct.201600313.

(193) Linton, B.; Hamilton, A. D. Calorimetric Investigation of Guanidinium-Carboxylate Interactions. *Tetrahedron* **1999**, *55* (19), 6027–6038. https://doi.org/10.1016/S0040-4020(99)00277-X.

(194) Schug, K. A.; Lindner, W. Noncovalent Binding between Guanidinium and Anionic Groups: Focus on Biological- and Synthetic-Based Arginine/Guanidinium

Interactions with Phosph[on]Ate and Sulf[on]Ate Residues. *Chem. Rev.* **2005**, *105* (1), 67–114. https://doi.org/10.1021/cr040603j.

(195) Rether, C.; Schmuck, C. Carboxylate Binding by Indole-Based Guanidinium Receptors: Acylguanidinium Cations Are Better than Aromatic Guanidinium Cations. *European Journal of Organic Chemistry* **2011**, *2011* (8), 1459–1466. https://doi.org/10.1002/ejoc.201001465.

(196) Muttathukattil, A. N.; Srinivasan, S.; Halder, A.; Reddy, G. Role of Guanidinium-Carboxylate Ion Interaction in Enzyme Inhibition with Implications for Drug Design. *J. Phys. Chem. B* **2019**, *123* (44), 9302–9311. https://doi.org/10.1021/acs.jpcb.9b06130.

(197) Heberle, F. A.; Feigenson, G. W. Phase Separation in Lipid Membranes. *Cold Spring Harb Perspect Biol* **2011**, *3* (4), a004630. https://doi.org/10.1101/cshperspect.a004630.

(198) Del Frate, G.; Macchiagodena, M.; Akhunzada, M. J.; D'Autilia, F.; Catte, A.; Bhattacharjee, N.; Barone, V.; Cardarelli, F.; Brancato, G. Probing Liquid-Ordered and Disordered Phases in Lipid Model Membranes: A Combined Theoretical and Spectroscopic Study of a Fluorescent Molecular Rotor. *J. Phys. Chem. B* **2022**, *126* (2), 480–491. https://doi.org/10.1021/acs.jpcb.1c08324.

(199) Xu, L.; Anchordoquy, T. J. Cholesterol Domains in Cationic Lipid/DNA Complexes Improve Transfection. *Biochimica et Biophysica Acta (BBA) - Biomembranes* **2008**, *1778* (10), 2177–2181. https://doi.org/10.1016/j.bbamem.2008.04.009.

(200) Campbell, R. B.; Balasubramanian, S. V.; Straubinger, R. M. Phospholipid-Cationic Lipid Interactions: Influences on Membrane and Vesicle Properties. *Biochimica et Biophysica Acta (BBA) - Biomembranes* **2001**, *1512* (1), 27–39. https://doi.org/10.1016/S0005-2736(01)00290-5.

(201) Xu, J.; Adepoju, S.; Pandey, S.; Pérez Tetuán, J.; Williams, M.; Abdelmessih, R. G.; Auguste, D. T.; Hung, F. R. Effects of Lipid Headgroups on the Mechanical Properties and In Vitro Cellular Internalization of Liposomes. *Langmuir* **2025**, *41* (4), 2600–2618. https://doi.org/10.1021/acs.langmuir.4c04363.

(202) Hedger, G.; Rouse, S. L.; Domański, J.; Chavent, M.; Koldsø, H.; Sansom, M. S. P. Lipid-Loving ANTs: Molecular Simulations of Cardiolipin Interactions and the Organization of the Adenine Nucleotide Translocase in Model Mitochondrial Membranes. *Biochemistry* **2016**, *55* (45), 6238–6249. https://doi.org/10.1021/acs.biochem.6b00751.

(203) Gudyka, J.; Ceja-Vega, J.; Krmic, M.; Porteus, R.; Lee, S. The Role of Lipid Intrinsic Curvature in the Droplet Interface Bilayer. *Langmuir* **2024**, *40* (22), 11428–11435. https://doi.org/10.1021/acs.langmuir.4c00270.

(204) Campelo, F.; Arnarez, C.; Marrink, S. J.; Kozlov, M. M. Helfrich Model of Membrane Bending: From Gibbs Theory of Liquid Interfaces to Membranes as Thick Anisotropic Elastic Layers. *Advances in Colloid and Interface Science* **2014**, *208*, 25–33. https://doi.org/10.1016/j.cis.2014.01.018.

(205) Gomez-Vega, J.; Vasquez-Cornejo, A.; Juárez-Sánchez, O.; Corona-Martínez, D. O.; Ochoa-Terán, A.; López-Gastelum, K. A.; Sotelo-Mundo, R. R.; Santacruz-

Ortega, H.; Gálvez-Ruiz, J. C.; Pérez-González, R.; Lara, K. O. Thiourea-Based Receptors for Anion Recognition and Signaling. *ACS Omega* **2024**, *9* (4), 4412–4422. https://doi.org/10.1021/acsomega.3c06861.

(206) Morakot, N.; Rakrai, W.; Keawwangchai, S.; Kaewtong, C.; Wanno, B. Design and Synthesis of Thiourea Based Receptor Containing Naphthalene as Oxalate Selective Sensor. *J Mol Model* **2010**, *16* (1), 129–136. https://doi.org/10.1007/s00894-009-0526-x.

APPENDIX

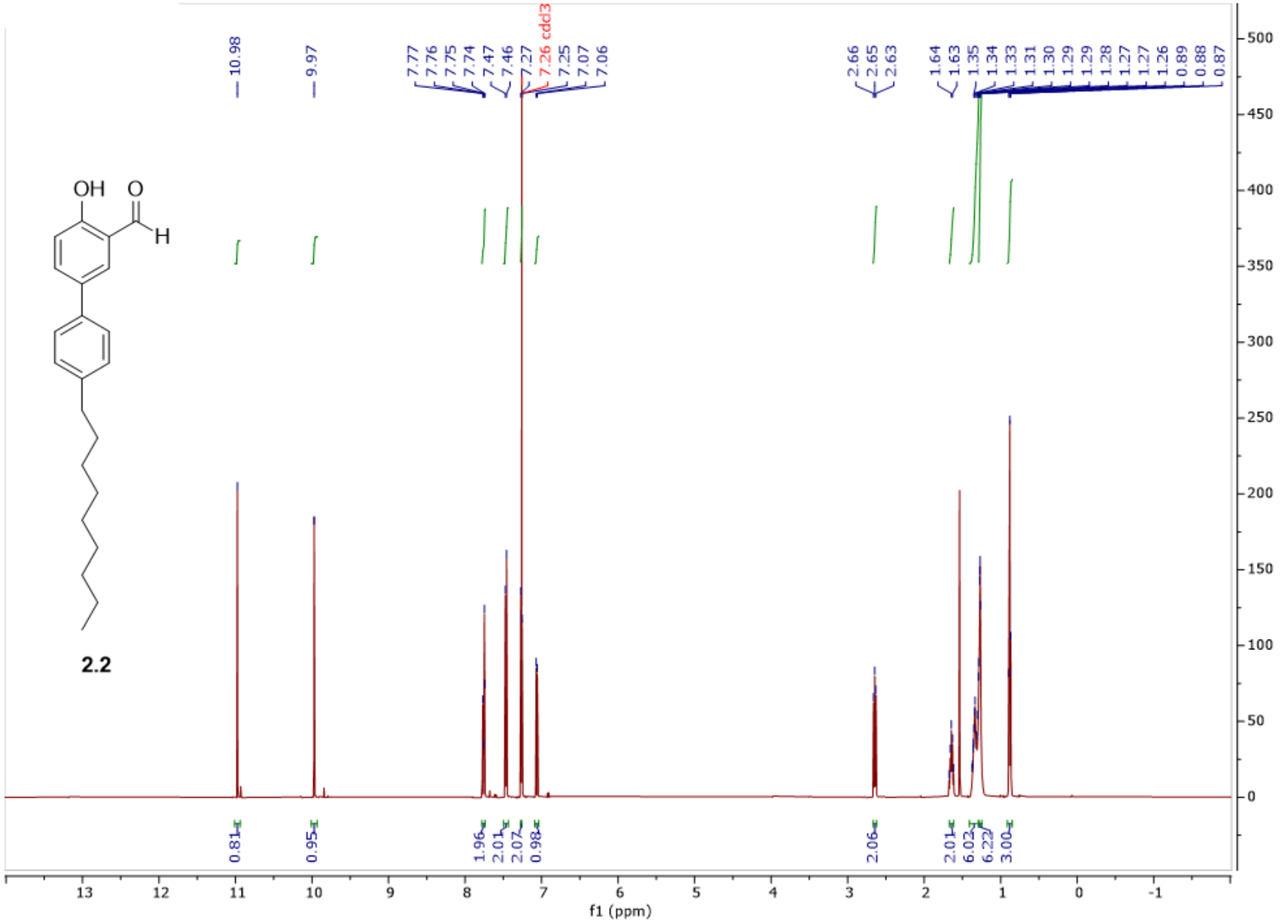
OH
O
H
2.2
10.98
9.97
7.77
7.76
7.75
7.74
7.47
7.46
7.27
7.26 cdd3
7.25
7.07
7.06
2.66
2.65
2.63
1.64
1.63
1.35
1.34
1.33
1.31
1.30
1.29
1.29
1.28
1.27
1.27
1.26
0.89
0.88
0.87
0.81
0.95
1.96
2.01
2.07
0.98
2.06
2.01
6.03
6.22
3.00
f1 (ppm)

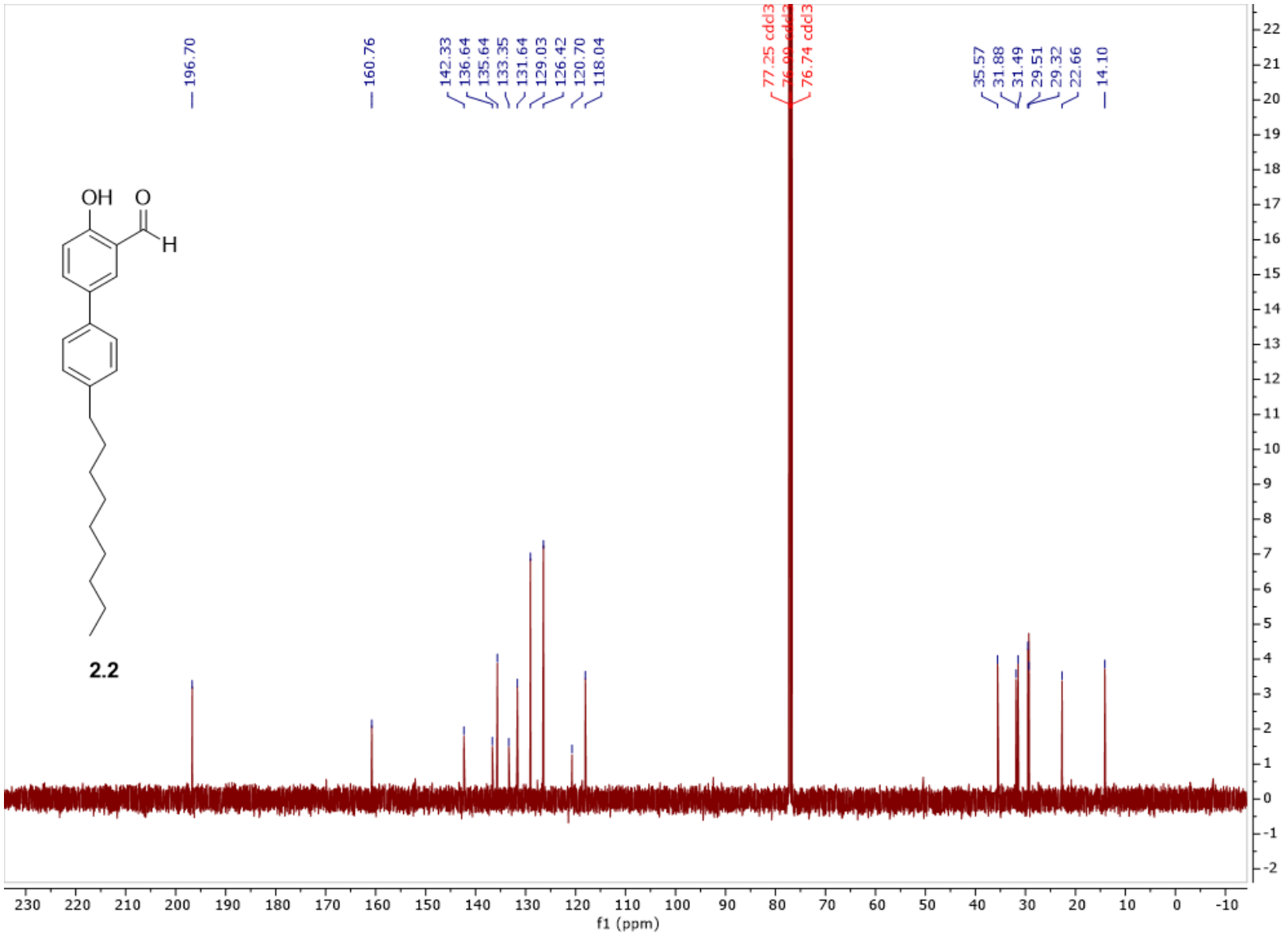
196.70
160.76
142.33
136.64
135.64
133.35
131.64
129.03
126.42
120.70
118.04
77.25 cdd3
76.74 cdd3
35.57
31.88
31.49
29.51
29.32
22.66
14.10
OH
O
H
2.2
f1 (ppm)

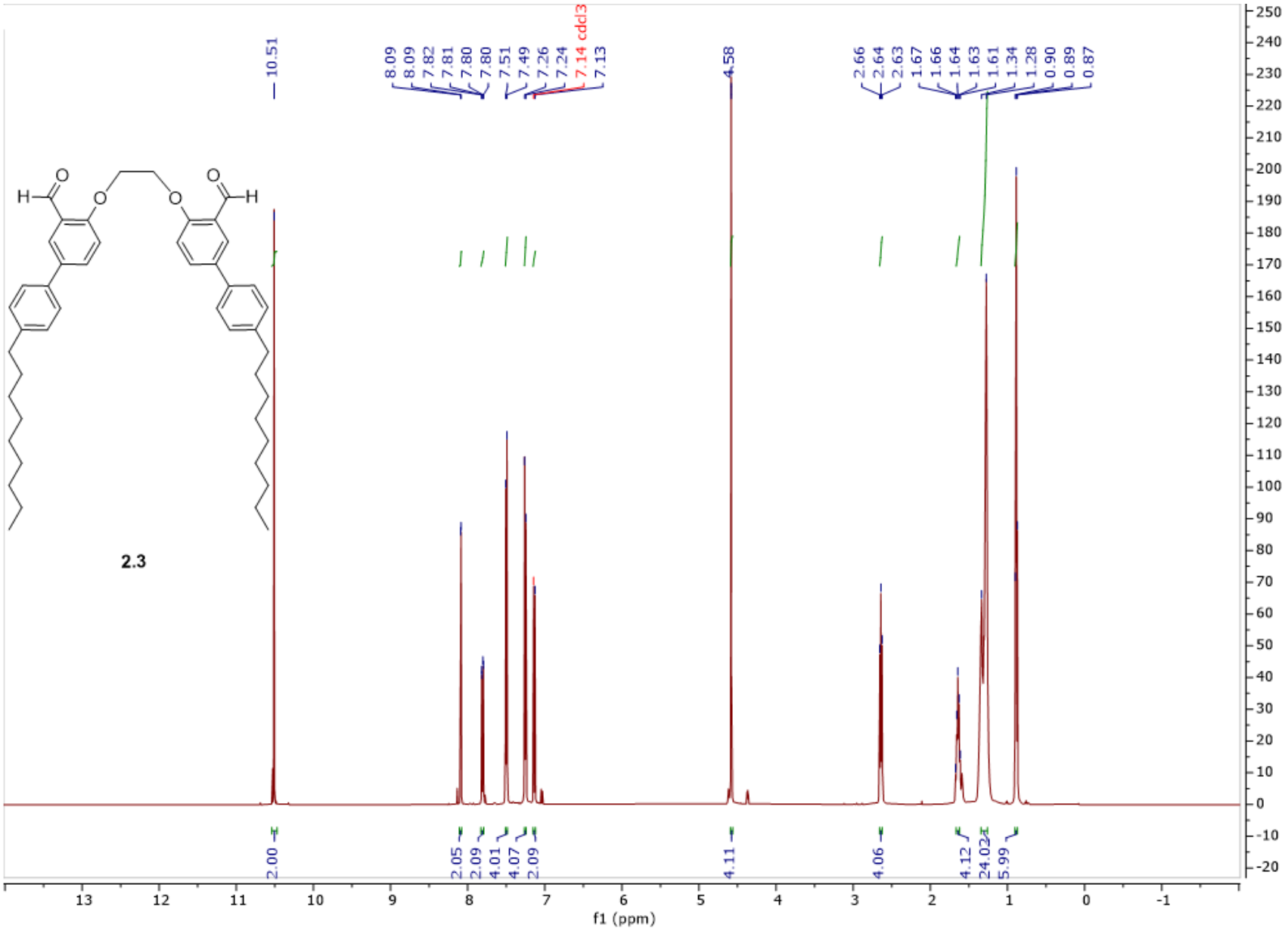
10.51
8.09
8.09
7.82
7.81
7.80
7.80
7.51
7.49
7.26
7.24
7.14 cdcl3
7.13
4.58
2.66
2.64
2.63
1.67
1.66
1.64
1.63
1.61
1.34
1.28
0.90
0.89
0.87
2.00
2.05
2.09
4.01
4.07
2.09
4.11
4.06
4.12
24.02
5.99
f1 (ppm)
2.3

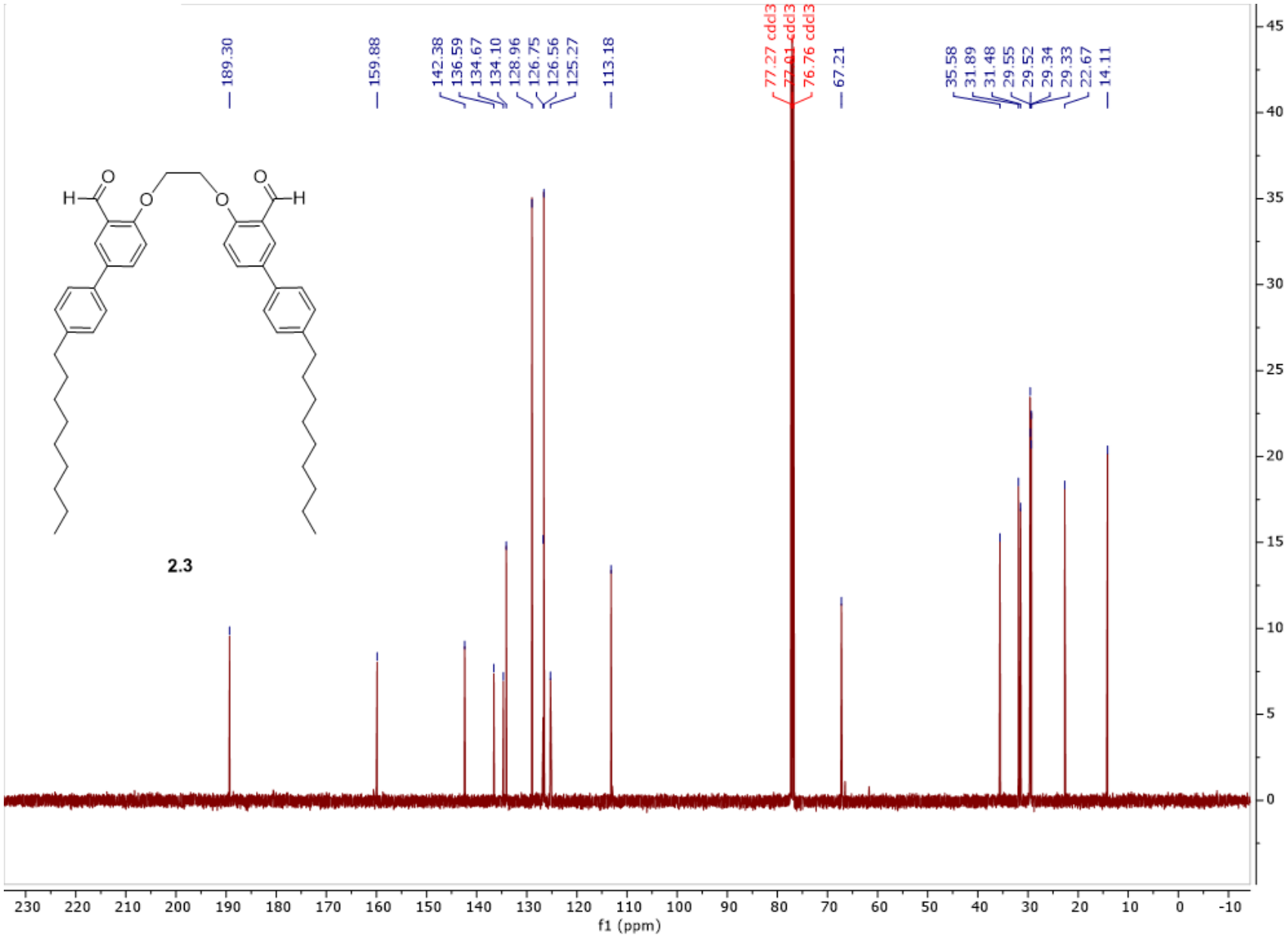
189.30
159.88
142.38
136.59
134.67
134.10
128.96
126.75
126.56
125.27
113.18
77.27 cdcl3
77.01 cdcl3
76.76 cdcl3
67.21
35.58
31.89
31.48
29.55
29.52
29.34
29.33
22.67
14.11
2.3
f1 (ppm)

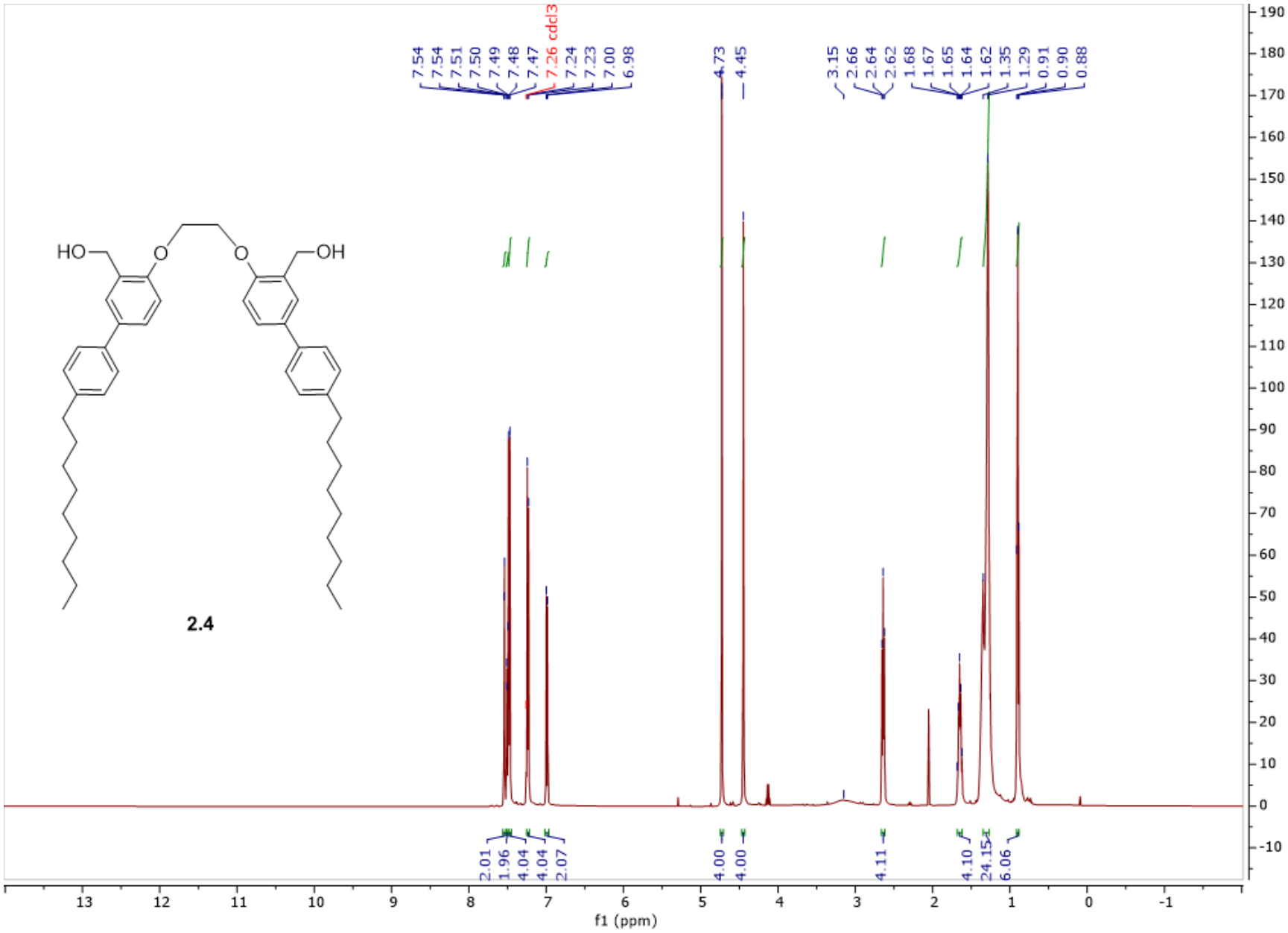
7.54
7.54
7.51
7.50
7.49
7.48
7.47
7.26 cdcl3
7.24
7.23
7.00
6.98
4.73
4.45
3.15
2.66
2.64
2.62
1.68
1.67
1.65
1.64
1.62
1.35
1.29
0.91
0.90
0.88
HO
O
O
OH
2.01
1.96
4.04
4.04
2.07
4.00
4.00
4.11
4.10
24.15
6.06
f1 (ppm)

2.4

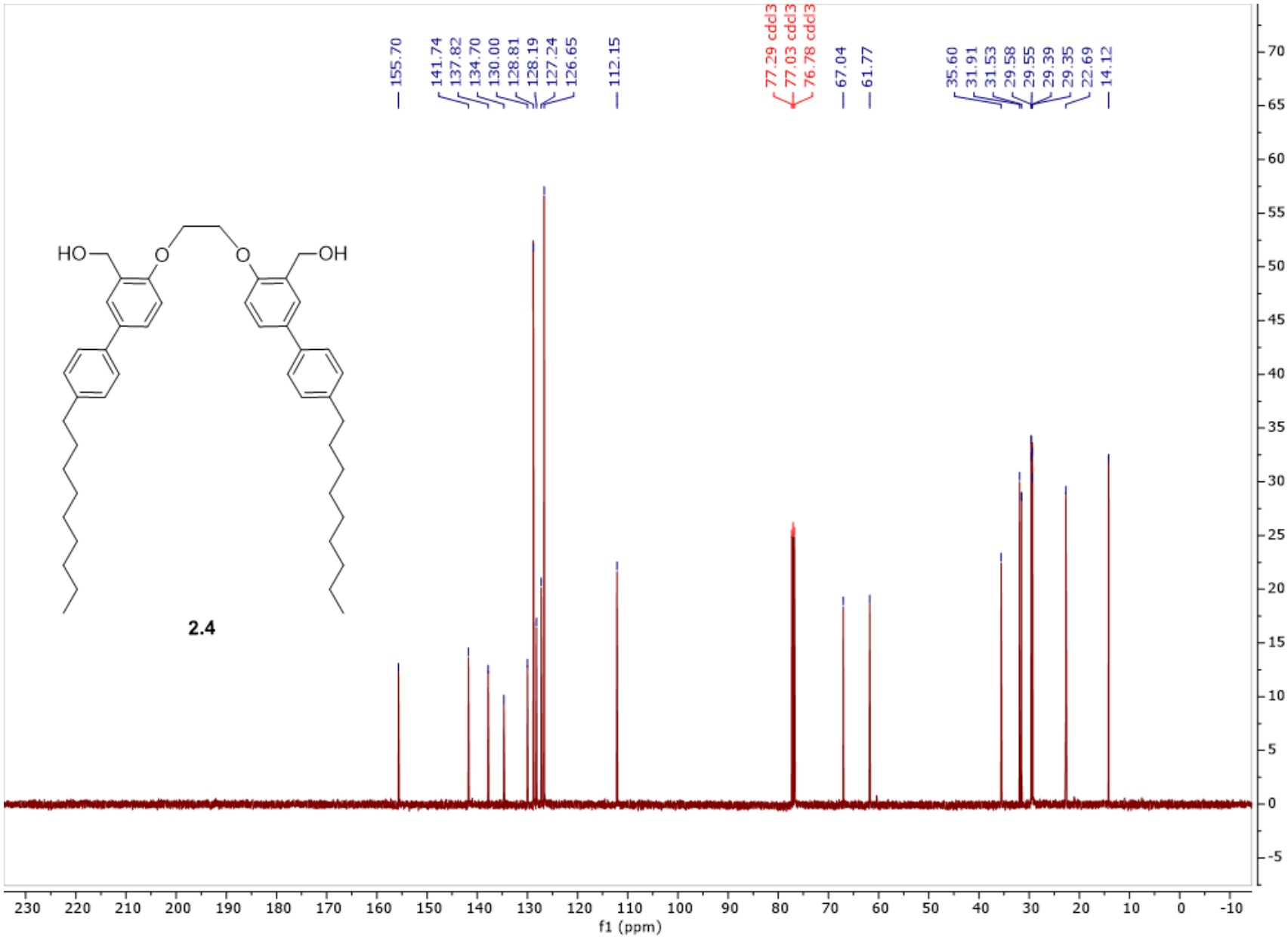
155.70
141.74
137.82
134.70
130.00
128.81
128.19
127.24
126.65
112.15
77.29 cdcl3
77.03 cdcl3
76.78 cdcl3
67.04
61.77
35.60
31.91
31.53
29.58
29.55
29.39
29.35
22.69
14.12
HO
O
O
OH
2.4
f1 (ppm)

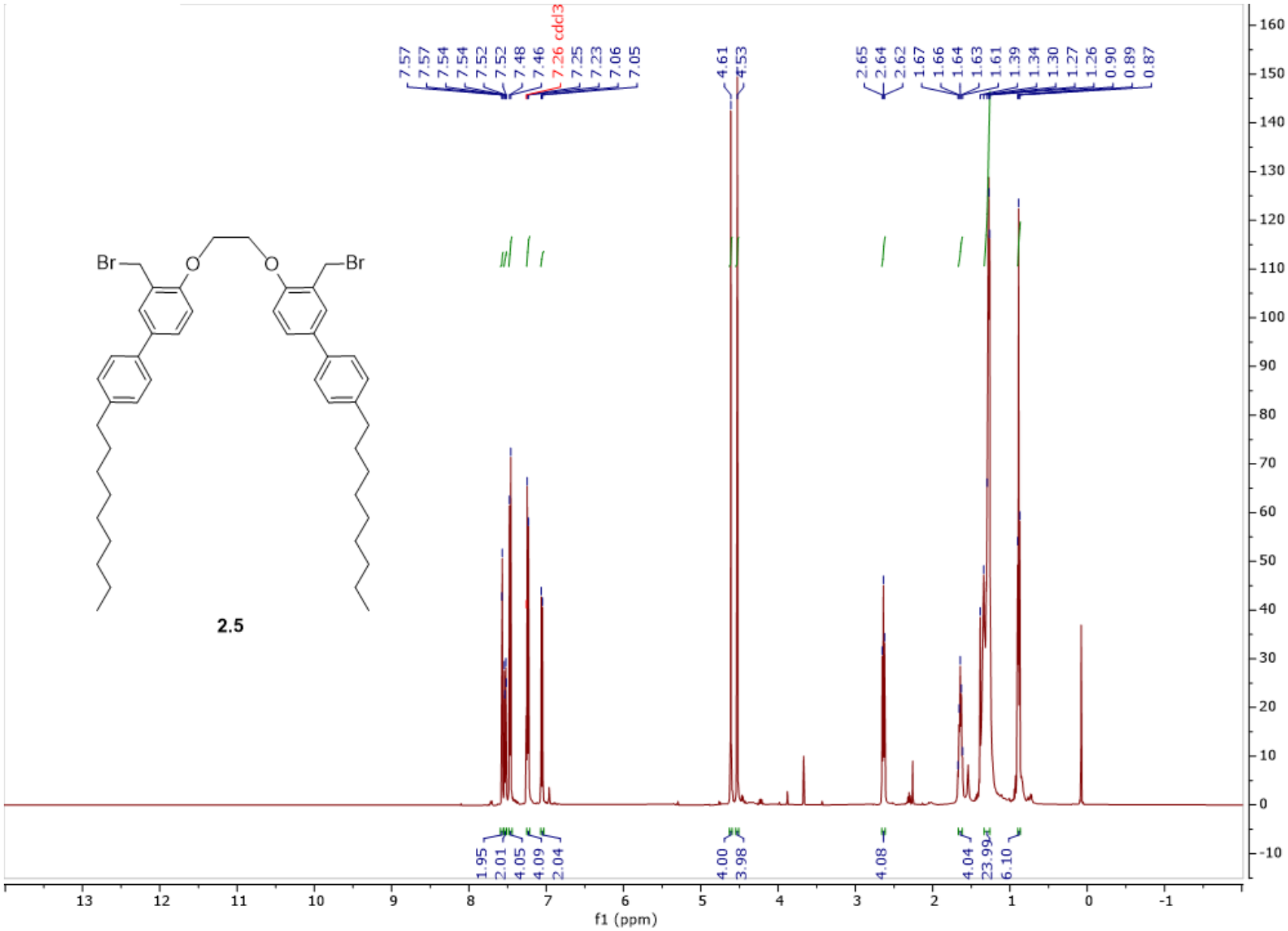
7.57
7.57
7.54
7.54
7.52
7.52
7.48
7.46
7.26 cdcl3
7.25
7.23
7.06
7.05
4.61
4.53
2.65
2.64
2.62
1.67
1.66
1.64
1.63
1.61
1.39
1.34
1.30
1.27
1.26
0.90
0.89
0.87
Br
O
O
Br
2.5
1.95
2.01
4.05
4.09
2.04
4.00
3.98
4.08
4.04
23.99
6.10
f1 (ppm)

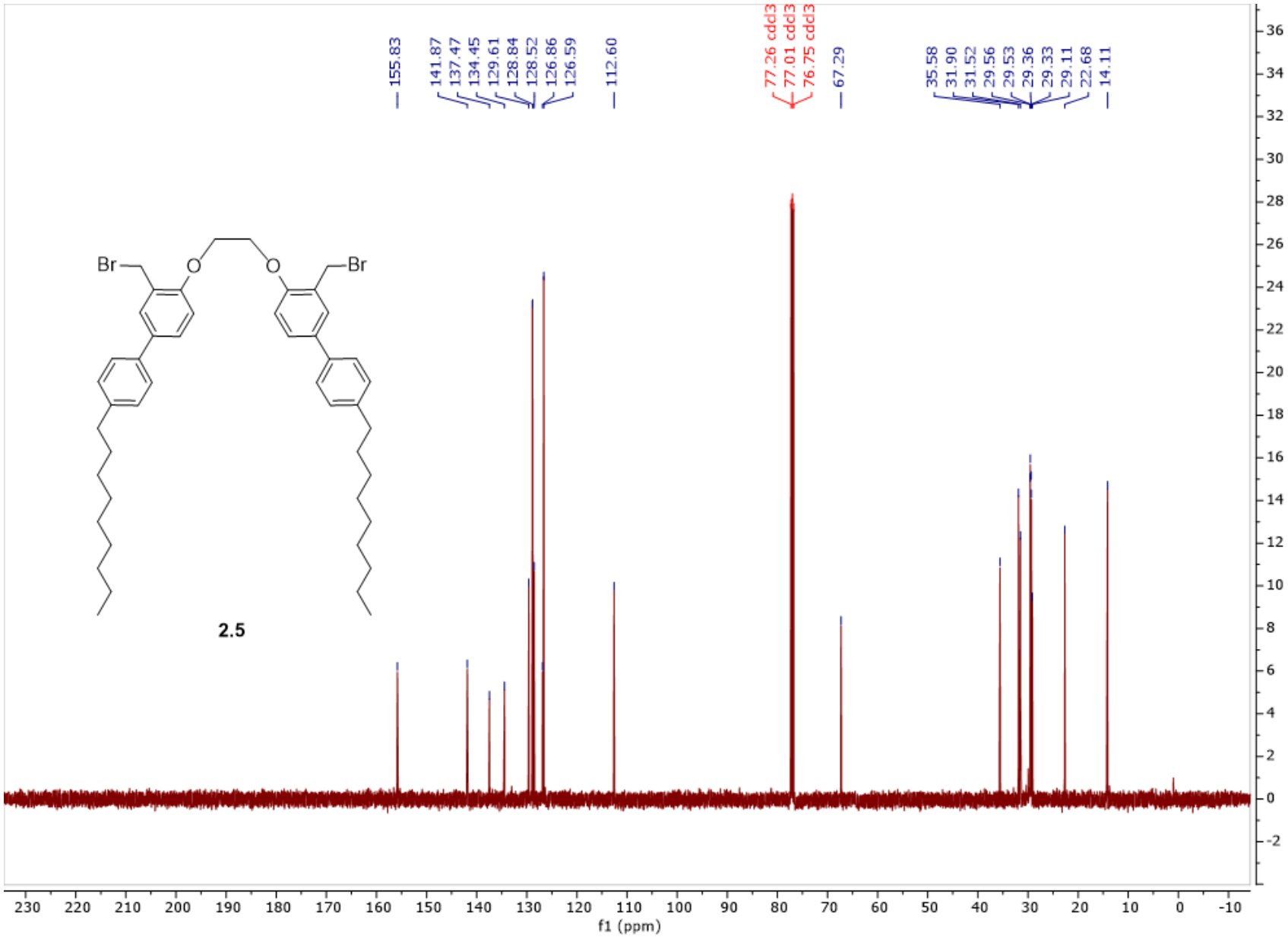
155.83
141.87
137.47
134.45
129.61
128.84
128.52
126.86
126.59
112.60
77.26 cdd3
77.01 cdd3
76.75 cdd3
67.29
35.58
31.90
31.52
29.56
29.53
29.36
29.33
29.11
22.68
14.11
Br
O
O
Br
2.5
f1 (ppm)

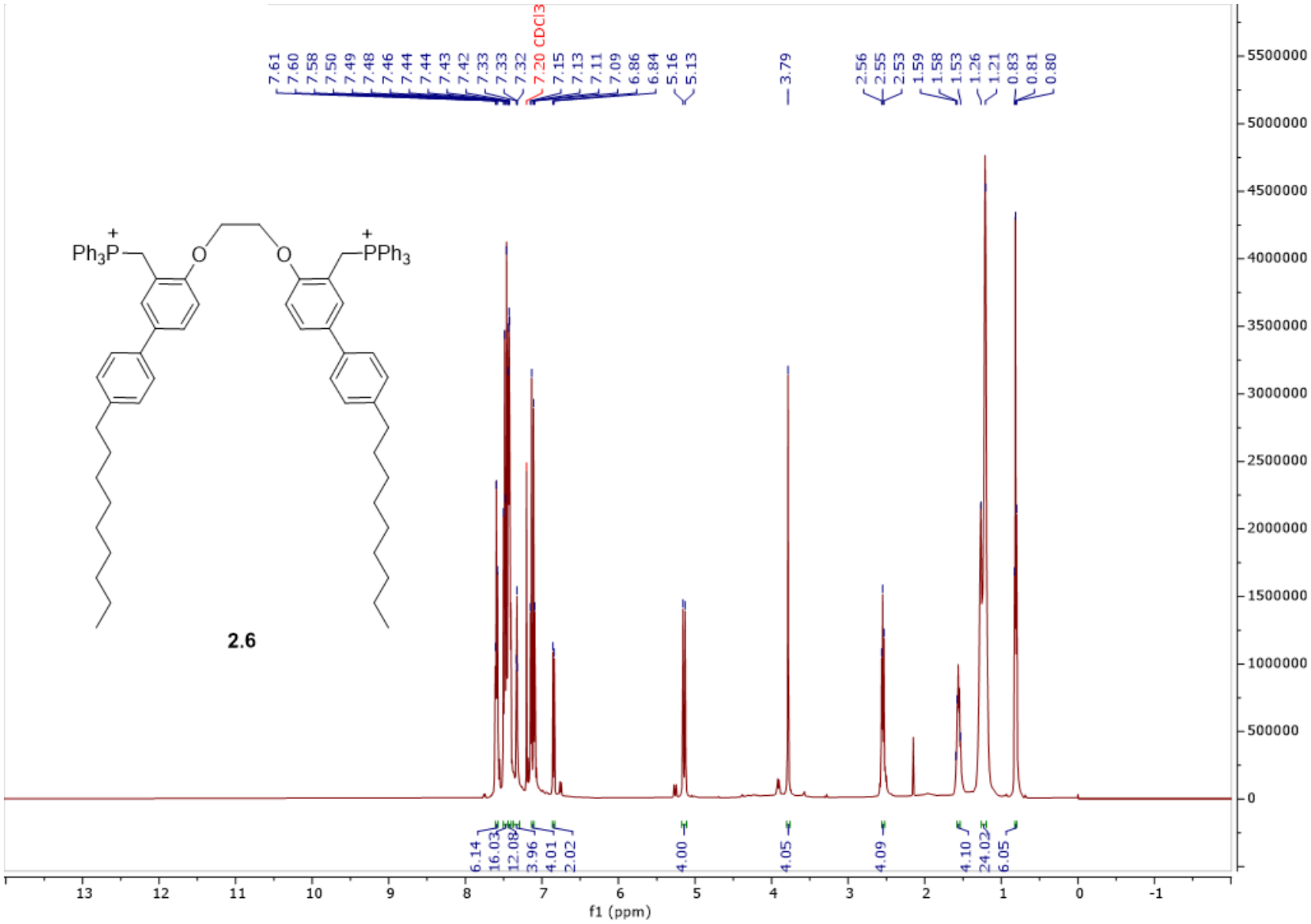
7.61
7.60
7.58
7.50
7.49
7.48
7.46
7.44
7.44
7.43
7.42
7.33
7.33
7.32
7.20 CDCl3
7.15
7.13
7.11
7.09
6.86
6.84
5.16
5.13
3.79
2.56
2.55
2.53
1.59
1.58
1.53
1.26
1.21
0.83
0.81
0.80
Ph3P
O
O
PPh3
2.6
6.14
16.03
12.08
3.96
4.01
2.02
4.00
4.05
4.09
4.10
24.02
6.05
f1 (ppm)

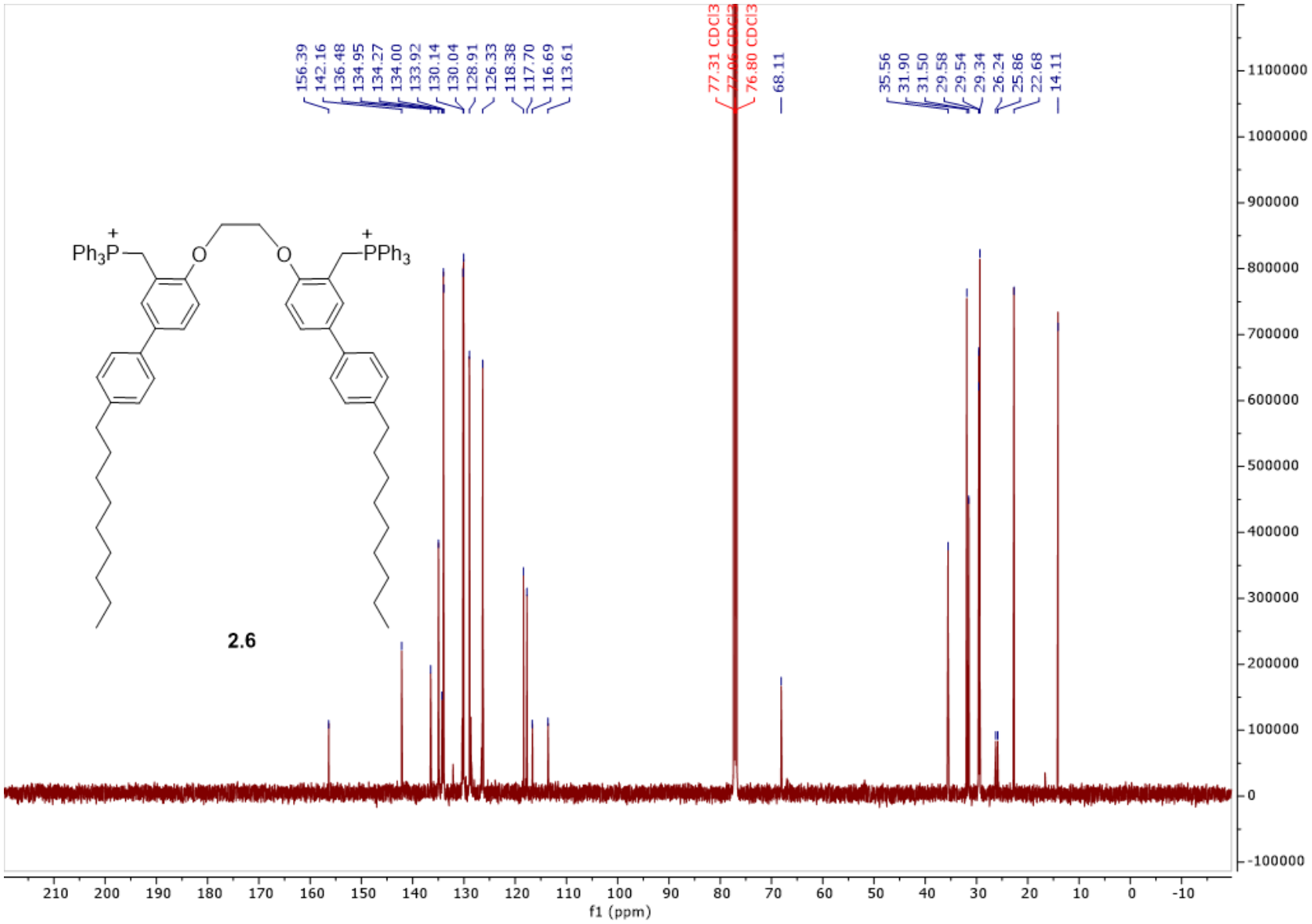
156.39
142.16
136.48
134.95
134.27
134.00
133.92
130.14
130.04
128.91
126.33
118.38
117.70
116.69
113.61
77.31 CDCl3
77.06 CDCl3
76.80 CDCl3
68.11
35.56
31.90
31.50
29.58
29.54
29.34
26.24
25.86
22.68
14.11
Ph3P
PPh3
O
O
2.6
f1 (ppm)

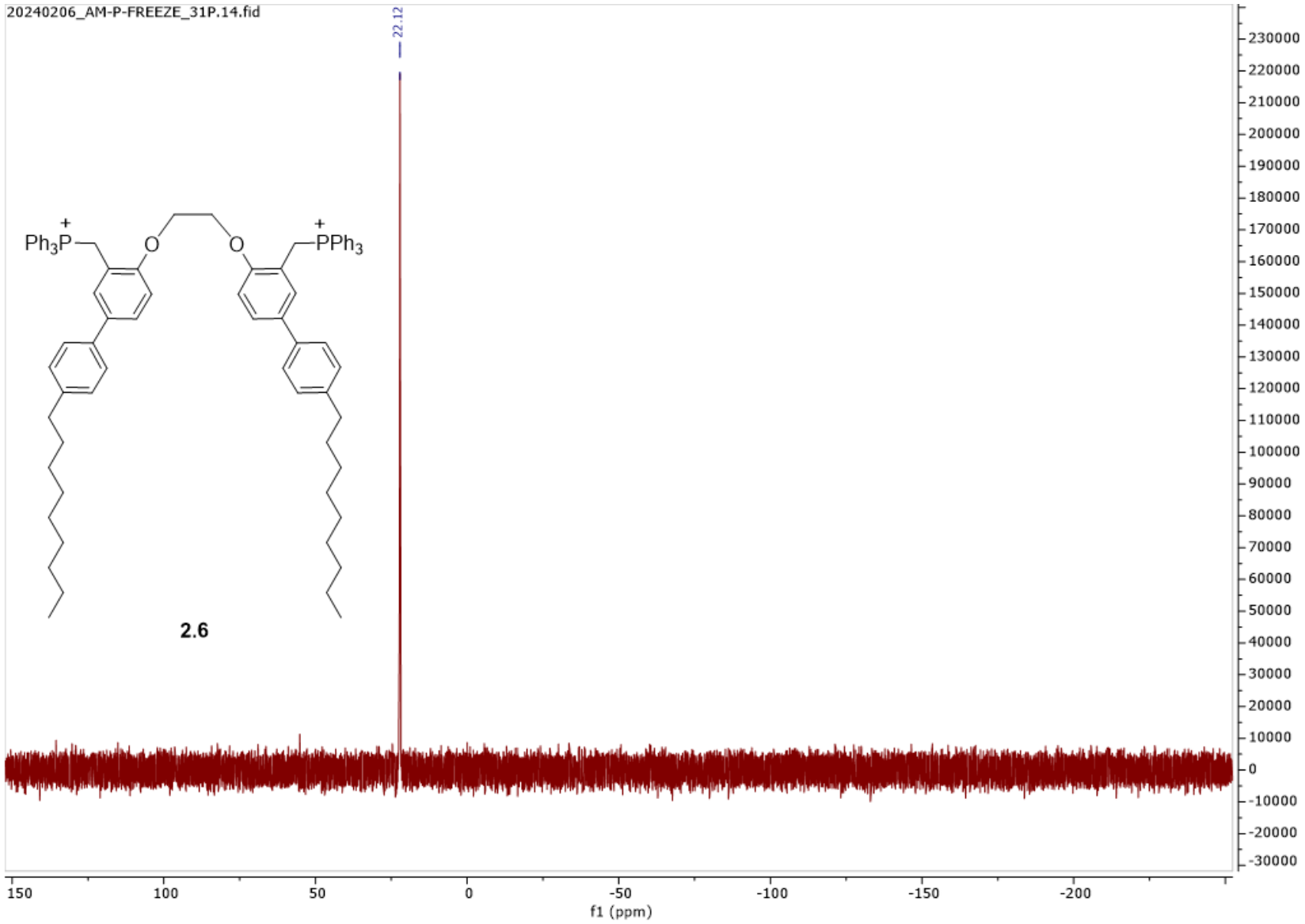
20240206_AM-P-FREEZE_31P.14.fid
22.12
Ph3P
PPh3
O
O
2.6
230000
220000
210000
200000
190000
180000
170000
160000
150000
140000
130000
120000
110000
100000
90000
80000
70000
60000
50000
40000
30000
20000
10000
0
-10000
-20000
-30000
150
100
50
0
-50
-100
-150
-200
f1 (ppm)

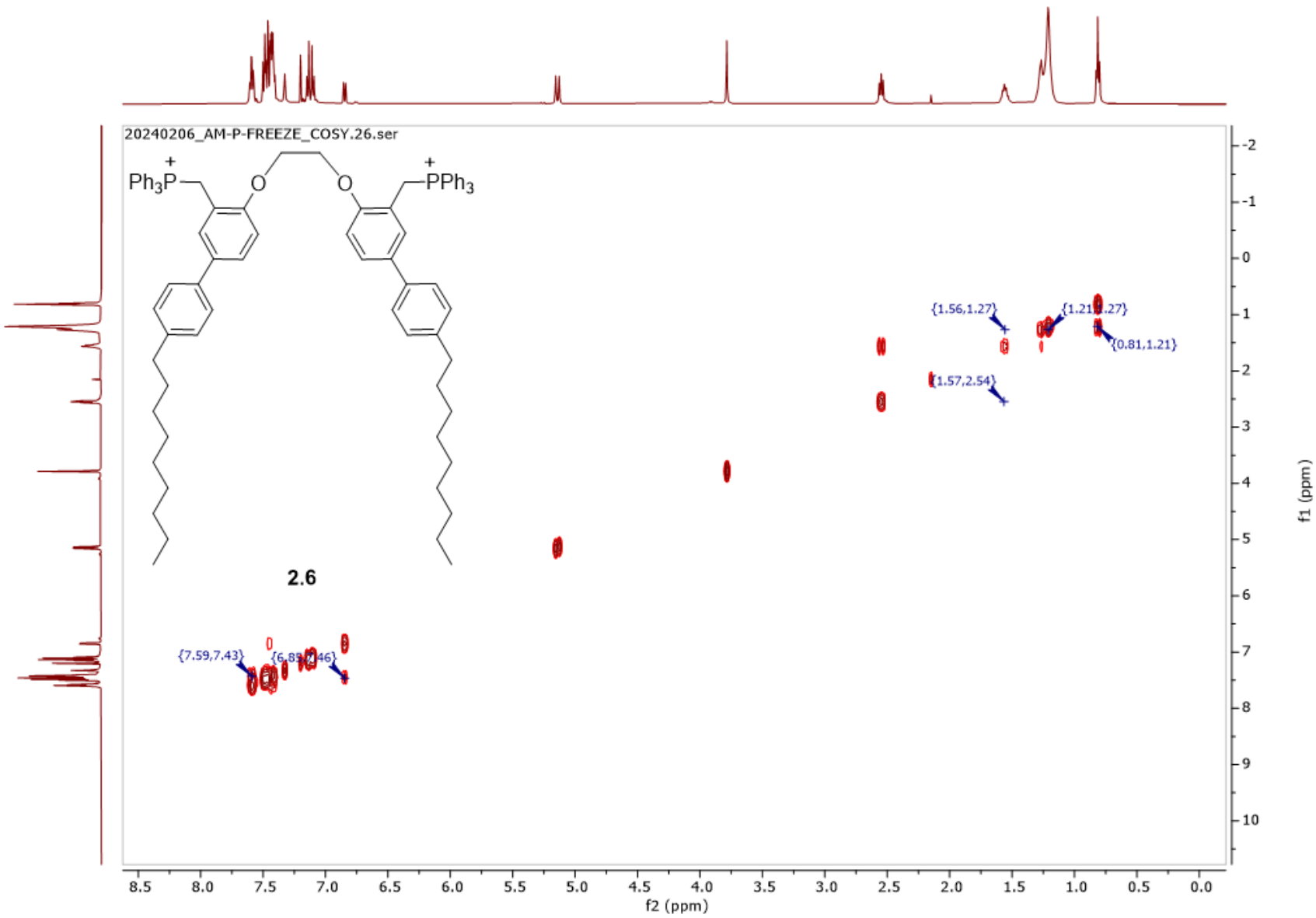
20240206_AM-P-FREEZE_COSY.26.ser
Ph3P
PPh3
O
O
2.6
{7.59,7.43}
{1.56,1.27}
{0.81,1.21}
{1.57,2.54}
f2 (ppm)
f1 (ppm)

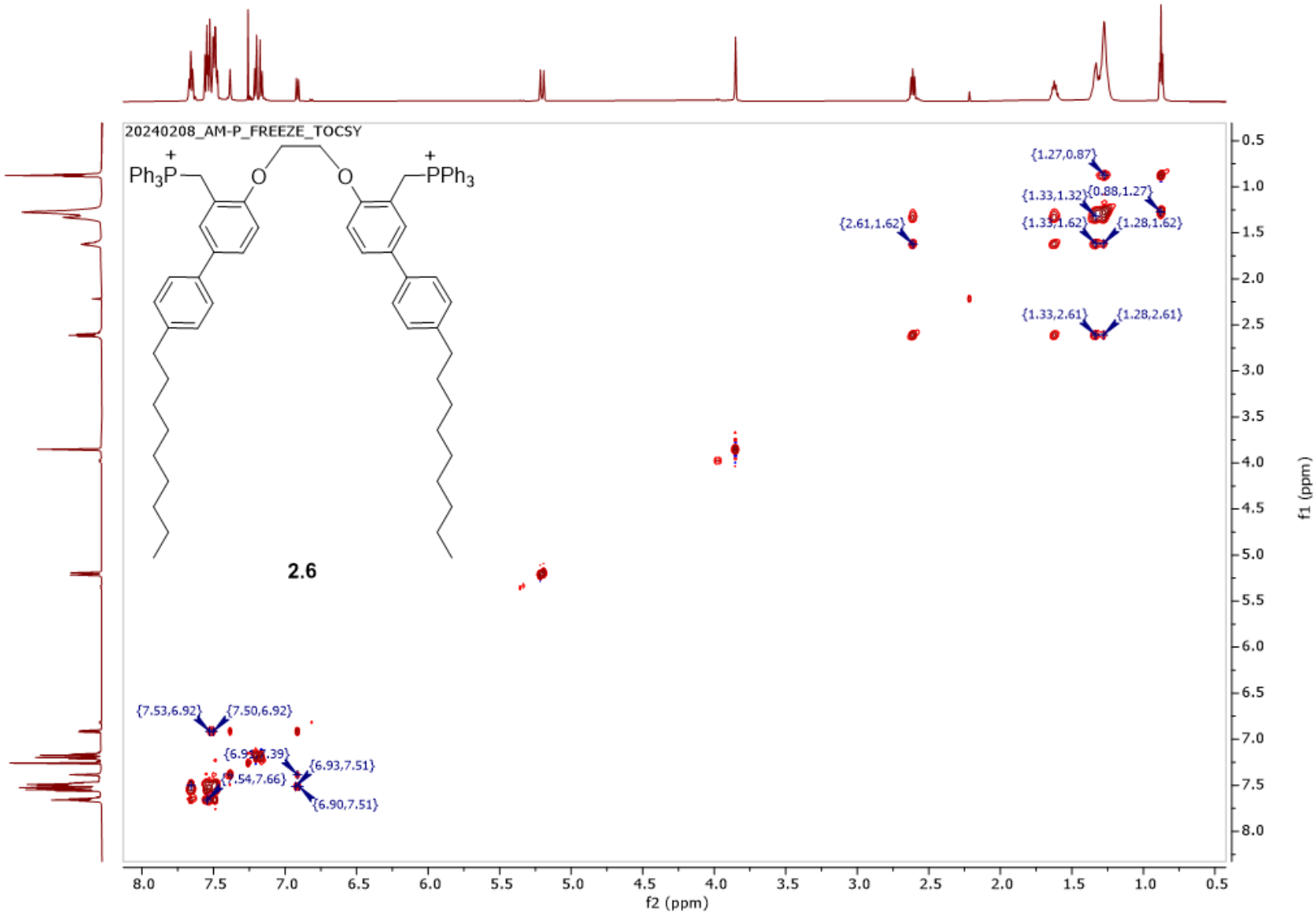
20240208_AM-P_FREEZE_TOCSY
Ph3P
O
O
PPh3
2.6
{1.27,0.87}
{1.33,1.32}
{0.88,1.27}
{1.33,1.62}
{1.28,1.62}
{2.61,1.62}
{1.33,2.61}
{1.28,2.61}
{7.53,6.92}
{7.50,6.92}
{6.93,7.51}
{6.90,7.51}
f2 (ppm)
f1 (ppm)

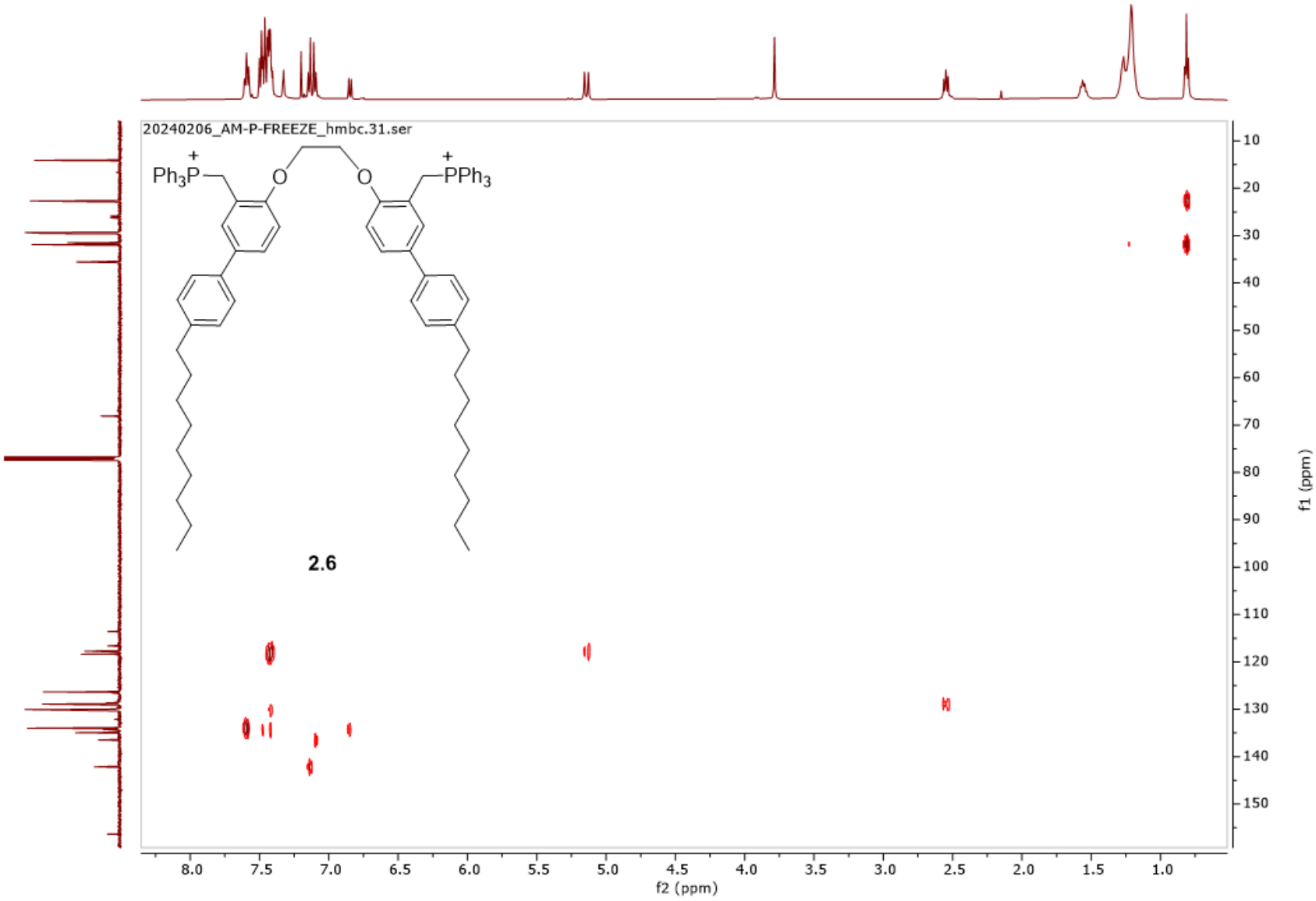
20240206_AM-P-FREEZE_hmbc.31.ser
Ph3P
O
O
PPh3
2.6
f2 (ppm)
f1 (ppm)

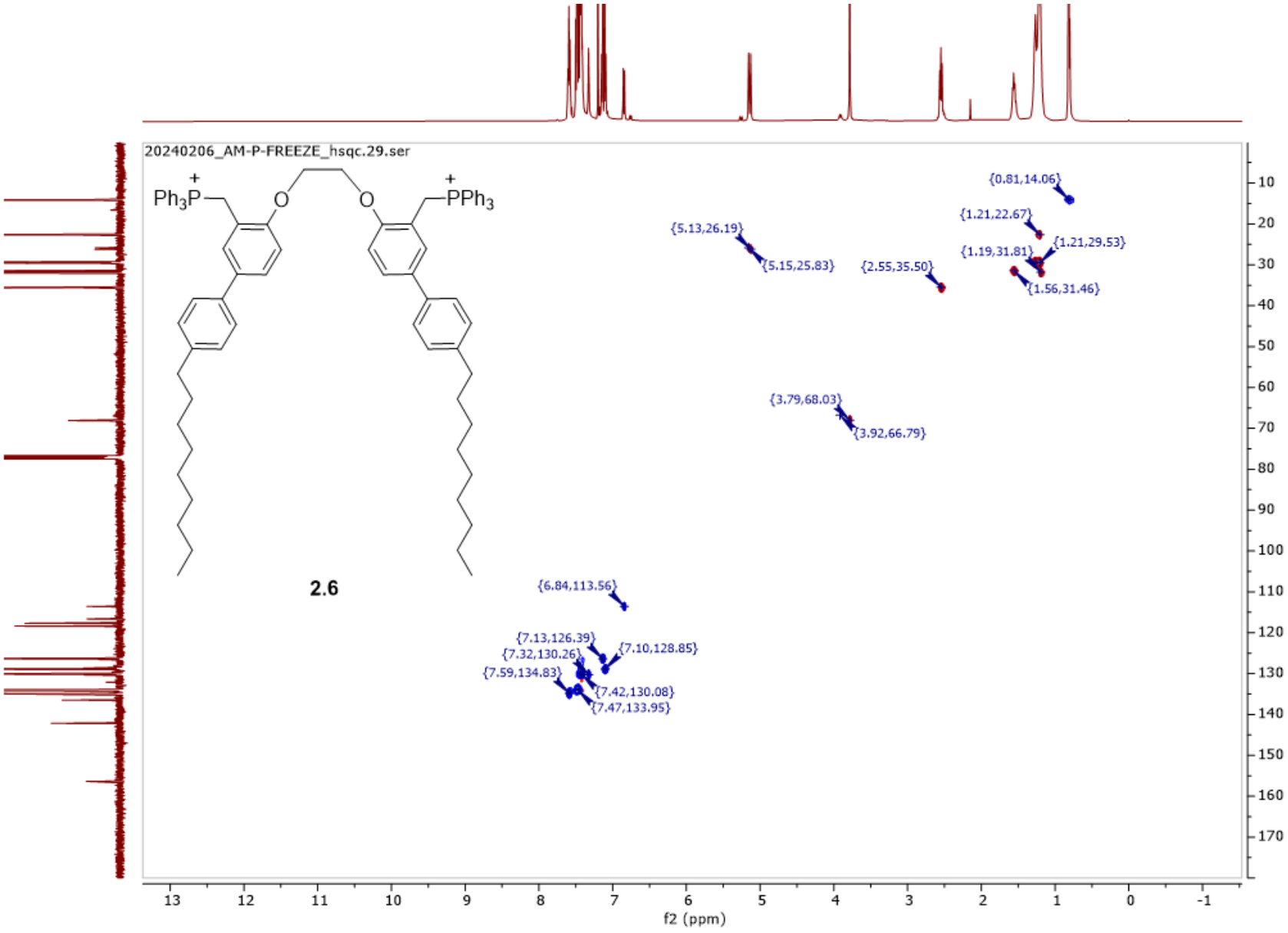
20240206_AM-P-FREEZE_hsqc.29.ser
Ph3P
PPh3
O
O
2.6
{0.81,14.06}
{1.21,22.67}
{1.21,29.53}
{1.19,31.81}
{1.56,31.46}
{5.13,26.19}
{5.15,25.83}
{2.55,35.50}
{3.79,68.03}
{3.92,66.79}
{6.84,113.56}
{7.13,126.39}
{7.32,130.26}
{7.10,128.85}
{7.59,134.83}
{7.42,130.08}
{7.47,133.95}
f2 (ppm)

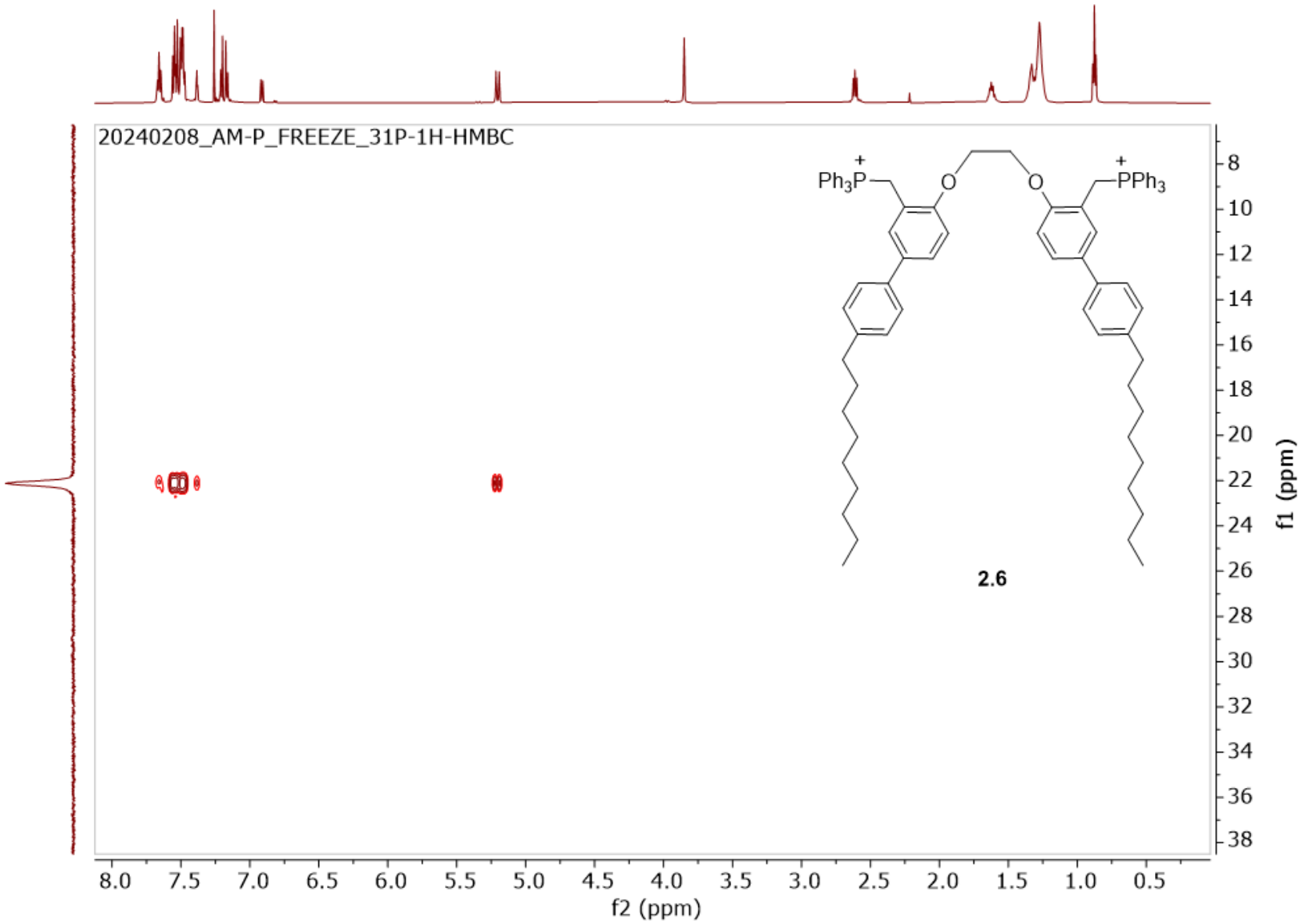
20240208_AM-P_FREEZE_31P-1H-HMBC
Ph3P
O
O
PPh3
2.6
f1 (ppm)
f2 (ppm)

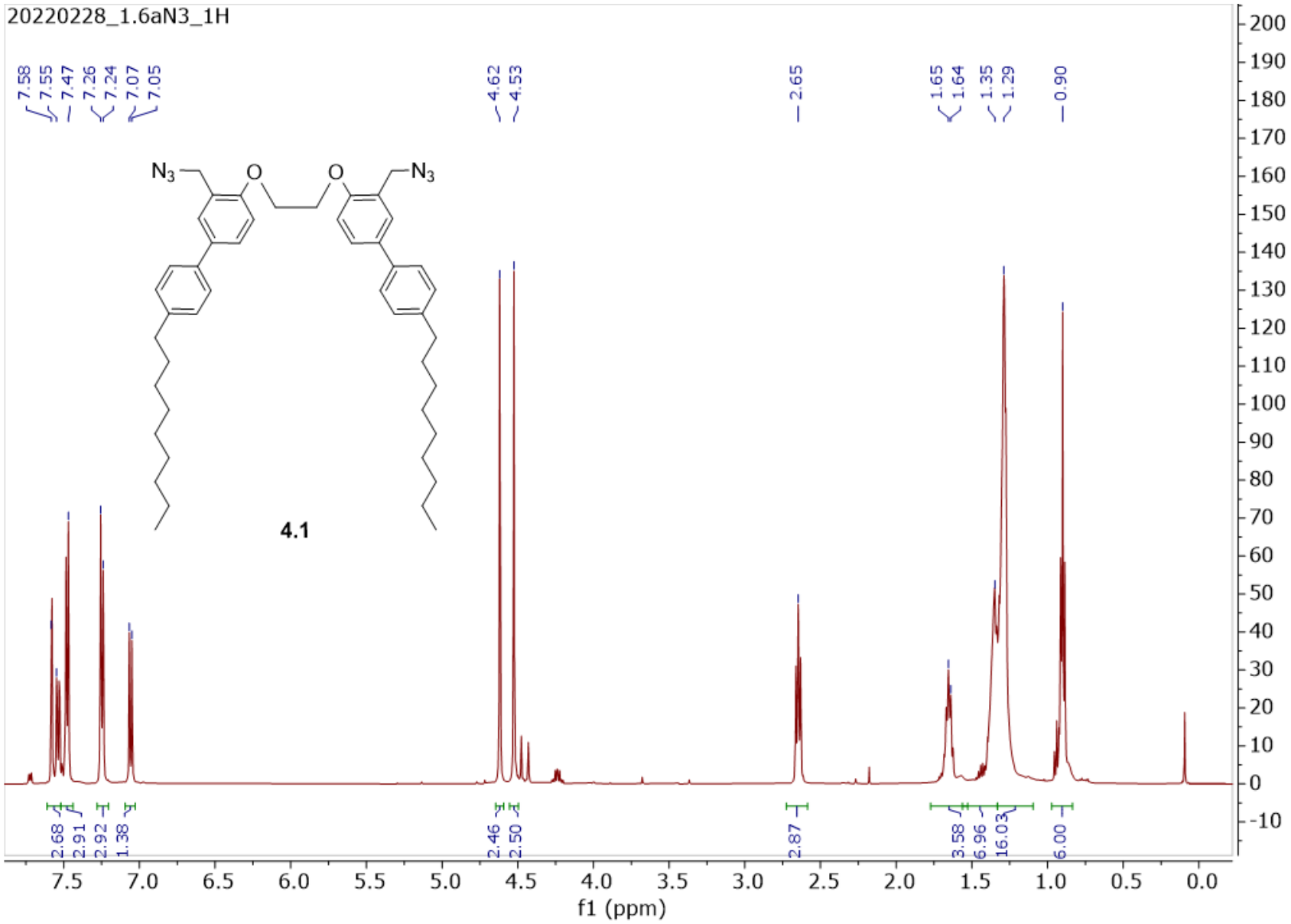
20220228_1.6aN3_1H
7.58
7.55
7.47
7.26
7.24
7.07
7.05
4.62
4.53
2.65
1.65
1.64
1.35
1.29
0.90
N3
O
O
N3
4.1
2.68
2.91
2.92
1.38
2.46
2.50
2.87
3.58
6.96
16.03
6.00
f1 (ppm)

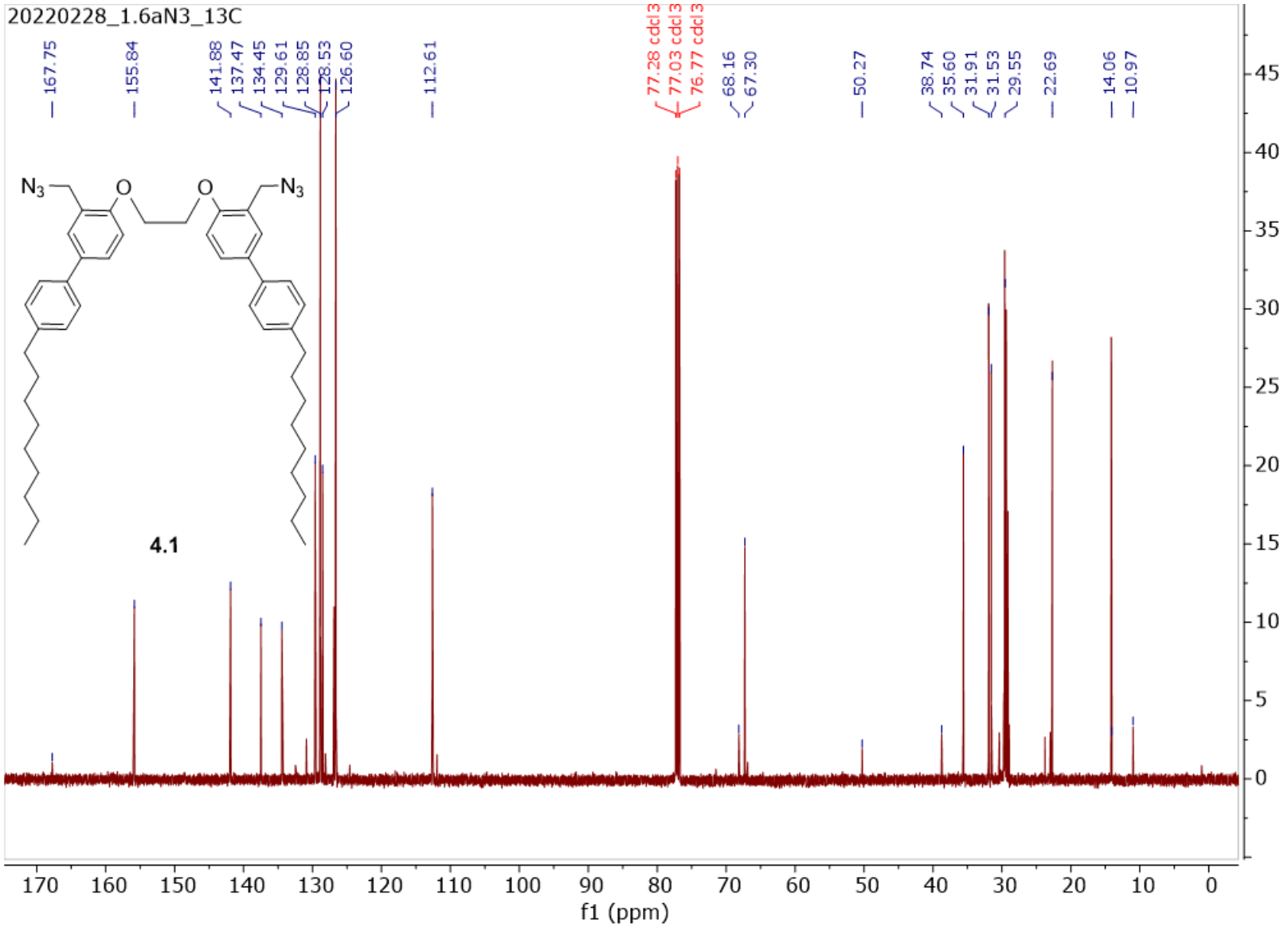
20220228_1.6aN3_13C
167.75
155.84
141.88
137.47
134.45
129.61
128.85
128.53
126.60
112.61
77.28 cdcl3
77.03 cdcl3
76.77 cdcl3
68.16
67.30
50.27
38.74
35.60
31.91
31.53
29.55
22.69
14.06
10.97
N3
O
O
N3
4.1
f1 (ppm)

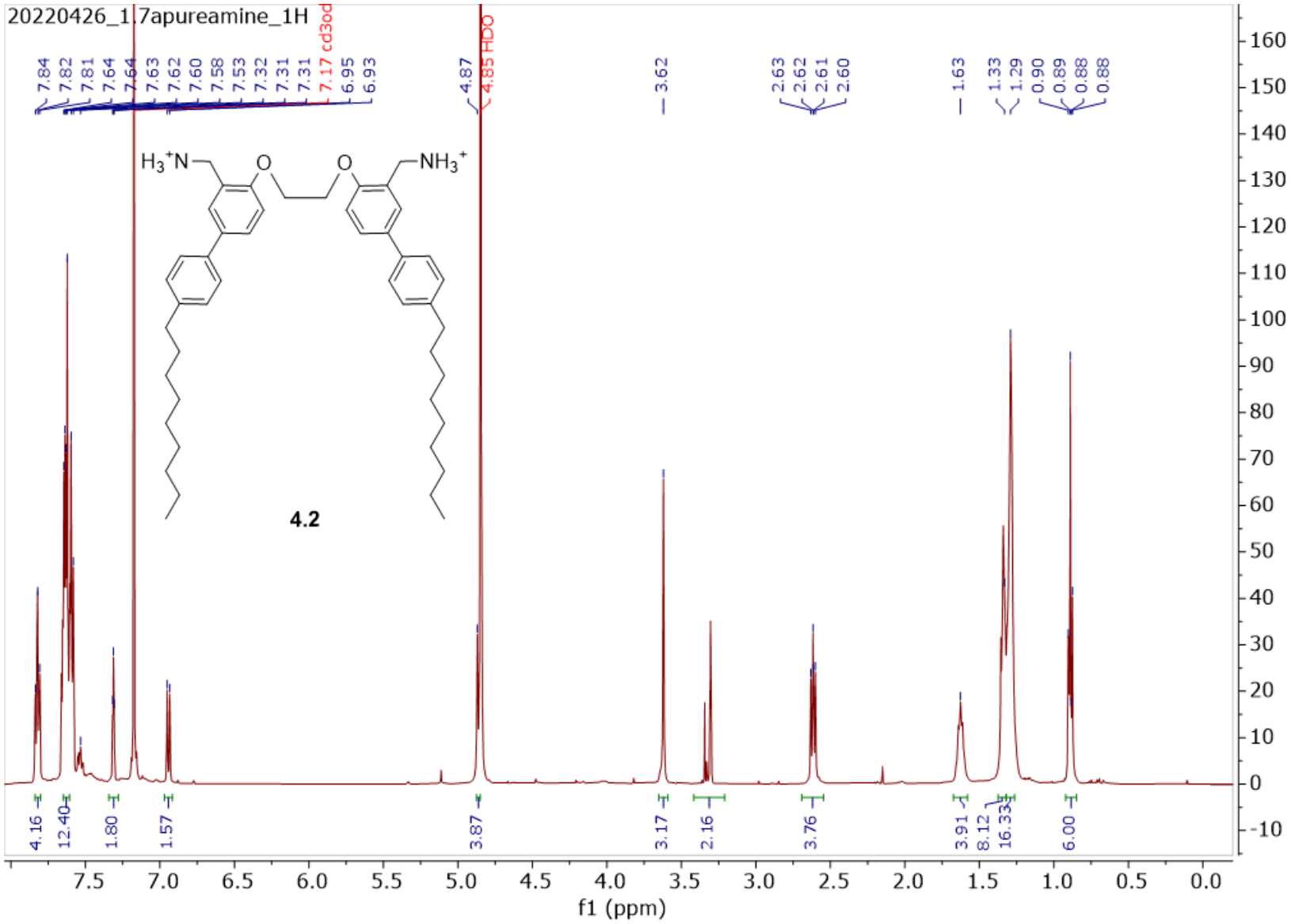
20220426_1.7apureamine_1H
7.84
7.82
7.81
7.64
7.64
7.63
7.62
7.60
7.58
7.53
7.32
7.31
7.31
7.17 cd3od
6.95
6.93
4.87
4.85 HDO
3.62
2.63
2.62
2.61
2.60
1.63
1.33
1.29
0.90
0.89
0.88
0.88
H3+N
O
O
NH3+
4.2
4.16
12.40
1.80
1.57
3.87
3.17
2.16
3.76
3.91
8.12
16.33
6.00
f1 (ppm)

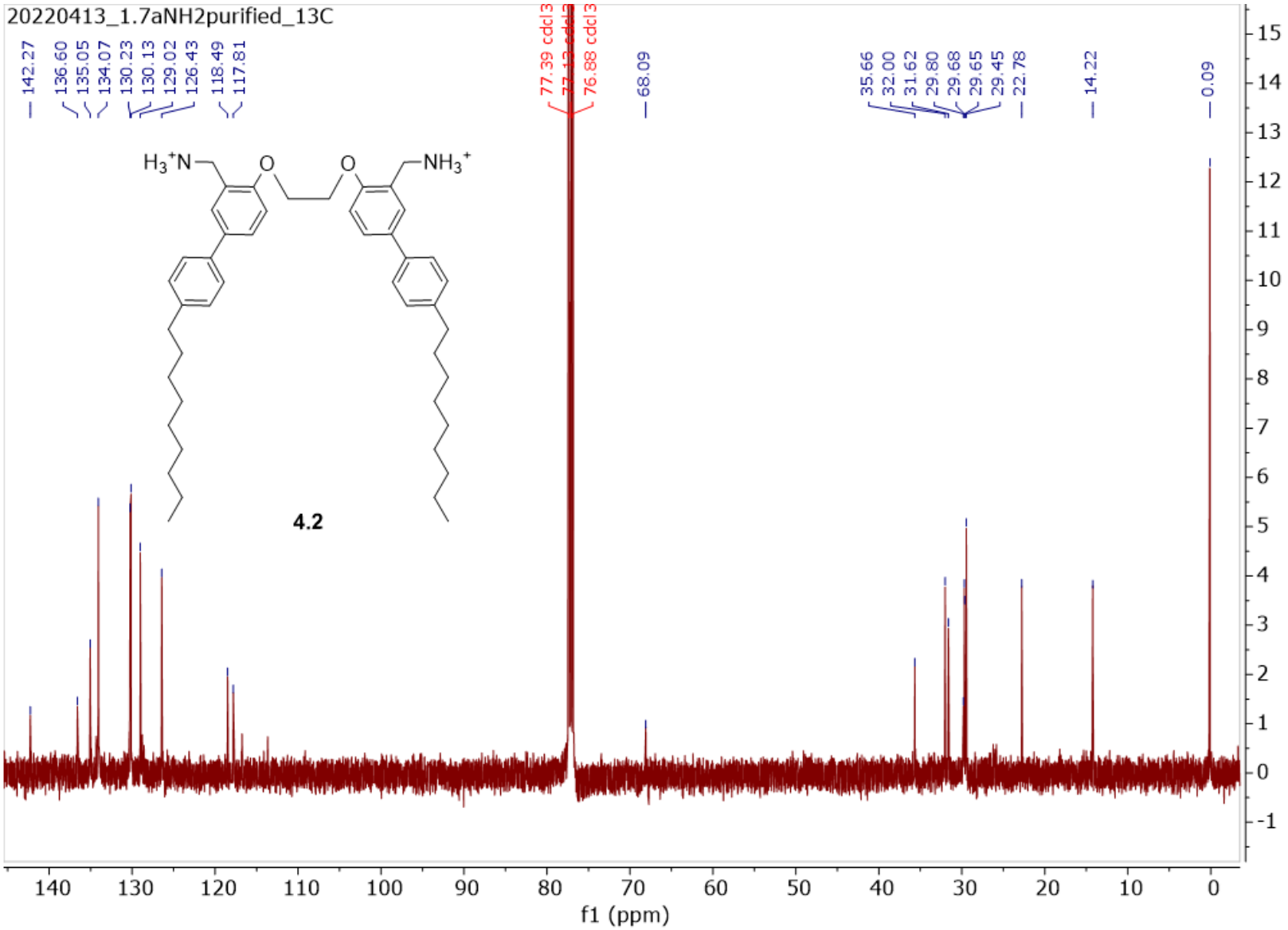
20220413_1.7aNH2purified_13C
142.27
136.60
135.05
134.07
130.23
130.13
129.02
126.43
118.49
117.81
77.39 cdcl3
76.88 cdcl3
68.09
35.66
32.00
31.62
29.80
29.68
29.65
29.45
22.78
14.22
0.09
H3+N
O
O
NH3+
4.2
f1 (ppm)

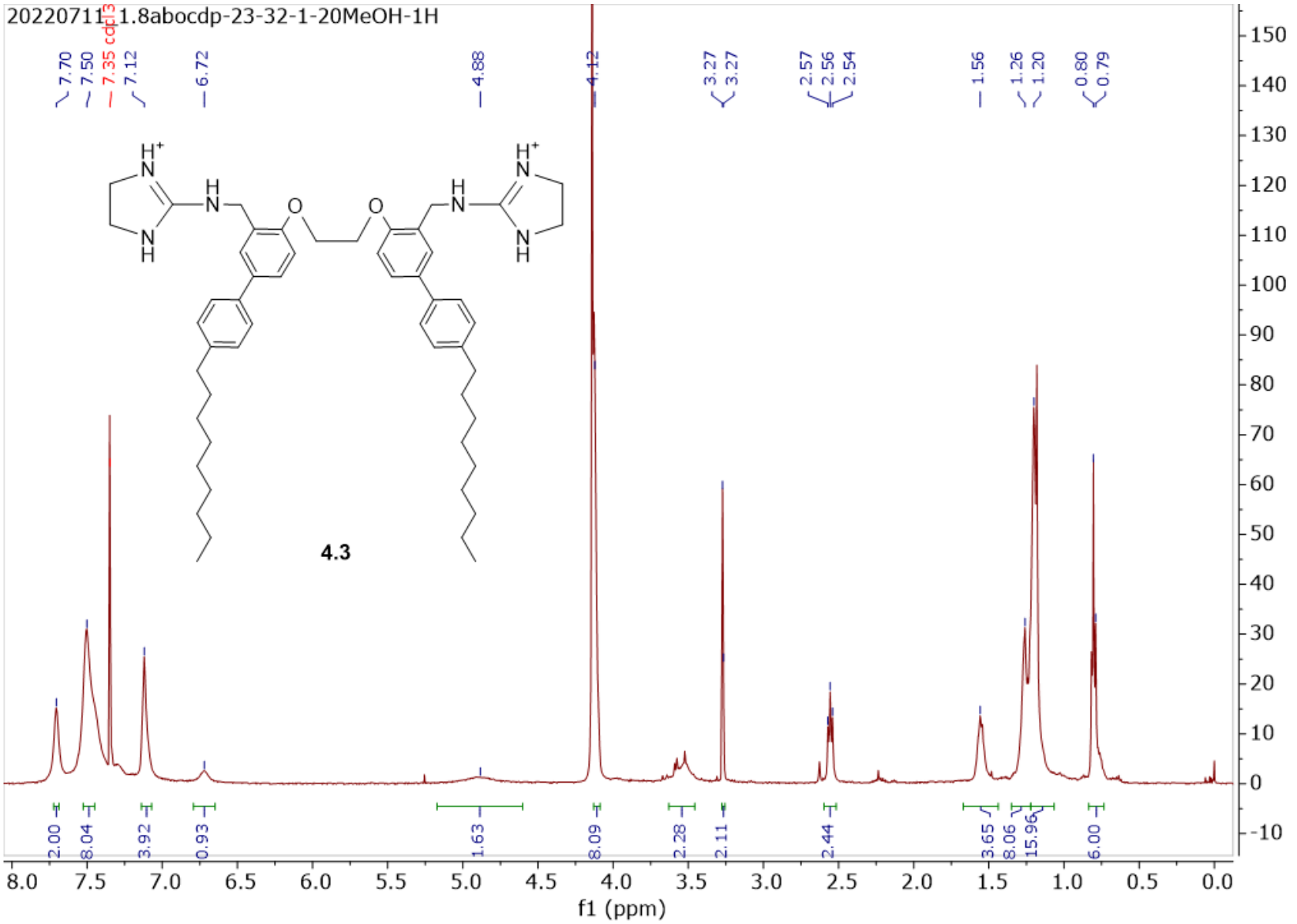
20220711 1.8abocdp-23-32-1-20MeOH-1H
7.70
7.50
7.35 cdcl3
7.12
6.72
4.88
4.12
3.27
3.27
2.57
2.56
2.54
1.56
1.26
1.20
0.80
0.79
4.3
2.00
8.04
3.92
0.93
1.63
8.09
2.28
2.11
2.44
3.65
8.06
15.96
6.00
f1 (ppm)

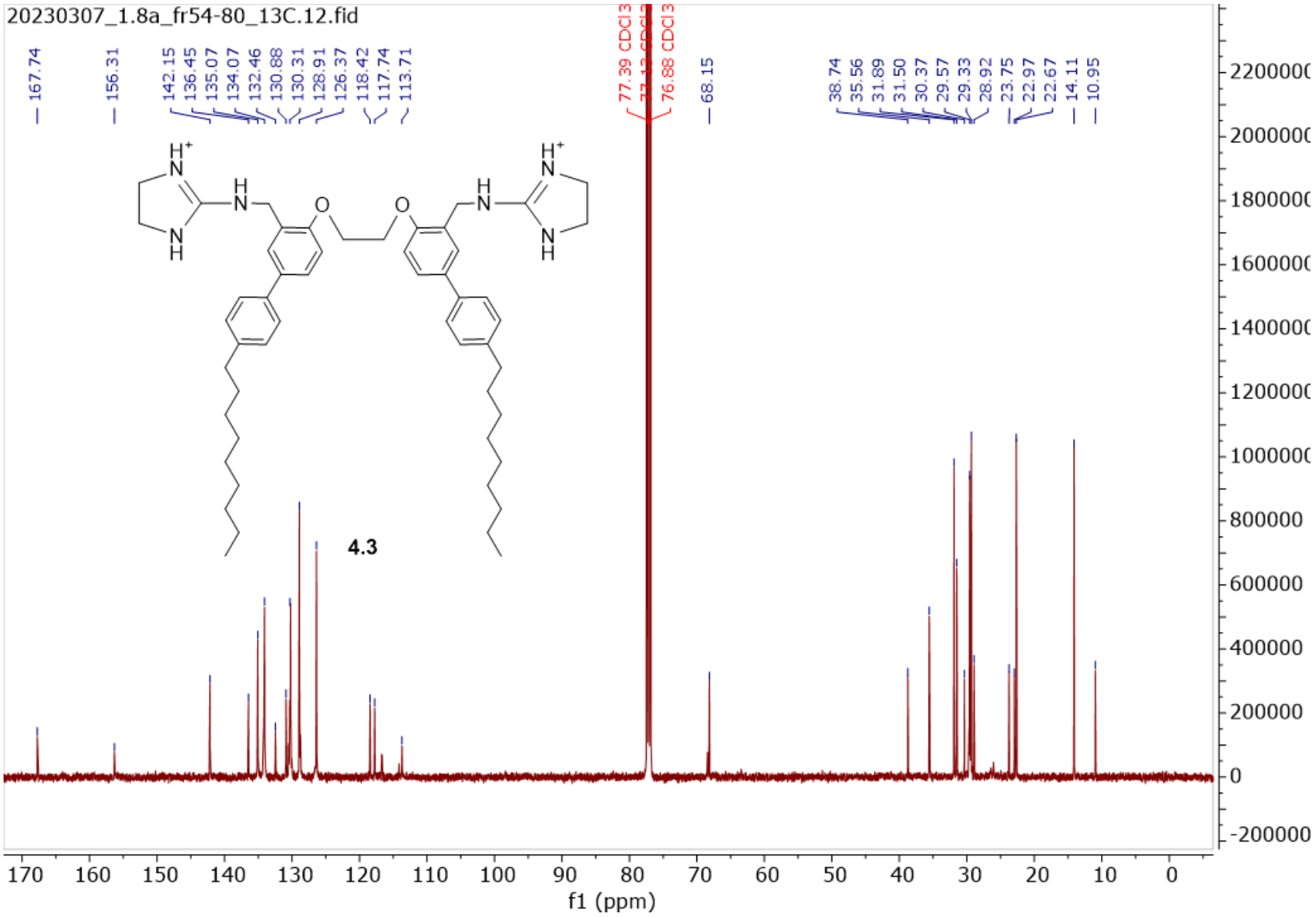
20230307_1.8a_fr54-80_13C.12.fid
167.74
156.31
142.15
136.45
135.07
134.07
132.46
130.88
130.31
128.91
126.37
118.42
117.74
113.71
77.39 CDCl3
76.88 CDCl3
68.15
38.74
35.56
31.89
31.50
30.37
29.57
29.33
28.92
23.75
22.97
22.67
14.11
10.95
4.3
f1 (ppm)

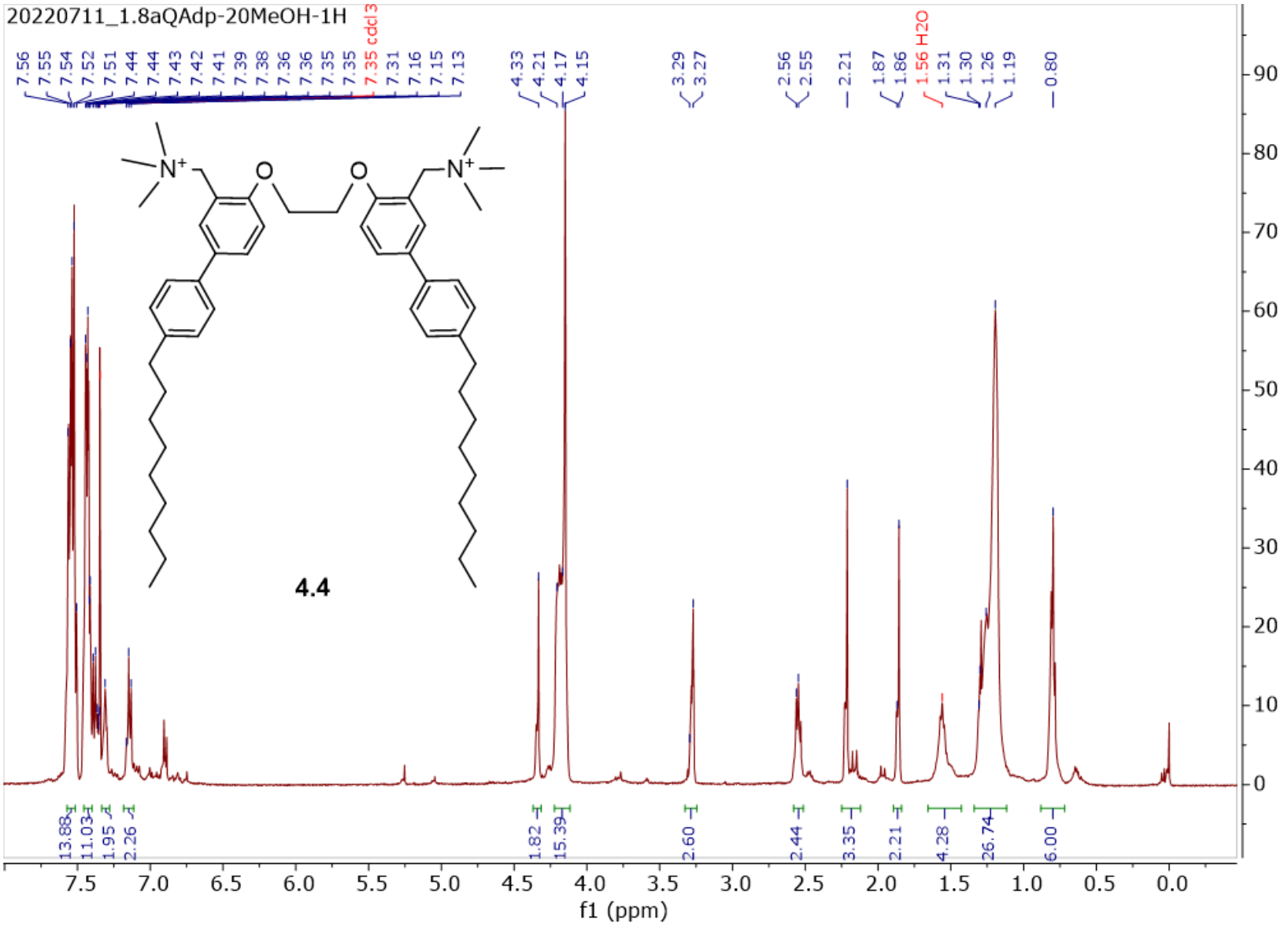
20220711_1.8aQAdp-20MeOH-1H
7.56 7.55 7.54 7.52 7.51 7.44 7.44 7.43 7.42 7.41 7.39 7.38 7.36 7.36 7.35 7.35 7.35 cdcl3 7.31 7.16 7.15 7.13
4.33 4.21 4.17 4.15
3.29 3.27
2.56 2.55
2.21
1.87 1.86
1.56 H2O
1.31 1.30 1.26 1.19
0.80
4.4
13.88 11.03 1.95 2.26
1.82 15.39
2.60
2.44
3.35
2.21
4.28
26.74
6.00
f1 (ppm)

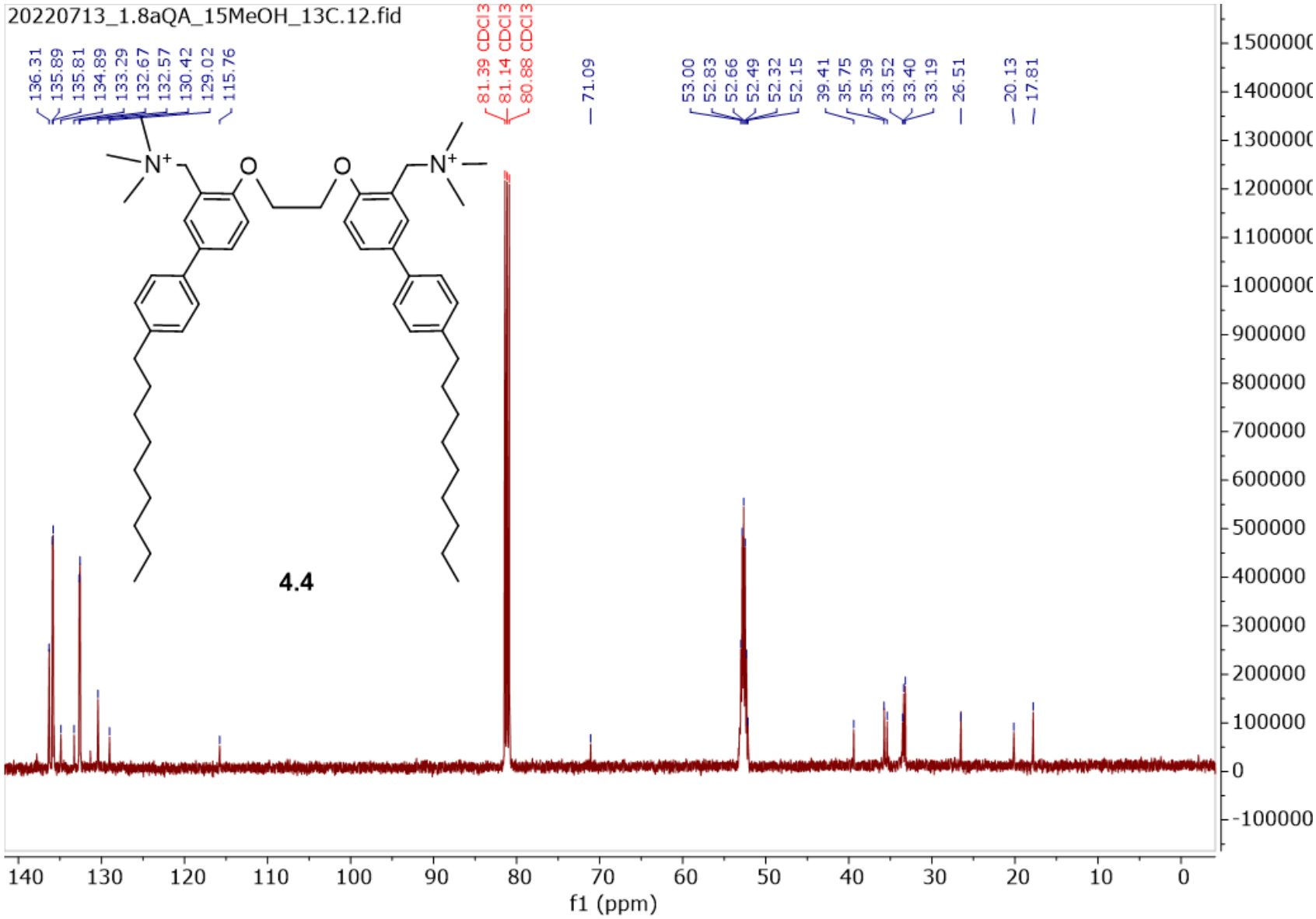
20220713_1.8aQA_15MeOH_13C.12.fid
136.31
135.89
135.81
134.89
133.29
132.67
132.57
130.42
129.02
115.76
81.39 CDCl3
81.14 CDCl3
80.88 CDCl3
71.09
53.00
52.83
52.66
52.49
52.32
52.15
39.41
35.75
35.39
33.52
33.40
33.19
26.51
20.13
17.81
4.4
f1 (ppm)

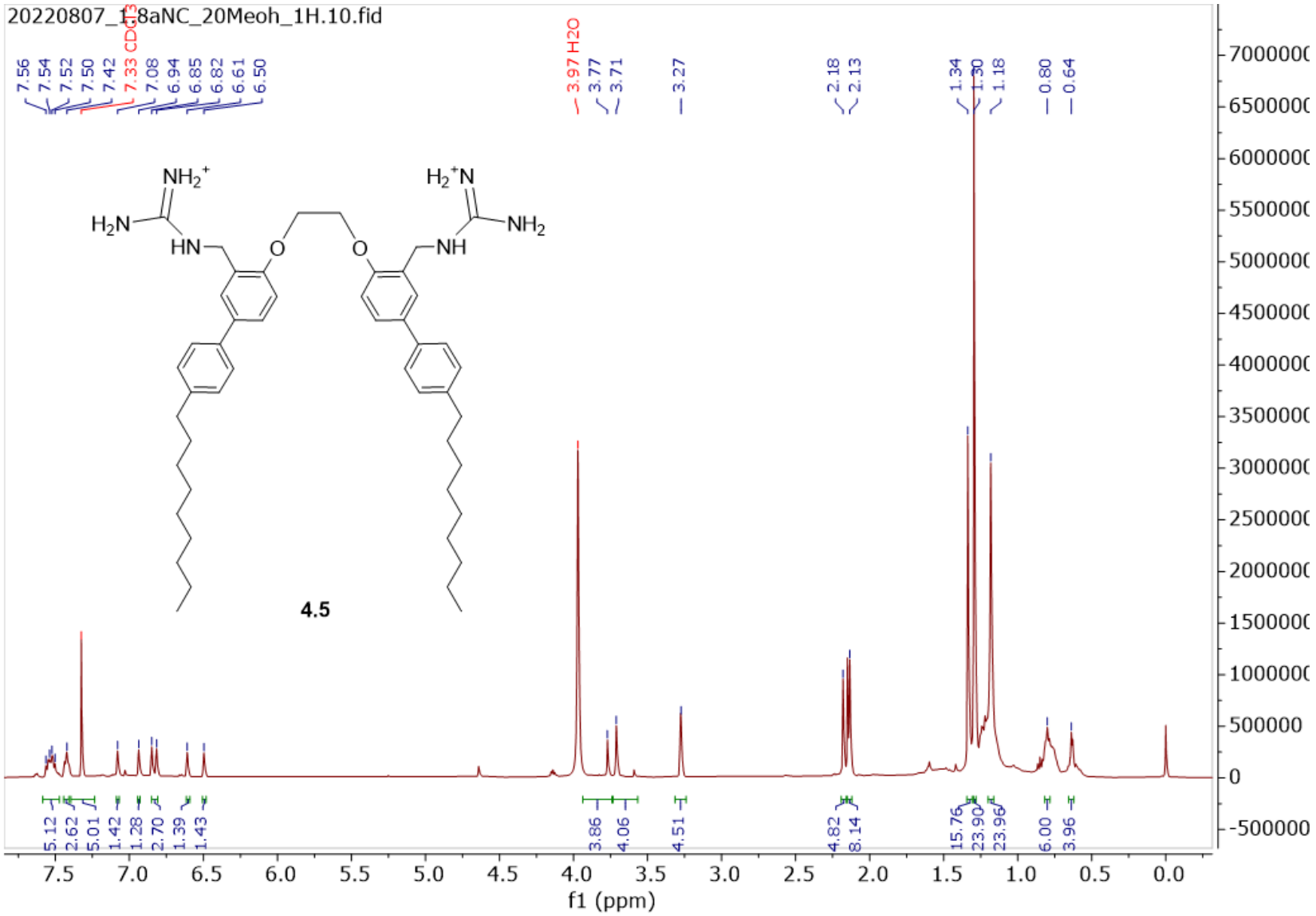
20220807_1_8aNC_20Meoh_1H.10.fid
7.56
7.54
7.52
7.50
7.42
7.33 CD3OD
7.08
6.94
6.85
6.82
6.61
6.50
3.97 H2O
3.77
3.71
3.27
2.18
2.13
1.34
1.30
1.18
0.80
0.64
4.5
5.12
2.62
5.01
1.42
1.28
2.70
1.39
1.43
3.86
4.06
4.51
4.82
8.14
15.76
23.90
23.96
6.00
3.96
f1 (ppm)

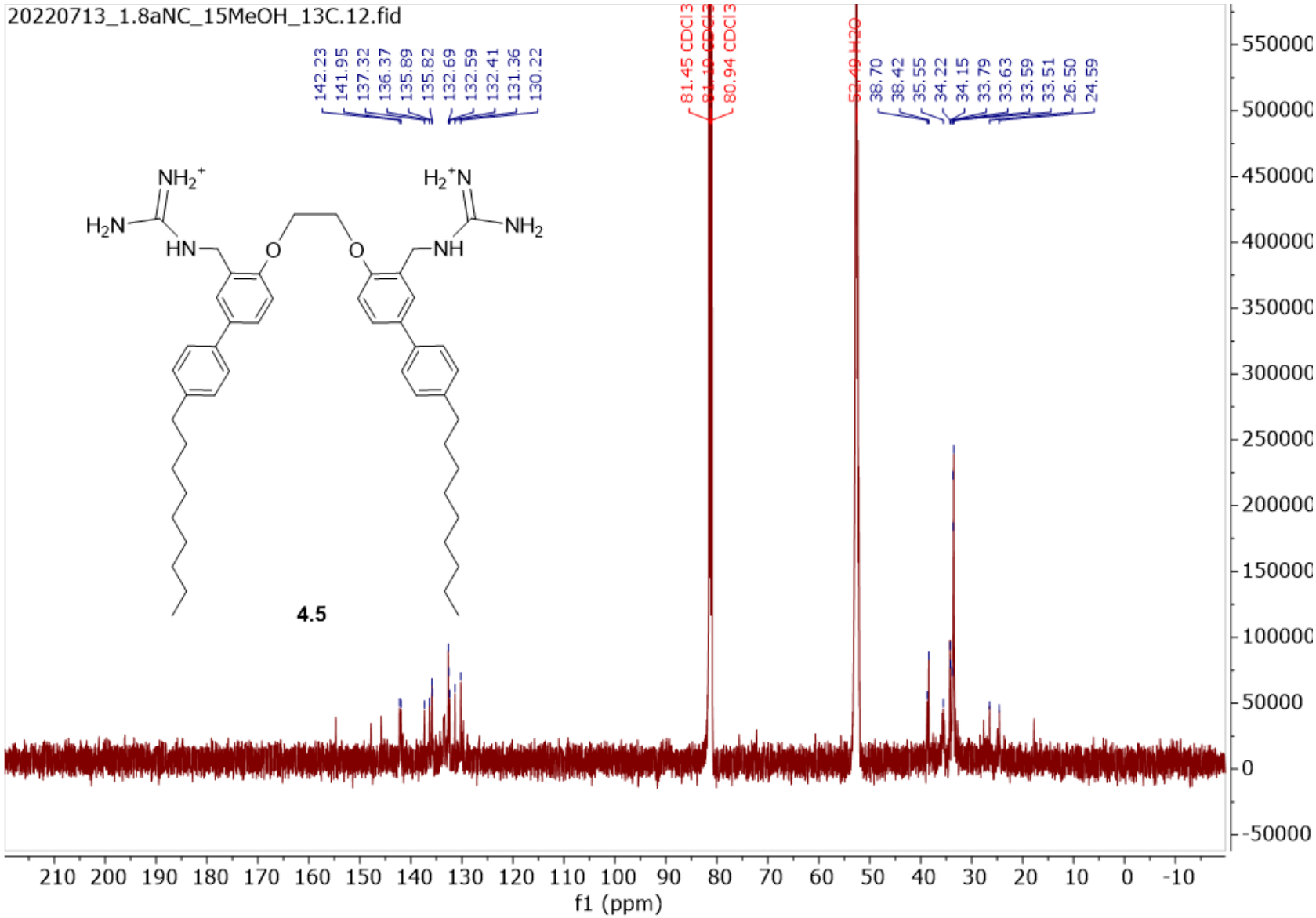
20220713_1.8aNC_15MeOH_13C.12.fid
142.23
141.95
137.32
136.37
135.89
135.82
132.69
132.59
132.41
131.36
130.22
81.45 CDCl3
81.10 CDCl3
80.94 CDCl3
52.49 H2O
38.70
38.42
35.55
34.22
34.15
33.79
33.63
33.59
33.51
26.50
24.59
NH2+
H2N
HN
O
O
H2+N
NH
NH2
4.5
550000
500000
450000
400000
350000
300000
250000
200000
150000
100000
50000
0
-50000
210 200 190 180 170 160 150 140 130 120 110 100 90 80 70 60 50 40 30 20 10 0 -10
f1 (ppm)

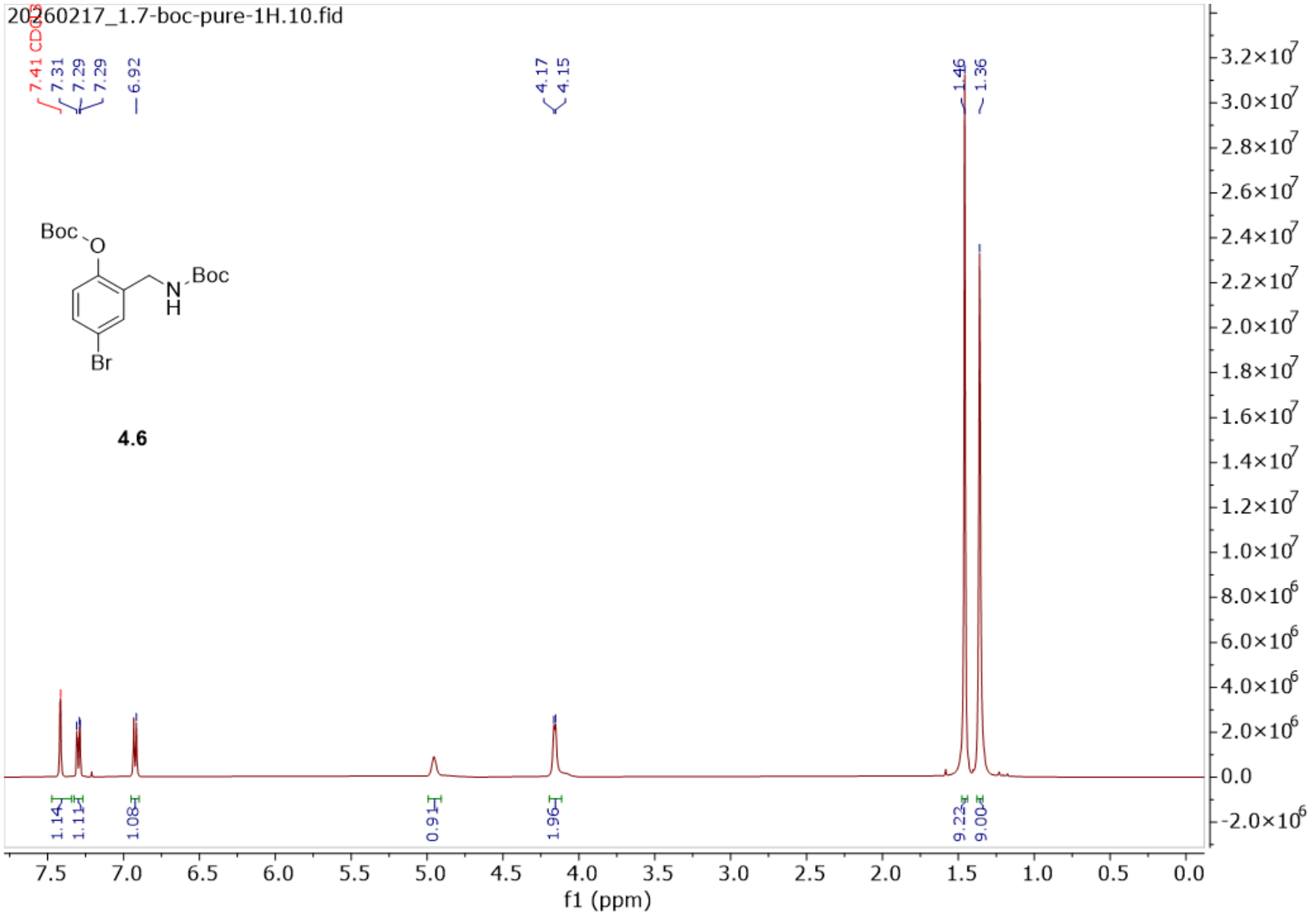
20260217_1.7-boc-pure-1H.10.fid
7.41 CDCl3
7.31
7.29
7.29
6.92
4.17
4.15
1.46
1.36
Boc
O
N
H
Boc
Br
4.6
1.14
1.11
1.08
0.91
1.96
9.22
9.00
f1 (ppm)

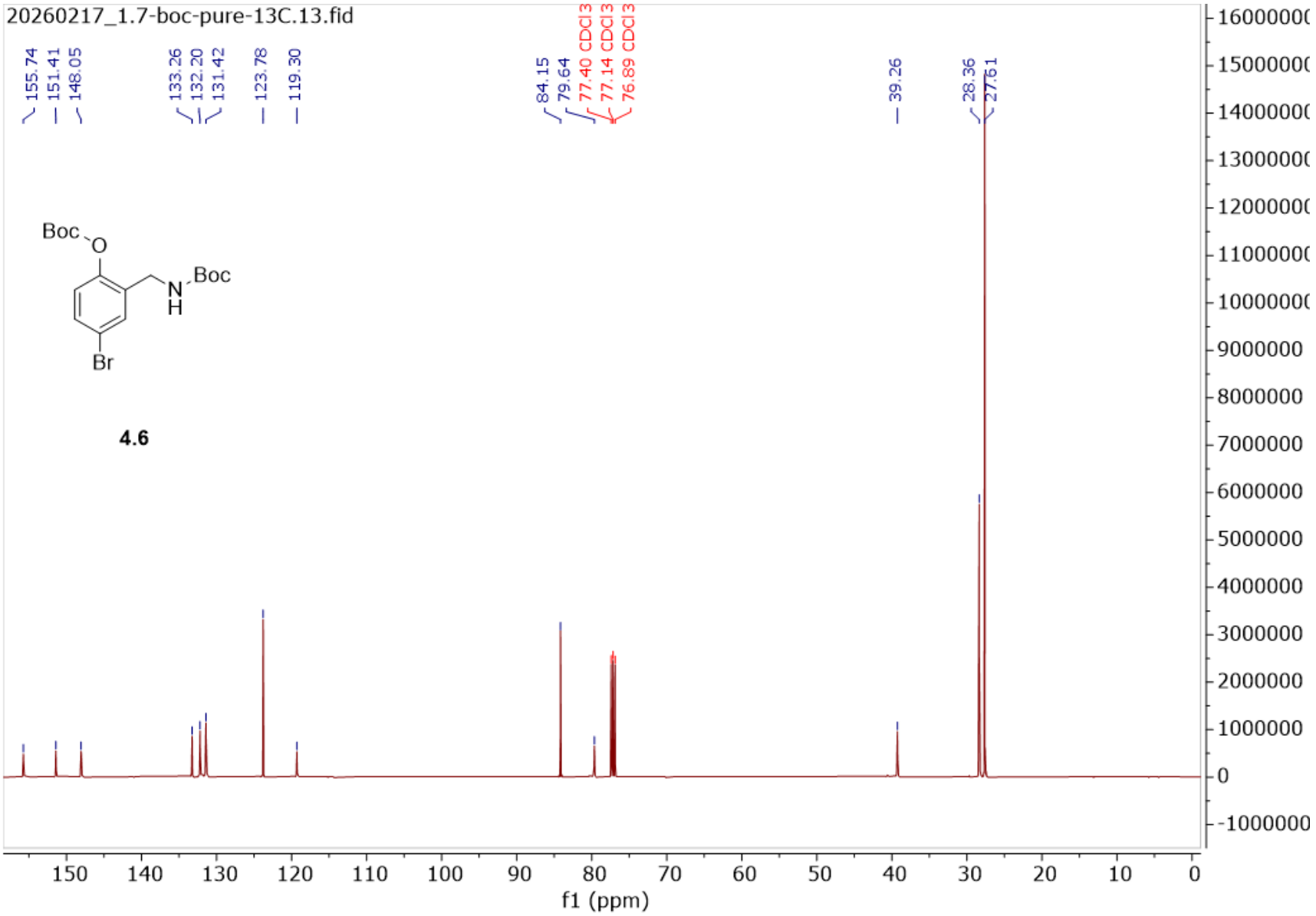
20260217_1.7-boc-pure-13C.13.fid
155.74
151.41
148.05
133.26
132.20
131.42
123.78
119.30
84.15
79.64
77.40 CDCl3
77.14 CDCl3
76.89 CDCl3
39.26
28.36
27.61
Boc
O
N
Boc
H
Br
4.6
f1 (ppm)

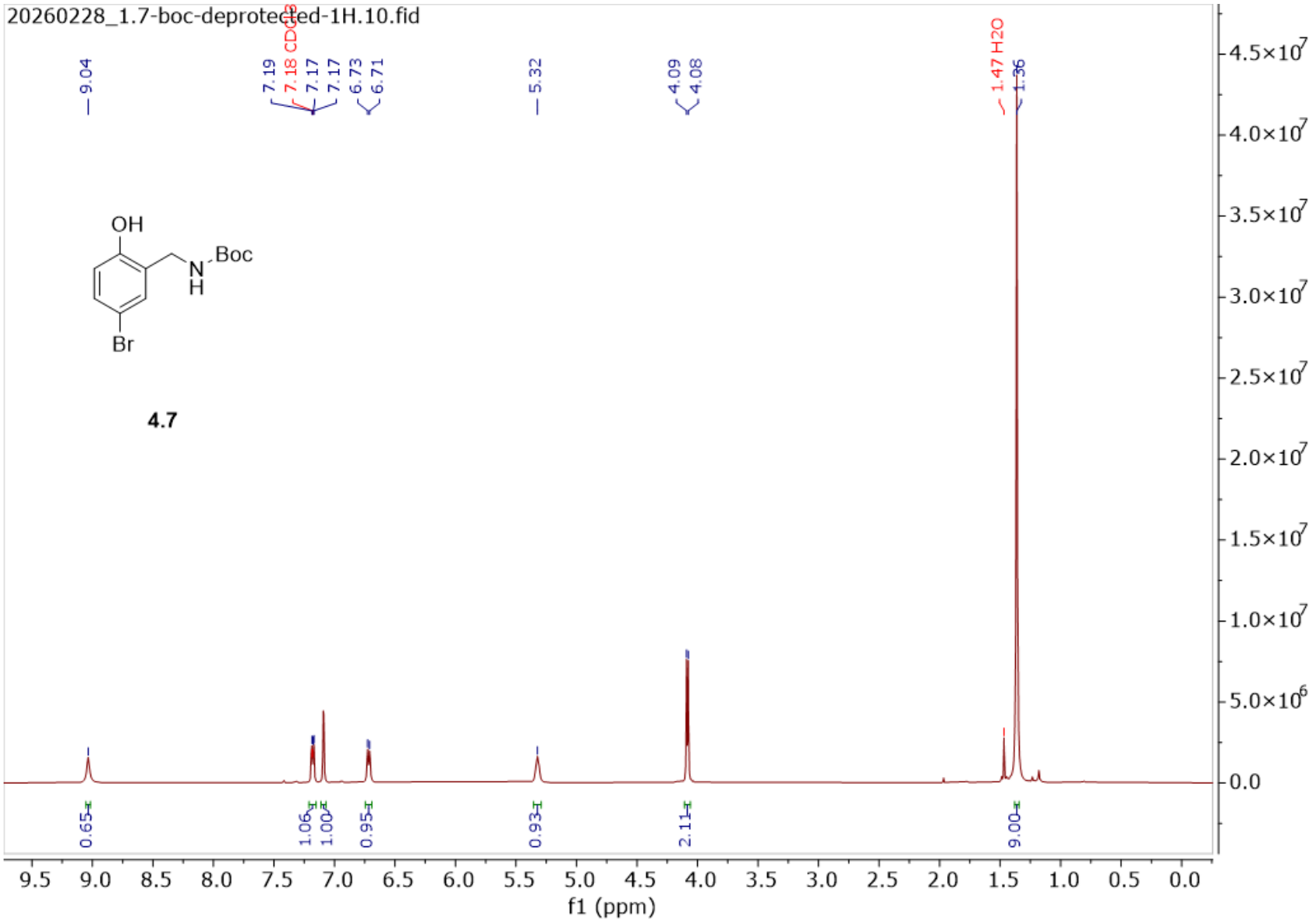
20260228_1.7-boc-deprotected-1H.10.fid
9.04
7.19
7.18 CDCl3
7.17
7.17
6.73
6.71
5.32
4.09
4.08
1.47 H2O
1.36
OH
N
H
Boc
Br
4.7
0.65
1.06
1.00
0.95
0.93
2.11
9.00
f1 (ppm)

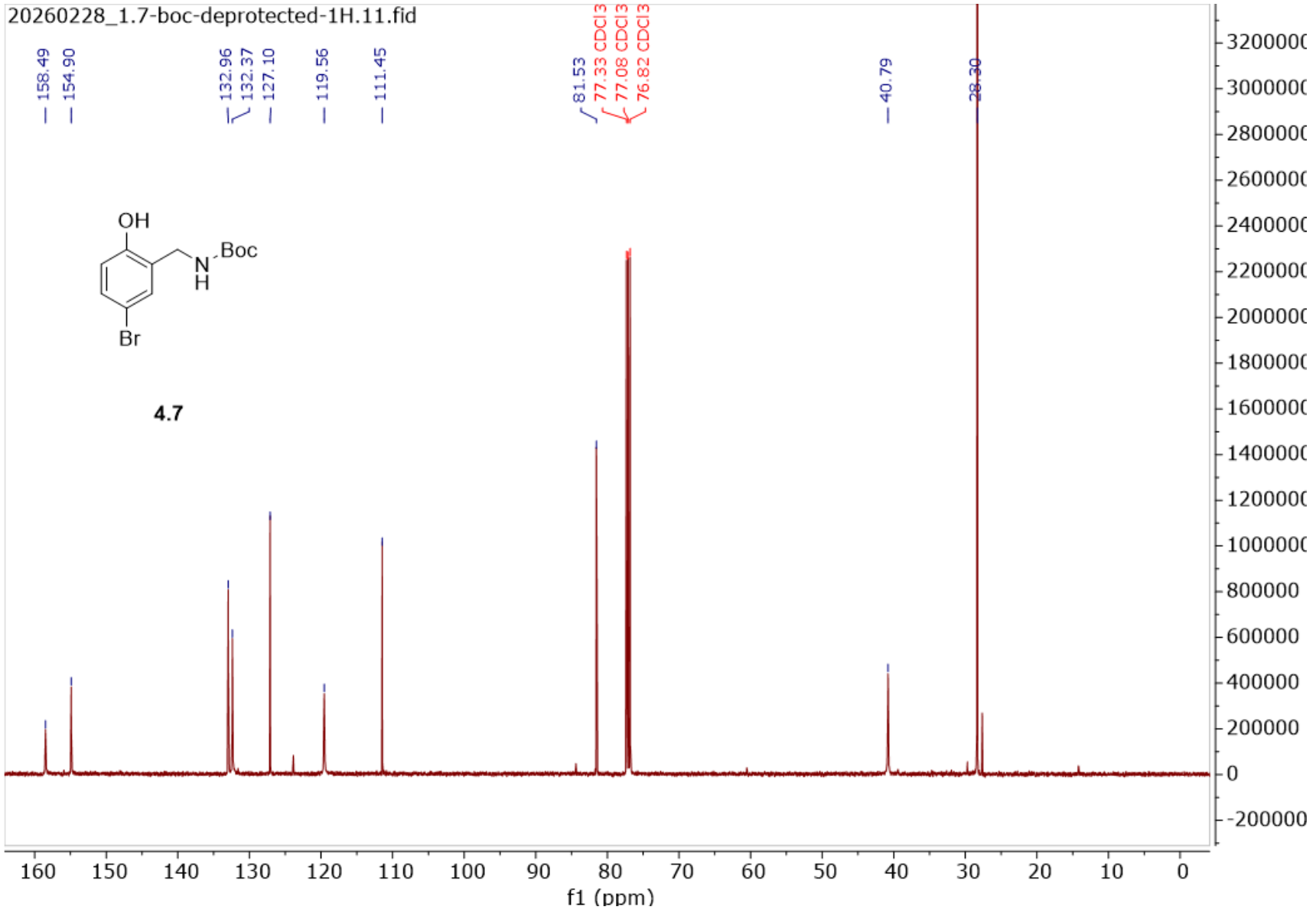
20260228_1.7-boc-deprotected-1H.11.fid
158.49
154.90
132.96
132.37
127.10
119.56
111.45
81.53
77.33 CDCl3
77.08 CDCl3
76.82 CDCl3
40.79
28.30
OH
Boc
N
H
Br
4.7
f1 (ppm)

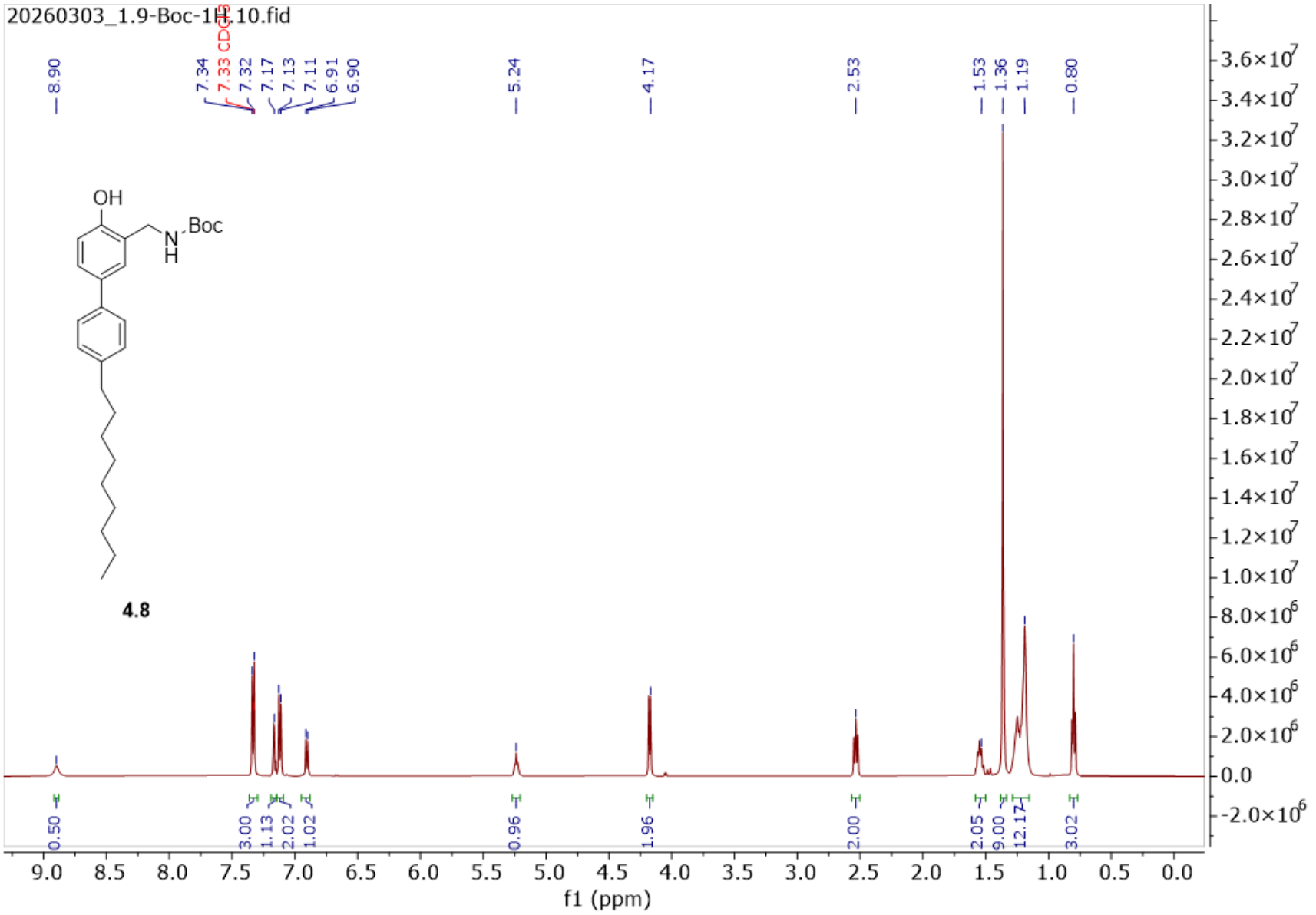
20260303_1.9-Boc-1H.10.fid
8.90
7.34
7.33 CDCl3
7.32
7.17
7.13
7.11
6.91
6.90
5.24
4.17
2.53
1.53
1.36
1.19
0.80
OH
N
H
Boc
4.8
0.50
3.00
1.13
2.02
1.02
0.96
1.96
2.00
2.05
9.00
12.17
3.02
f1 (ppm)

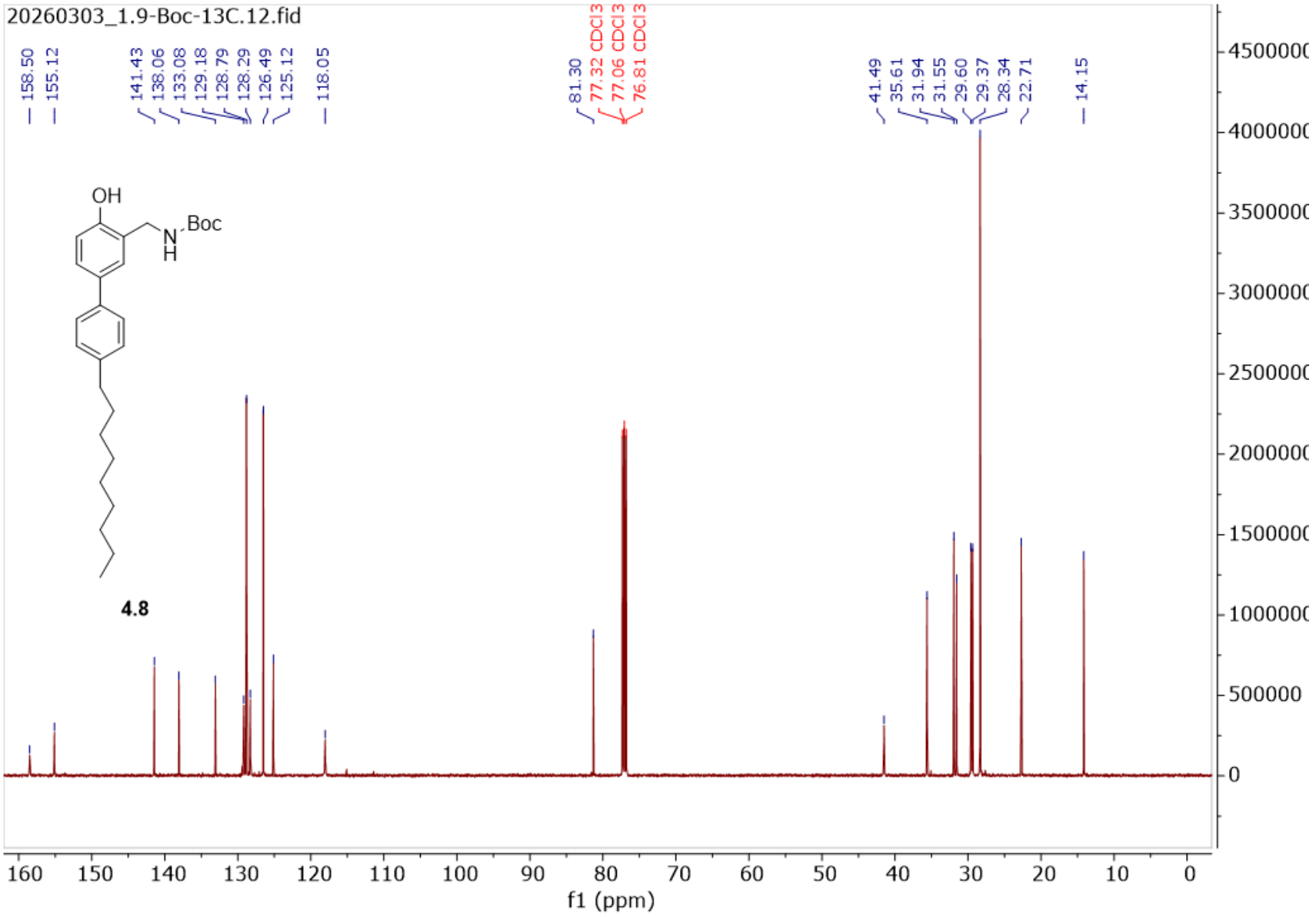
20260303_1.9-Boc-13C.12.fid
158.50
155.12
141.43
138.06
133.08
129.18
128.79
128.29
126.49
125.12
118.05
81.30
77.32 CDCl3
77.06 CDCl3
76.81 CDCl3
41.49
35.61
31.94
31.55
29.60
29.37
28.34
22.71
14.15
OH
N
H
Boc
4.8
450000
400000
350000
300000
250000
200000
150000
100000
500000
0
160
150
140
130
120
110
100
90
80
70
60
50
40
30
20
10
0
f1 (ppm)

VITA

Brooke E. Smith was born in 1999 in Fairfax, Virginia, and was raised in north Georgia. She first developed an interest in science through independent home experiments during her homeschool education. Her formal interest in chemistry began in high school under the instruction of Krista Mauldin, whose teaching fostered a lasting curiosity about chemical principles and problem solving. She earned a Bachelor of Science degree in Chemistry in 2017 from the University of North Georgia, graduating summa cum laude as a member of the Honors Program and a McNair Scholar. As an undergraduate, she conducted research in the laboratory of Dr. Royce Dansby-Sparks, developing sol–gel substrates incorporating gold nanoparticles for selective total reflection X-ray fluorescence detection of Cr(III) and Cr(VI). Her interest in lipid systems and nanocarrier design developed during a 2019 Research Experience for Undergraduates program under Dr. Jessica Rouge at the University of Connecticut. She began her doctoral studies in chemistry at the University of Tennessee, Knoxville, in 2021 and joined the laboratory of Dr. Michael D. Best in January 2022. Her graduate research focused on the design and mechanistic evaluation of stimulus-responsive lipid systems capable of translating endogenous biochemical signals into controlled liposomal cargo release.